MULTIDIMENSIONAL NONLINEAR OPTICAL SPECTROSCOPIES FOR CHEMICAL ANALYSIS

D. Jason Palmer

Submitted to the University of London in partial fulfillment of the degree of Doctor of Philosophy.

May 2005

Department of Chemistry
Imperial College London

Abstract

A central problem in analytical chemistry is the identification of components in complex mixtures and their relative concentrations. While many methods exist to accomplish this, no single methodology presently offers extremely high sensitivity, selectivity, and dynamic range. Recent advances in the generation of stable, tunable laser sources in the mid-infrared have allowed the development of optical analogues to 2-D NMR which probe the couplings between vibrational transitions. As in NMR, these couplings are indicative of the structure and composition of the samples under study. One of these novel 2-D optical methods, known as doubly vibrationally enhanced (DOVE) spectroscopy, shows great promise as a highly selective, sensitive method of probing vibration/vibration coupling, with time resolution on the order of picoseconds (10^{-12} s).

In this work, a DOVE spectrometer has been designed, constructed, and implemented. DOVE spectroscopy has been quantitatively analysed and issues of spectral reproducibility have been addressed. The sensitivities of the method to the experimental parameters are explored, and the development of protocols to ensure reproducibility has allowed proof-of-principle experiments to be carried out on simple liquids. The method was carried forward to produce the first-ever DOVE spectra of the vibrations of solvated amino acids, providing evidence that the method is viable for fingerprinting and structure determination. The variation of 2-D spectra in the time domain is also explored, suggesting the possibility of the use of DOVE spectroscopy as a probe of molecular dynamics. Improvements to the methodology which will make DOVE spectroscopy comparable to existing analytical methods have been proposed.

Acknowledgements

D. Jason Palmer[†]

Department of Chemistry, Imperial College London, London SW7 2AY, UK

It is only fitting that I dedicate this work to my wonderful parents—their unqualified and unwavering support and friendship made it possible to survive the worst of and thereby get to the best of it all. However, a great many other folk were involved in various ways and I would like to express my gratitude for their help and ask them to join me in a sigh of relief that this book is finally done.

Firstly of course I have Dr. Ian Mercer to thank for bringing me to Imperial from sunny California to make the transition "from technician to scientist". Dr. Mercer laid much of the groundwork academically and psychologically for me to continue on after his departure for Powerlase®, and I am grateful that we could both go on to do what we wanted to do and maintain our friendship.

However, the work presented in this thesis was accomplished under the tutelage, and sometimes the rule, of Dr.-cum-Prof. David Klug, who has performed the roles alternately of supervisor, confidant, dim sum menu interpreter, despot, interview coach, funding-finder, sounding board for ideas of varying ludicrousness, cigarette borrower, and demander of numbers. I thank him for setting a great example in the multi-disciplinary approach, for usually keeping out of the lab, and for never mincing words.

Truly completing the triumvirate of supervision is Dr. Alan Taylor, who always made time to listen to my woes and never failed to provide a unique perspective and sound advice, even when I didn't take it.

There have been a couple of people during the course of this Ph.D. who started off as colleagues but in the end became lifelines. With great pleasure I now address one of them as Dr. James Levitt,[1] and my time in London would doubtless have been less rich without him as a drinking partner, radio show co-host, fellow occasionally moody misanthrope, and preternaturally informed music guru. The deepest ruts were escaped and the best ideas formulated sitting with James on the bench at the front of the Chemistry Department—those were not squandered hours.

Dr. Laura Barter has been an invaluable source of advice on countless matters both professional and personal. Her determination and dedication are to my mind without parallel anywhere, and I am proud to have worked with her and to call her a friend. This whole ship would have sunk, and I with it, without her.

If Laura is the glue that holds the group together, then surely Dr. Chris Barnett is the solder. His electronic expertise seems to know no bounds, and I owe him a debt of gratitude for help with the electronics in the experiment, as well as a barely finite number of detection discussions.

Thanks also to Dr. Dave Russell for lots of help in finding the elusive first T_0 and for whipping up our Labview code in characteristic style, and to Paul Donaldson for thoroughness in the unenviable task of trawling through the mode assignment literature and a countless number of amino acid solutions to get us on track for the really interesting science that's going to come out of this.

Many faces have come and gone in my just-a-little-bit-too-long in the group, and without exception have made this group a dynamic, if occasionally odd, place to work. Andy, Bruno, Byung, Chris J., Claire, Dan, Dave, Elizabeth, Halima, Ivan, Je, Soberg, Stefan, Yasu...thanks to you all for the laughs and discussions scientific and otherwise.

My time spent outside the lab was populated with a number of absolutely indispensable friends too, and it is fair to say that their companionship has contributed to the completion of this work (if only to preserve my tenuous grip on sanity). To that end, and cast in order of appearance, thanks to Megan, Emma, Ian 'n' Charlotte, Alli, Tracy & Michael and the kids, Kate 'n' Freya, Marianne, Jody and the anti-South London brigade, Michael E., Felicity and the Usual Suspects, Rob, Scott, Sara and Gabe, me Kate before it all went wrong, Alice, Chloë, Loueeee, Camilla, Joe, Claudia, Johnny Mil$, Alex, Pete, Paolo, Mel... Thanks guys for being there, being patient, being willing to get the next round in, and being a wicked circle of friends. Keep your couches free, I'll be back.

[†]Present address: LENS, Università degli Studi di Firenze, 50019 Florence, Italy.

[1] Levitt, J. A. Ph.D. Thesis, University of London, London, UK, 2005.

Table of contents

Abstract **2**
Acknowlegements **3**
Table of contents **4**
List of figures and tables **7**
List of abbreviations and symbols **11**

Chapter 1. Introduction **12**

1.1. DOVE as a candidate for an analytical technique 12
1.2. An appraisal of present bioanalytical techniques 13
1.3. An introduction to CMDVS techniques 14
1.3.1. Existing CMDVS techniques 15
1.4. Outline of this thesis 16

Chapter 2. An Introduction to the Theory of DOVE spectroscopy **18**

2.1. Fundamentals of vibrational spectroscopy 18
2.1.1. The first approximations 20
2.1.2. Anharmonicity 21
2.1.3. Vibrational dephasing and broadening mechanisms 23
2.1.4. Mode coupling 26
2.2. Nonlinear optics: a brief introduction 27
2.2.1. The nonlinear susceptibility χ 27
2.2.2. The density matrix ρ 30
2.2.3. Resonance enhancement 32
2.2.4. Phase matching 33
2.2.5. Wave mixing electronic level diagrams 36
2.2.6. Examples of nonlinear processes 38
2.2.7. Interference and cascading 40
2.3. Introduction to DOVE-FWM spectroscopy 41
2.3.1. Components of the total measured signal 42
2.3.2. Effects of windows, absorption, refractive index dispersion 47
2.4. Calculations of 2-D spectral data 49

Chapter 3. DOVE spectrometer design **51**

3.1. Introduction – light source 51
3.1.1. Optical parametric amplifiers 53
3.2. Signal size calculations and predictions 56
3.2.1. Initial signal size calculations 56
3.2.2. Signal size calculations: photomultiplier tube 57
3.3. Modelling 57
3.3.1. Phase matching model 58
3.3.2. Index of refraction determination 59

3.3.3. Further considerations in the phase matching model 63
3.4. DOVE Experimental setup 64
3.4.1. Spatial alignment procedure 67
3.4.2. Beam waist size measurements 67
3.4.3. Temporal alignment procedure 68
3.4.4. Detection 72
3.4.5. Constraints of the spectrometer: tuning 76
3.5. Protocols and diagnostics 77
3.5.1. Beam pointing 78
3.5.2. Power/energy 79
3.5.3. Autocorrelators 79
3.5.4. Spectral measurements 79
3.5.5. Protocols - general alignment concerns 81
3.5.6. Seed laser 81
3.5.7. Regenerative amplifier 82
3.5.8. Pump source for regenerative amplifier 83
3.5.9. OPAs 85
3.5.10. SDG – timing 86
3.5.11. Output monitoring 86

Chapter 4. First DOVE Results: Simple liquids 88

4.1. Introduction 88
4.2. Outline of the samples employed 89
4.3. Sample preparation, containment, and analysis 98
4.3.1. Sample cell and holder 98
4.3.2. FTIR analysis of samples 101
4.3.3. Sample preparation 104
4.4. General features of signal and data acquisition 104
4.4.1. Optimisation 105
4.4.2. Linearity 108
4.4.3. Correction/manipulation of data 109
4.5. First DOVE results 111
4.5.1. Acetonitrile/Deuterobenzene 111
4.5.2. Carbon Disulphide/Bromochloromethane 112
4.6. Signal sizes 114
4.6.1. Signal sizes of possible FWM signals 114
4.6.2. DOVE signal as a function of spacer thickness 115
4.7. Sample cell window effects 117
4.8. Temporal behaviour of DOVE signals 120
4.8.1. Build-up of signals and discussion of interferences 120
4.8.2. Suppression of signal components 126
4.8.3. Two-dimensional temporal scans 127
4.9. Dilutions in D_2O 136
4.10. Concluding remarks 138

Chapter 5. Further DOVE Results: Amino acids and polypeptide 139

5.1. Introduction 139
5.2. Survey of amino acids and solvents 139
5.2.1. Choice of solvent 140
5.2.2. Sample preparation 141
5.3. Overview of the relevant amino acid absorptions 142
5.3.1. Absorptions of L-alanine and poly-L-alanine – methyl groups 142
5.3.2. Absorptions of L-glycine and L-arginine – methylene groups 146
5.4. Studies toward a $\delta_a/2\delta_a$ DOVE feature 148
5.5. Studies toward a $\delta_a/\delta_a + \nu$ DOVE feature 152
5.6. 2-D DOVE spectra of alanine, polyalanine, arginine and glycine 158
5.6.1. Alanine 162
5.6.2. Polyalanine 164
5.6.3. Arginine 169
5.6.4. Glycine 171
5.7. Concluding remarks 173

Chapter 6. Conclusions, Perspectives, Current and Future Work.174

6.1. Throughput improvements—ratioing 174
6.1.1. Automation 175
6.1.2. Multiplexing model 176
6.2. Sensitivity improvements 183
6.2.1. Titanium dioxide (TiO2) films 183
6.2.2. Reflection geometries 185
6.2.3. Active heterodyning 185
6.2.4. Background suppression techniques 186
6.2.5. Resonance enhancement with visible excitation 187
6.3. Further dimensionality of the technique 188
6.4. Future research directions 189
6.5. Conclusions and perspectives 190

References 191

List of figures and tables

Chapter 2

Figure 2.1	Functional dependence of the phase matching level on Δkl	35
Figure 2.2	WMEL diagrams for linear processes	37
Figure 2.3	WMEL diagrams for second-order processes	38
Figure 2.4	WMEL diagrams for signal components in the DOVE experiment	43

Chapter 3

Figure 3.1	Schematic diagram of the commercial laser system	53
Figure 3.2	Phase matching condition with and without refractive index dispersion	59
Figure 3.3	Refractive indices for acetonitrile near ν_2	60
Figure 3.4	Refractive indices for acetonitrile near $\nu_2 + \nu_4$	61
Figure 3.5	Phase matching condition in ω_1 for acetonitrile experiments	62
Figure 3.6	Phase matching condition in ω_2 for acetonitrile experiments	62
Figure 3.7	Schematic diagram of the DOVE spectrometer	66
Figure 3.8	Typical ω_1/ω_2 cross-correleation	69
Figure 3.9	Curve describing FWHM scaling factors for cross-correlation	71
Figure 3.10	Absorbance vs. angle of incidence for dielectric mirror	73

Chapter 4

Figure 4.1	FTIR of neat acetonitrile, ω_1 region	90
Figure 4.2	FTIR of neat acetonitrile, ω_2 region	90
Figure 4.3	FTIR of deuterobenzene/acetonitrile solutions, ω_1 region	92
Figure 4.4	FTIR of deuterobenzene/acetonitrile solutions, ω_2 region	92
Figure 4.5	FTIR of neat carbon disulphide, ω_1 region	93
Figure 4.6	FTIR of neat carbon disulphide, ω_2 region	93

Figure 4.7	FTIR of carbon disulphide/bromochloromethane solution, ω_1 region	94
Figure 4.8	FTIR of carbon disulphide/bromochloromethane solution, ω_2 region	94
Figure 4.9	FTIR of neat propan-1-ol, ω_1 region	96
Figure 4.10	FTIR of neat propan-1-ol, ω_2 region	96
Figure 4.11	FTIR of solutions of propan-1-ol in D_2O, ω_1 region	97
Figure 4.12	FTIR of solutions of propan-1-ol in D_2O, ω_2 region	97
Figure 4.13	Picture of the sample cell disassembled	98
Figure 4.14	FTIR of alanine/D_2O solution before and after experiment	101
Table 4.1	Summary of errors in spacer thickness measurement	103
Figure 4.15	Plot of signal vs. sample stage position	106
Figure 4.16	1-D DOVE spectra in alanine/D_2O with and without nitrogen purge	107
Figure 4.17	Plot of signal linearity with ω_3 pulse energy	109
Figure 4.18	1-D DOVE spectra in acetonitrile for different optimisation frequencies and timings	112
Figure 4.19	2-D DOVE spectrum of carbon disulphide in bromochloromethane	113
Table 4.2	Summary of phase matched parameters for two coherence pathways	115
Figure 4.20	Plot of DOVE signal vs. spacer thickness	116
Figure 4.21	Polar plot of window signal vs. rotation, 2 mm sapphire	118
Figure 4.22	Polar plot of window signal vs. rotation, 100 μm sapphire	119
Figure 4.23	Plot of decay of signal components vs. ω_3 delay	121
Figure 4.24	Plot of decay of propan-1-ol signal vs. ω_3 delay showing oscillations	122
Figure 4.25	1-D DOVE spectra in neat propan-1-ol	124
Figure 4.26	Standard deviations of 3 daily points of figure 4.25	124
Figure 4.27	1-D DOVE spectra of propan-1-ol for varying ω_2 values	125
Figure 4.28	1-D DOVE spectra showing suppression of CARS contribution	127
Figure 4.29	Schematic representation of various pulse orderings	128

Figure 4.30	Temporal scans of propan-1-ol DOVE signal in t_{12}	129
Figure 4.31	Schematic of pulse orderings in 2-D temporal space	130
Figure 4.32	Temporal 2-D contour plot of DOVE signal in neat propan-1-ol	131
Figure 4.33	Temporal 2-D contour plot of DOVE signal in neat D_2O	132
Figure 4.34	Temporal 2-D contour plot of DOVE signal in carbon disulphide/bromochloromethane	133
Figure 4.35	WMEL diagrams of DOVE signal components	134
Figure 4.36	1-D DOVE spectra of dilutions of propan-1-ol in D_2O	137

Chapter 5

Figure 5.1	FTIR spectra of H_2O and D_2O in ω_2 region	141
Figure 5.2	FTIR of alanine/D_2O solution, Fermi doublet region	143
Figure 5.3	FTIR of alanine/D_2O solution, methyl bend region	143
Figure 5.4	FTIR of alanine and polyalanine/D_2O solutions, combination band region	144
Figure 5.5	FTIR of alanine and polyalanine/D_2O solutions, methyl bend region	145
Figure 5.6	FTIR of glycine and alanine/D_2O solutions, combination band region	146
Figure 5.7	FTIR of glycine and alanine/D_2O solutions, methylene bend region	147
Figure 5.8	WMEL diagrams representing harmonic and anharmonic energy level progressions	149
Figure 5.9	Temporal 2-D contour plot of DOVE signal from alanine/D_2O solution	150
Figure 5.10	1-D temporal plots from figure 5.9	151
Figure 5.11	1-D DOVE spectra in alanine/D_2O for various pulse timings	152
Figure 5.12	Temporal scans in t_{12} showing alanine/D_2O signal variation at two pulse timing pairs	154
Figure 5.13	Comparison of 1-D DOVE spectra in alanine/D_2O for the pulse timing pairs of figure 5.12	154
Figure 5.14	WMEL diagrams of DOVE signal components	155
Figure 5.15	Schematic representation of pulse overlap and CARS vs. DOVE-Raman contributions	156

Figure 5.16	WMEL diagrams showing conditions for DOVE-IR and DOVE-Raman dominance in signal	157
Figure 5.17	2-D DOVE spectrum of alanine/D_2O	160
Figure 5.18	2-D DOVE spectrum of polyalanine/D_2O	161
Figure 5.19	Repeat of figure 5.17 with peaks numbered	162
Table 5.1	Summary of peaks in figure 5.19	162
Figure 5.20	Repeat of figure 5.18 with peaks numbered	164
Table 5.2	Summary of peaks in figure 5.20	165
Figure 5.21	2-D DOVE spectrum of arginine/D_2O	167
Figure 5.22	2-D DOVE spectrum of glycine/D_2O	168
Figure 5.23	Repeat of figure 5.21 with peaks numbered	169
Table 5.3	Summary of peaks in figure 5.23	169
Figure 5.24	Repeat of figure 5.22 with peaks numbered	172
Table 5.4	Summary of peaks in figure 5.24	172

Chapter 6

Figure 6.1	Schematic representation of "forward-box" geometry	178
Figure 6.2	Output angle map for multiplexing model	179
Table 6.1	Summary of input parameters for multiplexing model	180
Figure 6.3	2-D and 3-D plots of phase matched multiplexed signal level	181
Figure 6.4	SEM of a TiO_2 film and picture of substrate with protein-loaded TiO_2 film	184

List of abbreviations and symbols

ACN/MeCN	acetonitrile (methyl cyanide)
BBO	β-barium borate
CARS	coherent anti-Stokes Raman spectroscopy
CMDVS	coherent multidimensional vibrational spectroscopy
DFM	difference frequency mixing
DOVE	doubly vibrationally enhanced
FTIR	Fourier transform infrared
FWHM	full width at half maximum
FWM	four wave mixing
IR	infrared
MS	mass spectrometry
NMR	nuclear magnetic resonance
OPA	optical parametric amplification/amplifier
OPG	optical parametric generation
PMT	photomultiplier tube
SFM	sum frequency mixing
SWM	six wave mixing
TWM	three wave mixing
WMEL	wave mixing electronic level

t_{12} *(t_{23})*	time between arrival of pulses 1 and 2 *(2 and 3)*
T_0	complete temporal overlap of pulses
ω_i	frequency of the i^{th} pulse
γ_r	molecular rocking vibration
γ_w	molecular wagging vibration
δ	molecular bending vibration
ν	molecular stretching vibration

1. Introduction

This thesis presents a recently developed nonlinear optical spectroscopy known as doubly vibrationally enhanced four wave mixing (DOVE-FWM) as a powerful analytical technique for the detailed study of the composition and dynamics of complex molecular systems and mixtures. It employs infrared pulsed laser excitations to selectively probe coupled vibrations, yielding multidimensional data which gives insight into structure and dynamics on an ultrafast timescale.

Existing analytical methodologies individually exhibit the qualities of high sensitivity at low concentrations, the ability to study condensed phase samples, high throughput, or temporal resolution down to the timescale of molecular interactions. However, no single method presently exists to nondestructively accomplish a full frequency- and time-resolved fingerprint of a condensed-phase sample consisting of a large number of components at a wide range of concentrations. Though the technique is still in its infancy, the pilot studies presented in this thesis constitute a convincing demonstration that DOVE-FWM is a method which with further development can accomplish this task.

1.1. DOVE as a candidate for an analytical technique

The key to DOVE-FWM and related techniques is that they directly probe vibration/vibration coupling, in analogy to the coupling of spins in NMR. The resultant spectra spread information into two spectral dimensions, reducing the spectral congestion which plagues linear techniques. Further, DOVE-FWM in particular succeeds in removing the influence of the individual modes because it is generally carried out in a 2-D spectral space where two infrared laser frequencies are far from one another, known as the off-diagonal region. In this region, peaks (crosspeaks) only appear for coupled modes, so that DOVE-FWM gives exclusively information on coupled modes and their relative coupling strength. It is this feature which makes DOVE-FWM an exceedingly promising technique for structural determination as well as simply "fingerprinting"—structural changes in a given sample induce changes in the coupling, and advances in calculational methodologies

will in the future bring DOVE-FWM to the fore as a structural probe. The extreme utility of the ultrafast laser system with which the DOVE-FWM experiments have been carried out ensure an enormous spectral space available for future studies, so that certain "fingerprint regions" analogous to the linear infrared spectroscopy fingerprint region can be found. Further, the ultrafast nature of the excitations, shorter than many of the dynamical processes in biological systems, shows that systematic changes in the timing of the excitations can provide a snapshot of structural information on picosecond (10^{-12} s) or even femtosecond (10^{-15} s) timescales, easily outperforming existing techniques in terms of temporal resolution.

1.2. An appraisal of present bioanalytical techniques

The fields of analytical chemistry, proteomics, and molecular and cell biology have benefited enormously from the development of a number of powerful analytical techniques. In particular, multidimensional nuclear magnetic resonance (NMR) and mass spectrometric (MS) methodologies have allowed the structural determination for a wide range of biologically relevant molecules and mixtures, with molecular masses in excess of 100 kDa, and advances in instrumentation will certainly continue to improve the resolution and efficacy of these methods. However, each of the predominant bioanalysis methods suffers from limitations.

NMR is extraordinarily powerful as a structural probe but is not particularly sensitive because it probes the extremely small nuclear magnetisation, requiring milligrams of sample for full structural determination. The NMR experiment averages over the spin-spin dephasing time, on the millisecond timescale, so that direct measurement of dynamical information is limited to similar timescales.

MS techniques that have been developed into bioanalytic tools such as MALDI-TOF generally require very labour-intensive sample preparation and are necessarily destructive, requiring that the molecular samples be ionised, fragmented, and launched into the gas phase for analysis. Further, MS techniques suffer from a trade-off between mass resolution (and thereby molecular specificity) and dynamic range: existing instruments cannot analyse a sample comprising a large range of masses at very high resolution.

Two-dimensional polyacrylamide gel electrophoresis, or 2D-PAGE has particular strengths in terms of molecular specificity but is time-intensive to carry out

and labour-intensive to analyse. Recent advances in gel image analysis software are improving the throughput of the method, but the fundamental limitations in terms of reproducibility and insensitivity to varying abundances of proteins have not yet been addressed.

Of course, linear optical spectroscopies have matured in recent years in an attempt to tackle the analysis of complex molecules and mixtures, but the incredible structural complexity of biological systems has limited the ultimate utility of linear spectroscopies because of the significant spectral congestion. The long-sought optical analogue to multidimensional NMR has been realised recently, largely due to the development of commercially available, widely tuneable laser sources, and the techniques that comprise this analogue are broadly brought together under the umbrella of Coherent Multidimensional Vibrational Spectroscopy (CMDVS), of which DOVE-FWM is just one example. However, it will be shown that for the purposes of developing a bioanalytical technique, DOVE-FWM is particularly appropriate, showing potential for sensitivity, temporal resolution, and throughput exceeding that of existing techniques.

1.3. An introduction to CMDVS techniques

The underlying physics of multidimensional NMR and CMDVS techniques is conceptually very similar—both can be cast in the Bloch equation picture of coupled two-level systems, with the formalism describing the magnetic dipole transitions of NMR in perfect analogy with that describing the electric dipole transitions of vibrations. Additionally, there are a great many experimental details which are analogous between the two approaches, and it is not without reason that several recent publications have detailed these analogies.[1-4] A full exposition of the similarities from both an experimental and theoretical standpoint is developed in a recent publication[3] and not repeated here, but it is worthwhile considering a few of the dissimilarities between the methods. NMR methods have reached their tremendous utility and ubiquity for two primary reasons: firstly, the availability of a limitless number of easily generated magnetic pulse sequences allows the manipulation of spin coherences to elucidate particular couplings or eliminate others. The second reason is that the spectra obtained with these carefully constructed pulse sequences can be deconvoluted without extensive theoretical modeling to provide

structural information in terms of a set of bond lengths and bond angles. In the optical analogue, only a few pulses are available, and the presence of each optical pulse exponentially complicates the experimental process. Phase cycling techniques that are standard in NMR are not possible in IR analogues, as the particular choice of coherence manipulation is determined by a fixed phase matching condition (explored in Chapter 2). Though simulations of some CMDVS experiments have shown good agreement with experimental data, it is not presently possible to invert the 2-D spectra and achieve quantitative structural data for biomolecules larger than peptides of ~10 residues. Thus, though the analogy between these two methodologies is fair, a few fundamental differences must be overcome before CMDVS methods are comparable to multidimensional NMR for structural analysis.

1.3.1. Existing CMDVS techniques

A number of techniques exist in the literature which fall under the category of CMDVS, and a large amount of work has been published on implementing these techniques for the purpose of structural and dynamical investigations of biomolecules. A full exposition of these techniques is beyond the scope of this introduction, but the reader is referred to a recent review in which all of these techniques are put into a common framework and their experimental implementations are compared.[5] In particular, 2-D pump-probe and vibrational photon echo techniques and their variants have proven very useful in elucidating the coupling of modes in various oligopeptides, leading to structure determination and providing experimental data which, in tandem with calculational methodologies, is advancing the state of CMDVS techniques as valuable structural probes.

For the specific interest presented here, however, it is important to note that both of these approaches utilise infrared detection as well as excitation, and the efficiency of detection for infrared radiation is markedly lower than for visible radiation. DOVE-FWM provides an output in the visible region of the spectrum, and the ability to detect visible light down to the single photon level will permit DOVE-FWM spectroscopy to exceed the detection limits of competing CMDVS techniques. Moreover, the great majority of the CMDVS work carried out to date is in the diagonal region of 2-D spectral space, i.e., where two infrared excitations are near in frequency. This region is particularly spectrally crowded (though a method exists for removing diagonal features to isolate cross-peaks in analogy to NMR pulse

sequences with the same effect[6]) and limits the total spectral space that can be investigated—as will be shown, DOVE-FWM succeeds as an analytical technique because there is no limitation on the frequency difference between the infrared excitations.

1.4. Outline of this thesis

In Chapter 2, some fundamentals of linear vibrational spectroscopy and nonlinear optics are presented with relation to DOVE-FWM. The complex physical processes which give rise to the detected signal are presented from a theoretical and diagrammatic standpoint to provide a framework on which to present the experimental results.

Chapter 3 details the design, construction, and implementation of the DOVE-FWM spectrometer, outlining some of the ultrafast laser technology which has been the enabling advancement for these nonlinear vibrational spectroscopies. The development of a novel temporal alignment technique was necessary for these experiments, and is outlined in detail. A model for the optimisation of output signals is presented. As the laser system utilised in this work was only the second of its kind, a great many protocols had to be developed to keep the system in an optimal working condition, and the chapter closes with a detailed discussion of these protocols, which have been necessary to acquire repeatable data with high signal-to-noise ratio.

Chapters 4 and 5 outline the experiments carried out and data acquired with the spectrometer. Chapter 4 focuses on the development of the technique from the repeats of experiments by DOVE-FWM's progenitor to a viable method for bioanalysis. This remains one of only few research groups in the world carrying out DOVE-FWM experiments, and the first group worldwide to use the method on biological systems. As such, it was necessary to develop the methodology from the ground up, and a great many experiments were carried out to verify the efficacy of the method and study the sensitivities of the technique to various experimental conditions and parameters. With questions of data veracity and reproducibility addressed, a number of experiments are discussed as a prelude to DOVE-FWM spectra on biologically relevant molecules.

Chapter 5 focuses on the DOVE-FWM spectra of three amino acids and a polypeptide as a powerful demonstration of the unique structural information provided by DOVE-FWM. Amino acid residue side chains exert a significant influence on peptide and protein secondary structure, and the side chains are largely where the molecular reaction mechanism can be traced. Thus the studies undertaken in amino acids were specifically to probe the vibrational coupling in aliphatic side chains, which are conveniently well separated from the congested amide I region. This choice of spectral regions is particularly illustrative for future experiments because of the presence of alkyl groups in all amino acids. The chapter demonstrates the first-ever 2-D optical spectra of amino acid side chain vibrations and relates the results to published linear spectra, providing for the first time assignments of vibrational bands which are obscured in linear spectra.

The experimental chapters provide a striking demonstration of the power of DOVE-FWM spectroscopy but several improvements are necessary to make it competitive with existing techniques in terms of sensitivity and throughput. Chapter 6 includes an appraisal of DOVE-FWM spectroscopy as well as presenting a number of these improvements. In particular, an extension of the model presented in Chapter 3 is outlined, demonstrating the potential of a technique that will enormously improve throughput. Along with the strengths of DOVE-FWM presented in Chapters 4 and 5, the improvements outlined in Chapter 6 are certain to bring DOVE-FWM into the family of more familiar bioanalytic techniques.

2. An Introduction to the Theory of DOVE spectroscopy

In this chapter, some fundamental concepts and theory for multidimensional spectroscopy will be presented. DOVE-FWM spectroscopy is only one of several related techniques under the rubric of Coherent Multidimensional Vibrational Spectroscopies (CMDVS) and these related techniques are discussed with reference to their strengths and weaknesses in terms of the specific purpose of this project. A brief review of vibrational spectroscopy is presented, including discussions of a few concepts key to the understanding of the nonlinear optical processes involved. All of the laser-based techniques employ a number of nonlinear optical steps in order to generate the infrared radiation that makes these spectroscopies possible, and some fundamental theory of nonlinear optics is presented to put these various steps into context. This introductory text is only to provide a framework for the experimental details and results presented in further chapters; it is by no means complete. There have been excellent reviews published particularly on the theoretical aspects of CMDVS techniques, and the interested reader is referred to them for more complete descriptions.[5,7-9]

2.1. Fundamentals of vibrational spectroscopy

Molecular vibrations are simply the relative motion of nuclei in molecular systems, and the nuclei of atoms and the chemical bonds between them are approximated classically as motions of masses on springs. These motions are developed theoretically as elements of the system's Hamiltonian, and the resulting eigenstates are known as vibrational modes. The development of the masses-on-springs view from a classical mechanics standpoint leads to solutions from simple harmonic motion. This approximation is not only incomplete, it precludes the very processes that will be experimentally explored in further chapters.

While the majority of this thesis focuses on infrared transitions, it is worth noting that two forms of (linear) vibrational spectroscopy exist: infrared and Raman, with selection rules pertinent to each process. Infrared spectroscopy simply

measures the absorption of incoming radiation as a function of frequency. Raman transitions come about when incoming radiation is inelastically scattered by a molecule or crystal lattice, and the difference in energy between the incident and emitted radiation corresponds to vibrational energy level spacing. The selection rules for the spectroscopies are such that they provide different but complementary information about the molecules under study. Modes which appear in an infrared spectrum are said to be infrared active, and only appear if the dipole moment of the molecule or moiety changes during the relative motion of the nuclei. Raman-active modes on the other hand only come about when the polarisability of the molecule or moiety changes during the relative motion of the nuclei. Except where noted, the theoretical development in this chapter makes no distinction between the two mechanisms.

Lines in a vibrational spectrum are significantly narrower at room temperature than electronic transitions. This is in part because of the great difference in masses of nuclei and electrons, making nuclear motions much less polarisable than electron clouds, and also because electronic transitions have a significantly stronger interaction with the local environment. Thus electronic transitions are spectrally very broad at room temperature, whereas vibrational transitions are narrow.

Further, the mechanical view of vibrations as masses on springs leads to very well defined frequencies for various pairs or groups of atoms (functional groups). These "group frequencies" form the basis for interpretive infrared spectroscopy of unknown samples—in general, group frequencies occur in narrow frequency ranges regardless of the molecule that contains the group. More detailed study of the exact position of the group frequency gives some information as to the environment local to that group. The specificity of the modes' occurrences at characteristic frequencies makes vibrational spectroscopy a powerful tool in identifying the different molecules or moieties that are present in a given sample. For simple molecules, the vibrational spectrum is uncluttered, and the contributions of the relatively small number of narrow vibrational bands can be easily assigned to well-known group frequencies for various moieties. However, in more complex molecular systems where hundreds or thousands of groups are present and similar moieties may occur many times, each in a different environment, the characteristic bands overlap, and an assignment of all of the modes from just the linear spectrum becomes impossible. Multidimensional techniques overcome this limitation of the 1-dimensional or linear approaches. To

introduce these multidimensional approaches, it is useful to build up the theoretical background from the simplest case.

2.1.1. The first approximations

The development of vibrational spectroscopy from a theoretical standpoint begins with a number of assumptions, some of which break down at various levels when applied to real polyatomic systems. Considered here are the normal mode picture and the harmonic potential energy surface, whose assumptions are appropriate for many experiments, but are incomplete in the case of nonlinear vibrational spectroscopy.

2.1.1.1. The normal mode analysis

In considering polyatomic molecules that are not of a linear structure consisting of n atoms, it can be shown that there are $3n - 6$ displacements of the nuclei corresponding to molecular vibrations. It is possible to develop the total energy function for a polyatomic system by judicious choice of coordinates (the normal coordinates) such that there are no cross-terms in the energy expression corresponding to motions along different normal coordinates. Then the 3N – 6 displacements are cast along these coordinates and become the normal modes for the system. These normal modes are a sort of orthogonal basis set for all of the possible motions of the system. In the equations presented henceforth, the displacements (the degree to which the "spring" is stretched) from equilibrium designated x or x_i in equations will be taken to be along a normal coordinate.

2.1.1.2. The harmonic potential energy surface

We consider first the molecular potential energy of a diatomic molecule, with a displacement x from equilibrium nuclear positions and expand the potential energy in a Taylor series:[10]

$$V(x) = V(0) + \left(\frac{dV}{dx}\right)_0 x + \frac{1}{2!}\left(\frac{d^2V}{dx^2}\right)_0 x^2 + \frac{1}{3!}\left(\frac{d^3V}{dx^3}\right)_0 x^3 + \ldots. \qquad \textbf{(equation 2.1)}$$

Here as elsewhere, the zero subscript requires that the derivatives be taken at zero displacement. A first approximation to the total potential energy involves discarding the terms in x higher than quadratic. Given a zero potential at zero displacement (V(0) = 0), the remaining quadratic term leads to a parabolic potential energy surface

which is perfectly analogous to the classical harmonic oscillator. However, these higher order terms cannot always be ignored, and a more realistic potential energy surface must be considered. It will be shown that these higher order terms for the potential are essential for the understanding of complete vibrational spectra of polyatomic molecules, and thus for the crucial understanding of mode coupling.

2.1.2. Anharmonicity

In a system with a harmonic potential, energy levels are evenly spaced. However, many systems have some degree of anharmonicity. Generally two kinds of anharmonicity are discussed: mechanical and electronic. Each has its own effect on the allowed transitions and thus on the vibrational spectrum.

Mechanical anharmonicity occurs when a potential energy surface is not purely parabolic, so the restoring force to an equilibrium bond length is no longer linearly related to the displacement. The result is an uneven spacing of energy levels.

Electronic anharmonicity on the other hand is a nonlinearity in the dipole moment. In a harmonic system, the dipole moment is linearly related to the displacement, but electronic anharmonicity introduces higher-order terms for the dipole moment. The effect of this kind of anharmonicity is to change the intensity of given transitions, but contrary to mechanical anharmonicity does not change their frequencies.

To investigate the effects of electronic anharmonicity, we consider the transition dipole moment operator and its associated matrix. The development here is adapted from reference 10. Energy levels are denoted by their vibrational quantum number v. In short, the intensity of a transition from molecular energy level v to v' (by convention, $v' \leftarrow v$) is proportional to the square of the transition dipole moment μ, given by

$$\mu_{v'v} = \langle v' | \mu | v \rangle \qquad \textbf{(equation 2.2)}$$

where μ is the dipole operator. Assuming that, like the molecular potential energy, the dipole operator depends solely on the displacement from equilibrium x, it can be expanded as

$$\mu = \mu_0 + \left(\frac{d\mu}{dx}\right)_0 x + \frac{1}{2}\left(\frac{d^2\mu}{dx^2}\right)_0 x^2 + \ldots$$

(equation 2.3)

The μ_0 term on the right is the permanent dipole of the system, and the remaining terms describe the variation of the net dipole with displacement along a normal coordinate. For a many-level system, the values that the vibrational quantum numbers v and v' can take result in a transition dipole matrix corresponding to all the possible transitions between levels. The matrix element corresponding to the $v' \leftarrow v$ transition is then obtained by substitution of equation 2.3 into 2.2:

$$\mu_{v'v} = \mu_0 \langle v'|v\rangle + \left(\frac{d\mu}{dx}\right)_0 \langle v'|x|v\rangle + \frac{1}{2}\left(\frac{d^2\mu}{dx^2}\right)_0 \langle v'|x^2|v\rangle + \ldots$$

(equation 2.4)

The first term vanishes in the normal mode picture because states v and v' are orthogonal. Here the selection rule for vibrational transitions becomes clear; the matrix element is nonzero only if the derivative of the dipole with respect to displacement is nonzero. The harmonic approximation is to also discard the third term, assuming that the dipole moment varies purely linearly with the displacement. In the harmonic approximation, the only nonzero transition dipole matrix elements correspond to changes in vibrational quantum number equal to ±1. The most common example of this is the fundamental transition $1 \leftarrow 0$.

Electronic anharmonicity requires that the higher order terms in equation 2.3 to be taken into account. If we generalise equation 2.3 to

$$\mu = \mu_0 + \sum_i \left(\frac{\partial\mu}{\partial x_i}\right)_0 x_i + \sum_{i,j} \left(\frac{\partial^2\mu}{\partial x_i \partial x_j}\right)_0 x_i x_j + \ldots$$

(equation 2.5)

it can be seen that there are cross terms in the dipole moment proportional to $x_i x_j$ and so on. For $i \neq j$, this is effectively mixing the motions along different normal coordinates, and the orthogonality of these coordinates has thus been relaxed. The result is a nonzero transition dipole for transitions to eigenstates which would

normally be two orthogonal modes. The physical manifestation of this is the appearance of combination bands, wherein the excitation of a mode near the frequency sum of two modes becomes possible. If we consider the case $i=j$ (motion along the same normal coordinate), this corresponds to changes in vibrational quanta such that $\Delta v > 1$, previously disallowed. These are overtones of the fundamental mode ($\Delta v = 1$).

Combination bands can also come about because of mechanical anharmonicity. If we generalise equation 2.1 as the potential energy function for polyatomic molecules, the result is

$$V = \frac{1}{2}\sum_{i,j}\left(\frac{\partial^2 V}{\partial x_i \partial x_j}\right)_0 x_i x_j + \frac{1}{3!}\sum_{i,j,k}\left(\frac{\partial^3 V}{\partial x_i \partial x_j \partial x_j}\right)_0 x_i x_j x_k + \ldots \qquad \textbf{(equation 2.6)}$$

where the summation is over all normal coordinates *i, j, k,* etc. The second and any higher order terms are now included in the presence of any mechanical anharmonicity, and effectively reduce the independence (orthogonality) of the normal coordinates x_i, x_j, etc. and mixing of these coordinates can equally lead to the existence of combination bands.

2.1.3. Vibrational dephasing and broadening mechanisms

The frequencies of vibrational transitions discussed in the context of this chapter may appear to be discrete, i.e. at a single well-defined frequency. Indeed, even in the anharmonic case, the classical solutions give rise to infinitely narrow, nondecaying oscillation frequencies. If we consider the equation of motion for a single diatomic oscillator, there is a phase term in the sinusoidal motion. When an ensemble of identical oscillators is excited with the same frequency and phase, in the absence of any interaction between the oscillators, there is still a discrete frequency for the excitation. In real systems, however, there is always some degree of interaction between the oscillators, and between each oscillator and its local environment, or the "bath". This coupling is ultimately what causes vibrations to decay. Transition frequencies in the condensed phase are therefore not discrete, rather they are modulated on various timescales by various mechanisms. While vibrational transitions give rise to bands which are narrow compared to electronic

transitions, they are more broadened compared to bands acquired in gas-phase samples, and the relative influence of the environment on the linewidth is easily seen.

The distinction between different mechanisms of the decay of the oscillations is best explored using one lineshape derivation known as the Kubo model, an approach which considers the transition frequency ν as time-dependent and modulated by a small amount[11]

$$\nu(t) = \nu_0 + \delta\nu(t) \qquad \textbf{(equation 2.7)}$$

and the modulation amplitude is defined as the RMS value of δν:

$$\Delta = \left\langle [\delta\nu(t)]^2 \right\rangle^{\frac{1}{2}} \qquad \textbf{(equation 2.8)}$$

The timescale of the modulation τ is indicative of the mechanism that induces it. Two cases can now be defined. If τ is longer than $1/\Delta$, the modulation is said to be "slow" and the decay of the state is promoted by the interference of different oscillators with different phase terms. This effect results in an absorption line which is representative of the distribution of modulation, often resulting in a Gaussian lineshape. This spreading of the absorption line (consisting of a statistical distribution of overlapping bands representing the different static frequencies) is known as inhomogeneous broadening. Conversely, if τ is shorter than $1/\Delta$, the modulation is said to be "fast" and the phase shifts and interferences tend to be averaged out. This typically results in a Lorentzian lineshape and is known as homogeneous broadening.

Typically these two broadening mechanisms are differentiated by their macroscopic manifestations; for instance, increasing the temperature of a sample from 0 K induces a statistical distribution of collisional energies, which in turn induces a statistical distribution of transition energies. This uniform spreading of the average transition frequency is the effect of homogeneous broadening. On the other hand, in complex molecules in solution, identical moieties may be present in very different local environments in terms of secondary structure or exposure to solvent, and so each has its isolated transition frequency shifted by a different amount, an

effect of inhomogeneous broadening. Both arise because of a dephasing of the vibrational excitation, and this dephasing is made up of more than one component.

Consider a band in an absorption spectrum with a linewidth Γ (FWHM) of $1/\pi T_2$. Its Fourier transform is a decaying exponential with time constant T_2, and we consider the different mechanisms which can affect the value of T_2. If the amplitude of individual oscillators goes to zero, this is termed "population relaxation" and the timescale of this process is designated T_1—effectively the upper state lifetime. The local environment or bath of the oscillator which gives rise to this spectral band can modulate the frequency of the transition because of thermal fluctuations. This changes the phase terms in the oscillators, or shifts the frequencies of individual oscillators, and will cause interference between the different phases. The ensemble will decay with a time constant dictated by the degree to which the environment exerts an influence. The isolated contribution from these frequency and phase shifts is termed "pure dephasing" and is designated T_2^*. The total dephasing T_2 (and the linewidth it defines) is then made up of both of these terms:

$$\frac{1}{T_2} = \frac{1}{2T_1} + \frac{1}{T_2^*} \qquad \textbf{(equation 2.9)}$$

and the linewidth Γ can be defined as

$$\Gamma = \frac{1}{2\pi T_1} + \frac{1}{\pi T_2^*} + \Gamma_{or} \qquad \textbf{(equation 2.10)}$$

Γ_{or} is the orientational contribution to the linewidth, arising because of the actual rotation of dipoles. Its contribution is normally taken to be negligible, and only the first two terms of equation 2.10 are considered. It is normally assumed in theoretical developments that pure dephasing is a dominant effect in the overall dephasing in condensed phase systems because the measured pure dephasing is roughly an order of magnitude shorter than the population relaxation.[11,12]

2.1.4. Mode coupling

Many vibrational modes are coupled to one another to a greater or lesser degree—a fact which is very intuitive if the picture of masses on springs is considered. This coupling can be intramolecular, describing the influence of one vibration on another within the same molecule, or intermolecular, with vibrations on different molecules influencing one another. The situation can be further complicated by the coupling of molecular modes to the bath. The anharmonicities as described in section 2.1.2 allow the mixing of normal coordinates and transitions of various symmetries, so that overtones and combination bands appear in the vibrational spectrum. While the intensities of these bands give insight into the degree of coupling between the modes that comprise the combination bands, anharmonicity and coupling are not one and the same—anharmonic but uncoupled systems are common, but combination bands do not exist for uncoupled modes.

There is an enormous number of normal modes for a typical biological molecule (Barth estimates in excess of 20,000 for an average yeast protein[13]), so that the vibrational spectrum is hopelessly crowded by overlapped absorption lines consisting of all of the fundamentals, overtones, and combination bands, each of which can be inhomogeneously broadened by local structure variations, solvent/solute interactions, etc. While the method of interpretive spectroscopy, employing assignment of bands based on well-known group frequencies, is very powerful in simpler cases, it is extraordinarily difficult to unravel the details of composition or structure in this situation. The purpose of multidimensional techniques is to reduce this spectral crowding by isolating only the coupled modes, removing the fundamental vibrations and, in some cases, vastly reducing the inhomogeneous broadening that obscures structural information. This is accomplished by selectively enhancing particular coupled transitions within an inhomogeneously broadened envelope, as the couplings for different components within the envelope will almost certainly be different. DOVE-FWM spectroscopy will be shown to simplify molecular spectra and to begin to give compositional and structural information heretofore impossible to determine from 1-D or linear spectroscopies alone. In order to understand the physical processes underpinning these techniques, an introductory exposition of nonlinear optics is presented.

2.2. Nonlinear optics: a brief introduction

The whole of the field of spectroscopy is the study of the polarisation that is induced by an applied electric field or fields. This polarisation is basically an induced dipole brought about by the field and can occur by distorting the electron cloud around atoms and molecules (in the case of, e.g., UV/Vis absorption spectroscopy) or by exciting nuclear vibrational degrees of freedom (in the case of, e.g., FTIR). The most commonly encountered cases are linear spectroscopies. This is to say that the polarisation that is induced by the electric field has a linear relationship with the magnitude of the field. To a very good approximation, this is indeed the case in standard absorption spectroscopies. For the work presented in this thesis, however, an alternate case must be considered.

2.2.1. The nonlinear susceptibility χ

The polarisation induced in a sample as a consequence of an input electric field E is effectively a time-dependent induced dipole and is phenomenologically described by a Taylor expansion in the net field magnitude:

$$P = \chi^{(1)}E + \chi^{(2)}E^2 + \chi^{(3)}E^3 + \ldots + \chi^{(n)}E^n \qquad \textbf{(equation 2.11)}$$

Here, the $\chi^{(i)}$ are tensors known as the i-th order susceptibility, and the origin of "nonlinear" becomes apparent. While the higher order (nonlinear) terms exist in any induced polarisation, the $\chi^{(i)}$ represent very small coefficients to the higher order terms in the field, so that for low field strengths, these terms are negligible. In this case, an incident low-field laser would induce a sinusoidally varying polarisation which launches its own field at the same frequency—interactions between the incident and resultant fields culminate in the familiar effects of absorption and refractive index dispersion. In the case of higher-intensity or focused lasers, however, the higher order terms in equation 2.11 must be considered because the field strengths present at the focus of lasers make them significant.

The $\chi^{(i)}$ have tensor as opposed to scalar character because the induced molecular polarisation has a dependence on the plane of polarisation of (all of) the input field(s). There is thus a tensor element for all the combinations of the input and output field polarisation directions. Thus the $\chi^{(i)}$ in three spatial dimensions have

$3^{(i+1)}$ elements, each of which has a functional dependence on the frequency of the field, temperature, etc. For most cases, symmetry considerations limit the number of independent, nonzero elements in the tensor. These $\chi^{(i)}$ are not so unfamiliar; consider the refractive index n or dielectric constant ε:

$$n_0 = (1+4\pi\chi^{(1)})^{1/2} = \varepsilon^{1/2} \qquad \textbf{(equation 2.12)}$$

For isotropic media, the tensor nature of $\chi^{(1)}$ can be ignored, and the index of refraction as well as the dielectric constant ε can be considered as scalars, but it is easy to see how the elements of $\chi^{(1)}$ play a part in, for instance, birefringent media. For the purposes of this work, the tensor character of χ is not explored; in a given experiment, fixed polarisations of the input beams set the particular tensor element of χ that is being probed, and for this work, only one set of polarisations is considered.†

The mixing of *n* intense input beams induces an oscillating nonlinear polarisation in a sample. The spatial variation of the induced polarisation is distorted somewhat from the sinusoidal variation of the low-intensity case, and the Fourier components of this distortion give rise to new fields launched at the linear combinations of all of the input fields.[7] These resultant fields are measured in multi-wave mixing schemes where *n* fields are incident on a sample and the output is measured as the (*n+1*)th beam, a process known as *n+1* wave mixing, or n^{th} order spectroscopy. The *n* input fields can be said to probe the $\chi^{(n)}$ in these processes, some of which will be further pursued in the following sections. For the moment we consider a four-wave mixing scheme with input fields $E_{1\text{-}3}$. An oscillating polarisation *P* is induced by these fields, given by[14]

$$P = \sum_n \chi_n^{(3)} E_{net}^3 \qquad E_{net} = E_1 + E_2 + E_3 \qquad \textbf{(equation 2.13)}$$

The $\chi^{(3)}$ is actually a bulk quantity, and the microscopic polarisability for each molecule is related to this macroscopic variable by

† The input beams in the DOVE experiment are all horizontally polarised, resulting in a horizontally polarised output beam. By convention, this experiment probes only $\chi^{(3)}_{1111}$ but this subscript will be henceforth omitted.

$$\chi^{(3)} = NF\gamma \qquad \textbf{(equation 2.14)}$$

N is the number density and γ is the microscopic polarisability. F is a local field enhancement factor, which takes into account the fact that the local electric field in the sample is enhanced by alignment of the induced dipoles with the externally applied field. F is formally defined as

$$F = \left(\frac{n_1^2+2}{3}\right)\left(\frac{n_2^2+2}{3}\right)\left(\frac{n_3^2+2}{3}\right) \qquad \textbf{(equation 2.15)}$$

where the n_i are the indices of refraction at the frequencies of the input fields E_i. The polarisation produced in this way in turn launches a fourth time-evolving field E_4 related to the polarisation by the Maxwell equation

$$\nabla^2 E_4 - \frac{1}{c^2}\left(\frac{dE_4^2}{dt^2}\right) = \frac{4\pi}{c^2}\left(\frac{dP^2}{dt^2}\right) \qquad \textbf{(equation 2.16)}$$

With the benefit of the transition dipole matrix element and the density matrix element relevant to the output coherence, we can cast P in a more straightforward relation. The polarisation is related to the output coherence by[15]

$$P = NF\sum_{m,n}\mu_{mn}\rho_{mn} \qquad \textbf{(equation 2.17)}$$

and the summation is over all states m and n. Equation 2.18 shows a more compact form of the output field (E4) launched by this polarisation P4 and relates it to the experimental observable, the intensity. Here c is the speed of light, and n_4 is the index of refraction at the output frequency ω_4.

$$E_4 = \frac{4\pi\omega_4 P_4}{n_4 c} \qquad I = \frac{n_4 c}{8\pi}E^2 \qquad \textbf{(equation 2.18)}$$

2.2.2. The density matrix ρ

There is a distinct difference between the physical processes occurring in different types of spectroscopies. In the familiar transient absorption example (in the narrow-band excitation limit), an initial excitation leads to the population of a vibrational mode, and a weaker probe pulse queries the state of this population by measuring the degree to which the probe is absorbed at a given frequency. Here, the molecules are in a quasi-steady-state and there is no induced polarisation. Conversely, wave-mixing techniques create and manipulate states of the system called coherences. These fundamental differences in the physical process make the density matrix approach more appropriate for our case, and a very brief introduction to the density matrix formalism is presented here.[16]

It is useful to consider the quantum mechanical picture of the states created in various spectroscopic techniques by way of the density matrix. Consider a wavefunction Ψ expanded in an arbitrary basis set:

$$|\Psi(t)\rangle = \sum_n |n\rangle c_n(t)$$
$$\langle\Psi(t)| = \sum_m c_m^*(t)\langle m| \qquad \textbf{(equation 2.19)}$$

If a density operator $\rho(t)$ is introduced as $\rho(t) = |\Psi(t)\rangle\langle\Psi(t)|$, the expansion in the given basis is

$$\rho(t) = \sum_{n,m} c_n(t)c_m^*(t)|n\rangle\langle m| \qquad \textbf{(equation 2.20)}$$

and it is convenient to introduce the $\rho(t)$ as matrix elements, defining the density matrix.

$$\rho(t) = \sum_{n,m} \rho_{nm}(t)|n\rangle\langle m| \qquad \textbf{(equation 2.21)}$$

where the matrix elements are simply the coefficients $\rho_{nm}(t) = c_n(t)c_m^*(t)$ and the subscripts *n* and *m* denote what state the ket and bra parts of the wavefunction are in, respectively. Now considering the density matrix for an n-level system as a whole:

$$\rho(t) = \begin{pmatrix} \rho_{11} & \rho_{12} & \cdots & \\ \rho_{21} & \rho_{22} & & \\ \vdots & & \ddots & \\ & & & \rho_{nn} \end{pmatrix} = \begin{pmatrix} c_1(t)c_1^*(t) & c_1(t)c_2^*(t) & \cdots & \\ c_2(t)c_1^*(t) & c_2(t)c_2^*(t) & & \\ \vdots & & \ddots & \\ & & & c_n(t)c_n^*(t) \end{pmatrix} \quad \textbf{(equation 2.22)}$$

The density matrix is essentially a probability matrix, the time evolution of which is normally depicted by the time-dependent Liouville equation, a discussion of which is omitted here. The elements along the diagonal, where $n=m$, are known as populations of the given state $|1,2...\rangle$ and represent the probability of finding the system in that state at time *t*. The trace of the density matrix (the sum of the diagonal elements) is equal to 1 because it is certain to find the system occupying one or more of these states.

The off-diagonal elements, where $n \neq m$, are known as coherences. These are quantum mechanical superpositions of the states *n* and *m*, and the magnitude of element ρ_{nm} is again a probability of finding the system in a coherence between the two states. Equivalently, it is proportional to the transition probability between states *n* and *m*.[14] Furthermore, coherences are oscillatory in nature; this can be seen by considering a simple two level system occupying a coherence, whose wavefunction is defined by:[5]

$$\Psi(x,t) = c_n(t)\psi_n(x)\exp(i\omega_n t) + c_m(t)\psi_m(x)\exp(i\omega_m t) \quad \textbf{(equation 2.23)}$$

An expansion of the probability function $\Psi\Psi^*$ bears out the oscillatory nature of coherences; there is a cross-term involving $\exp[i(\omega_m-\omega_n)t]$ so that the system oscillates between the states at the frequency (i.e. energy) difference between them. Further, there is a time-dependent phase term in the *c* coefficients and the time evolution of $c_n(t)$ and $c_m(t)$ are different in the off-diagonal case. These coherences are thereby effectively damped and have characteristic damping times (coherence

lifetimes) because of destructive interference between the two terms in each density matrix element.

It is now instructive to consider the two cases of population (incoherent) spectroscopies and coherent spectroscopies. In transient absorption experiments, only diagonal elements of the density matrix are being manipulated. For wave-mixing spectroscopies such as DOVE-FWM, generally only off-diagonal elements are being measured, though both on- and off-diagonal elements may be manipulated.

2.2.3. Resonance enhancement

We now consider a generalised representation in the density matrix of a single transition from one population to a coherence, or from a coherence to another coherence or a population. The probability for the transition is significantly heightened if the energy levels involved are resonant—an effect known as resonance enhancement. This effect is exactly that which makes these nonlinear vibrational spectroscopies possible; normally vibrational transition moments are dominated even in the resonant case by the nonresonant electronic polarisability. By exciting multiple resonant transitions, this nonresonant electronic polarisability can be overcome. Consider a transition changing a coherence between states i and j to one between states i and k. The Rabi frequency Ω is defined as

$$\Omega_{jk} \equiv \frac{\vec{\mu}_{jk} \bullet \vec{E}}{2\hbar} \qquad \textbf{(equation 2.24)}$$

where E is the net electric field and μ_{jk} is the transition dipole matrix element for the transition. Then we define a detuning factor Δ_{ik} as

$$\Delta_{ik} \equiv \omega_{ik} - \omega_{lasers} - i\Gamma_{ik} \qquad \textbf{(equation 2.25)}$$

The first term is the frequency difference between the states i and k. The second is the frequency of one or a combination of input laser frequencies needed for the resonance, and in the third Γ_{ik} is the dephasing rate of the ik coherence. With these definitions in hand, the density matrix elements for the two coherences can be related:[17]

$$\rho_{ik} = \frac{\Omega_{jk}}{\Delta_{ik}} \rho_{ij} \qquad \textbf{(equation 2.26)}$$

It is now possible to make some qualitative assessments of the preceding equations. Firstly, the Rabi frequency, and therefore the density matrix element, increases with field strength, and as expected increases with the transition dipole moment. It is in the denominator of equation 2.26 that the resonance enhancement factor becomes clear; as the excitation frequency approaches the transition frequency, the denominator shrinks to a negligible value whose limit is determined on resonance by the magnitude of the dephasing term. This point will be further explored in section 2.3, where it will be shown that the probabilities for the coherence pathways involve several of these Ω/Δ resonance terms. Indeed, it is the combination of more than one resonance enhancement that allows the vibrational resonances to be seen above the electronic nonresonant background, for which the transition dipole moment is much larger but which is significantly more detuned when excitations are in the infrared.

2.2.4. Phase matching

The refractive index has already been shown to be related to the susceptibility tensor, the elements of which have a functional dependence on frequency. Thus, in bulk media, the refractive index, and thereby the local speed of propagation of electromagnetic radiation, depends on the frequency of the radiation. This dependence is known as refractive index dispersion, and greatly complicates experiments where a number of different fields are present in a sample of finite extent. The optimisation of an experimental geometry to keep various fields in phase is known as phase matching.

The phase matching condition is at its simplest an expression of the conservation of energy and of momentum of the input and output beams. Conservation of energy is ensured by a simple addition or subtraction of the input frequencies (or energies, used interchangeably here), and conservation of momentum is ensured by performing a vector sum of the input wavevectors $\boldsymbol{k}_i$, defined as

$$\vec{k}_i = \frac{\omega_i n_i}{c} \hat{k}_i \qquad \textbf{(equation 2.27)}$$

Here, n_i is the index of refraction at the given frequency ω_i, $\hat{k}_i$ is a unit vector along the direction of propagation for ω_i, and c is the speed of light. Each of the excitation beams in the experiment can be represented by an associated wavevector, and the output wavevector of the induced nonlinear polarisation is simply a vector sum of the inputs. For a given process (or coherence pathway, see the following section), a different vector sum is calculated. Take for example here the vector sum of the $\boldsymbol{k}_i$ relevant to the DOVE-FWM process and the associated energy conservation relation:

$$\begin{aligned} \overrightarrow{k_{out}} &= \vec{k}_1 - \vec{k}_2 + \vec{k}_3 \\ \omega_4 &= \omega_1 - \omega_2 + \omega_3 \end{aligned} \qquad \textbf{(equation 2.28)}$$

The output wavevector $\boldsymbol{k}_{out}$ depends as equation 2.27 on the refractive index at the output frequency. Because of refractive index dispersion, the wavevector obtained by the simple vector sum will not be the same as the actual output wavevector—i.e., the wavevector of the polarisation in the sample will not necessarily be the same as that of the field it launches. The nonlinear polarisation and the output field will thus become out of phase and limit the spatial extent over which the field can propagate. The difference between the two is defined as the phase mismatch, $\Delta\boldsymbol{k}$:

$$\Delta\vec{k} = (\vec{k}_1 - \vec{k}_2 + \vec{k}_3) - \vec{k}_4 = \overrightarrow{k_{out}} - \vec{k}_4 \qquad \textbf{(equation 2.29)}$$

The vector sums are simple considerations of trigonometry, so that the magnitude of $\Delta\boldsymbol{k}$ can be minimised by changing the angles of the input beams in such a way that the two wavevectors are coincident, thereby matching the phases of the two. It is easy to see how this can be done for a given set of input frequencies ω_i, but in frequency-domain experiments in which the input frequencies are tuned but the input angles remain fixed, the phase matching condition is only perfectly met (that is, $\Delta\boldsymbol{k}$=0) at one set of ω_i. As the phase mismatch grows, the signal varies as equation 2.30:

$$Signal \propto \left(\frac{\sin \Delta kl}{\Delta kl}\right)^2 = \mathrm{sinc}^2(\Delta kl) \qquad \textbf{(equation 2.30)}$$

The spatial dimension over which the fields are out of phase determines the degree to which they interfere, and appears in equation 2.30 as the pathlength *l*. The $sinc^2$ function has a functional form as shown in figure 2.1, and optimisation steps

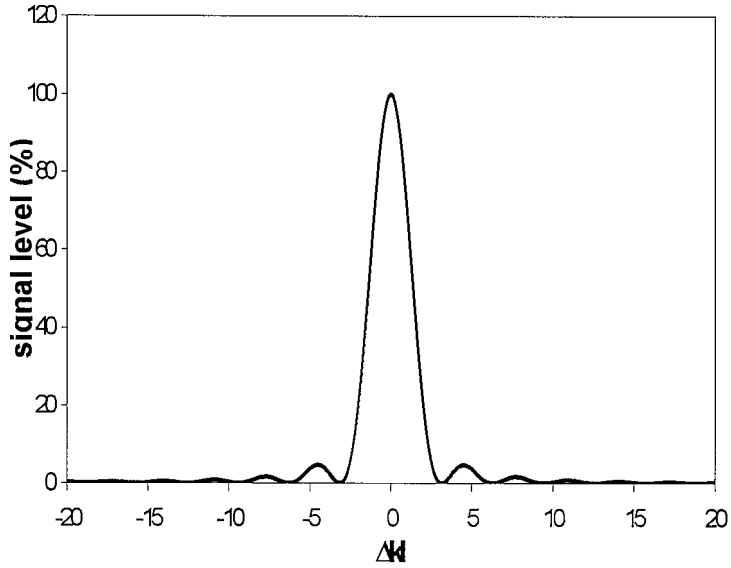


Figure 2.1. Functional dependence of the signal level on the phase mismatch Δkl.

for the geometry of DOVE-FWM experiments will show that the predicted signal level can be maintained on the large central lobe of the $sinc^2$ function. This clear, symmetrical functional dependence only comes about in the absence of refractive index dispersion for the frequencies of the input beams; in practice the signal varies in a more complicated way when the refractive indices are properly accounted for. While the phase mismatch can be minimised and thus the signal maximised by appropriate orientation of the input beams, the relative angles between the input beams limits the beam overlap region, and thereby reduces the mixing pathlength over which signal can be produced. The final determination of an experimental geometry is thus a trade-off between these competing effects, and in particular the phase matching geometry is chosen such that the signal level has a minimal sensitivity to the frequency tuning of the excitation beams.

The refractive index dispersion in the sample and the sample cell windows will in general not be the same, so it is impossible to simultaneously phase match the windows and the sample. This consideration will be discussed further in section 2.3.2.

2.2.5. Wave mixing electronic level diagrams

Many diagrammatic techniques have been introduced to more easily visualise the complex interaction of multiple excitation and output beams in optical experiments, including Mukamel diagrams, Bordé diagrams, double-sided Feynman diagrams, Liouville diagrams, etc.[18] Each has its strengths and weaknesses in terms of the information it encodes about the molecular processes, experimental geometry, or its ease of implementation for a given experiment. For the purposes of this work, it is useful and intuitive to visualise optical processes using wave-mixing energy level (WMEL) diagrams. Several conventions are introduced here that will be common to the WMEL diagrams elsewhere in this thesis: firstly, the length of an arrow is proportional to the frequency (energy) of the transition. Electronic states are not to scale in the diagrams and are taken to be far from vibrational resonance. Solid horizontal lines represent resonant states, and dotted horizontal lines represent nonresonant (virtual) states. All the interactions are assumed to originate in the electronic ground state. Arrows represent the creation and destruction of coherences (not populations); a solid arrow represents a transition of the ket side of the wavefunction and a dashed arrow represents the bra side. When both the bra and ket side are shown to create coherences between the same two resonant levels, a population is created, signifying the change of the probability in a diagonal element in the density matrix. Wavy lines represent an output coherence. For the majority of cases, the complex conjugate of any one WMEL diagram (that is, exchanging every bra side interaction with a ket side interaction and vice versa) is also occurring when the given interaction is occurring, but for brevity is not explicitly repeated. In some cases, the time ordering of the incident fields does not substantially change the process that is occurring, but each possible combination and ordering of the fields is

known as a coherence pathway. By way of example, figure 2.2 shows the WMEL diagrams for some familiar optical processes.

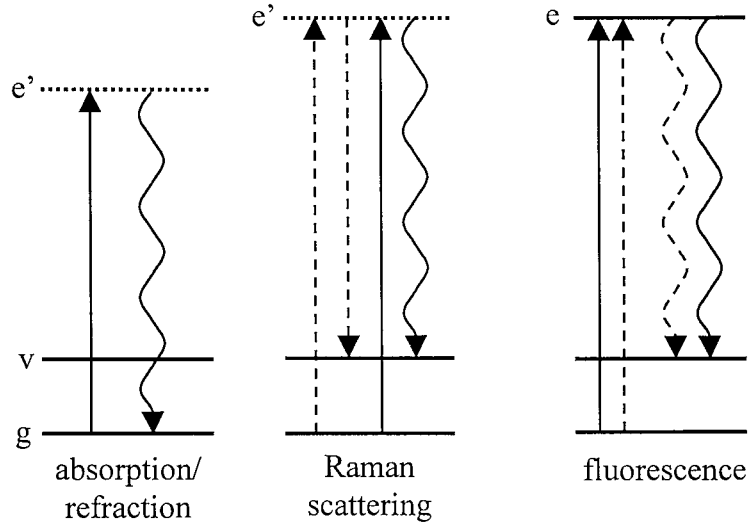


Figure 2.2. WMEL diagrams for a few familiar optical processes, leading to linear spectroscopies.

The energy levels are labelled *g* (ground state), *v* (resonant vibrational state), *e'* (nonresonant electronic state) and *e* (resonant electronic state). The first diagram represents simple refraction, or in the case where *e'* becomes resonant, absorption. The second represents Raman scattering, showing the second vacuum field interaction and the Stokes-shifted output coherence. The frequencies of the field interactions are the same for the third diagram, but the upper level is electronically resonant, the bra and ket side interactions create a population in the electronic excited state (photon absorption), and the output fields now represent fluorescence (photon emission). Despite the fact that strictly speaking Raman scattering and fluorescence are four-wave mixing processes, they query only single energy levels directly, and in the low intensity case only probe the $\chi^{(1)}$ susceptibility. The diagrams could represent three linear spectroscopies if the input fields are scanned in frequency and the intensity of the output field is measured: UV or visible absorption spectrometry, Raman spectrometry, and fluorimetry, respectively.

2.2.6. Examples of nonlinear processes

The diagrams in figure 2.2 represent linear optical processes, consisting of the interaction of two fields (or two pairs of fields at the same frequency). By introducing a third field, nonlinear processes can occur. The interaction of two input

fields and the third output field is known as three-wave mixing (TWM), and is the first example of a nonlinear process (second-order, probing $\chi^{(2)}$). An interesting consequence of second-order and in fact all even-order spectroscopies is that the interactions do not occur in isotropic or centrosymmetric samples. This can be understood by again considering equation 2.11. The net polarisation must be fitted with even-order terms, which will be symmetric in the electric field magnitude—that is, upon reversing the electric field, the polarisation contributions due to even-order terms remain the same, so that the second-order (and other analogous even-order) contributions satisfy the relation

$$P(E) = \chi^{(2)} E^2 \qquad \textbf{(equation 2.31)}$$

so that on reversing the electric field each cycle,

$$P^{(2)}(-E) = -P^{(2)}(E) = P^{(2)}(E) \rightarrow P^{(2)} = 0 \qquad \textbf{(equation 2.32)}$$

Thus, in isotropic media, even-order signals cannot propagate, and spectroscopic methods based on these signals are at their most useful when probing regions where symmetry is broken, namely at surfaces. Even-order processes, in particular sum-frequency and second harmonic generation, are well-known for being extraordinarily surface-sensitive and exhibit very little contribution from the bulk medium. Figure 2.3 presents a few examples of TWM processes.

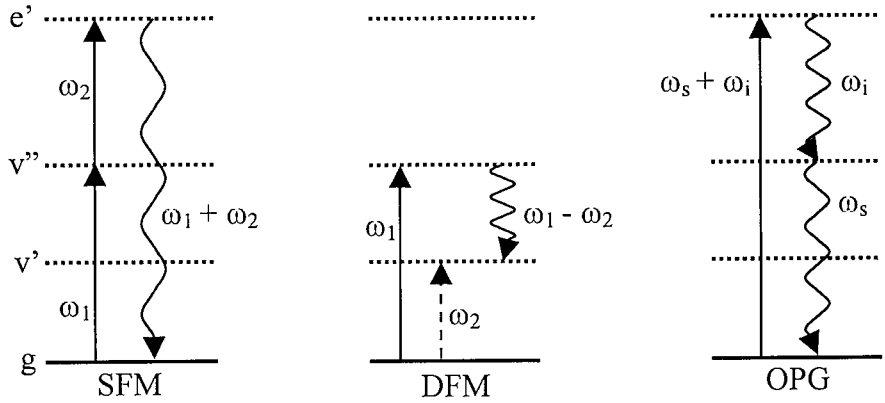


Figure 2.3. WMEL diagrams for three second-order (TWM) processes.

Here, the input fields may but do not need to be resonant with states *v'*, *v''*, and *e'*— any interaction with a resonant level will result in a resonance enhancement of the signal, but is not necessary for these wave mixing processes. In sum frequency mixing (SFM), two input fields' frequencies are added and the output coherence is at the sum. A special but common case is second harmonic generation, in which ω_1 and ω_2 are at the same frequency and result in the production of a field at $2\omega_1=2\omega_2$. Conversely, in difference frequency mixing (DFM), it is the difference between the two excitation frequencies that creates a coherence. In optical parametric processes an intense pump beam is split into constituent fields, one at higher energy known as the signal ω_s, and one at lower energy known as the idler ω_i. This process can be seen as the "reverse" of the SFM case. The third WMEL diagram in figure 2.3 shows optical parametric generation (OPG), where the output coherences are produced spontaneously in a medium such as a crystal. For higher conversion efficiency to a particular desired ω_s, a seed source can be used, not unlike the case of injection-seeding a laser amplifier. In this case, the process is known as optical parametric amplification (OPA). In the DOVE-FWM spectrometer outlined in the following chapter, the laser system employs OPA as an amplification step, and in a separate step, the signal and idler beams from this OPA process are focused into a crystal optimised for the DFM step, creating the tuneable infrared light with which the DOVE-FWM experiments are carried out.

With the addition of another excitation beam, four-wave mixing (FWM) processes can occur, of which DOVE-FWM is just one example. There is an enormous family of FWM techniques, including pump/probe, photon echo, three-pulse photon echo peak shift (3PEPS), transient grating, AC Kerr effect, and a host of other related techniques. A review of all of these FWM examples is beyond the scope of this chapter, but an excellent review puts all of these techniques in a common framework.[5]

2.2.7. Interference and cascading

It is worth noting that, as mentioned in section 2.2.1, the output coherences are Fourier components of the distortions in the polarisation created in the sample. In the presence of a number of incident high-intensity fields, all of the sum, difference, and linear combinations of the fields are being produced in the sample. When TWM

processes occur, all of the same-order and lower-order processes are occurring as well, to a greater or lesser degree, depending on the experimental geometry and the sample's energy level structure. Similarly, when FWM processes occur, all the lower-order processes can occur simultaneously, and so on to arbitrarily high order, unless certain processes are precluded by symmetry considerations. However, the efficiency of each process is optimised in a given application, and in most cases the other possible processes are discriminated against quite strongly. This can be accomplished for instance by judicious choice of nonlinear crystal or phase matching conditions for the creation of just one of the mixing types. The situation is more complicated when the output from one higher-order process can actually mix again with one or more of the input fields and stimulate another process of the same order or lower, generally referred to as cascading. This effect has long been known in the case of stimulated Raman processes, but manifests itself in nonlinear spectroscopies as well.

A central issue in the interpretation of multi-wave mixing spectra is interference between signals due to different coherence pathways. The presence in a complex sample cell of windows, solvent, and a number of different solutes provides a rich overall energy level structure in which nonlinear processes defined by different coherence pathways can occur. Each pathway leads to an emitted field from a single given molecule or moiety, and it is the collective emission of these fields that leads to a measured signal. In the case of a neat liquid and negligible contribution from the sample cell, this signal is quite straightforward to unravel: there will be only one energy level structure to consider and a small number of available coherence pathways. However, when the situation becomes more complex because of the sample or sample cell, a number of different fields occur locally in the sample and these fields interfere constructively or destructively, i.e., the local electric fields add or subtract. The net emitted field is then the vector sum of all of the fields emitted by all the molecules in the beam overlap region.

A consideration that will become important in the interpretation of DOVE spectra is the interference between two particular pathways of different types. In order to define them, it is instructive to return to figure 2.3, in which two fundamentally different kinds of processes are happening. In the first pathway (SFM), only the ket is involved in the pathway. An analogous pathway involving just the bra is simultaneously occurring but is not shown. With the output coherence,

the system returns to its initial state, so that no exchange of energy has occurred. These interactions are known as parametric. On the other hand, in the DFM case, both bra and ket are involved in the first two interactions, and it can be seen from the final transition between the vibrational levels that the system does not return to the initial state. In this case, the system has gained energy from the field, and the interaction is known as nonparametric. Equivalently, the pathways could be described as parametric if only the bra or the ket changes in the interaction and nonparametric if both change.[5] The fields associated with parametric and nonparametric coherence pathways are out of phase (precisely out of phase within the harmonic approximation), so that destructive interference at the field level occurs between fields emitted from parametric and nonparametric pathways of the same output frequency.

Another consideration is interference due to so-called level-dependent dephasing, or quantum number-dependent dephasing, which leads to changes in the degree to which certain pathways interfere. First noted in a general theoretical treatment for four- and six-wave mixing spectroscopies,[19] it has been considered specifically for the case of 2-D IR studies by Khalil and Tokmakoff,[20] where it has been taken with mechanical and electronic anharmonicity as a third "selection rule" for 2-D IR features. The different coherence lifetimes of each of the coherences created in the pathways leads to different temporal behaviour of the emitted fields, so that the interference between different pathways that might otherwise cancel is incomplete. Temporal data to be presented in Chapters 4 and 5 will bear out the effects of this dependence of the dephasing on the energy level being accessed.

2.3. Introduction to DOVE-FWM spectroscopy

The overlapping of many bands in linear (first-order) vibrational spectroscopy can be overcome by spreading the spectral information into two dimensions, just as in multidimensional NMR techniques. As noted in section 2.2.6, TWM (second-order) techniques are limited by symmetry constraints to non-centrosymmetric media, but it has been shown that double vibrational enhancement is possible in a TWM experiment.[5] However, the output from such an experiment will be in the infrared, and therefore much more difficult to efficiently detect with presently available detectors. Thus, a FWM spectroscopy is the lowest order possible which

provides double vibrational resonance (and thus an indication of mode coupling), has no constraints on the symmetry of the sample, and has an output in the visible, which with existing technology can be detected down to the single photon level. Wright *et. al.*.'s first experiments to create a doubly vibrationally enhanced spectroscopy focused on creating the vibrational coherences via two Raman transitions comprising four input excitations, followed by a fifth nonresonant interaction, thereby creating a SWM (fifth-order) process. However, it was quickly discovered that the fifth-order signal was obscured by cascaded third-order processes, named by the authors as sequential CARS or SCARS.[21] With the advent of widely tuneable infrared sources in the following few years, the direct creation of the vibrational coherences became possible, and only three input excitations were needed to probe the same energy levels. DOVE-FWM's name (henceforth simply DOVE) reflects that it is a third-order spectroscopy accomplishing this task, and the following sections endeavour to outline a few of the theoretical details of the process and experimental considerations for its implementation.

DOVE experiments were carried out with the DOVE spectrometer outlined in the following chapter, which employs two tuneable infrared beams and a third, fixed frequency, visible beam which we take to be nonresonant with any electronic transitions in the samples. A brief discussion of the nonlinear processes which occur in the samples under these excitation conditions is presented in the following section.

2.3.1. Components of the total measured signal

There are a number of coherence pathways which can contribute to the signal measured in the DOVE experiment, each with its own required energy level structure. It has been shown that there are 12 possible coherence pathways for a given energy level structure which are doubly vibrationally enhanced.[22] Six of these are particularly convenient for the purposes of nonlinear experiments as their outputs are in the visible region of the spectrum. We will concentrate on two of these six which have the wave-mixing condition outlined in equation 2.28 and which have an anti-Stokes shifted output coherence (that is, the output frequency is larger than any one of the input frequencies). When implementing this spectroscopy in a complex sample, several processes can occur in the solvent, any of the solutes, and the sample cell windows. These possible processes, all with the same phase-matched direction and frequency, are depicted in the WMEL diagrams of figure 2.4, with the

energy levels labelled. Here, *g* represents the ground vibrational state, *v* and *v'* represent vibrational levels which may or may not be resonant, and *e* is a virtual electronic state.

The figure shows five different components of the measured signal. The interactions are with, from left to right, ω_1-ω_4 in all cases. It can be seen that the excitation frequencies are all identical, so that it is only the energy level structure of the solvent/solute/windows that determines which processes will be occurring. The

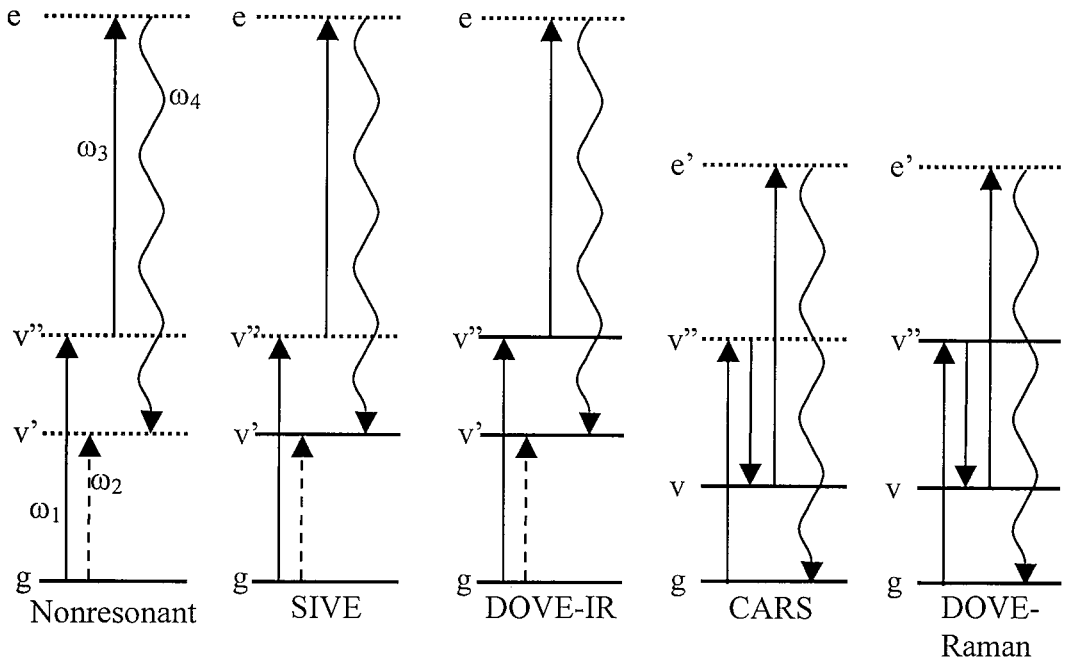


Figure 2.4. WMEL diagrams for the coherence pathways which contribute to the detected signal in the DOVE experiment.

nonresonant contribution is always present to a greater or lesser degree, mostly as a manifestation of the nonresonant electronic polarisability but also sometimes the off-resonant polarisability from strong vibrational transitions which are much closer in frequency than the electronic transition—this will be referred to in later chapters as pre-resonant background. SIVE can come about if either of the first two excited states *v* or *v'* is resonant; the depiction shown here is for the lower of the two to be resonant but equally there is a pathway where the real and virtual states are exchanged—these will be referred to as SIVE1 and SIVE2. These interactions result in lines in the 2-D spectra parallel to one of the frequency axes because SIVE is vibrationally enhanced regardless of the value of the off-resonant infrared excitation.

There are two contributions from DOVE-IR pathways, one for the time ordering ω_1, ω_2 and one for ω_2, ω_1—these will be referred to as DOVE-IR1 and DOVE-IR2. In the case where the excitation pulses are overlapped, it has been shown theoretically that interference between these two pathways results in a 2-D Lorentzian lineshape in the absence of pure dephasing, but results in a feature strongly broadened along the diagonal if pure dephasing is taken into account.[23]

The CARS pathway depends only on the difference frequency between ω_1 and ω_2, resulting in diagonal lines in the 2-D spectra where (ω_1 - ω_2) is a constant—parallel to the $\omega_1 = \omega_2$ axis. Finally, DOVE-Raman is very much like the CARS process, but accessing a resonant vibrational level at *v'*. This results in an additional resonance enhancement, and the dependence on both of the infrared excitations again results in peaks in the 2-D spectrum.

It can be seen that the first three pathways are nonparametric, whereas CARS and DOVE-Raman are parametric. The result is that the emitted fields from the first three pathways are out-of-phase with those of the final two and thus interfere within the sample, changing the spectral lineshapes of DOVE features when more than one of the pathways is available.

As an aside, this manifestation of the CARS process is quite unusual; typically the vibrational coherence is created by a small frequency difference between visible lasers, accessing virtual levels far above the ones depicted in the figure. However, despite the change in scale for the excitation frequencies, the coherence pathway depends only on the difference frequency between the first two excitations. DOVE-Raman is identical to the CARS pathway except that the higher energy vibrational level is resonant, leading to another resonance enhancement of the signal.

The diagrams show a specific time ordering, from left to right. In the case where all three excitation beams are overlapped, pathways involving any exchange of the ω_1-ω_3 beams are also occurring simultaneously. However, selection of certain pathways becomes possible by delaying the excitation beams relative to one another. For instance, if a small delay is introduced between the arrival of ω_1 and ω_2, and another between ω_2 and ω_3, the pathways shown in the figure will be selected. This is of great importance in the efforts to selectively enhance certain signal components. For example, in the case of delayed pulses in the CARS and DOVE-Raman pathways, the exchange in time of ω_1 and ω_2 will not result in an output coherence

because the first coherence shown must be created in order to create the second in a Raman-like transition. Further, it can be seen from the figure that in the case of the nonresonant and CARS pathways, the first interaction is with a nonresonant level. These nonresonant coherences dephase almost instantaneously outside the exciting pulse's temporal window, so that by appropriate choice of delay after the first excitation, this pathway can be selectively suppressed. Meanwhile, the DOVE-IR and DOVE-Raman pathways are still viable, because their resonant levels at the first excitation have a finite coherence lifetime and will decay much more slowly (on the order of ps), so that a delay between the first and second excitations will not significantly affect the efficiency of the overall pathway. With variable delays as experimental parameters, coherence pathways can be selected or suppressed, and the effects of varying these parameters will be explored in detail in Chapter 4.

The most significant feature of the presence of all of these signal components is their propensity to interfere in the sample. Each coherence pathway represents a radiated field, and the net field at any point is simply the sum of all of the local fields. Hence, there is additive interference of the signal components, each of which will have an associated magnitude and sign. It will be shown in Chapters 4 and 5 that these interferences can change lineshapes or even obscure resonances entirely.

With the benefit of the resonance enhancement description in section 2.2.3, it is possible to develop expressions for the density matrix elements which describe the transitions. Specifically presented here are the three doubly vibrationally enhanced pathways, DOVE-IR1/2 and DOVE-Raman, for the purpose of visualising the effects of multiple resonances—these resonance enhancements are shown to be multiplicative for coupled modes, whereas for uncoupled modes are simply additive. It is this multiplicative enhancement that allows the signal from vibrationally resonant interactions to exceed that of the electronically nonresonant interactions and ultimately makes nonlinear vibrational spectroscopy possible. The development here closely follows that of reference [5]. The density matrix elements for DOVE-IR1 and 2 and DOVE-Raman respectively are given by

$$\rho_{ev'}^{(DOVE-IR1)} = -\sum_{g,v',v'',e} \frac{\Omega_{gv''}\Omega_{gv'}\Omega_{v''e}}{8\Delta_{v''g}\Delta^{*}_{v''v'}\Delta_{ev'}}\rho_{gg}e^{i(k_{out}z-w_{out}t)}$$

$$\rho_{ev'}^{(DOVE-IR2)} = -\sum_{g,v',v'',e} \frac{\Omega_{gv''}\Omega_{gv'}\Omega_{v''e}}{8\Delta^{*}_{v'g}\Delta_{v''v'}\Delta_{ev'}}\rho_{gg}e^{i(k_{out}z-w_{out}t)} \qquad \textbf{(equation 2.33)}$$

$$\rho_{e'g}^{(DOVE-Raman)} = \sum_{g,v,v'',e'} \frac{\Omega_{gv''}\Omega_{v''v}\Omega_{ve'}}{8\Delta_{v''g}\Delta_{vg}\Delta_{e'g}}\rho_{gg}e^{i(k_{out}z-w_{out}t)}$$

where the summation is over all the available states. Here the detuning factors are defined as

$$\begin{aligned}
\Delta_{v''g} &= \omega_{v''g} - \omega_1 - i\Gamma_{v''g} \\
\Delta^{*}_{v''v'} &= \omega_{v''v'} - (\omega_1 - \omega_2) + i\Gamma_{v''v'} \\
\Delta_{ev'} &= \omega_{ev'} - \omega_4 - i\Gamma_{ev'} \\
\Delta^{*}_{v'g} &= \omega_{v'g} - \omega_2 + i\Gamma_{v'g} \\
\Delta_{v''v'} &= \omega_{v''v'} - (\omega_1 - \omega_2) - i\Gamma_{v''v'} \\
\Delta_{v''g} &= \omega_{v''g} - \omega_1 - i\Gamma_{v''g} \\
\Delta_{vg} &= \omega_{vg} - (\omega_1 - \omega_2) - i\Gamma_{vg} \\
\Delta_{e'g} &= \omega_{e'g} - \omega_1 - i\Gamma_{v''g}
\end{aligned} \qquad \textbf{(equation 2.34)}$$

where ω_{ij} is the frequency for the $j \leftarrow i$ transition, ω_i is the frequency of the i^{th} input excitation (ω_4 is defined as in equation 2.28), Γ_{ij} is the dephasing rate for the ij coherence, and the final exponential term involves the output wavevector and frequency also as in equation 2.28. Then the polarisation due to any one of the sample components is given by

$$P = NF[\mu_{ev'}(\rho_{ev'}^{(1)} + \rho_{ev'}^{(2)}) + \mu_{e'g}\rho_{e'g}] \qquad \textbf{(equation 2.35)}$$

and the total polarisation can be obtained by summation over all sample components. Given the relation between the output polarisation and the nonlinear susceptibility described in equation 2.13, it is instructive to view a rearranged expression for the nonlinear susceptibility, divided into terms describing the contributions from each available coherence pathway as depicted in figure 2.4.

$$\chi^{(3)}_{Total} = \sum_{\substack{i=all\ components \\ g,v,v',v''=all\ states}} A^i_{NR} + \frac{A^i_{Raman}}{\omega^i_{vg} - (\omega_1 - \omega_2) - i\Gamma^i_{vg}}$$
$$+ \frac{A^i_{SIVE1}}{\omega^i_{v''g} - \omega_1 - i\Gamma^i_{v''g}} + \frac{A^i_{SIVE2}}{\omega^i_{v'g} - \omega_2 + i\Gamma^i_{v'g}}$$
$$- \frac{A^i_{DOVE-IR1}}{(\omega^i_{v''g} - \omega_1 - i\Gamma^i_{v''g})(\omega^i_{v''v'} - \omega_1 + \omega_2 - i\Gamma^i_{v''v'})}$$
$$+ \frac{A^i_{DOVE-IR2}}{(\omega^i_{v'g} - \omega_2 + i\Gamma^i_{v'g})(\omega^i_{v''v'} - \omega_1 + \omega_2 - i\Gamma^i_{v''v'})}$$
$$+ \frac{A^i_{DOVE-Raman}}{(\omega^i_{v''g} - \omega_1 - i\Gamma^i_{v''g})[\omega^i_{vg} - (\omega_1 - \omega_2) - i\Gamma^i_{vg}]} \quad \textbf{(equation 2.36)}$$

The first term corresponds to the overall nonresonant susceptibility, grouped into a single constant. It is assumed that the electronically nonresonant contributions will not change appreciably during the course of spectral scans, so there is no frequency dependence in the first term. The second term corresponds to the CARS pathway. The third and fourth terms describe to possible SIVE interactions, in which either ω_1 or ω_2 is resonant with one of the vibrational states. DOVE-IR takes two possible forms in the fifth and sixth terms, depending on the time ordering of the infrared excitations. Finally, the seventh term describes DOVE-Raman. It is clear to see in the denominators of the final three (doubly vibrationally enhanced) terms that the detuning factors multiply for coupled modes. It is possible to consider that in the case of uncoupled modes, the final three terms vanish, but the SIVE1 and SIVE2 terms survive and are additive rather than multiplicative.

2.3.2. Effects of windows, absorption, refractive index dispersion

With the description of the total nonlinear susceptibility $\chi^{(3)}$ as defined in the previous section, it is possible to make an estimate for the output signal size. As outlined in section 2.2.4, however, the measured signal is dependent on the phase matching conditions, as well as the absorption in the sample. Given that refractive index dispersion is in general different in differing materials, it is impossible to simultaneously ensure phase matching in the sample and in the sample cell windows. Moreover, the gradient of the refractive index is highest around absorptions, so that refractive index dispersion has its greatest effects around the resonances that the

experiments probe. Absorption also plays a large part in the overall mixing efficiency: as one of the excitation frequencies is scanned through a resonance, the field will be attenuated by the sample and the overall mixing efficiency decreases. It is clear that for maximising the signal from the experiment, it is necessary to ensure experimental conditions that minimise these effects, and for accurate signal size estimates, these effects must be taken into account.

Signal size estimates for the general case FWM experiments in a sample cell comprising a sample of pathlength l_s between identical front and rear windows have been developed by Scholten *et. al.*.[24] and adapted for the DOVE experiments,[25] leading to a phase matching factor M which affects the magnitude of the output field. Subscripts s and w refer to sample and window, respectively, and the two windows are taken to be of the same composition and pathlength l_w.

$$M_s = e^{(i\Delta k_w - \Delta\alpha_w)l_w}\left[\frac{e^{(i\Delta k_s - \Delta\alpha_s)l_s} - 1}{(i\Delta k_s - \Delta\alpha_s)l_s}\right]$$

$$M_w = (1 + e^{(i\Delta k_w - \Delta\alpha_w)l_w + (i\Delta k_s - \Delta\alpha_s)l_s})\left[\frac{e^{(i\Delta k_w - \Delta\alpha_w)l_w} - 1}{(i\Delta k_w - \Delta\alpha_w)l_w}\right] \qquad \textbf{(equation 2.37)}$$

The contribution for Δk from sample and window is calculated as in section 2.2.4, and the $\Delta\alpha$ for sample and window are simply the absorption coefficients at all of the input and output frequencies:

$$\Delta\alpha = \frac{1}{2}(\alpha_1 + \alpha_2 + \alpha_3 - \alpha_4) \qquad \textbf{(equation 2.38)}$$

With these expressions it is possible to model the output from a DOVE experiment by calculating the net output field E_4 as

$$E_4 = \frac{12\pi\omega_4 E_1 E_2 E_3}{c}\left(\frac{F_s l_s \chi_s^{(3)} M_s}{n_{4s}} + \frac{F_w l_w \chi_w^{(3)} M_w}{n_{4w}}\right) \qquad \textbf{(equation 2.39)}$$

As the observable in the experiment is the intensity, which scales as E_4^2, there will be phase matching factor cross terms in the expression for the output field which complicate the lineshape, and, importantly, make it impossible to simply subtract the effects of the sample cell windows. Further, the phase matching factors in equations 2.38 have complex character and involve Δkl. Phase matching considerations attempt to minimise this value, but Murdoch notes that for imperfect phase matching, Δkl can be much greater than 2π, so that very small changes in either Δk or the pathlength can change the phase significantly,[25] an effect which manifests itself as an extreme sensitivity of DOVE experiments to the input angles and the sample pathlength. This sensitivity will be explored in Chapter 4.

2.4. Calculations of 2-D spectral data

The group of Wright *et. al.*. has done an extensive amount of calculation to model the experimental DOVE spectra they obtain. Their early publications on DOVE present simulations of the effects of absorptive samples and refractive index dispersion[26] and the effects of sample cell windows and the attendant phase mismatching.[25] Several publications have approached the subject of the contributions of lineshapes from different coherence pathways[22] and qualitatively produce similar lineshapes to those predicted by calculational methodologies developed for the interpretation of time-domain 2-D IR spectroscopies.[20,27] However, only very recent publications have shown simulated spectra in good agreement with DOVE experimental data.[23,28] Cho *et. al.*. collaborated with the Wright group, undertaking an *ab initio* calculation[29] which determined the mechanical and electric anharmonicities only up to the cubic terms, but which agrees quite well with the experimental data. The details of the calculations are beyond the scope of this appraisal of the current calculation standard, but their result in particular shows the need to consider the amplitude-level interferences between fields arising from different coherence pathways. Moreover, the calculation shows that in the case of acetonitrile, the dominant effect giving rise to the acetonitrile cross peak examined in Chapter 4 is in fact the coupling due to mechanical and electric anharmonicities, but that various C-H modes act as promoting modes for the coupling. This challenges the simplistic picture of vibrational coupling as a "nearest-neighbour" effect.

While no modelling of the results presented here and in Chapter 5 has been undertaken, it is clear that a full description of the 2-D experimental spectra must consider all the available coherence pathways and the influence of all of the vibrational modes of the molecule. Further developments by groups such as Cho's will lead the way for the interpretation of DOVE spectra on progressively more complex molecules.

3. DOVE spectrometer design

Having established that DOVE spectroscopy was the preferred method for the investigation of infrared mode coupling, it was necessary to design, assemble, and implement a DOVE spectrometer. The existence of commercially available tuneable infrared light sources is the key enabling technology for the accomplishment of such a spectrometer, and pioneering work by e.g. Hamm and Zinth[30] had by the time of the commencement of this project enabled commercial laser system companies to provide widely tuneable, stable, relatively high pulse-energy light sources. It was thus decided to purchase a laser system designed to provide the infrared light as opposed to the more inexpensive but significantly more labour-intensive option of constructing OPAs in-house. However, from the outset the flexibility was needed to change the spatial size of the infrared beams, their relative timings, and to achieve a number of diagnostic steps external to the lasers themselves. The commercial system, the beam conditioning setup and experimental enclosure, the diagnostics, and detection setup collectively constitute a DOVE spectrometer.

To open this chapter, the commercial laser system will be introduced in detail. Also, a number of key concepts relevant to the production of picosecond duration pulses of infrared light will be discussed. The two sections following describe the modelling undertaken to predict the output signal sizes, wavelengths, directions, and relative efficiencies. A description of the "experimental" part of the spectrometer (i.e. the part external to the commercial laser system) follows, including a description of the methods of spatial and temporal alignment of the input beams. The chapter closes with a detailed list of usage and maintenance protocols, provided largely for the benefit of future users of the system.

3.1. Introduction – light source

The majority of the laser system was purchased from Spectra Physics, comprising a standard Ti:sapphire-based chirped pulse amplifier (CPA) and two optical parametric amplifiers (OPAs). The dual OPA system as delivered was only the second of its kind ever produced by Spectra Physics, and the first installed in the UK. As such, the system suffered a great many teething problems, but with time and experience the optimisation and maintenance protocols presented herein were

instituted and the system has proven itself as reliable and flexible as it need be to accomplish the experiments described in the following chapters.

The seed laser or oscillator (numbered **(1)** in figure 3.1) is a Spectra-Physics Tsunami, producing a train of modelocked pulses at approximately 80 MHz. It is a standard Ti:Sapphire based Kerr-lens actively modelocked oscillator. The Tsunami is continuously tuneable from 690-1080 nm but for the purposes of this work was fixed at either 795 or 785 nm (the optimum wavelengths for operation of the optical parametric amplifiers). The output pulses were ~90 fs in duration (FWHM) and bandwidth ~12 nm (FWHM). The oscillator derives its gain from a dedicated pump laser, a Spectra-Physics Millenia frequency-doubled Nd:YVO_4 continuous wave (CW) laser (numbered **(2)** in figure 3.1), producing approximately 5W of CW power at 532 nm. The average output power of the oscillator with this input pump power is approximately 900 mW. The first optic outside the oscillator is a 33% beamsplitter, and therefore only ~300 mW of seed power is delivered to the following stage, corresponding to a pulse energy of ~4 nJ/pulse.

The seed pulse train is input to a Spectra-Physics Spitfire, a chirped-pulse amplifier (CPA) which comprises a standard zero-dispersion grating stretcher/compressor (numbered **(3)** in figure 3.1) and a regenerative amplifier (numbered **(4)** in figure 3.1). The stretcher/compressor setup can be used in two configurations employing different stretcher/compressor gratings: "femtosecond" (delivering at the output pulses of width ~100 fs) or "picosecond" (delivering pulses of width ~1.5 ps). For the purposes of the experiments described in this thesis, the picosecond stretcher/compressor grating pair was used. Applications for the implementation of the femtosecond grating pair will be discussed in section 6.1.2. The regenerative amplifier derives its gain from a separate pump laser, a Spectra-Physics Evolution X (numbered (**5**) in figure 3.1). The Evolution is an intracavity-doubled Nd:YLF laser delivering acousto-optically Q-switched pulses at 1 kHz. The average power delivered to the Ti:Sapphire crystal in the regenerative amplifier cavity is approximately 9 W.

The output of the Spitfire is a train of pulses with a width ~1.5 ps, and energy in the region of 1 mJ, depending on the overall performance of the system. At the repetition rate of 1 kHz, this corresponds to an average power of about 1 W. Finally, these pulses are delivered to two Spectra-Physics OPA-800 optical parametric amplifiers (numbered **(6)** and **(7)** in figure 3.1), in which the pump light is split and

converted through a number of nonlinear optical processes into the radiation required for the experiment. The details of the OPAs' outputs are summarised in figure 3.1, along with the rough specifications of the beams at each stage of the laser system.

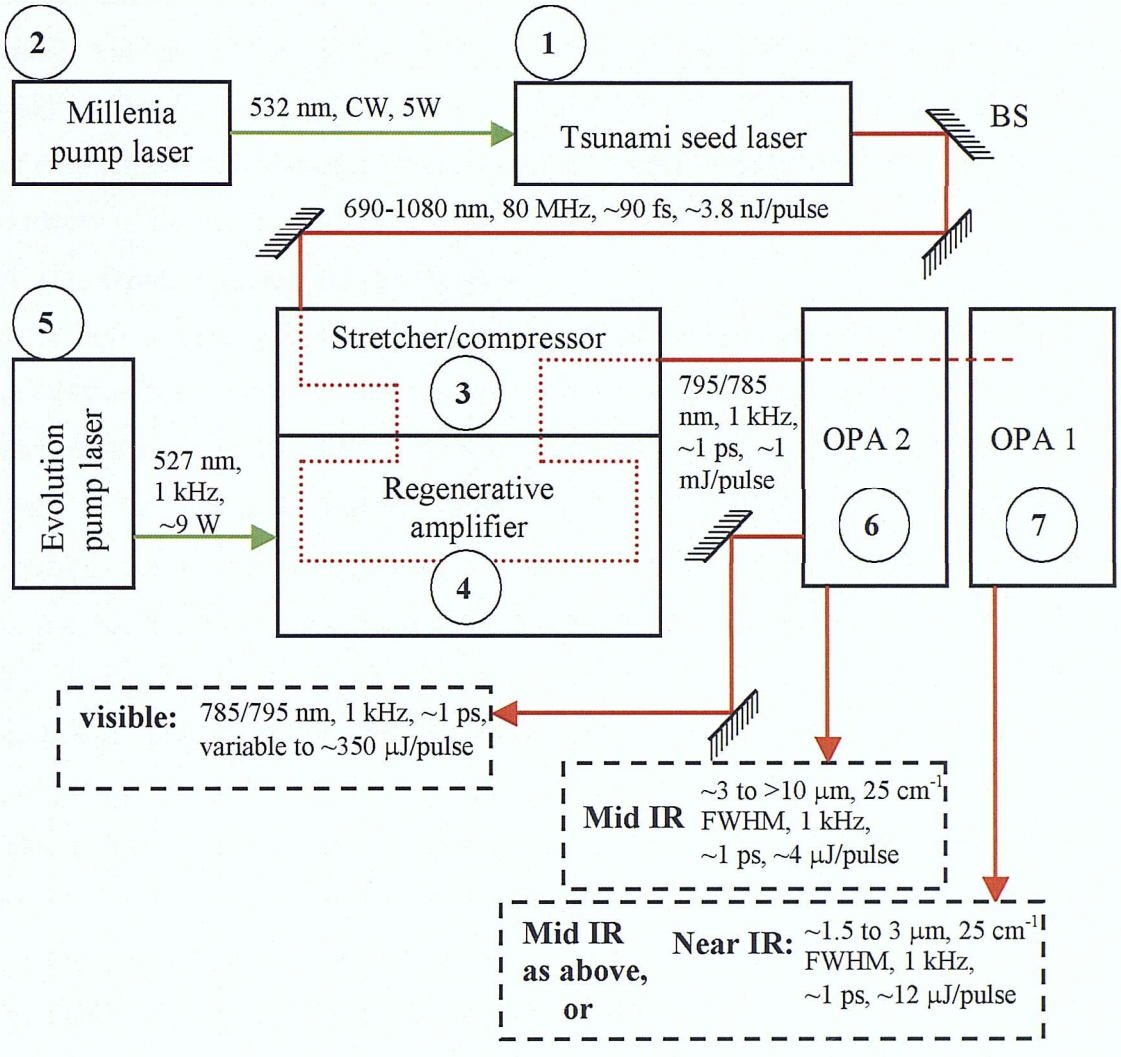


Figure 3.1 Schematic diagram of the laser system. BS=beamsplitter. See text for details.

The details of the generation of the output from the regenerative amplifier will be omitted here, as the laser system up to this point constitutes just a pump source for the OPAs, the true light source for the DOVE experiments. A brief exposition of the OPAs' operation is presented in the following section.

3.1.1. Optical parametric amplifiers

The pulses from the regenerative amplifier are then delivered to two Spectra-Physics OPA-800C tuneable OPAs. A 50% beamsplitter in the first OPA allowed

half the input pulse energy to be delivered to the second. Optical parametric amplification is a parametric three-wave mixing (second-order) down-conversion process by which some of the energy from a pump beam can be passed to a particular spectral portion of a seed source. This part of the seed becomes the "signal". In addition, conservation of energy requires that a second, lower energy photon is also created, known as the "idler". The particular portion of the spectrum that is amplified depends on the phase matching in the OPA crystal, a requirement that is in this case adjusted by changing the angle of the crystal itself. For further details of the theory of the optical parametric generation process, see Chapter 2.

3.1.1.1. Optical parametric generation

Briefly, approximately 4% of the input beam is reflected by a beamsplitter in the OPA and focused into an undoped yttrium aluminium garnet (YAG) crystal, which produces a white light continuum. This continuum becomes a broadband seed source for the first stage of amplification. The angle of the OPA crystal (in this case, β-barium borate, or BBO) could be adjusted in order to tune the amplified wavelength by selecting a portion of the continuum that is best phase-matched for the OPA process in the crystal. The remaining 96% of the input pump light is split again into two gain stages of the amplifier. In the first stage, the white light continuum is sent collinearly through the BBO crystal with 14% of the remaining pump beam. A dichroic mirror downstream passes this amplified signal beam and rejects the pump beam. The signal and idler are then reflected nearly collinearly off of a grating which is aligned for Littrow reflection and rotated to reflect the idler beam. In this way, the idler beam becomes a narrower-band seed source for another pass through the BBO crystal, instead of the white light continuum. Passing again through the dichroic mirror, the idler beam is aligned to be collinear with the remaining 86% of the pump beam for a second pass through the BBO crystal. For both of these amplification stages, a careful alignment had to be performed between the pump beams and the amplified beams, both in space and in time. The white light section of the OPA and the second stage of amplification included manual translation stages so as to control the temporal overlap of the pulses in the BBO crystal. A final dichroic mirror rejects the remaining unconverted pump light and delivers the signal and idler to the "wavelength extension" stage. Here, a number of different crystals could be employed, such as frequency doubling crystals, sum-frequency crystals, etc.,

effectively providing continuous tuning from ~300 nm in the ultraviolet to ~10 μm in the mid-infrared. For the purposes of the work described herein, the idler beam was used directly or passed with the signal beam to a difference frequency mixing (DFM) stage.

3.1.1.2. Difference frequency mixing

In all experiments reported herein, at least one of the output frequencies was created in a difference frequency mixing stage. Here, the signal and idler are crossed in a silver thiogallate ($AgGaS_2$) crystal where, through difference frequency mixing, a third beam is generated in the crystal at a frequency which is the difference between those of the signal and idler beam. For further details of the theory of difference frequency mixing, see Chapter 2. For this case, this difference frequency beam is in the mid-infrared, between ~3 μm and ~10 μm (3300 cm^{-1} to 1000 cm^{-1}), corresponding to fundamental molecular vibrations. Successive tuning of the BBO crystal, the reflection grating, and the angle of the $AgGaS_2$ crystal could tune the output wavelength continuously through this range.

When using the idler beam directly, the output polarisation is orthogonal to that of the DFM output. Because wide tuneability was needed with this beam, a broadband solution was required for rotating the polarisation. Normally this might suggest the use of a pair of polarisers, but the total transmittance of the polarisers that could be easily obtained (Glan-Taylor polarisers provided with the OPAs or wire grid polarisers) was too low to be acceptable, on the order of 10%. Other broadband solutions, such as a Fresnel rhomb, were not easily or inexpensively obtainable, particularly for infrared-transmissive materials. Instead, a removable 5-mirror polarisation rotator was inserted when the idler was used directly for near-infrared experiments. This rotator works completely in reflection, eliminating transmissive losses inherent in infrared polarisers. Further, the insertion of this polarisation rotator eliminated the need to change any of the existing setup and could be easily removed for experiments requiring a different polarisation. A number of other optical adjustments had to be made in order to make use of the idler beam. A dichroic mirror was inserted at the OPA output which rejected the signal beam, isolating the idler. In addition, a longpass filter (Spectrogon, cutoff wavelength 1700 nm) was inserted to increase the extinction ratio in favour of the idler wavelength. Finally, the longpass optical filter at the output of the OPA, normally in

place to spectrally isolate the DFM beam from both signal and idler, was removed. With the optics adjusted in this way, successive tuning of the BBO crystal and the reflection grating allowed the output wavelength to be tuned continuously between ~1.5 μm and 3 μm, corresponding to the spectral range where combination bands and overtones of vibrations could be found for the molecules of interest in this work.

3.2. Signal size calculations and predictions

Estimates of the expected signal sizes (in terms of absolute numbers of photons) were necessary to determine the detection setup that was needed, to compare with results on similar experiments published in the literature, and to predict signals from proposed new experiments. For a discussion of the theoretical background of the estimation procedure, refer to chapter 2. This section presents the way in which the first signals produced from the experiment were converted to photon numbers for comparison with published results.

3.2.1. Initial signal size calculations

In order to convert the signal sizes from the lock-in amplifier, measured in μV, it was necessary to divide out the attenuations and amplifications between the sample and the lock-in. Firstly were the optical filters, whose optical densities at various signal wavelengths were assessed by taking absorption spectra in a Shimadzu UV-1601 UV/vis spectrophotometer. The signal was measured with a standard large-area silicon photodiode, biased at 15 V. From product literature, it was established that the quantum efficiency of the photodiode at the signal wavelength was ~80%, i.e., there is an 80% probability that an incident photon at that wavelength will be converted in the silicon to a charge carrier. As the signal wavelength changes with tuning of the infrared wavelengths, it was important to note the dependence of the quantum efficiency on wavelength, but for this photodiode, the dependence was minimal. The signal from the photodiode was then amplified in a homebuilt variable gain amplifier, with a gain of $2 \times 10^4 - 2 \times 10^5$. From there, the signal is passed to an RC filter, consisting of a resistor and capacitor which "spreads" the signal out in time. This is necessary because the lock-in amplifier input stage does not respond linearly to signals with the extremely short durations that can be expected from a fast photodiode and amplifier. This filter has the effect, however, of attenuating the measured signal by a factor of ~3, a fact established by removing and replacing it,

and noting the difference in signal in the small-signal regime. Further, the lock-in measures RMS voltage, and a representation of the photon number is the peak-to-peak voltage, $2\sqrt{2}$ times the RMS value. Lastly, the component of the signal that is measured is only that which corresponds to the reference frequency, which is the difference frequency between the chopper slit sets (see section 3.4.4.2). Clearly there are more signal components present but unmeasured in this scheme, and by chopping each of the three beams separately with a single chopper wheel, it was established that the difference frequency component represents ~10% of the total signal.

3.2.2. Signal size calculations: photomultiplier tube

Although the signal levels were very high in the first experiments, a subsequent series of experiments were conducted which resulted in significantly smaller signal levels, and a Hamamatsu R928 photomultiplier tube (PMT) was employed. It was then necessary to determine a scaling factor for signal levels, based on the response of the PMT. The calibration was performed using a double monochromator setup and a calibrated photodiode. The procedure was to select a very narrow bandwidth of light from a white light source with the aid of two monochromators. This light was then focused onto a photodiode, whose spectral response and quantum efficiency were well known. In this way a number of incident photons could be established. Replacing the photodiode with a PMT, the output voltage from the PMT could then determined as a function of bias high-voltage input. Further, it was possible to scan the two monochromators and determine the spectral response of the PMT, ensuring that a number of photons from the experiment could be determined accurately from the PMT output voltage.

3.3. Modelling

In addition to the need to predict the full signal sizes estimated from experiments, the condition of phase matching also places constraints on the detection of the signal. Variations in the phase matching can, in the worst case, reduce signal by orders of magnitude. Moreover, the spectral and directional variation in signal must also be accounted for in terms of optical filtering solutions, detector placement, delivery optics' size and placement, etc. This section presents a phase matching

model that was used during the course of this research in order to probe these variations and to assess the feasibility of different experiments before they were attempted experimentally.

3.3.1. Phase matching model

In order to optimise the phase matching for the planned experiments, and to explore the phase matching conditions in other wavelength regimes or for other samples, a phase matching model was developed. The most basic format of the model considers the three input frequencies as monochromatic and that beams are incident at discrete angles. The model determines the sum **k** vector, the output frequency, and the phase mismatch $\Delta\mathbf{k}$ via equation 2.29 and the signal level by equation 2.30 in Chapter 2.

For completeness, however, the detailed functional dependence of the index of refraction on frequency (refractive index dispersion) must be considered. In the case where the index of refraction for all of the input beams is a constant, the change in the output direction is linear in the input frequency. However, given that the **k** vector of each of the input beams depends on the index of refraction, the resultant $\mathbf{k}_4$ vector will depend on any variations in the index. These variations have the highest gradient around absorptions and therefore the greatest change from linearity in frequency and change in signal level occurs around the very modes that are excited. The behaviour of the signal intensity as ω_2 is scanned can be viewed in an example spectrum shown in figure 3.2, comparing the cases in which the refractive index is taken to be constant (the symmetric curve, reminiscent of the central peak in figure 2.1) and in which the spectral variation of the refractive index is taken into account. In the following section, the determination of these refractive index values is described.

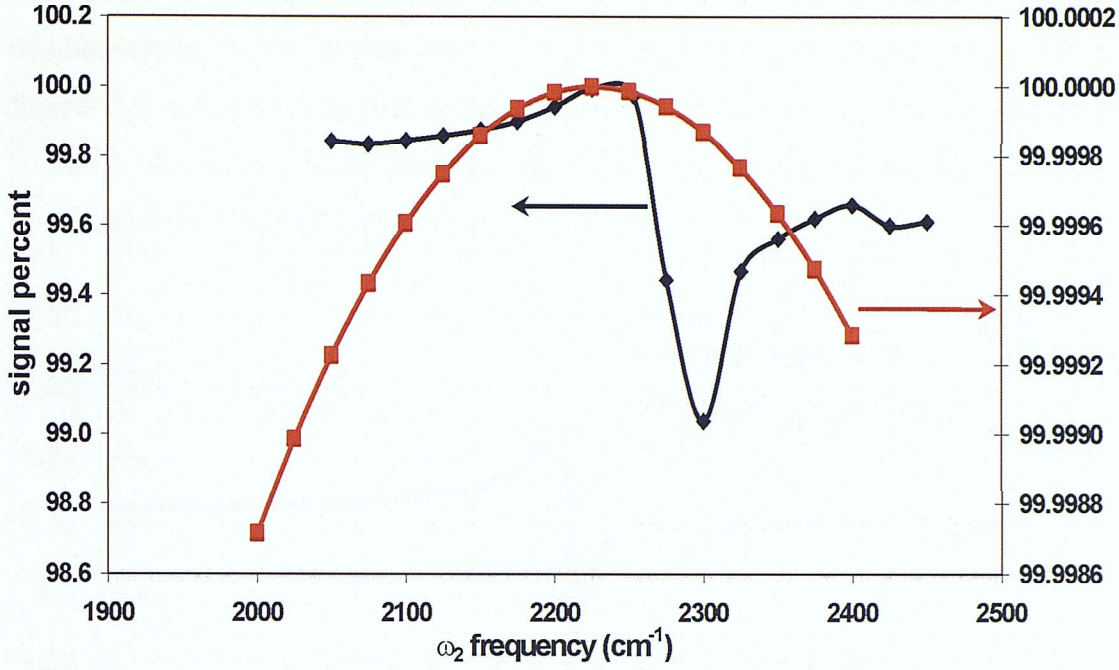


Figure 3.2 The phase matching condition for the cases where the index of refraction is taken to be nondispersive (equal to 1 at all frequencies, red, and identical to the central lobe of figure 2.1) and with the refractive index for acetonitrile substituted (blue). This simulation is for conditions optimized in a plane (ω_1 at 3164 cm^{-1} and 6.5°, ω_2 at 8°,and ω_3 at -2°) but as the absorptions are tuned through, the variation in signal level is clear.

3.3.2. Index of refraction determination

The phase matching condition and the output direction vary with the index of refraction, so it was important to have these values tabulated to input into the phase matching model. The multiplexing model was attempted initially for acetonitrile, whose indices of refraction at a variety of wavelengths have been measured or fitted. The near IR index was obtained to arbitrary resolution by fitting to a power series in the wavenumber, as per ref [31] with the coefficients a_n given therein:

$$n(\nu) \approx a_0 + a_2(\nu^2) + a_4(\nu^4) - \frac{a_2}{\nu^2} \qquad \textbf{(equation 3.1)}$$

For the mid-IR region, refractive index spectra obtained by multiple attenuated total reflection spectroscopy were collated from ref. [32] and obtained directly from Dr. John Bertie of the University of Alberta, Alberta, Canada.

Plots of the real and imaginary refractive index vs. wavenumber in the neighbourhood of the modes used for the acetonitrile experiments are shown in figures 3.3 and 3.4. The first is the spectral region surrounding the C≡N (cyano) stretch fundamental, and the second is the region around the combination band of the C≡N stretch and the C-C stretch at about 3160 cm^{-1}.

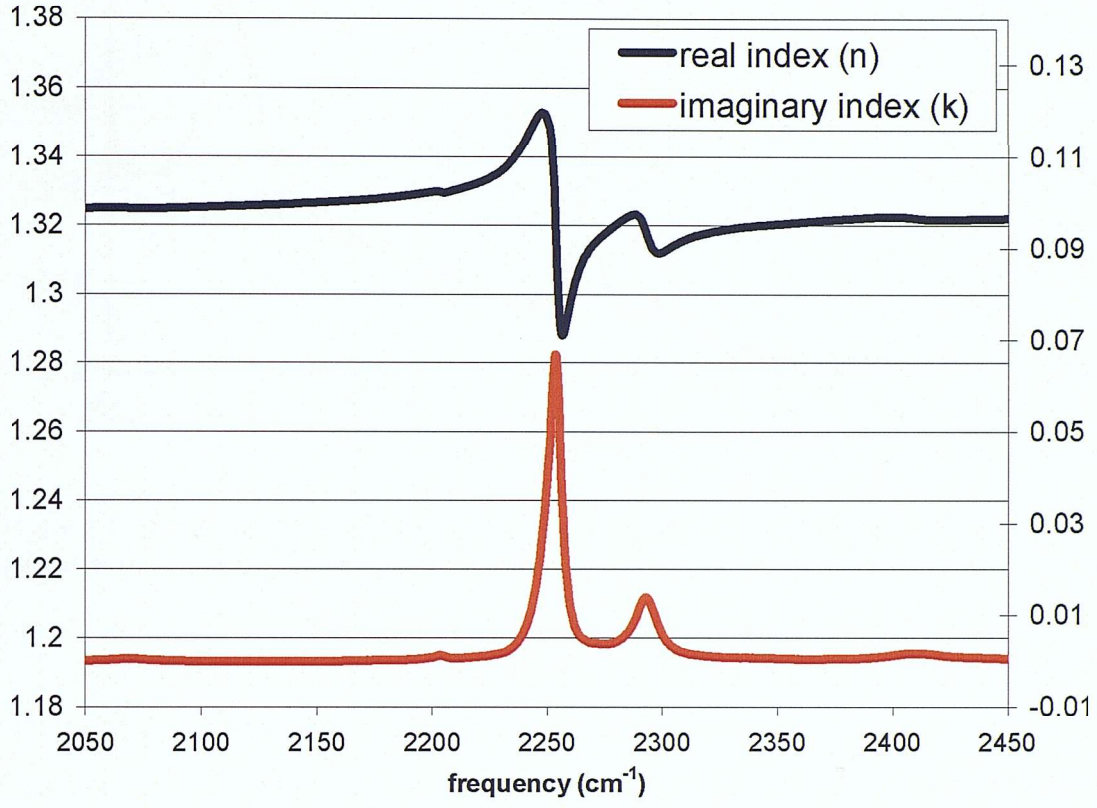


Figure 3.3. Real (blue, left ordinate axis) and imaginary (red, right ordinate axis) indices of refraction for acetonitrile in the vicinity of the ν_2 absorption.

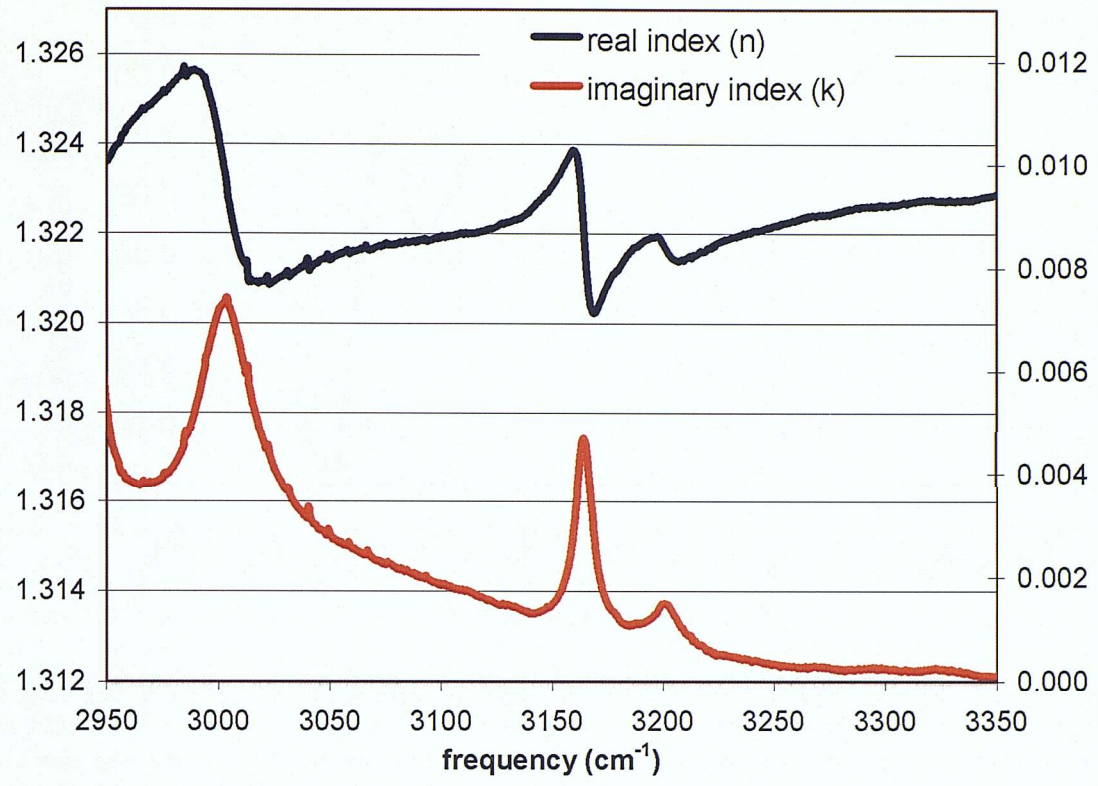


Figure 3.4. Real (blue, left coordinate axis) and imaginary (red, right coordinate axis) indices of refraction for acetonitrile in the vicinity of the $\nu_2 + \nu_4$ absorption.

Both of these traces span about 400 cm^{-1} in frequency, but it should be noted that the scale of the variation in refractive index is ten times higher in the case of the C≡N stretch. In practice, this means that the phase matching condition and absorption change most drastically as ω_2 is tuned through this spectral region. Figures 3.5 and 3.6 shown below are the plots of the output signal as a percentage in these two spectral regions, based on the calculation of the phase matching for the initial experimental set of input frequencies and angles: ω_1 at 0°, ω_2 at 8°, ω_3 at –2° and ω_3 at 795 nm (12579 cm^{-1}), ω_2 fixed at 2253 cm^{-1} for the scan in ω_1, ω_1 fixed at 3164 cm^{-1} for the scan in ω_2. It should be noted there is no absolute optimal arrangement of the input excitations; many orientations of the beams will result in $\Delta k = 0$ at some set of input frequencies. The optimisation of beam angles for the DOVE experiments resulted in those orientations which were experimentally achievable and which were the least sensitive to frequency changes. Figures 3.2 and 3.6 are for exactly the same range but show a different functional dependence on the ω_2 frequency because of slightly different input angles.

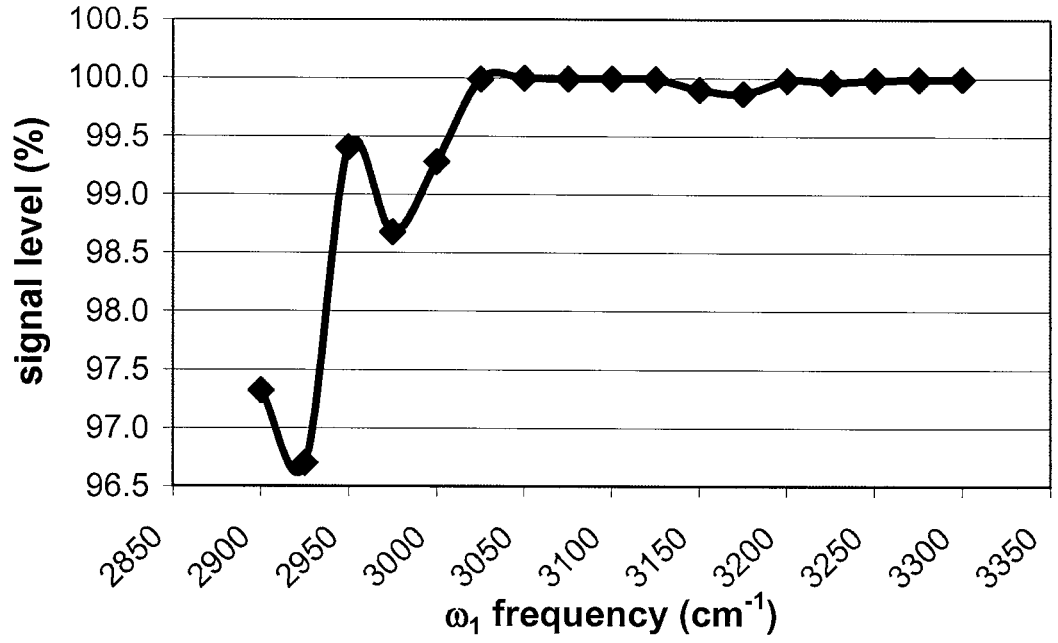


Figure 3.5. Phase matching condition as a function of ω_1 frequency in acetonitrile with ω_2 fixed at 2253 cm^{-1}. The experimental geometry has been fixed as close as experimentally feasible to an optimal geometry ($\Delta k=0$ at and near $\omega_1=3164$ cm^{-1}); ω_1 is at normal incidence, ω_2 at 8° and ω_3 at –2°, all in a plane parallel to the table.

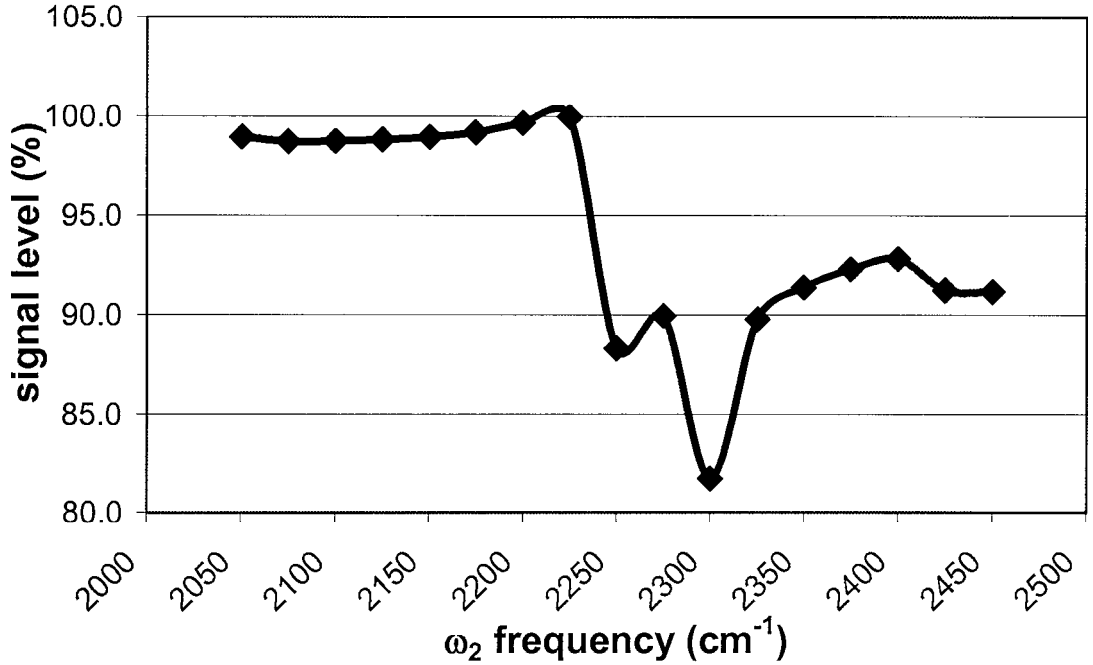


Figure 3.6. Phase matching condition as a function of ω_2 frequency in acetonitrile with ω_1 fixed at 3164 cm^{-1}. The experimental geometry is the same as figure 3.5. The scale of the change in signal as ω_2 is scanned through the strong ν_2 absorption is significantly higher than that of figure 3.5.

As a way to avoid the large changes in signal due to the large change in the refractive index around the C≡N stretch, spectra were acquired with a fixed ω_2 value,

scanning ω_1. The large signal changes could be mitigated by normalising the individual scans in the ω_2 axis. This would be accomplished by setting the signal values equal at a spectral point far from the DOVE resonances where the signal is near the limit imposed by the detection noise floor or by nonresonant background.

Of course, the experimental geometry was first optimised for the case of acetonitrile, and further experiments on different solvents suggest a different optimally phase-matched geometry. However, by testing the signal levels for different samples with the fixed initial geometry and with indices obtained from a Kramers-Kronig transformation of the FTIR spectra, it was found that the expected signal fractions in all of the ensuing experiments were not less than ~70% of the acetonitrile signals, and because of the difficulty inherent in changing the experimental geometry, this set of input angles was kept constant for all of the experiments reported in this thesis.

3.3.3. Further considerations in the phase matching model

In practice, the input beams are not monochromatic, spanning ~25 cm^{-1}, and do not arrive at discrete angles because of the focusing condition. Focusing a 3 mm beam with a 20 cm lens induces an input cone of rays spanning 15 mrad for each beam. The finite nature of the input angles and frequencies results in a spread in the output angles and frequencies. In the case of the single-channel detector (with an active area of ~190 mm^2) and the spectral constraints of the optical filters, this did not affect the detection of the beams. However, this spread in the output direction seriously complicates the process of multi-channel detection and calibration of any multi-channel detectors, a situation which will be described further in section 6.1.2. Additionally, it is known that the DFM process can result in chirped pulses and the model does not account for a distribution of frequencies at the input, it rather considers the excitations as well as sample as "point sources". Lastly, absorption of the beams in the medium around strong absorptions (particularly when any the excitation beams are resonant with fundamental transitions) changes the effective mixing pathlength, and the phase matching model does not account for these changes in signal level. This effect would be reduced in the case where the samples are not optically thick (OD<<1), but for neat solvents this was far from the case.

3.4. DOVE Experimental setup

For the DOVE experiments, two separate wavelength setups were employed. In all cases, two of the three input frequencies were in the infrared, corresponding to vibrational fundamentals in the mid-infrared or overtones and combination bands in the near-infrared. The only requirement on the third input frequency was that it be nonresonant with either vibrational or electronic states and thus it was possible to utilise the remaining pump light from the second OPA, rejected from the final dichroic mirror. For the experiments to repeat the work of Wright *et. al.*., both OPAs were used in DFM mode, operating in the mid-IR regime. When the proof-of-principle experiments on propanol and the amino acids were attempted, one of the OPAs was converted to output the idler beam in the near infrared, available in the range ~1.5 μm to 3 μm (3300 cm^{-1} to 6600 cm^{-1}).

All of the reflective optics designed for use with the infrared beams were protected gold mirrors on silicon substrates (Rocky Mountain Instruments). Gold is the only widely available coating that has good reflectivity in the infrared throughout the planned range. Mirrors for use with the visible beam ω_3 were all broadband dielectric coated mirrors (CVI), optimised for reflectivity at 800 nm.

All three of the output beams from the OPAs are passed through a spatial filtering setup, that is, a Galilean telescope with a pinhole at the focus. The purpose of these spatial filters is to improve the spatial mode of the beams. At the focus of a lens, higher spatial frequencies present at the input correspond to a higher distance from the centre of the focused spot. These higher spatial frequencies correspond to the inhomogeneous portions of the beam, and by placing a pinhole at the focus to block these higher spatial frequencies, the output of the spatial filter has much better mode quality (that is to say, more closely approximates a two dimensional Gaussian intensity profile) but at the expense of some of the energy present at the input. This improved mode quality results in a smaller focused spot size and more homogeneous intensity at the sample. Further, spatial filters act as a "point source" so that variations in beam position on the input side results only in a reduction of intensity at the output. If the output intensity is monitored and can be factored out (addressed in section 6.1.1), this will account for signal variations due to changes in mode quality, pointing, or position, which can otherwise be very difficult to quantify.

The spatial filtering lenses constitute a collimating telescope as well. In the case of ω_3 this is a one-to-one telescope, but for ω_1 and ω_2 the magnification is ~3 in order to bring them to a smaller focused waist size. The second lens in each telescope is mounted on a manual linear translation stage in order to correct for the divergence of the OPA output, which varies when tuning the output wavelengths or making internal adjustments to focusing into the OPA crystals, etc.

In general, the pulse energies available in the infrared beams were sufficiently low that it was not necessary to consider damage threshold issues (on the order of a few μJ in the mid-infrafed and ~12 μJ in the near-infrared), so that the infrared output was never attenuated. However, the output available in the visible beam is on the order of 350 μJ, easily high enough to damage the samples. As a consequence, a half-waveplate/polariser combination was installed as an attenuation measure, and the amount of pulse energy delivered to the sample was typically a few μJ. Several early experiments were performed with the ω_3 pulse energy set as high as 20 μJ, but the linearity of the measured signal was maintained even at this high intensity. In all probability, the pulses were too long for many higher order effects at this level of intensity (self-focusing, white light generation, etc.) but the pulse energy was kept low in future experiments as the detection was not limited by small total signals.

One of the infrared beams (ω_1) and the visible beam (ω_3) have delay lines in their optical path so as to be able to control the temporal alignment of all three pulses at the sample. These delay lines are linear translation stages (Newport) equipped with two 45° turning mirrors aligned exactly orthogonal to one another. Translation of the stage simply introduces a time delay to the input pulse without changing its direction. The delay stage for ω_1 and ω_3 are motorised and integrated through a GPIB interface with Labview software, which drives the stages and communicates with a lock-in amplifier.

After this "beam conditioning" section of the experiment, where the beam sizes, divergences, polarisations, and relative timings are set, the beams are aligned into the sample. All three are focused using 20 cm focal length plano/convex lenses (Coherent). In the case of ω_1 and ω_2 these are uncoated calcium fluoride lenses and in the case of ω_3 was a standard anti-reflection coated optical glass lens (broadband coating centred at 800 nm). Following the final focusing lenses, there is one more turning mirror to align the focusing beam into the sample.

Finally, the spectral region comprising many molecular fundamental modes (ω_2, around 1500 cm^{-1}) contains a great many atmospheric absorptions, for example from carbon dioxide and atmospheric water. There are many very narrow absorption lines for water in particular in this spectral region, so it was necessary to enclose the ω_1 and ω_2 beam paths in a sealed box. The box was then purged with dry nitrogen, which does not have any absorptions in the spectral regions that were explored in the course of this research. The box's enclosed area included the entire path between the OPA output port and a few cm prior to the sample. The flow was maintained just high enough to keep the box under positive nitrogen pressure. Although the worst-case change in ω_2 pulse energy measured at the sample position was <10%, there were significant changes in the nonlinear signal size and noise upon purging the box. It is quite likely that these changes are the result of timing differences induced by changes in the local index of refraction in the beam paths, delaying or even emporally breaking up the infrared pulses. The absorption of water at these wavelengths can be very high, and it is clear that the refractive index will change radically over these narrow spectral ranges. Given that the path length between the OPAs and the sample was greater than two metres, very small changes in the local refractive index could effect large changes in both the direction and, critically, the relative timing of the pulses.

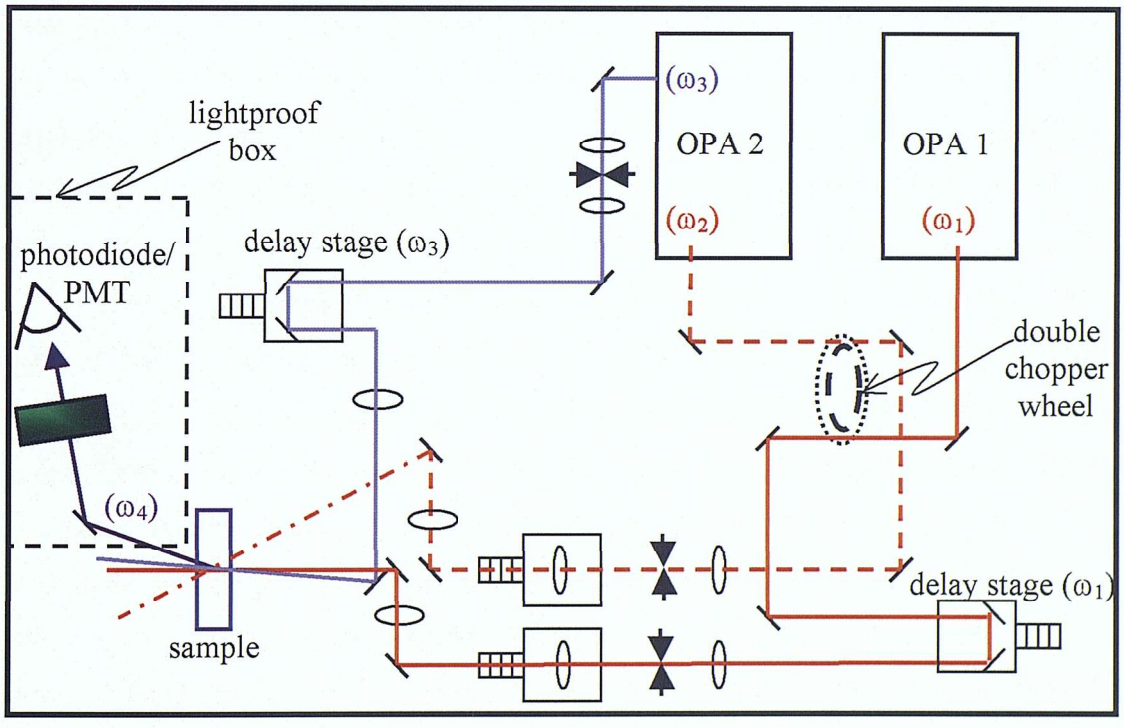


Figure 3.7. Schematic diagram of the spectrometer setup. Ovals are lenses, couble arrows are pinholes (spatial filters), and the green box represents optical filters.

Figure 3.7 presents a simplified plan view diagram of the spectrometer for ease of visualisation. In order to maximise the nonlinear optical signal produced in the samples, the input pulses must be aligned in space and in time in the sample. In the following section, the procedures for these alignments are outlined.

3.4.1. Spatial alignment procedure

In order to ensure that the three input beams cross at the sample position, a round pinhole (200 μm diameter, Coherent) was placed at the sample position. A pyroelectric Joulemeter (Molectron) was placed behind the pinhole to measure the energy passing through the pinhole. Each beam was allowed to be incident on the pinhole and the throughput was maximised using the final turning mirror and the moveable lens of the collimating telescope. A first method of checking the overall alignment of the light sources and the experiment was to check the pulse energies passing through the pinhole from one day to the next. On many days it was found that these pulse energies and the fraction they represented of the total pulse energy would vary only by a few percent.

3.4.2. Beam waist size measurements

Given that the nonlinear signal from the sample is linearly dependent on each of the input intensities, it was necessary to know the beam sizes at the focal plane as well as the pulse energies of the input beams. From Gaussian optics it is straightforward to determine an approximate spot size based on the percentage of the total energy that passes through the alignment pinhole mentioned in the previous section. For example, if 50% of the total energy is passed through the pinhole, the pinhole size is approximately the same size as the beam waist (measured at the full width at half maximum points, FWHM). If ~99% of the total energy is passed through the pinhole, the pinhole is ~3 times the FWHM of the beam waist. More accurate beam waist measurements were made by the "knife edge" method when necessary. In this method, a sharp edge such as a razor blade is passed across the focal plane and the power transmitted beyond the blade is measured as a function of blade position. By differentiating the resulting power transmitted vs. blade position curve, a Gaussian curve is generated, and the FWHM width of the beam is proportional to the FWHM width of this curve.[33] The beam waist sizes for all three

beams have been measured in this way and it was found that the mid-infrared beams measured ~100 μm at the focus, the near-infrared beam ~80 μm, and the visible beam ~70 μm.

3.4.3. Temporal alignment procedure

It is necessary to ensure that the pulses arrive at the same time as well as the same place. However, the overlap of infrared pulses is very difficult to ensure; most techniques for temporal alignment are based on the same techniques used to perform an autocorrelation of pulses to determine pulsewidth, e.g. second-harmonic generation (which relies on the pulses being of a single frequency, split from the same source), or sum-frequency generation (for two-colour or cross-correlations). These techniques are at their most mature for the case of high-energy photons in the visible or ultraviolet. However, for the case of two infrared pulses of very different wavelength, standard upconversion techniques such as these are impossible to implement.

It has long been known that the high peak powers available with short-pulse lasers can invoke a multiphoton response in bulk materials. Much progress has been made in the last ten years developing various techniques to exploit the multiphoton response of semiconductor photodiodes for the autocorrelation of visible[34,35] and near-infrared[36-38] pulses. Only recently, however, have measurements been made using the same technique in the mid-infrared spectral region,[39] and this methodology has been modified for the purposes of these experiments. Briefly, focused mid-infrared beams incident on a semiconductor photodiode can create an electron-hole pair at the surface of the photodiode by multiphoton absorption. This method is extremely convenient; there are no constraints on the geometry as would be the case in phase-matched techniques, the method is applicable to the two-colour case, and photodiodes are inexpensive and easy to implement.

Firstly, the ω_1 and ω_2 pulses are temporally overlapped and then the ω_1 pulse is overlapped with the ω_3 pulse. In the case of the ω_1/ω_2 cross-correlation, a standard silicon photodiode is employed. Research by Briggman *et. al.*. has shown that the response of silicon to ultrafast infrared pulses is proportional to E^n, where E is the pulse energy and n is the approximate number of photons needed to span the optical bandgap. Silicon's optical bandgap is 1.12 eV, corresponding to a roughly four-

photon process in the mid-IR regime in order to create one photoelectron. However, if two pulses are incident at the same time (strictly, within the dephasing time of the electronic transition in silicon, which is taken to be negligible in comparison to the pulsewidths), the probability of electron-hole pair generation is increased exponentially. Therefore, if ω_2 is kept fixed in time and the delay stage for ω_1 is scanned, the photocurrent vs. delay graph so generated shows a distinct Gaussian peak centred around zero delay ("T_0") between the pulses. A mechanical chopper is inserted into one of the beams and provides the reference frequency for a lock-in detector, which reads the signal from the photodiode. The GPIB interface and Labview-based software allows integration of the motorised delay stage with the lock-in detector, and to vary sampling parameters such as the amount of signal averaging at each delay stage position. A typical ω_1/ω_2 cross-correlation trace is shown in figure 3.8.

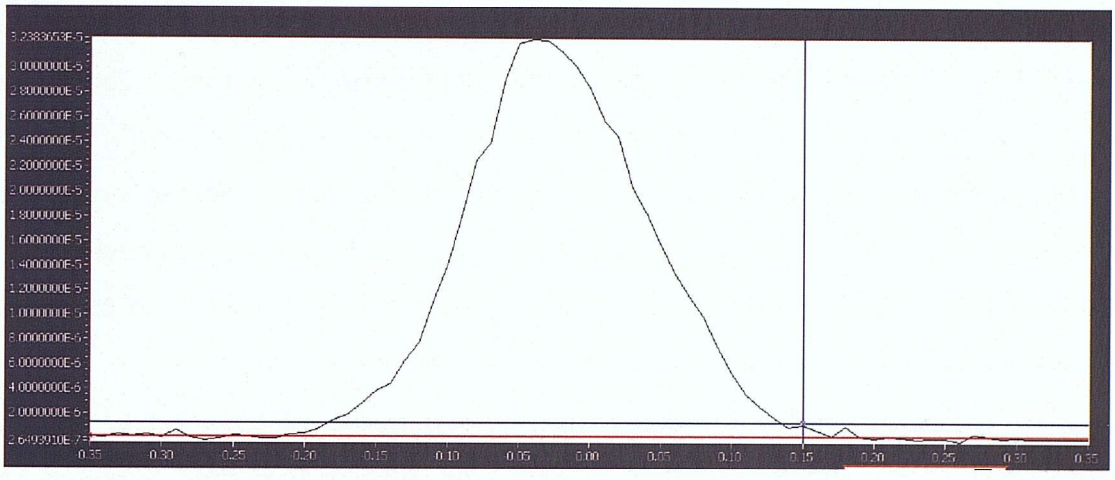


Figure 3.8. A typical ω_1/ω_2 cross-correlation trace obtained with a silicon photodiode. Here the units on the ordinate axis represent the position of the stage in mm (the timing corresponds to the linear distance of the stage as 6.67 ps/mm, i.e. twice the value obtained from the reciprocal of the speed of light, because the beam traverses the stage twice).

The trace is clearly not centred at 0, and it is possible to adjust and re-zero the stage based on the traces obtained. It is worth noting that the traces obtained in this way from liquid samples are never as symmetric as the example above, and data will be presented in Chapter 4 to examine the temporal response of signals. It is necessary for reproducibility of the timing to use either this method or a standard sample for the determination of the absolute T_0, as the traces are different for each sample. Moreover, it has been shown that the lineshapes in DOVE spectra are measurably

different if the relative timing of the infrared pulses is changed by as little as ~200 fs (10^{-13} s) so that very precise measurements of T_0 are absolutely necessary.

It is not possible to use the silicon photodiode for the cross-correlation of the ω_1 and ω_3 pulses because a single ω_3 photon will span the optical bandgap of silicon. The single photon process will lead to a signal that is orders of magnitude higher than that caused by any multiphoton processes. Therefore, a semiconductor with a higher bandgap was necessary. Cadmium telluride (CdTe) has an optical bandgap of 1.49 eV and CdTe photodiodes are commercially available. A 1 mm^3 photodiode (Eurorad) with a homebuilt preamplifier and biasing circuit was chosen for the purpose. For the ω_1/ω_3 cross-correlation, the chopper signal from the ω_1 ring of the chopper wheel was taken as the lock-in's reference frequency. Using this photodiode and a procedure similar to the ω_1/ω_2 cross-correlation, it was possible to temporally align ω_3 with ω_1 and thereby ensure temporal alignment of all three pulses.

The temporal overlap obtained in this way does not take into account the varying refractive indices (group velocity mismatch) at the various excitation frequencies. The relative delay induced by passage through a sample cell window which is absent during the cross-correlation procedure shifts the real zero delay as denoted on the graphs presented in this chapter, and the precise shift depends on the frequencies as well as the window material and thickness. This difference is greatest for the case of the thickest employed windows (2 mm CaF_2) and for the largest disparity in frequency between the excitation frequencies ($\omega_2 = 1500$ cm^{-1}, $\omega_3 = 12740$ cm^{-1}). In this case the relative delay induced by the window is ~360 fs, and temporal plots will actually be in the T_0 condition at this value of t_{23}. A significantly smaller effect will also shift the real zero in the t_{12} dimension. However, the temporal plots have not been corrected for this effect.

The cross-correlation traces obtained with the photodiodes provide a simple means to determine the pulsewidths of the beams. It is known that for pulses that are Gaussian in time, the autocorrelation trace for standard frequency-doubling techniques is $\sqrt{2}$ times the FWHM of the input pulses. In this case, n from the E^n scaling is equal to two. However, Briggman notes that the autocorrelation for n>2 is not perfectly Gaussian, and therefore performed numerical simulations to determine the pulse width scaling factor for a number of different n values.[39] Figure 3.9 plots a third-order curve which is fit to these values in order to interpolate and determine

scaling factors for pulses of arbitrary wavelength. It therefore only remains to determine how many photons of a given wavelength it takes to span the bandgap for the photodiode material.

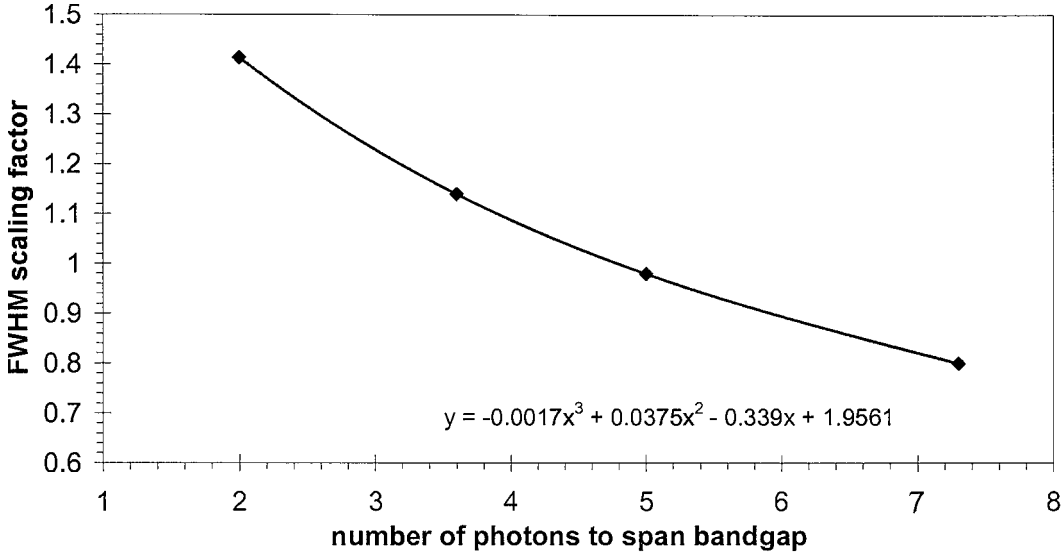


Figure 3.9. Curve fit to the data of Briggman *et. al.*. showing the relation between the FWHM time measured in an two-pulse autocorrelation trace and the number of photons needed to span the bandgap in the semiconductor material.

It is noted that this kind of pulsewidth determination is only applicable when $\omega_1 = \omega_2$, and no significant change in pulsewidth is assumed when tuning wavelengths in the mid-IR. While two-colour cross-correlation has been accomplished for the case where the photoconductivity is due to a strictly two-photon process (in GaAsP),[38] we believe that this work was the first to employ semiconductor diodes for two-colour cross-correlation-based determination of pulsewidth and temporal pulse overlap in the mid-infrared with arbitrary photon energy.

The need for cross-correlating pulses in this way was reduced somewhat upon finding the first nonlinear optical signals. Once an approximate T_0 has been found, the nonlinear signal from a standard liquid sample can be used to fine-tune the overlap, though in practice it has been found that the use of the laser system for other experiments shifts the alignment, and thus the relative delay of the pulses, a great deal. The use of this semiconductor alignment procedure isolates the sample and detection setup from the spatial and temporal realignment procedures, reducing the number of variables when attempting to re-acquire a nonlinear optical signal.

3.4.4. Detection

The optics, detectors, and electronics for the detection of the signal beam (henceforth "detection setup") will be described in this section. Initially, signal levels were high enough to permit the use of a standard silicon photodiode and preamplifier. However, later samples resulted in much smaller signal levels and the photodiode was replaced with a PMT. A PMT has extraordinary sensitivity, able to measure the arrival of single photons, but this sensitivity comes at the expense of dynamic range; that is, the measured signal must be within a narrow range of intensities in order to not saturate the PMT, resulting in an inaccurate count of photons.

In all forms of detection utilised for this work, the contribution of the relatively intense ω_3 beam to the detected intensity had to be mitigated. DOVE, as a coherent third-order spectroscopy, produces an output beam that is both spectrally and spatially separated from any of the input beams. Neither of the detectors employed in these experiments were sensitive to either the ω_1 or ω_2 radiation, but both were sensitive to the ω_3 beam. The optimum phase matching conditions result in the signal beam being very close spatially to the ω_3 pump beam, and recall that the frequency shift of the signal beam is only the frequency difference between the two infrared beams, corresponding to a shift of frequency of the visible beam of just a few tens of nanometres towards the blue (higher energy). While spatial blocking (by means of an iris diaphragm) can reduce some of the contribution from the visible beam, there is some overlap of the visible and signal beams and so the visible beam cannot be completely blocked in this way. On the other hand, spatial filtering of the signal beam (by means of a Galilean telescope with a pinhole at the focus) would have significantly reduced the visible beam contribution, but the change in output direction of the signal beam with tuning would have seriously complicated alignment of the post-sample optics and calibration of detectors. Therefore, the most effective method of limiting this contribution was with optical filters (to reduce saturation of the detector) and lock-in detection.

3.4.4.1. Optical filtering

The ω_3 beam constitutes $>10^{13}$ photons/pulse and a number of optical filtering combinations were attempted in order to block these photons. For early experiments, a dielectric mirror designed for operation at 800 nm at a 45° angle of incidence was

employed as a filter for the signal beam. It was discovered that the contrast ratio of the mirror (reflection coefficient of the dielectric coating for 795 nm compared to the signal wavelength of ~760nm) was very sensitive to the angle of incidence. A graph of the measured reflection coefficient (log scale) is shown in figure 3.10 as a function of angle of incidence.

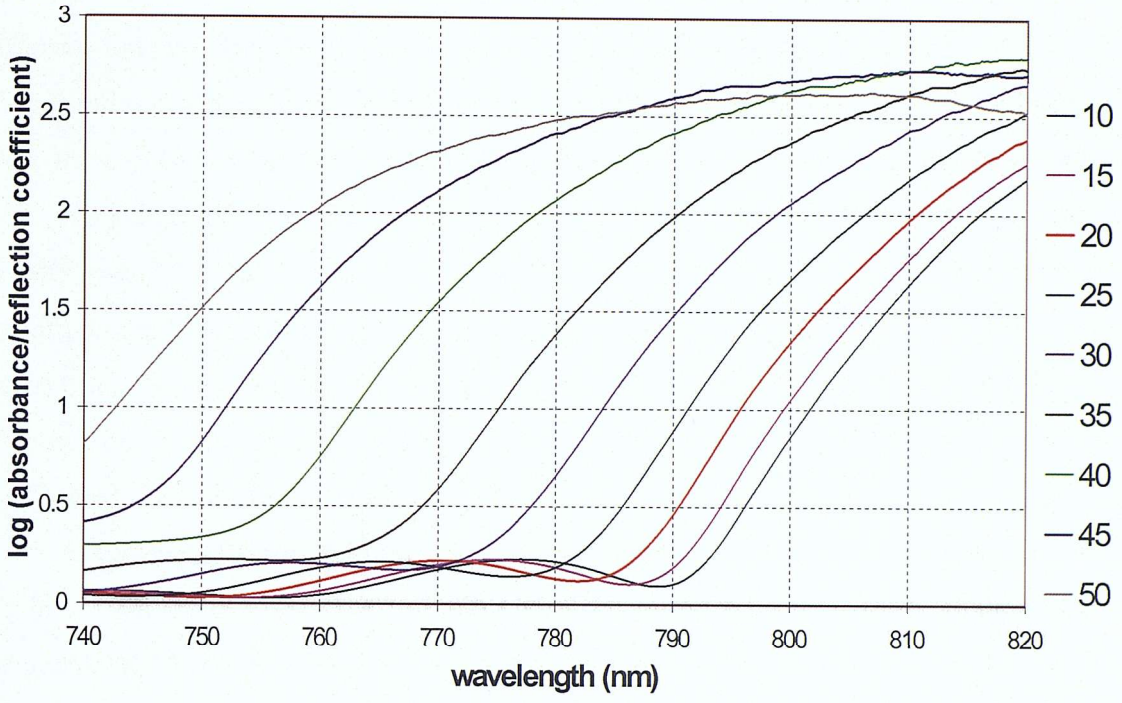


Figure 3.10. Absorbance values of an 800nm-optimised dielectric mirror as a function of wavelength and angle of incidence (relative to the normal, indicated in the legend).

By using the mirror in transmission and oriented at an angle of incidence of 35°, it was possible to reflect the 795 beam and pass the signal beam with a contrast ratio of ~100, providing a cheap and readily available source of optical filtering. However, much more optical density to the visible wavelength was needed. A more standard option for blocking the ω_3 beam would have been to employ holographic notch filters to eliminate just the visible beam wavelength. However, easy and quick availability of bandpass filters made them a better option, passing just the signal beam wavelength and blocked any wavelengths outside this region. These filters (Coherent) had a passband centred at 740 nm, the signal wavelength corresponding to the predicted first signal wavelength. However, the passband curve is very narrow (~13 nm at the OD=0.3 points) and when tuning either of the mid-IR beams, the signal wavelength quickly approached the edges of the passband, where the optical

density gradient is high. The additional variable of optical density for the signal wavelength introduced another source of error in the measurements, which strongly depended on the accuracy of wavelength measurements. In order to maintain flexibility in the experimental setup, the bandpass filters were replaced with shortpass filters (Omega Optical), which pass wavelengths below ~760 nm with optical density <0.1 and block wavelengths above ~780 nm with optical density >5. The OD=0.3 points for three of these filters varied somewhat as they were from different batches, but the slope and peak of the absorption curve beyond ~770 nm were similar enough to warrant their use. Finally, calibrated neutral density filters were used between the sample and the detector to keep the signal level below the level of saturation. However, it was found that these neutral density filters' optical density was far from the specified value at signal wavelengths, so that absorption spectra were taken from each to determine their exact optical density. For the determination of signal levels in terms of photon number, the individual absorption spectra from each filter were added and the signals were corrected for the sum optical density provided by the suite of optical filters.

A number of simulations were run with the phase matching program, exploring a wide range of possible infrared input wavelengths. These simulations demonstrated that the signal wavelength should not exceed 760 nm. In addition, a longpass filter (OD=0.3 point at ~718 nm) was added to eliminate contributions in the visible region. Finally, a lightproof box was constructed and placed around the final turning mirror into the detector and the PMT itself to reduce the effects of e.g. stray room light and equipment lights, and an anodised aluminium tube was placed between the entrance of this box and the sample to reduce the solid angle for the entry of light into the detection setup.

3.4.4.2. Lock-in detection

Lock-in detection is a means by which exceedingly small AC signals can be measured with high signal-to-noise ratio. Lock-in detectors measure signals as small as the nanovolt regime, and can separate signal components orders of magnitude smaller than noise that may be present in the total signal. This is accomplished effectively by frequency filtering; the signal is detected at a specific frequency and definitive phase relative to an externally provided reference frequency source.

We employed a Stanford SR830 two-channel digital lock-in detector and designed a reference frequency source to isolate the component of the photodetector

signal which is due to both infrared beams. Firstly, a double chopper wheel was inserted. This comprised an optical chopper wheel with two sets of slits centred at two diameters on the wheel. In this way, two reference frequencies are generated, and manipulation of these frequencies could be used to isolate a given component of the total signal corresponding to modulation in two input beams. The wheel was oriented such that the ω_1 beam passed through one set of slits and the ω_2 beam passed through the other. Photodiodes and small LEDs within the chopper wheel assembly measured the pass/block repetition rate of each of these sets of slits, resulting in two trains of square wave pulses at two different frequencies ν_1 and ν_2 but with a fixed phase difference. The fact that the two sets of slits were on the same wheel eliminated the need for two separate single choppers and a means to phase-lock the two. The two reference frequencies were sent into a homebuilt difference frequency generator circuit. This circuit is composed of a TTL exclusive OR integrated circuit that has as its output all combinations of the two input frequencies and their harmonics. This signal is then passed to a state-variable filter, which isolates the difference frequency (ν_1-ν_2). This resulting frequency is then used as the reference frequency for the lock-in detector. In this way, the component of the signal which is present at the frequency (ν_1-ν_2) is isolated. Since the component of the total photodiode signal that is due to ω_3 beam is present at a different frequency, this contribution to the measured signal is eliminated (provided that the number of ω_3 photons present does not saturate the detector). Values for the in-phase component of the signal at (ν_1-ν_2) were read directly from the display of the lock-in, so that all signal size data reported herein are signal sizes acquired at this difference frequency.

The total number of photons incident on the detector was much higher than the number generated within the sample, and these non-signal photons resulted in a great deal of noise on the lock-in signal. A standard method of reducing these non-signal photons is by gating the signal, that is, effectively blocking the signal from the detector except during a short specified time interval. For this purpose an Ortec linear gate was employed, triggered by the trigger pulse available from the laser system's timing electronics. The gate has a variable width, which was set to its lowest width of 4 μs. In this way, the PMT signal was blocked by the gate, except for a 4 μs time window at the time of arrival of the laser pulses and thus the signal. This serves to reduce signal caused by background light or room lights.

Unfortunately, most of the photons incident on the PMT are scattered from the ω_3 beam at exactly the time the gate is open. Nevertheless, all signal generated by the PMT outside of this window was rejected, resulting in a 2.5×10^5 reduction in PMT signal caused by ambient light, and a significant improvement on the noise figures from the lock-in signal.

3.4.5. Constraints of the spectrometer: tuning

The specifications and tuning curves provided by Spectra-Physics suggest only the wavelength range over which the OPA and DFM crystals operate; no specification is provided for any resultant changes in output pointing, divergence, pulse broadening, etc. as the OPAs are tuned. Tuning of the grating in the OPAs changes the selected wavelength, and as the gratings are aligned for Littrow reflection, this should not result in any change in direction. However, the BBO crystal and $AgGaS_2$ crystal had to be rotated (about a horizontal and vertical axis, respectively) in order to optimise the phase matching—and thereby the conversion efficiency and output pulse energies—for a range of wavelengths. Because these crystals are of quite high refractive index, their rotation results in a displacement of the output beam from simple refraction. It was also unclear if large changes in the set wavelength had any effect on the output divergence. Another consideration is the achromaticity of the delivery optics; as the wavelength changed, any variations of refractive index with wavelength of the telescope or final focusing lenses would translate to different transmission through the spatial filters or to different spot sizes at the sample position. Finally, the temporal alignment of the input pulses must be considered; by changing the effective pathlength for the pulses by varying the crystal angles, the relative timing of the pulses clearly will change with tuning. The sum consequence of all these effects was a limitation on the amount of tuning which was possible without changing the alignment of the output beams, position of focusing lenses, etc. In the interest of maximising reproducibility, mid-experiment changes to the spectrometer were to be minimised. The scale of at least the spatial (beam size and overlap at the sample position) limitation was borne out with a simple experiment. Firstly, the transmission of the output beams through a pinhole placed at the sample was optimised. Then each beam was tuned until the transmission through the pinhole dropped by 50%. For OPA1, operating near 3000 cm^{-1}, this change was ~320 cm^{-1}. For OPA2, operating near 1360 cm^{-1}, this change was only 130 cm^{-1}. (It

is interesting to note that these changes in wavenumber represent a similar fractional change in frequency, constituting 10 and 11% of their values.) While a drop in transmission through the pinhole of 50% of one of the beams will not necessarily result in a drop of 50% of the signal, this test provided an idea of the scope of the changes induced by tuning, suggested a limit for the range of wavelengths to be pursued in the experiments, and highlighted another consideration for absolute comparisons of resulting spectra.

3.4.5.1. Noise and drifts

As the intensities of the third-order signals from the sample are proportional to the intensities of each of the three input beams, pulse-to-pulse variations in energy in any one of the beams will translate directly to noise on the signal. The pulse-to-pulse standard deviation of pulse energy at the output of the regenerative amplifier over 10 seconds was kept below an upper limit of ~0.33% and the same measure of pulse energy stability from the OPAs was at best ~0.8%, so it is clear that the limiting noise level was that created in the OPAs themselves. Further, simultaneous acquisition of the pulse energies from both OPAs has shown that the noise on each beam is not correlated. In fact, even though the ω_3 beam is just the remaining unconverted pump light, itself only undergoing linear processes through the OPA, its noise was uncorrelated to the noise at the output of the regenerative amplifier.

A far greater consideration for the integrity of the 2-D data was the long-term drifting of the laser system's pulse energies and stabilities, on timescales from minutes to hours. The painstaking nature of manual frequency tuning meant that 2-D data was collected often over many hours, so that the variation in pulse energy over these timescales reduced the reproducibility of spectra and resulted in large error bars on the data. Some straightforward improvements to the spectrometer to mitigate these short- and long-term noise sources will be discussed in Chapter 6.

3.5. Protocols and diagnostics

The laser system for the experiments described in this thesis was installed at the beginning of this project, and every alignment and maintenance protocol was developed during the course of this research. Many of the scheduled maintenance and cleaning protocols were developed over a great deal of time, assessing each component of the system in turn and determining a metric for performance and

experientially determining a schedule or criterion for maintenance. As such, a number of the day-to-day running protocols are relevant to discuss. Also in this section, a number of diagnostic tools and protocols will be described. The laser system is a complex and commercially novel light source, comprising a number of separate but interdependent stages. Each of these stages had to be monitored to ensure optimal performance of the system as a whole, and commissioning of the laser system at the outset of this project necessarily required the implementation of the diagnostic tools and procedures described below.

The reader is again cautioned that this section is provided largely for the benefit of future users; the most scientifically relevant details have been provided in prior sections of this chapter.

3.5.1. Beam pointing

Between each stage of the commercial system, quadrant photodiodes were installed. The purpose of these detectors was to measure the beam pointing (variation in directionality) out of each component of the system. The detectors comprise four separate photodiodes, arranged in a square or, in this case, a "pie" shape—round and divided into four equal sections.

A portion of the beam at each stage is collected by, e.g., the leak-through of a mirror or the beam off the back face of a reflective optic and is focused onto the centre of the "pie" with parts of the beam incident on all four of the photodiodes. Homebuilt data acquisition cards register the amount of energy incident on each of the four, subtracting the contribution of the top from the bottom photodiode, and the left from the right. In this way, a positional "zero" is defined, i.e., the point at which the contribution on all four photodiodes is equal. By fixing the detectors and aligning the beams to this zero point, it was possible to monitor any change in the output pointing of the seed (Tsunami), regenerative amplifier pump source (Evolution), or the regenerative amplifier itself. Two similar quadrant detectors were built for the purpose of monitoring the OPA outputs, but employed pyroelectric detectors instead of standard silicon photodiodes in order to be responsive to infrared input light.

3.5.2. Power/energy

Average power from the Millenia pump laser, the Tsunami oscillator, and the Evolution pump laser were measured with a Molectron PM-30 thermopile detector. Pulse energies from the regenerative amplifier were measured by a Molectron J5 pyroelectric detector and pulse energies of all of the beams within the OPAs as well as the OPA output energies were measured by a Molectron J3 pyroelectric detector. All these detectors were used in conjunction with a Molectron EPM1000 readout, which in the case of the pyroelectric detectors could be triggered at a repetition rate up to 1 kHz. The EPM1000 could in turn be connected via an RS-232 interface to Labview-based software for use with a computer. The EPM1000 provided instantaneous average power or single-shot pulse energies or could be configured to display statistics such as the average and standard deviation of pulse energies.

3.5.3. Autocorrelators

Two autocorrelators were available for direct measurement of the pulsewidths of the outputs from the Tsunami, the Spitfire, and the OPAs. These were standard scanning autocorrelators (PulseCheck, APE Berlin), which measure a pulse's width by splitting it in a Michelson interferometer and recombining the pulse halves in a nonlinear crystal, measuring the second harmonic intensity as a function of delay in one of the arms of the interferometer. However, it was found that an autocorrelation could be obtained indirectly from the cross-correlation trace produced during the temporal alignment procedure (see section 3.4.3). The autocorrelators were employed at the installation of the laser system to check initial pulsewidths but were largely unused after this point, as easier cross-correlation measurements became part of the experimental protocol.

3.5.4. Spectral measurements

An Ocean Optics multichannel spectrometer comprising four S2000 fixed grating spectrometers allowed measurement of the wavelengths between 180 and 1100 nm. Each S2000 contains a fixed grating and linear CCD array to detect wavelength in a given region. The CCD array is integrated with a Windows-based program which displayed the intensity vs. wavelength trace. Its purpose was primarily to keep track of the centre wavelength of the seed laser, which drifted

considerably during system warm-up and after any alignment of the cavity end mirrors.

For wavelengths between 1 μm and 12 μm, a Jobin Yvon Triax three-grating imaging spectrometer was used. A mercury cadmium telluride (MCT) detector (Infrared Associates) in a 12-hour dewar for liquid nitrogen cooling was placed at the exit slit of the monochromator. The detector signal is passed through a low-noise preamplifier and then into a lock-in detector. An optical chopper wheel was inserted into the beam just before the monochromator. GRAMS-based software integrated the scanning monochromator and the lock-in detector, providing automated acquisition of spectral scans. The monochromator included two gratings, one for measurement between 1 μm to 4 μm (blaze wavelength 2 μm, ruled at 300 lines/mm) and one for measurement between 3 μm and >12 μm (blaze wavelength 5 μm, ruled at 150 lines/mm). Initially a calcium fluoride (CaF_2) plate was inserted into the beamline at the output of the first OPA and aligned into the spectrometer. In this way, a small fraction (~1 %) of the OPA output was always incident at the spectrometer. For the purposes of measuring the wavelength of the second OPA, a gold mirror was inserted at the output of the OPA identically along the path of the first OPA's output to the spectrometer. It was therefore not possible to simultaneously monitor the wavelengths of both OPAs, and time-consuming to align the second OPA into the spectrometer. The experimental protocol was therefore to set the second OPA at a given wavelength, scan the first, monitoring its wavelength point-by-point, then inserting the gold mirror and adjusting the wavelength of the second OPA. It was thus possible to build up 2-D maps from "slices" at fixed ω_2. However, it was found that the measured wavelengths of the OPA outputs were very repeatable in terms of the settings on the OPA micrometers, so a set of tuning curves were taken and checked weekly, eliminating the need to measure the wavelength point by point. Initially a few spectral points were taken across a wide spectral range and, once a functional form for the tuning curves were established from wave mixing and geometric considerations, a curve could be fit and the entire tuning curve could be interpolated to arbitrary precision with an accuracy of ± 3 cm^{-1}. Further checks on the curves on different days proved that the functional form of the tuning curves did not vary, and even after major realignments of the system, it was only necessary to find a linear offset to re-establish the curves.

3.5.5. Protocols - general alignment concerns

The initial setup of all of the optics external to the laser system was accomplished by back-aligning diode lasers through the optics. That is, diode lasers were installed and sent counter-propagating to the infrared beams, which were clearly much more difficult to find and align. In this way, the desired input angles could be set at the sample position through the use of appropriately placed iris diaphragms on either side of the sample. Near to the output of the OPAs, a pair of these iris diaphragms and two alignment mirrors for each beam were installed, so that once the diode laser beam had been aligned through the spectrometer optics and sent into the OPAs themselves, it remained only to align the counter-propagating infrared beams through the irises closest to the OPAs and thereby through the rest of the spectrometer. In the earliest stages of setup, the infrared beams were located by the use of liquid crystal paper (Edmund Scientific), whose colour changed with temperature. However, the very low pulse energies and the enlarged sizes of the beams once in the spectrometer optics precluded the accurate measure of position with the liquid crystal paper, and more precise alignments were made by placing the pyroelectric Joulemeter behind the partially closed alignment irises and optimising the energy transmitted through the irises by adjusting the alignment mirrors.

While the alignment accomplished in this way varied very little from day to day, any adjustments to the laser system necessitated realignment. A cause for much alignment concern was that the laser system was in use for more than one experiment on the laser table. For much of the time of the project, biweekly changeovers were made between these different experiments, drastically changing the optical setup and the alignment throughout the OPAs and thus through the spectrometer. It was therefore necessary to institute protocols for the alignment of not only the three input beams to the sample, but also the diagnostic beamlines, e.g. from the output of the first OPA to the monochromator at the end of the table.

3.5.6. Seed laser

The pump source (Millennia) for the seed laser proved to be the most reliable component of the entire commercial system. As such, no regular adjustments were necessary. The seed laser (Tsunami) most often only needed an adjustment to the output centre wavelength (an externally available adjustment of the placement of the slit in a prism-pair dispersion-compensation mechanism in the oscillator). This

adjustment was normally necessary only a few hours after system start-up, as the centre wavelength drifted somewhat during system warm-up. The Tsunami exhibited a roll-off of average power over a period of about a month. At times when the measured input average power to the regenerative amplifier dropped below ~300 mW, the regenerative amplifier's output pulse-to-pulse energy stability worsened. The means were not readily available to precisely measure the pulse-to-pulse stability at that repetition rate, but it was found that the thermopile detector's statistics were a sufficient measure of any changes in stability. Acquiring a measurement of power at approximately 7 Hz and averaging for 60 s, a typical standard deviation of about 1 mW, or 0.33%, was found which would rise as the average power fell. Usually this problem could be mitigated by cleaning the output Brewster window of the seed laser and the Ti:sapphire crystal inside, as well as slight changes to the cavity alignment. In most cases, these adjustments made no significant change to the output pointing of the seed laser, aside from the fact that any alignment changes within the seed laser inevitably shifted the centre wavelength of the output, the correction of which was quite straightforward. Also, the position of the Tsunami's output beam was monitored on its associated quadrant photodiode so that if the laser performance of the regenerative amplifier or OPAs had degraded as a result of alignment changes in the seed laser, appropriate adjustments to the pointing could be made with mirrors available between the Tsunami and the input to the regenerative amplifier.

3.5.7. Regenerative amplifier

The regenerative amplifier unit (Spitfire) actually comprises a stretcher and compressor setup as well as the actual amplifier. In practice, upon aligning the stretcher and compressor, no further adjustments were necessary, as is consistent with a component with all passive components and a means of precisely controlling the input direction. However, the regenerative amplifier was by far the most labour-intensive element of the commercial system. The performance of the regenerative amplifier was the ultimate limiting factor in terms of signal to noise in the experiment, as the OPAs were operating at or very close to threshold. Hence, any change in the output characteristics of the regenerative amplifier propagated to the OPAs and further to the experiment. The greatest contributors to the degradation of performance were changes in the pump laser pointing or pulse energy. While no

significant change in the output pointing of the pump laser (Evolution) was evident by inspection of the quadrant photodiode output, both the short- and long-term noise characteristics of the regenerative amplifier were extraordinarily sensitive to the pointing of the pump beam input, most likely the consequence of a very small mode size in the Ti:sapphire crystal. Further, small changes in the output average power of the Evolution affected the long-term stability of the pulse-to-pulse energy. Usually a good compromise of input power and careful alignment of the pump beam into the crystal would achieve the pulse-to-pulse stability that was required. This stability was measured by capturing a pulse energy for each pulse at 1 kHz, and typical values for the pulse energy and standard deviation were ~900 μJ and <3 μJ (0.33%) respectively. Below this value for energy or above the value for the standard deviation, the OPAs' output began to degrade. In practice, the output power of the Evolution only changed over a relatively long timescale, on the order of weeks, but small changes to the pump pointing were necessary on most days during the course of this research. If the other input characteristics (i.e., seed power) were not at their peak, this adjustment became necessary more than once throughout the day. The signal output from the experiment was often acquired and statistically analysed and any variations in the standard deviation of the signal output through the course of taking a data set were noted and most often the stability could be regained simply by tiny adjustments to this pump pointing.

3.5.8. Pump source for regenerative amplifier

The pump laser for the regenerative amplifier (Evolution) is in principle another sealed-box source of pump light, but in practice its output power and direction are quite sensitive to utility supply, changes in temperature, etc. As discussed in the previous section, this has large knock-on effects in the remainder of the laser system and the experiment. A relatively small number of adjustments are available to the user with this system: cavity end mirror alignment, temperature of the frequency doubling crystal, and input water temperature.

At installation, the pump laser was only running at ~91% pump power (diode light delivered to the crystal in the Evolution). This resulted in an output that has been the standard since then, measuring an average power of ~9.5 W with the standard deviation (acquired for 60 s at ~7 Hz) of ~10 mW or about 0.1%. The available increase from 91 to 100% pump power was "headroom" for the laser side

of the experiment; as other aspects of the system degraded, as diodes aged, as portions of the system slipped out of alignment, there should have been an overall improvement in system stability and energy as more energy was delivered to the regenerative amplifier crystal, pushing the regenerative amplifier closer to, or over, the point of saturation. In practice, however, it was found that an increase in this fractional pump power delivered to the Evolution did not often reduce problems which were identified to have originated elsewhere in the system. Nevertheless, as the Evolution power fell to unacceptable levels, it was often possible to simply increase the pump power delivered to the diodes percent-by-percent to keep the Evolution power up. Although this should have increased the degree to which the regenerative amplifier was running in saturation, it was often found that simply increasing the pump power delivered to the Evolution, and thus to the regenerative amplifier crystal, did not improve the long-term noise characteristics of the regenerative amplifier output. Beyond a certain point, increases to the pump power delivered to the Evolution did not result in reaching the specified output power, and necessitating the use of the few user-accessible adjustments to the Evolution. For instance, minute changes to the alignment of the cavity end mirrors had a small effect on output power. Additionally, it was discovered that lowering the temperature of the chiller water increased performance in terms of both output power and pulse energy stability. The reasons for this have not been yet determined, but as it was an easy adjustment to make, it was attempted a number of times to increase the performance of the pump laser. The dedicated chiller originally provided with the Evolution was found to have been assembled with materials incompatible with the laser itself, both in terms of dissimilar metals and reaction with the anti-algal solution recommended for use with the chiller. This original chiller was duly replaced after approximately six months. The replacement chiller has been found to develop particulate material in the chilling water over a short time period, visible to the eye after two months. Because the diode pump light delivered to the crystal in the Evolution passes through the chiller water, this obviously has a negative effect on the laser's performance and the established protocol is to change the chiller water approximately once every six weeks.

3.5.9. OPAs

Each of the independent laser systems described in the opening sections of this chapter in total constitute the pump source for the optical parametric amplifiers. In general, it can be assumed that degradation of performance of the regenerative amplifier translates directly to a degradation of performance of the OPAs, both in terms of pulse energy and pulse-to-pulse stability. The OPAs, consisting of entirely passive components, do not in general need regular maintenance, but of course changes to alignments within the regenerative amplifier or compressor will inevitably create a need for realignment within the OPAs. It is feasible that two turning mirrors and iris diaphragms could be implemented between the regenerative amplifier and the first OPA for the purpose of correcting changes in output pointing, but experience has shown that the OPAs are so extraordinarily sensitive to alignment that it is unlikely that the two mirror/two iris protocol could provide a precise enough adjustment to obviate the need for careful alignment of the individual OPAs. In the absence of input alignment changes, however, a slight drop in output pulse energy (~10%) or, more likely, a rise in the standard deviation of the pulse-to-pulse variation, was noted over the timescale of a few weeks. Most often, this could be corrected by small changes to the position of the lens which focused a small part of the pump beam into the white light plate. The generation of the continuum from which the signal of the first pass of the BBO crystal is derived is the most sensitive part of the optical parametric amplification process, and very small changes to the parameters of the input beam (divergence, mode quality, etc.) have proven to affect the conversion efficiency and stability of the amplification. It has also been noted that the pulse-to-pulse stability can often be improved by adjusting the position of the lenses which focus the pump beams of the two amplification passes, effectively changing the mode size in the BBO crystal. By focusing these beams (and in particular, the second pass beam) too tightly, the stability degrades. By focusing too loosely, the conversion efficiency of the OPA process is reduced. A narrow optimal window for this positioning exists, and slight changes to the input beam into the OPAs, presumably through mode quality or mode structure, tended to shift the optimal position slightly over time.

3.5.10. SDG – timing

The laser system also includes a user interface which controls the relative timings of the Pockels cell Q-switches in the regenerative amplifier, as well as providing a useful trigger source relative to these timings. It is designed to make small adjustments to the number of round trips that the seed pulses make in the regenerative amplifier cavity or their precise switching times, an adjustment that must always be made when large alignment changes occur at the input side or within the regenerative amplifier cavity itself. However, small changes to these settings in tandem with changes to the pump pointing have been found to effect small changes to the long-term noise of the regenerative amplifier.

3.5.11. Output monitoring

As previously mentioned, the protocols established for the laser system were developed during the course of this research. Initially, a great many criteria were measured twice daily in order to establish connections between degradations of performance throughout the system. The average power and standard deviation of the power were measured for the seed laser and regenerative amplifier pump source, the pulse energies and their standard deviations were measured for the regenerative amplifier and both of the OPAs, an oscilloscope trace was saved to disk of the build-up of pulses in the regenerative amplifier (available via a photodiode measuring the leak-through from one of the regenerative amplifier cavity end mirrors), and the relative pointing of the seed, regenerative amplifier pump source, and regenerative amplifier were checked via quadrant photodiodes, outlined in earlier sections. While slow changes to the performance of each component could be monitored in this way, the collection of these data twice daily was a very time-consuming task. Having established the "mean time to loss of energy or stability" for each system component, it became possible (excepting any equipment failures) to choose just one or two measurements to establish the overall performance of the system. It was found that the performance of the OPAs at the output was a sufficient measure of this performance. Daily peak-to-peak variation of the output pulse energies and standard deviations was established over a course of weeks and on many days only this measurement was taken to ensure the laser was performing well enough to carry out experiments. Later in the course of this research, after much work had been accomplished to ensure reproducibility of signals, it was possible to simply use the

signal itself from a standard sample to check that everything upstream of the sample was performing sufficiently. This involved using a Labview interface to query the signal size measured by the lock-in detector and performing statistical analysis on the results over a fixed time period, typically 1 min.

4. First DOVE Results: Simple liquids

4.1. Introduction

In this chapter, a description will be given of the first experiments accomplished with the DOVE spectrometer. These experiments were crucial for establishing the efficacy of the method, outlining pitfalls in experimental technique, and determining the ultimate level of detectivity. The utility of DOVE spectroscopy had already been established by the recent publications of Wright *et. al.*.[14,17,25,26,40-47] and this work suggested that the method was applicable for our purposes. However, these publications focused on the DOVE methodology from a theoretical standpoint, and while they provided experimental evidence of the method's functionality, they provided precious few experimental details. In particular, there was no mention of absolute signal levels. Also, it was not until later publications that the temporal character of the DOVE signals was investigated. As a consequence, the first experiments were aimed not only at commissioning the spectrometer, but also at observing the effects of adjusting some of the many experimental variables. The data presented in this chapter provide answers to specific questions about the method, the nature of the results, and the sensitivity of DOVE spectra to various experimental conditions. No rigorous attempt was made to characterise or compare the physical chemistry of the samples themselves. These studies on simple molecules were merely a prelude to planned experiments on amino acids, peptides, and, ultimately, proteins.

The chapter opens with an outline of all of the samples for the experiments undertaken prior to the amino acid studies, providing a justification for the choice of each sample, and supplying a logical framework for the experimental sections to follow. Each sample is described and supported with FTIR spectra of the neat solute, solvent, and the solutions used for the experiments. References will be made in this section to DOVE experiments which will appear later in the chapter, and the presentation of the data in this order is only because the samples do not appear sequentially in the experimental results sections; the reader may need to refer to this section later in the chapter. Next, a description of the sample preparation and analysis protocols is presented. A brief discourse about the acquisition and verification of DOVE signals precedes the results. In the remaining sections,

particular aspects of the results from various samples will be presented quantitatively and discussed. Finally, the chapter closes with some conclusions and an appraisal of the methodology and the spectrometer before moving on to the results of the amino acid/peptide studies in Chapter 5.

4.2. Outline of the samples employed

Upon initial assembly of the DOVE spectrometer, the first task was to repeat the work of Wright *et. al.*. in order to test equipment and check calibrations and signal estimates. While this published work provided invaluable guidance in the initial design and commissioning of the spectrometer, it described experiments undertaken with a very different laser system, producing pulses of width ~5 ns. While the fundamental physics underlying the transitions required for DOVE spectroscopy is unchanged with pulsewidth, experiments had not yet been published employing a picosecond system such as ours, and the experimental parameters were somewhat different. Obviously, the time-bandwidth constraint meant that while the system's bandwidth of ~25 cm^{-1} made the experiment somewhat less sensitive to exact wavelengths, the extremely short durations of the pulses made the experiments far more sensitive to the relative timing of pulse sequences.

As with any multi-wave mixing spectroscopy, there are a great many variables in the experimental setup: timing and precise direction of the input pulses, wavelengths of the input beams, alignment of the as-yet unmeasured output beam onto delivery optics and ultimately onto the detector, etc. Fortunately, Wright *et. al.*.'s early published work established acetonitrile (CH_3CN) as an ideal simple molecule on which to start, providing large signals due to the high oscillator strengths of the modes that were probed. The very first DOVE spectra measured in this laboratory were on neat acetonitrile, which became the first standard sample. The absorptions relevant to this work are shown in the FTIR spectra in figures 4.1 and 4.2; the mode assignments are collated from references 12 and 48.

The DOVE spectra that were acquired demonstrated specifically the coupling between the ν_2 C≡N stretch at 2253 cm^{-1} and the $\nu_2 + \nu_4$ combination band at 3164 cm^{-1} comprising the C≡N stretch and the C-C stretch of the neighbouring carbon atoms (ν_4=918 cm^{-1}). Also nearby spectrally (in the ω_1 scanning region) are ν_1 and ν_5, both C-H stretches at 2944 cm^{-1} and 3003 cm^{-1}, respectively, and a

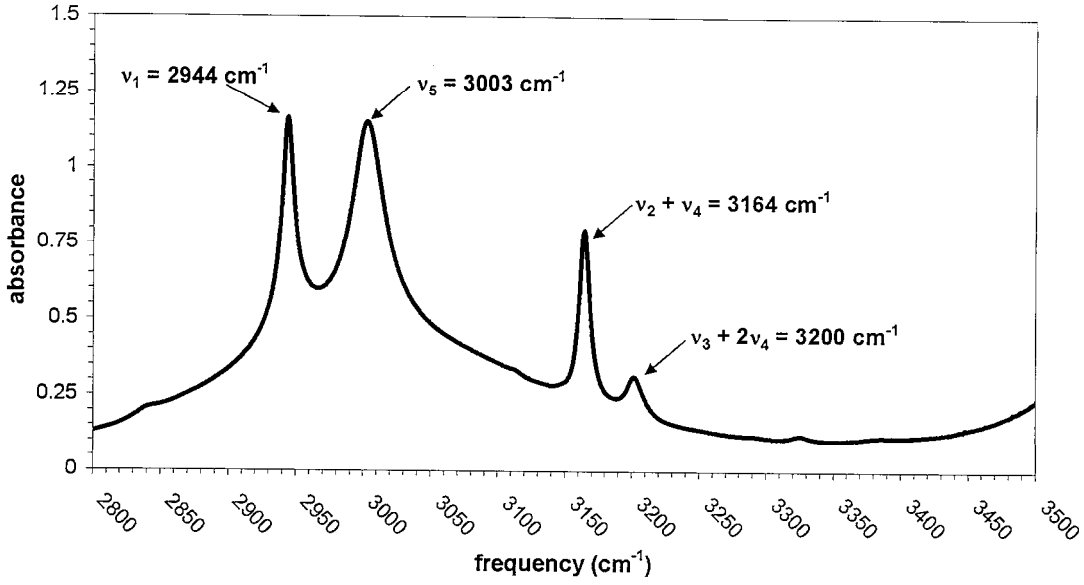


Figure 4.1. FTIR spectrum of neat acetonitrile in the region of the ω_1 scan.

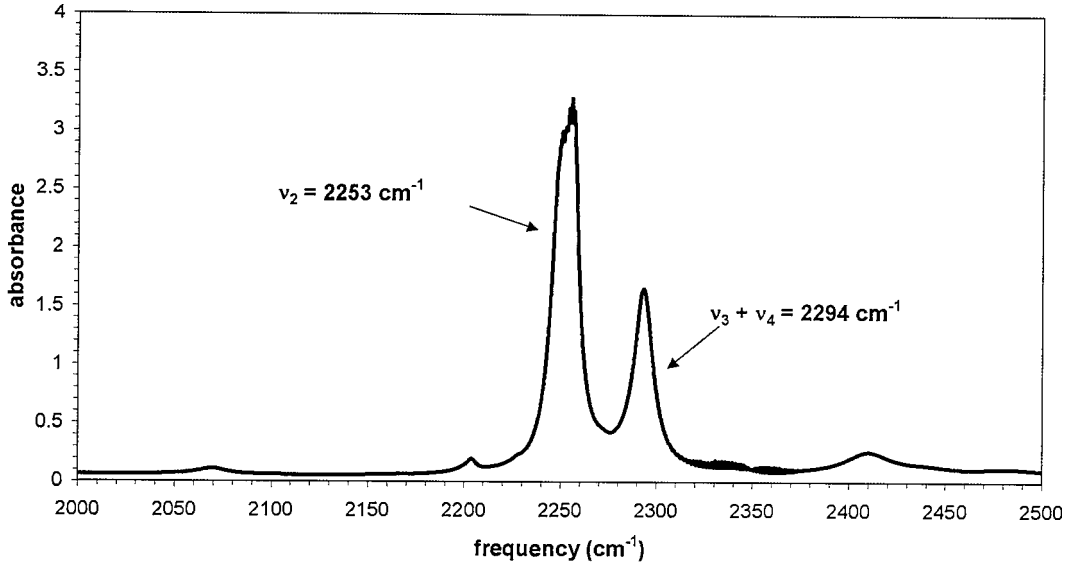


Figure 4.2. FTIR spectrum of neat acetonitrile in the region of the ω_2 scan.

combination band involving the ν_3 C-H bend (1372 cm^{-1}), $\nu_3 + 2\nu_4$ at 3200 cm^{-1}. In the ω_2 region, another peak is clearly visible, assigned as the combination band $\nu_3 + \nu_4$ at 2294 cm^{-1}.

For the spectrum shown in figure 4.2, the detailed feature at ~2350 cm^{-1} is the partially resolved atmospheric carbon dioxide line showing evidence of rotational substructure. This contribution varied from sample to sample but always remained less than ~6% of the peak height of the ν_2 absorption.

Wright's work included fully deuterated benzene (C_6D_6, or deuterobenzene) as an "internal standard". Deuterobenzene had been extensively studied in the

spectroscopic literature, and its third-order nonlinear susceptibility ($\chi^{(3)}$) is well known both for the nonresonant electronic contribution and for the Raman contribution at the Raman-active breathing mode of the carbon ring at $\nu_1 = 944$ cm^{-1}. This mode is excited in the DOVE experiment, resulting in a CARS process, when the difference in frequency between the ω_1 and ω_2 excitation beams reached 944 cm^{-1}. This CARS feature forms a diagonal ridge in the spectra very close to the DOVE-IR features, and because of its independence from either of the ω_1 or ω_2 values, serves to normalise the spectra in terms of intensity. By adding a known quantity of deuterobenzene to the acetonitrile samples, the $\chi^{(3)}$ of acetonitrile relative to the deuterobenzene could be measured, removing the need for signal magnitude measurements in terms of absolute numbers of photons. The early experiments described in this chapter included deuterobenzene as well, both as a relative measure of signal size and providing another DOVE feature on which to focus. During this time, the experiments focused on determining absolute signal levels, assessing the reproducibility of signals from sample to sample and day to day, measuring the effects of different window materials and orientations, and changing the relative contribution of signals from acetonitrile and deuterobenzene by varying the delays between input pulses. FTIR spectra of neat deuterobenzene and the deuterobenzene/acetonitrile solution most commonly used for experiments (a 3:1 mol:mol ratio, chosen to make the acetonitrile and deuterobenzene DOVE peaks of roughly equal size) are shown in figures 4.3 and 4.4 for the two spectral regions of interest.

The next experiments explored a DOVE feature in a dilute solution of carbon disulphide (CS_2) in bromochloromethane (CH_2BrCl), in part to investigate the effects of changing the relative pulse timings, repeating Wright's work on the same system.[49] Carbon disulphide was chosen because of its simplicity, having only three normal modes, and because the oscillator strengths for the relevant transitions were known to be among the highest in liquids. The symmetric stretch ν_1 occurs at 656 cm^{-1}, and the antisymmetric stretch ν_3 at 1520 cm^{-1}, and the ω_1 scanning region was adjusted to be near CS_2's $\nu_1 + \nu_3$ combination band at 2168 cm^{-1}. The ω_2 scanning region was changed to be near the ν_3 mode. The FTIR spectra for neat CS_2 in the ω_1 and ω_2 spectral regions are shown in figure 4.5. The very high oscillator strength of the ν_3 transition makes it practically impossible to acquire FTIR spectra

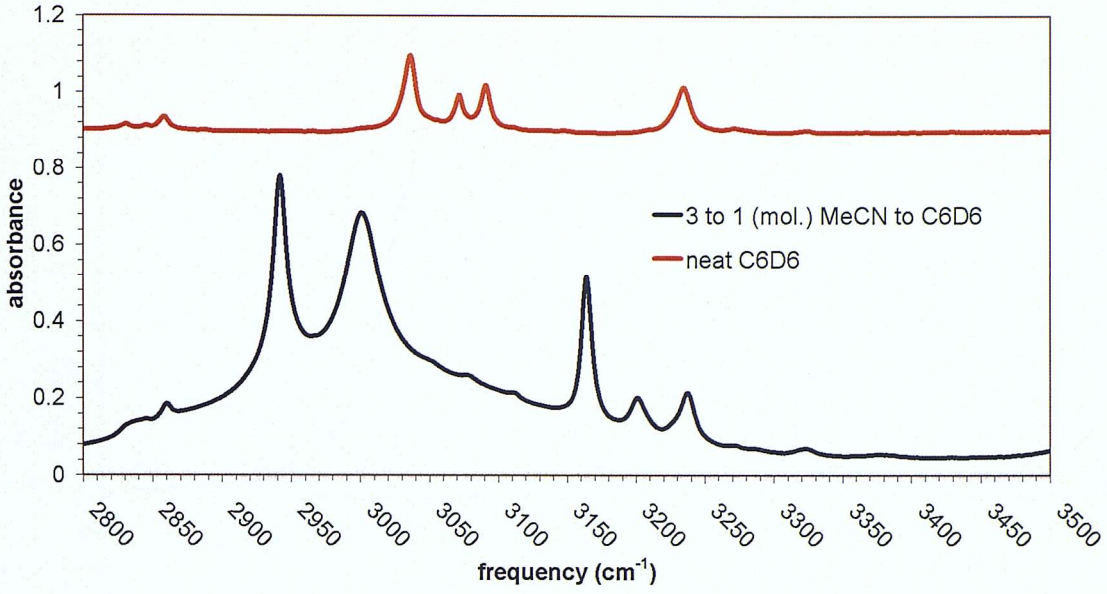


Figure 4.3. FTIR spectra of neat deuterobenzene (red) and a 3:1 mol:mol ratio acetonitrile to deuterobenzene solution (blue) in the region of the ω_1 scan.

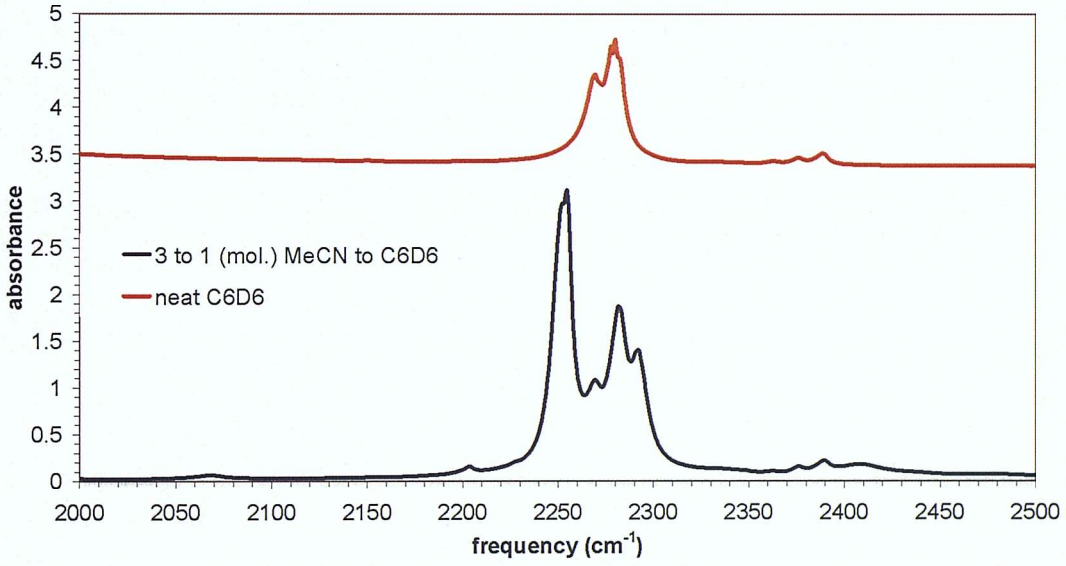


Figure 4.4. FTIR spectra of neat deuterobenzene (red) and a 3:1 mol:mol ratio acetonitrile to deuterobenzene solution (blue) in the region of the ω_2 scan.

of neat CS_2 in which this absorption does not saturate; the spectra in figures 4.5 and 4.6 below are for a sample of pathlength 10 μm. Inset in figure 4.6 is a portion of the 0.6 M CS_2/CH_2BrCl solution to show the detail of the CS_2 absorption in this region. The CH_2BrCl has no absorptions nearby, so this lineshape should represent that in neat CS_2 but without saturation.

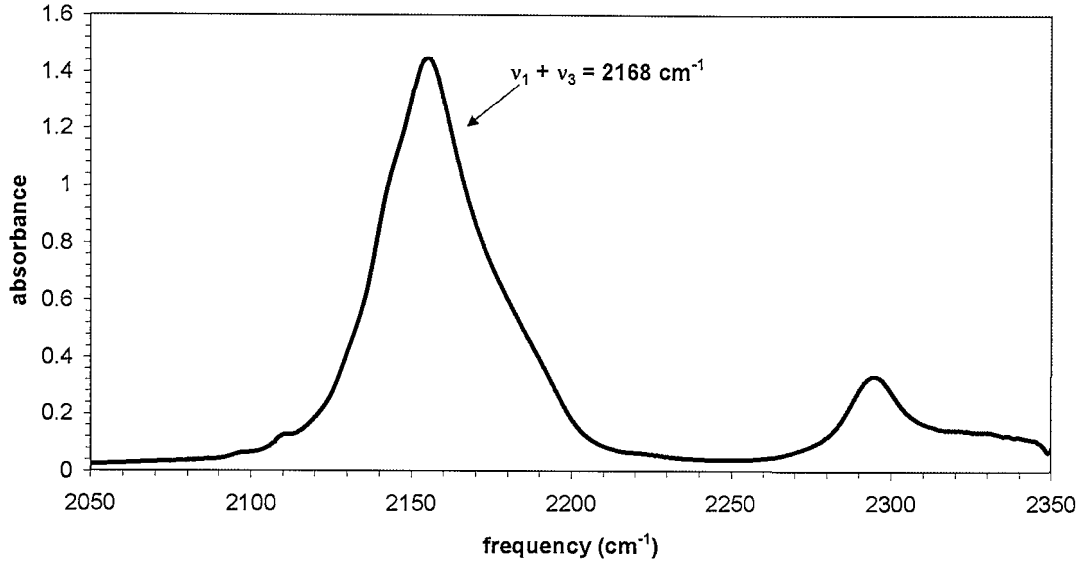


Figure 4.5. FTIR spectrum of neat carbon disulphide in the region of the ω_1 scan.

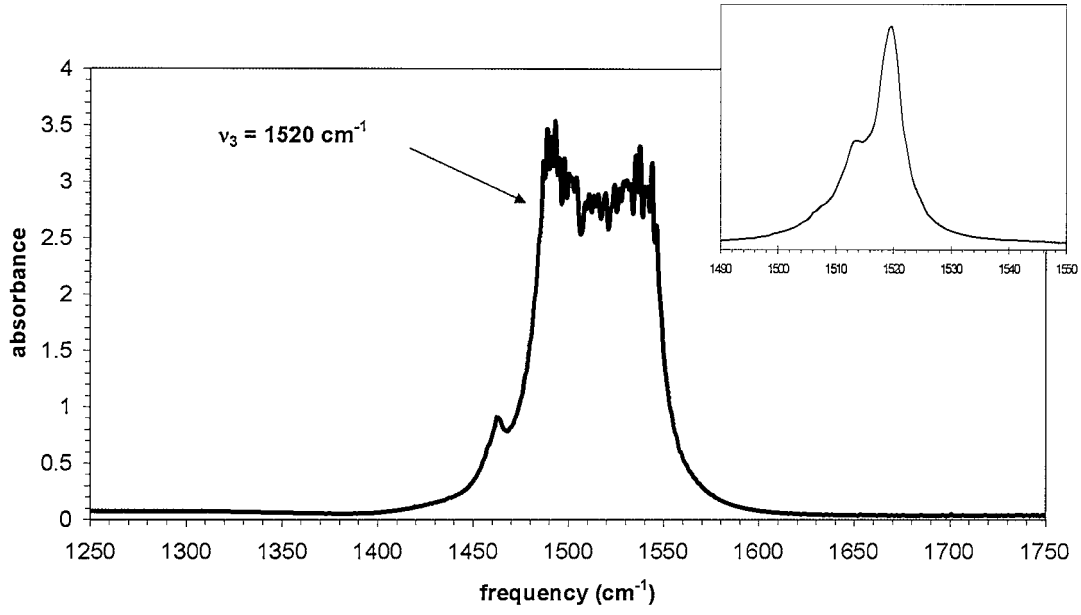


Figure 4.6. FTIR spectrum of neat carbon disulphide in the region of the ω_2 scan. Inset is from a 0.6 M solution of carbon disulphide in bromochloromethane to observe the ν_3 absorption in the absence of saturation.

Figures 4.7 and 4.8 show the FTIR spectra of neat CH_2BrCl and a 0.6 M CS_2 in CH_2BrCl solution prepared for the CS_2 experiments. This particular set of experimental parameters was much more difficult to achieve, namely because the fundamental transition excited in the experiment was much further into the infrared in the second OPA. The conversion efficiency for the optical parametric process dropped off radically as the signal/idler pair approached the values needed to

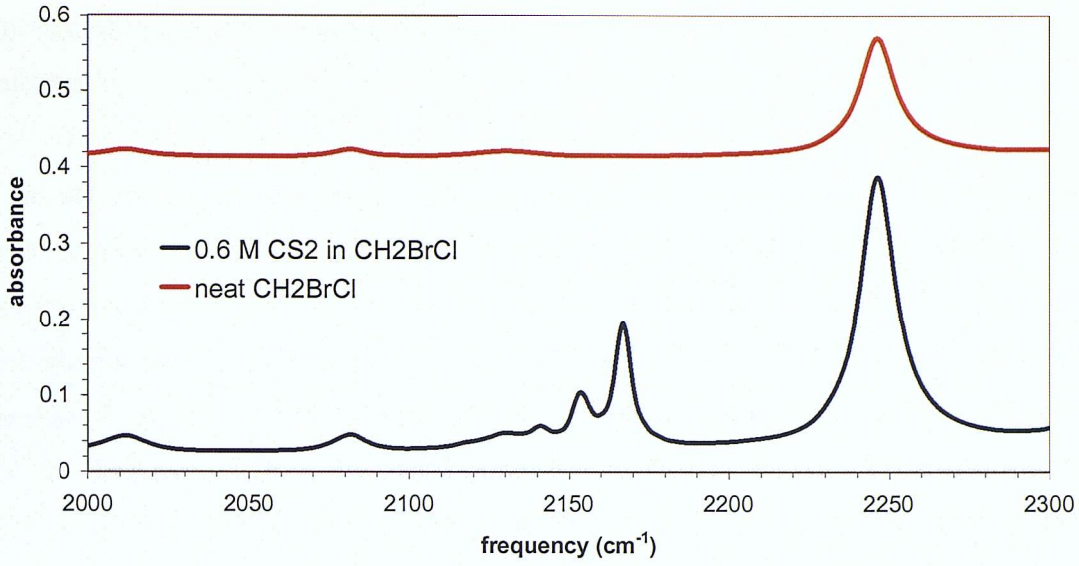


Figure 4.7. FTIR spectra of neat bromochloromethane (red) and a 0.6 M solution of carbon disulphide in bromochloromethane (blue) in the region of the ω_1 scan.

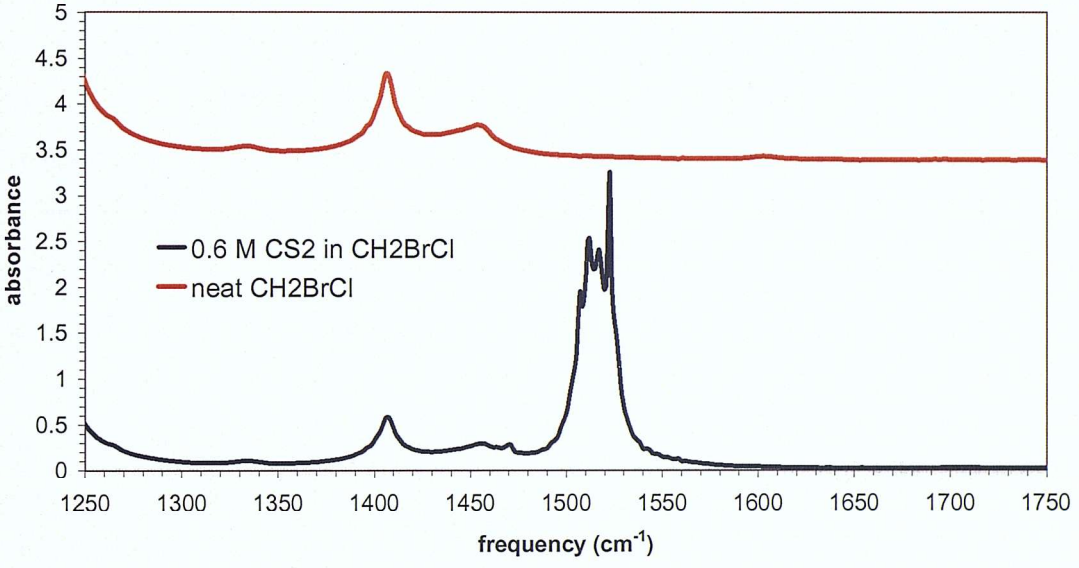


Figure 4.8. FTIR spectra of neat bromochloromethane (red) and a 0.6 M solution of carbon disulphide in bromochloromethane (blue) in the region of the ω_2 scan.

generate 1500 cm^{-1} in the difference frequency stage, so that the output pulse energy dropped and the pulse-to-pulse stability degenerated. A solution to this problem was to change the excitation wavelength from the pump source; for a given signal wavelength, the idler wavelength is determined purely (through conservation of energy) by the pump wavelength. Thus, by shortening the wavelength of the pump beam from the initial 795 nm to 785 nm, the wavelength of the idler is effectively changed, bringing the energies of the signal and idler closer together, and hence,

making their difference frequency smaller. With this simple adjustment and the concomitant alignments downstream of the oscillator, it was then possible to maintain high pulse energies of high stability further into the mid-infrared.

The experiments on the samples to this point had resolved a number of critical issues about the spectrometer, providing a lower limit on detectivity and highlighting issues of reproducibility. With the confidence in the instrument provided by these preliminary experiments, the next step was to consider acquiring DOVE spectra in biologically relevant molecules. However, a move to any other samples raised a number of questions. Signal levels to date had been quite high, and there had been little trouble with the non-resonant background obscuring signals. The step towards studies in amino acids implied relatively dilute solutions and comparatively small integrated absorption cross-sections, suggesting small signals. It stood to reason then that DOVE experiments should be attempted in the new wavelength regime first with another, neat liquid that exhibited coupled bands at or near the wavelengths for the amino acids. There existed a limitation on the range of tuning available before various spatial and temporal variations at the sample position could skew or entirely obscure the results (section 3.4.5). It would therefore have been unwise to optimise the conditions for any of the previous samples and then simply tune to the appropriate wavelengths for the amino acid studies. Moreover, because the combination bands identified in amino acids were in the region of 4400 cm^{-1}, the configuration of one of the OPAs had to be changed because the difference frequency mixing stage of the OPAs only generated IR up to approximately 3300 cm^{-1}. As a consequence, it was necessary to employ the idler beam directly instead of mixing it with the signal, as in the DFM case. A further consequence of this was the need to change the polarisation of the beam; the idler beam emerges from the OPA vertically polarised, in contrast to both the signal and the DFM, which are horizontally polarised. The changes to the OPAs are described in fuller detail in section 3.1.

A literature search into possible solvents for the studies to be performed in this new wavelength regime resulted in the choice of propan-1-ol (C_3H_7OH), whose near-IR spectrum showed a combination band at ~4336 cm^{-1}, made up of the asymmetric stretch (~2883 cm^{-1}) and the bend (1458 cm^{-1}) of the CH_2 moiety.[50] These bands corresponded very closely with the projected spectral region for the amino acid

experiments; L-alanine has a fundamental asymmetric CH_3 deformation mode at 1465 cm^{-1} and a combination band comprising the deformation and the asymmetric stretch at ~4370 cm^{-1}. Representative FTIR spectra for propan-1-ol (henceforth propanol) are shown in figures 4.9 and 4.10 below in the region of the C-H bend and the combination band.

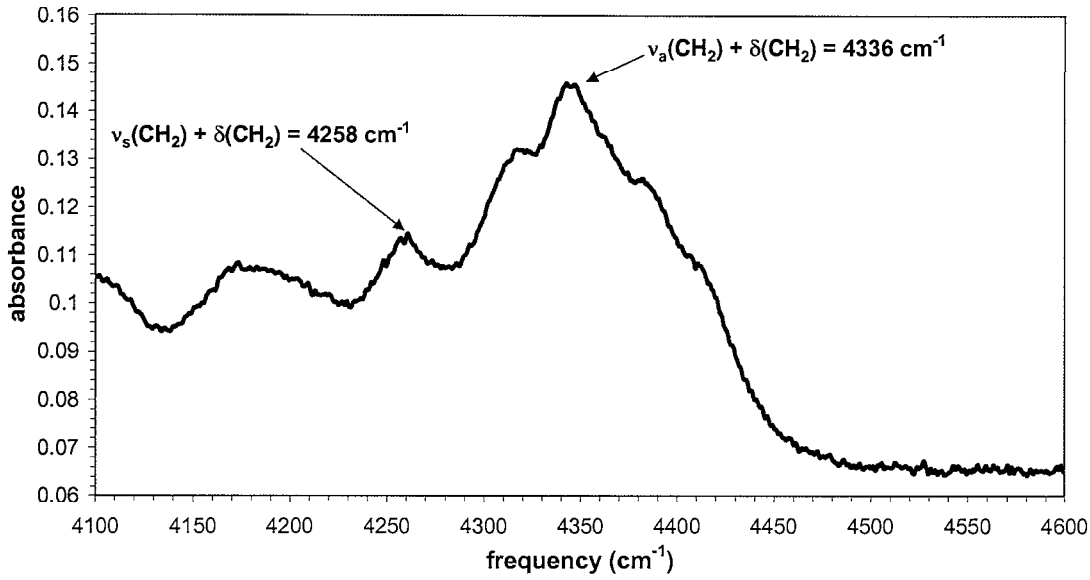


Figure 4.9. FTIR spectrum of neat propanol in the region of the ω_1 scan.

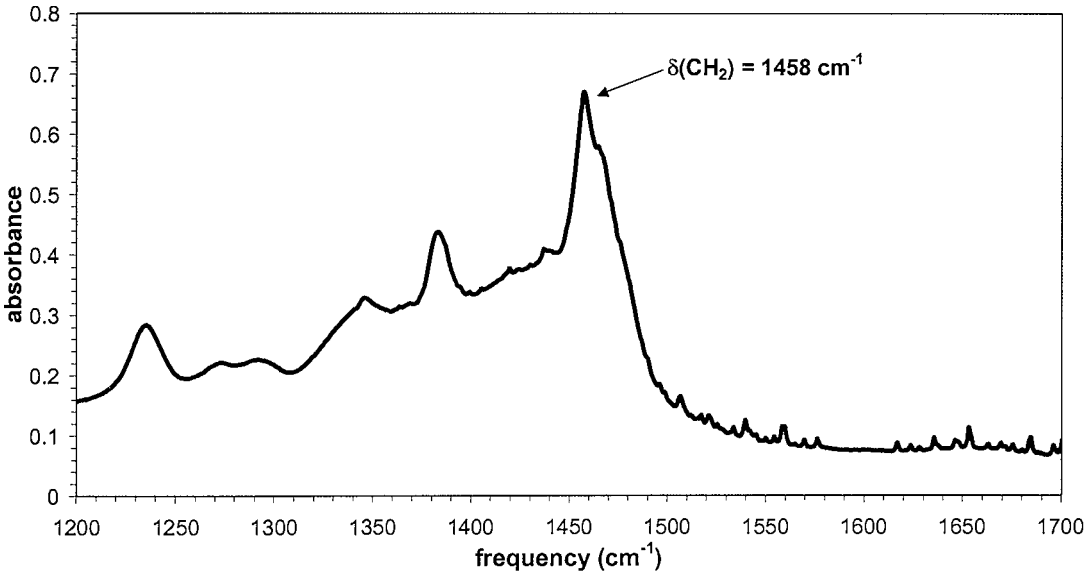


Figure 4.10. FTIR spectrum of neat propanol in the region of the ω_2 scan.

Having identified an appropriate sample for the first experiments in the near-IR, the first test was to find and characterise a DOVE peak. Once this was accomplished, a number of experiments were undertaken with neat propanol to study

the reproducibility of signal sizes and lineshapes. A series of dilutions of propanol in D_2O were prepared in order to observe the changes the signal behaviour as the solutions were progressively diluted. The final dilution step was to ensure that the number density of propanol was comparable with that of the alanine solutions.

Figures 4.11 and 4.12 are two sets of FTIR spectra for the dilution steps

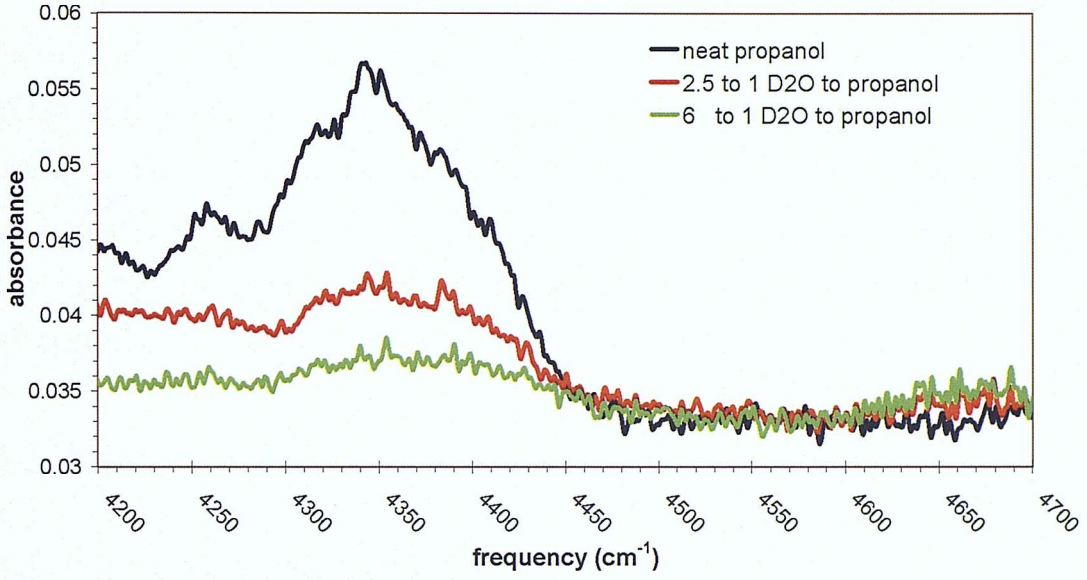


Figure 4.11. FTIR spectra in the region of the ω_1 scan of neat propanol (blue) and two dilutions of propanol in D_2O, 2.5:1 mol:mol (red) and 6:1 mol:mol ratio (green)..

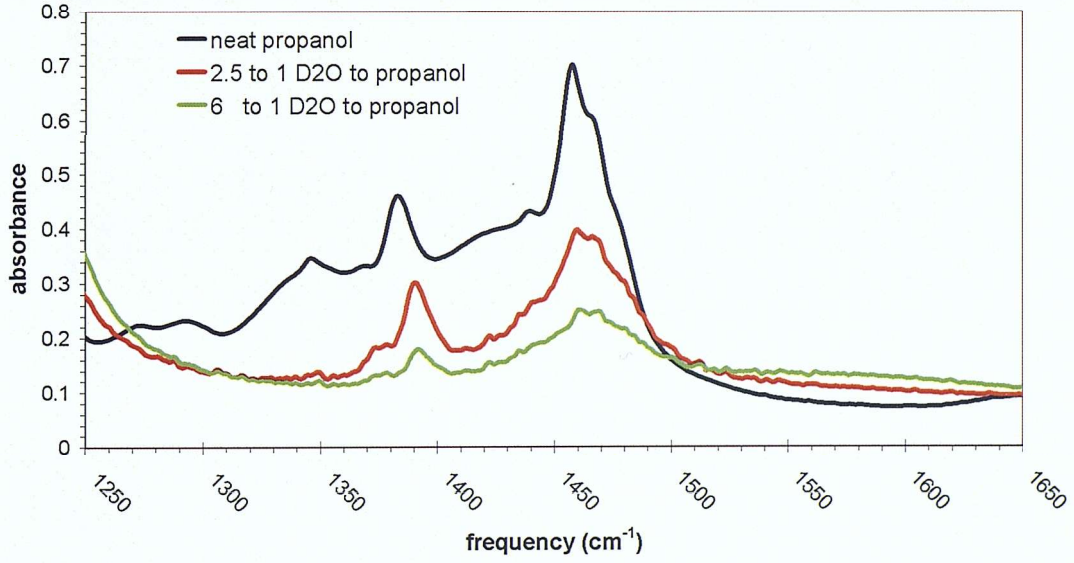


Figure 4.12. FTIR spectra in the region of the ω_2 scan of neat propanol (blue) and two dilutions of propanol in D_2O, 2.5:1 mol:mol (red) and 6:1 mol:mol ratio (green).

Once the initial experiments in the mixed near-infrared/mid-infrared wavelength regime had been accomplished, the next step was to begin studies on

amino acids. However, it was necessary to establish a standard sample on which to perform a number of diagnostic steps as a prelude to each experiment on new samples. As has been exhaustively discussed previously, a great many experimental variables exist in multi-wave mixing experiments. It therefore was and continues to be necessary to have a consistent, easily prepared, stable sample with which to check in one step the spectrometer as a whole, from light source to detection electronics. As such, propanol became the standard by which to check the day-to-day variations of the system. The first step in acquiring new DOVE spectra became checking the reproducibility of a single 1-D DOVE spectrum of propanol (with ω_2 fixed, varying ω_1, timings fixed at T_0). As will be discussed later in the sections on reproducibility and timing, the propanol signal's lineshape was extremely sensitive to both wavelength and relative pulse timing and thus provided a precise measure of both.

4.3. Sample preparation, containment, and analysis

4.3.1. Sample cell and holder

The cell used for all of the work described in this thesis is pictured in figure 4.16.

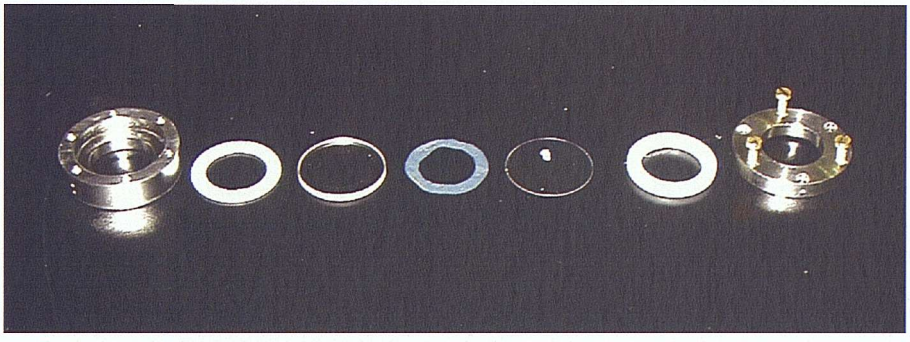


Figure 4.13. Picture of the sample cell disassembled.

The top and bottom of the cell are stainless steel, drilled with six holes to clamp the cell together. Inside the cell, two PTFE spacers separate the outside edges of the sample windows from the steel. The actual sample is contained between two windows of varying materials and thicknesses (see following section) with another, thinner, annulus-shaped PTFE spacer to set the path length through the sample. At the sample position of the experiment, a post holder was mounted on a manual linear translation stage. Initial experiments established the setting for the sample stage

which corresponded to the sample being in the crossing region of the input beams. This was accomplished by tuning the stage position and observing the highest signal, and this position was kept constant through all experiments which employed a back window of the same thickness. Later changes to the window pairs necessitated an adjustment of the sample stage peak position.

The peak position of the sample stage was to be kept the same, but it is important to note that the signal should not be very sensitive to this position. This can be borne out with a quick calculation considering the geometry of the overlap region and the Rayleigh range of the input beams. The Rayleigh range is a measure of the "depth of focus" or the spatial extent over which the beam spreads out before and after focusing, and is defined as the distance between the focal plane and the plane where the beam waist is $\sqrt{2}$ times larger (or the beam area is twice as large, or the intensity half as high). Clearly, moving far from the focal spot reduces the intensity, reduces the signal, and renders signal estimates inaccurate. The Rayleigh range is formally defined as

$$Z_R = \frac{\pi d_0^2}{\lambda} \qquad \textbf{(equation 4.1)}$$

where d_0 is the focused beam waist diameter and λ is the wavelength, so that the beam of highest wavelength has the shortest Rayleigh range and is therefore most sensitive to sample position. If we consider d_0 = 100 μm and an upper limit on wavelength of ~7 μm, this corresponds to a Rayleigh range of >4 mm. However, in considering the geometry of the input beams (two nearly collinear, one at 8°, all three focusing to spot sizes ~100 μm) and the region of space where they overlap, it was estimated that the overlap region was in total approximately 700 μm along the beam propagation direction, so that the actual spatial overlap of the beams was a more limiting factor than the spread in any one of them. With sample path lengths between 10 and 100 μm, it is clear that the precise sample stage positioning should not affect the signal sizes greatly. Nevertheless, in the case of thin samples, phase matching considerations as well as the relative phases of the various signal components (i.e. from window/solvent/sample) are very sensitive to sample positioning, so that precise sample stage positioning was necessary to ensure signal size reproducibility.

4.3.1.1. Spacers

Spacers between the windows, varying from 10 μm to 500 μm thick, were cut from sheets of PTFE of a given thickness purchased from Sigma-Aldrich. The thickness of the spacers actually employed were chosen based on the absorption coefficients of the samples; in order to estimate signal sizes and conversion efficiencies in the samples, it was necessary to ensure that the majority of the path length in the cell contributed to the emitted signal. If the absorption coefficient for any one of the input beams was too high, that beam would be mostly absorbed in the first few microns of the sample and therefore the remainder of the sample would not contribute to the signal, making a full estimate of the conversion efficiencies difficult. Therefore spacers were chosen to keep the optical density of the sample at all wavelengths below ~0.3, corresponding to a transmission of about 50%.

4.3.1.2. Windows

Windows in the sample cell were chosen based on their spectral as well as physicochemical properties. All were of 22 mm diameter to fit into the standard sample cell. For the most part, calcium fluoride windows of 2 mm thickness (Spectroscopy Central) were employed because of their favourable spectral range, transmitting up to ~11 μm in the infrared. Zinc selenide windows were also purchased but it was found that the windows actually acted as frequency doubling crystals for the visible beam when placed into the experiment, suggesting a high two-photon cross section in bulk zinc selenide. As a consequence, these windows were not used in any of the reported experiments. Sapphire windows were also purchased in two thicknesses: 2 mm (Spectroscopy Central) and 100 μm (Marketech International). While sapphire has better physical properties, it was provided as single crystal, as opposed to the amorphous calcium fluoride, so that exact orientation of the windows became important for signal size calculations, reproducibility experiments, etc. (see section 4.7). Further, sapphire begins to absorb appreciably beyond 6 μm, so that the thicker sapphire windows were therefore inappropriate for the amino acid studies.

4.3.2. FTIR analysis of samples

FTIR spectra were acquired in order to assess the concentrations, path lengths, and purity of samples both before and after experiments. Spectra were generally acquired in the range between 1000 and 4500 cm^{-1}, either at 1 or 2 cm^{-1} resolution (more than enough to resolve the bands relevant to the experiment, generally of width >15 cm^{-1}). In the case of volatile samples such as acetonitrile and particularly carbon disulphide, it was often found that in the course of experiments the sample had leaked or evaporated from the cell. In other cases, it was clear that there had been a change in solvent concentration in the cell. As such, it was important to take FTIR spectra of the samples immediately after taking DOVE spectra to ensure that the sample had not materially changed during the course of experiments. Because the samples of the amino acids were saturated solutions, it was occasionally found after long experiments that the D_2O had evaporated somewhat, causing the amino acid to precipitate out of solution. However, this effect was not always as obvious as seeing aggregate in the sample cell. By way of example, figure 4.14 below is a pair of FTIR spectra taken before and after a set of DOVE experiments on a saturated solution of alanine in D_2O.

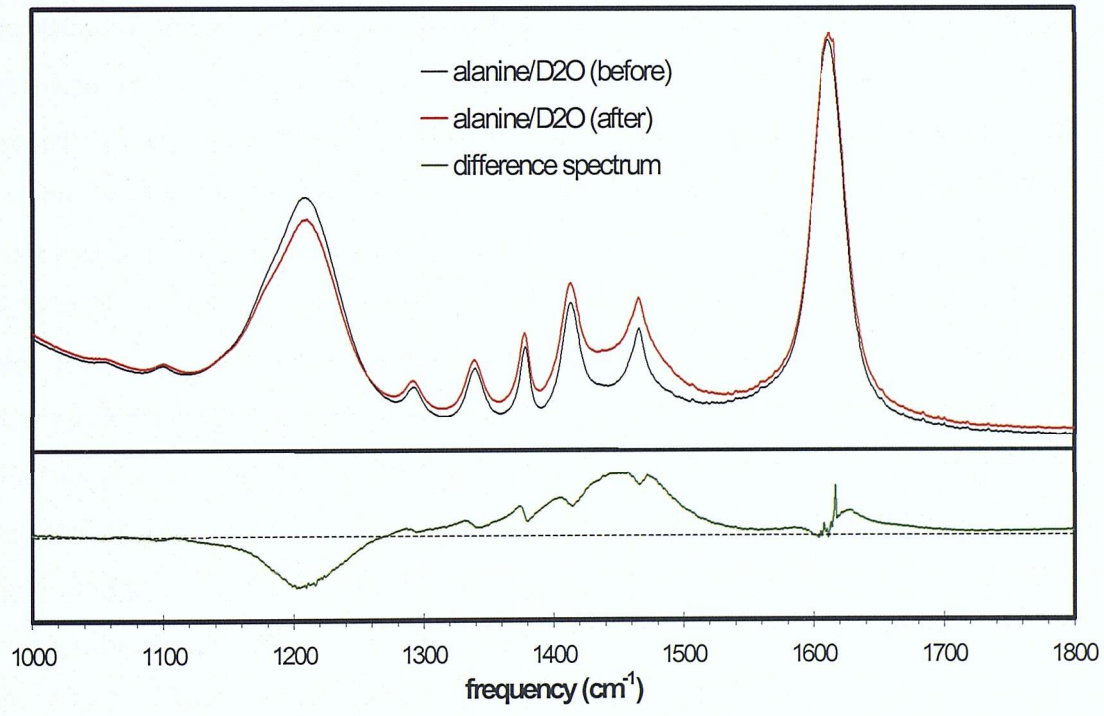


Figure 4.14. FTIR spectra of a saturated solution of alanine in D_2O, before (blue) and after (red) a number of experiments. The difference spectrum is shown below in green.

A difference spectrum is plotted in green below the spectra to elucidate the changes (not to scale), with a dotted line marking the zero point. The most notable changes evident from the difference spectrum are the drop in the peak at 1200 cm^{-1} (D-O-D bending mode) and a shift of the carboxylate ν_{as} at ~1610 cm^{-1}. It is likely that this is due to a small amount of $^1H/^2H$ exchange from the carboxyl end of the amino acid backbone, as OH radicals in particular are noted for rapid exchange when D_2O is the solvent,[51] and the ν_s vibration (~1410 cm^{-1}) of the same moiety is seen to be very broadened in the after spectrum, presumably due to the environmental effects of partial $^1H/^2H$ exchange. Further, the methyl group modes between ~1300 and 1500 cm^{-1} are significantly broadened and occur on a higher background, suggesting the onset of aggregation. Clearly this sample is markedly different from the beginning to the end of the experiment, and these data provide evidence that a careful analysis of the post-experiment FTIR spectrum is necessary to ensure that the DOVE spectrum obtained does not reflect aggregation or evaporation effects.

4.3.2.1. Comparing FTIR spectra

Sample concentrations could be calculated exactly from a single FTIR spectrum if the absorption cross section for a given transition was known. In addition, the concentrations were calculated relative to other samples if just a comparison of signal sizes was needed. This was accomplished by measuring the heights of absorption peaks in the FTIR spectra, as long as the sample background scan and the path length were the same for both samples. In order to establish the uniformity of the sample background, it was necessary to prepare a number of samples of the same composition in the same cell and acquire spectra, comparing the background level. It became clear that the rotational orientation of the cell affected the background to a small degree, so care was taken to ensure the cells were always oriented the same way in the FTIR, and in the experiment. This was accomplished by marking the sample windows, indicating an "up" orientation as well as a "front" orientation, and marking the outside edges of the cell itself so that all parts of the cell lined up and were oriented identically from sample to sample.

It was necessary to establish the consistency of sample thicknesses. In general, the same spacer was employed for all experiments requiring the same path length. However, wear and tear on the spacers necessitated their occasional replacement, and

it was necessary to determine the absolute thickness of each spacer (and therefore path length in the cell, assuming non-compressibility). For this purpose the well-known fringe method was employed, whereby the path in the cell can be calculated from the interference fringes present in the FTIR scan. These fringes are a consequence of interference of reflections between plane parallel surfaces in close proximity, and are a clear and definite indicator of the path length, given (in mm) by the following formula:

$$l = \frac{n(10)}{2(\omega_1 - \omega_2)} \qquad \textbf{(equation 4.2)}$$

Here, n is the number of fringes to be counted between two frequencies ω_1 and ω_2, given in cm^{-1}. The greater the difference in ω_1 and ω_2, the more accurate the measurement is. While the fringes are most easily obtained in an empty cell, measurements of the path lengths were also taken in full cells, ensuring that the presence of samples did not alter the ultimate path length. In the case of full cells, a spectral region far from any absorptions had to be found so that contributions from the sample itself could be discounted and interference fringes could be easily identified. It was found from the measurements of the cell path lengths that the actual path varied markedly from the specified thickness of the PTFE sheet, but less than 5% from sample to sample. The measured thickness was consistently higher than the specified. The table below presents average measured and specified thicknesses of the spacers, standard deviations of the measurements, and the concomitant change in predicted signal level based on the disparity between the measured and specified thicknesses:

Specified thickness (μm)	**Average measured thickness (μm)**	**Standard deviation (μm)**	**Change in predicted signal level (%)**
10	15.6	0.51	+230
25	35.3	1.53	+200
50	79.3	2.89	+260

Table 4.1. Summary of the errors in spacer thickness measurement and the concomitant change in signal level.

It is clear from the above data that it was crucial to measure the thickness of each different spacer to ensure the accuracy of predicted signals, but as the standard deviations of several measurements represented less than 5% of the measured value, sample-to-sample variations with the same spacer were minimal (corresponding to a variation in nonlinear optical signal of <10%). However, as discussed in section 2.3.2, slight variations in path length, particularly in the case of very thin samples, can adversely affect reproducibility.

4.3.3. Sample preparation

Neat solvents of >99% purity (acetonitrile, carbon disulphide, propanol) were obtained from Sigma-Aldrich and used without further purification. In the acetonitrile experiments, fully deuterated benzene (C_6D_6) was also employed and was used from 1 mL vials. As many of these solvents are known to be hygroscopic (water-absorbing), care was taken to ensure that containers for the solvents and prepared sample mixtures were exposed to air as little as possible. This was accomplished by decanting solvents into small beakers sealed with Subaseal rubber stoppers. In the case of the deuterobenzene, any unused portion of the vials was discarded.

4.4. General features of signal and data acquisition

In the course of searching for the first DOVE signal, a number of experimental artefacts were encountered, and a number of criteria were established to ensure before optimisation that the signal measured by the lock-in had indeed arisen from the DOVE process. Firstly, the signal had to disappear when any one of the beams was blocked. By blocking either of the IR beams, the possibility was eliminated that the signal was generated by solely the ω_3 beam (this is the only input beam to which the detectors were sensitive, but comprising many orders of magnitude more photons) or by any lower-order processes such as sum frequency generation (SFG) which happened to be in roughly the same direction as the DOVE signal.

Further, the spectral variation of the detected signal had to be checked. Nonresonant background, scattered room light or ω_3 light, window or solvent signal, etc. should all be roughly wavelength independent, but the DOVE experiments were first attempted with the wavelengths fixed at what should have been the DOVE peak;

a lack of spectral variation on either side of these points indicated that the observed signal was not in fact from the DOVE process.

4.4.1. Optimisation

Once a signal was detected and measured with the lock-in amplifier and determined to be a verifiable DOVE signal, a number of optimisation steps were required in order to maximise it. The first optimisation step was to check alignment of the post-sample optics into the detector. The direction of the signal beam is in part dependent on the frequencies of the input infrared beams, but a far greater contributor to changes in this direction is the precise direction of the input ω_3 beam. The reason for this was that the ω_3 beam was by far the largest in frequency and therefore represents the largest influence on the output direction—a consideration clear from the momentum conservation condition of phase matching. Changes upstream, for instance when converting the laser system from one experiment to another, often resulted in small changes to the ω_3 direction and hence the alignment onto the post-sample optics. Upon optimising these alignments, it was required to peak the signal by adjusting the final turning mirrors of just the IR beams ω_1 and ω_2 into the sample, in tandem with varying the position of the sample stage. The stage had to be moved when changing from the alignment pinhole to the sample holder, simply in order to put the sample in the same transverse plane as the pinhole itself. However, in the first experiments, the optimal position of the sample stage with a sample in place had not been established. Of course, beam overlap and sample position are impossible to mutually optimise, so scans of the signal with position were taken, and a final position for the sample stage was determined. This value was kept as standard for sample cells of the same composition (in terms of window and spacer thickness). With this value set, it was possible to optimise the beam overlap with the final delivery optics. Figure 4.15 shows the variation of the signal with the sample position:

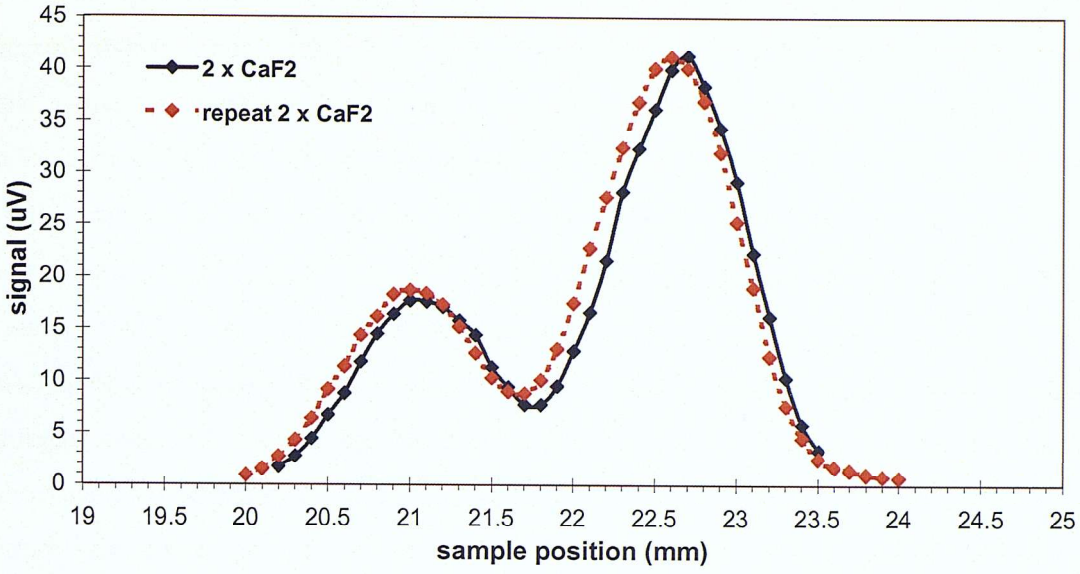


Figure 4.15. A plot of the signal vs. the position of the translation stage on which the sample was mounted for a 100 μm acetonitrile sample between 2, 2 mm CaF_2 windows. The frequencies are set for the DOVE peak at 3164/2253 cm^{-1}. A repeat is shown in red. The significant contribution from the front window is seen at ~21 mm, and the signal is at a maximum near 22.5 mm.

The large lobe at approximately 22.5 mm represents the optimal position of the sample in the overlap region. Note that the rate of roll-off with position is consistent with the 100 μm sample thickness; because the overlap region is estimated from geometric considerations of the angled beams to be ~700 μm in the propagation direction. The side lobe at ~21 mm represents the signal due to the front CaF_2 window being optimised for position. Although the contribution from the windows was predicted to be generally small, the windows for these experiments were 2 mm thick, some 20 times the thickness of the sample. Combined with the large overlap region, it is clear to see that the window contribution under these conditions is quite large. Note also the absence of such a peak on the other side of the main peak; this is because the high optical density of the sample at the incident wavelengths precludes much light reaching the back window. Repeats of this experiment with an empty cell exhibit these side lobes on both sides of the central peak due to contributions when the front and rear cell windows are centred in the beam overlap region.

Another effect on the nature of the spectra obtained was noted when the wavelengths employed were in the region of the infrared spectrum densely populated with water or carbon dioxide absorptions. A significant difference was noted

between spectra acquired when the optimisation of the final beam pointing was accomplished under the conditions of complete purging of the experimental enclosure. Because the final turning mirrors were inside this box, it was a difficult procedure to optimise these four degrees of freedom (vertical and horizontal for two of the excitation beams) and allow time in between each pointing change for the box to fully purge again. Speeding up the purging process by changing the nitrogen flow rate was undesirable, as the different flow rate and any nitrogen currents within the enclosure could affect the results. While the optimisation step under the condition of purging was time consuming, figure 4.16 bears out the importance of the procedure, showing two spectra, acquired consecutively on the same sample under identical conditions, the only difference being the degree to which the enclosure was purged while optimising the final beam pointing. The relative peak sizes and in fact the lineshapes are noticeably different under these two conditions, and as a result care was always taken to optimise the pointing with the box carefully purged between each change.

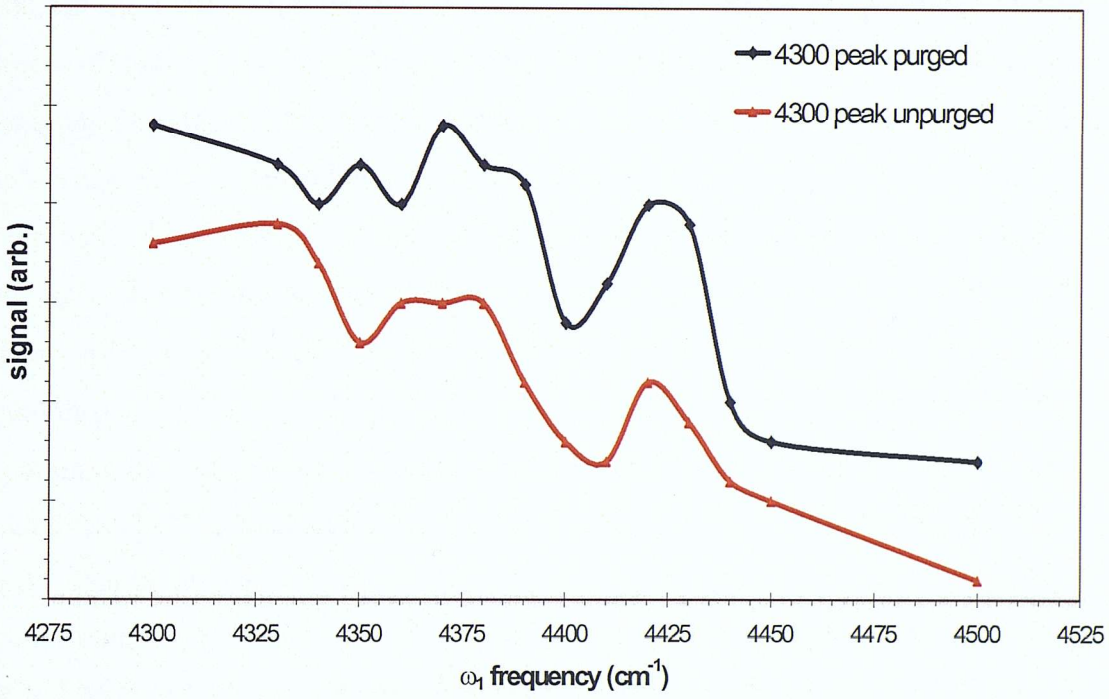


Figure 4.16. DOVE 1-D spectra in alanine and D_2O with ω_1 fixed at 1465 cm^{-1}. The spectral differences between the cases of alignment with the experimental enclosure purged (blue) and unpurged (red) are clear.

A final concern in the signal optimisation was the relative timing of the input pulses, the precision of which was unclear until many successful DOVE experiments

had been accomplished. In the earliest stages of experimenting, optimisation of the time delays involved varying the positions of the delay stages around the values determined by the temporal alignment procedure, under the assumption that the signals would be at their highest when the pulses were exactly overlapped in time at the sample, so the stages were set to the position at which the signal was highest. It was not until later experiments explored the temporal character of the DOVE signals that it was discovered that the highest signal did not necessarily reflect the best temporal overlap of the pulses.

4.4.2. Linearity

Another check of measured signals was a check for linearity of the signal with intensity. As the signal size depends linearly on the input intensity of each of the excitation beams, it should be possible to attenuate any one of them and see a concomitant change in the measured signal level. For the case of the infrared beams, absorptive ND filters optimised for the infrared were available to accomplish this task, but the filters' high refractive index would have caused change in the relative timing of the pulses by adding pathlength to the path of the attenuated beam, changing the signal level via both intensity and timing. However, the ω_3 path included a half-waveplate/polariser combination to control the intensity of the ω_3 beam without introducing any further changes. Checking the linearity in this way at the input side of the sample always resulted in a highly linear signal response. Figure 4.17 is a plot of the measured DOVE signal from a 100μm sample of acetonitrile as a function of input ω_3 pulse energy with a number of different window combinations. For each experiment depicted here, the wavelengths were set at the acetonitrile DOVE peak, and the pulses were overlapped at T_0. Each of the linear fits to the data below has a different slope; this is because the output signal intensity is proportional to all three input intensities, so that the slopes of these linear plots should be the product of the two infrared intensities. These slopes differ because the intensities of the infrared beams (both in terms of pulse energy and of spot size) were different for each plot. It should also be noted that the linearity checks always resulted in a nonzero intercept, but this has been attributed to an electronic offset in the detection setup as opposed to a real optical effect.

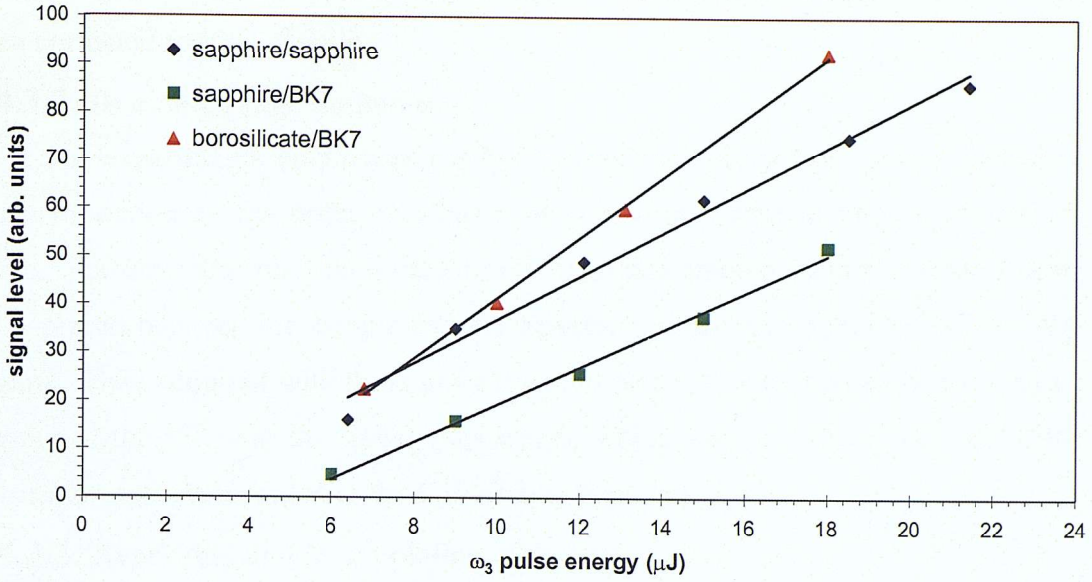


Figure 4.17. A plot showing the functional relationship between the measured acetonitrile signal and the input pulse energy in the ω_3 beam, shown for a number of different sample cell configurations. The frequencies are again set for the acetonitrile DOVE peak, and the signal is very linear in ω_3 pulse energy in all cases.

It is also possible to use ND filters placed between the sample and detector to check the linearity of the signal with intensity of just the output beam. This check constitutes a means of checking for saturation effects in the detection electronics. For this purpose, an absorptive ND filter of optical density 0.3 (transmission ~ 50%) was inserted to ensure that the measured signal dropped by half. It was in this way that a limitation of the PMT-based detection setup was identified; a saturation effect was found in the timing gate (employed to block out PMT signals outside the temporal window corresponding to the arrival of the pulses). This result provided a range of signal levels over which linearity (lack of saturation) could be relied upon, and signal levels were kept within this range by the use of various ND filters in place between the sample and the detector.

4.4.3. Correction/manipulation of data

4.4.3.1. Pulse energy

The output pulse energy from the OPAs varied somewhat when tuning over broad frequency ranges. For most of the data presented in this chapter, the variations amounted to less than ±2% of the mean pulse energy value, and given that the long-term variations of the laser output itself often varied as much as this the resultant spectra were not corrected for these variations. Where the pulse energy for

any one of the input beams varied more than 5% of the mean value, the spectra have been corrected for this variation.

4.4.3.2. Dynamic range limitations

For experiments employing the PMT detection setup, there was a dynamic range limitation on the order of a factor of 100 from lowest to highest detectable value. For any data sets which varied more than this amount, neutral density filters were placed between the sample and the detector to bring the signal value into this regime. Data acquired with these extra filters in place were corrected for the optical density of the filters at the signal wavelength, which was determined directly from absorption spectra recorded in the UV/vis spectrophotometer.

4.4.3.3. Averaging and interpolating of spectra

For some of the one-dimensional (1-D) and all of the two-dimensional (2-D) data presented in this thesis (contour plots with two frequency or time axes), multiple scans were taken and averaged. Rather than tuning each time from lowest frequency to highest monotonically, each data set was recorded by randomly choosing frequency values from the set to avoid any systematic error in data acquisition. When recording 2-D data, ω_2 was kept fixed for scans in ω_1, because as noted in section 2.3.2, the refractive index dispersion around absorptions can significantly distort lineshapes. Strictly, the 2-D data should be normalised along the ω_2 axis, because the ω_2 frequency was always near the strong fundamental absorption of the solute or neat sample. Tuning through this value has two effects on the signal: firstly, the sharp changes in refractive index around the absorption changes the phase matching condition and thus the relative signal levels (see section 2.3.2). Secondly, strong absorption in the sample changes the mixing pathlength available to contribute to the signal. However, the data were not normalised in this way because the comparisons of spectra were to be largely qualitative and this normalising procedure would be somewhat subjective in the case where the spectral space is dense with features.

Finally, all of the 2-D data were interpolated in both dimensions to smooth the contours in the 2-D plots. A bilinear interpolation was used on spectral data acquired at 10 cm^{-1} resolution, yielding a resolution of 2.5 cm^{-1}. Temporal data were acquired at a resolution of between 0.25 ps and 0.50 ps, usually interpolated to half the time between the acquired points.

4.5. First DOVE results

4.5.1. Acetonitrile/Deuterobenzene

The initial approach in acquiring a DOVE signal from an acetonitrile/deuterobenzene mixture was to set the frequencies for the acetonitrile DOVE peak (ω_1=3164 cm^{-1}, ω_2=2253 cm^{-1}), optimise the alignments and timings, and then take spectral scans, varying ω_1 while keeping ω_2 fixed. In these scans, two peaks were predicted; one at 3164 cm^{-1} due to the DOVE feature, and one at 3197 cm^{-1}, a CARS feature which should appear when exciting the deuterobenzene ring breathing mode at 944 cm^{-1}. This mode was excited whenever the difference frequency between the two infrared beams reached 944 cm^{-1} (resulting in a diagonal ridge through any 2-D spectra). These two peaks did appear in early experiments, but their relative sizes varied depending on which pair of frequencies was used for optimisation. When the signal was first acquired with the frequencies set for the deuterobenzene line and then optimised, it was found that the acetonitrile line was comparatively smaller. Moreover, adjustment of the timing delay for the ω_3 beam by ~1.5 ps recovered this "lost" signal, suggesting that the timing condition for peak signal from the acetonitrile was different from that for deuterobenzene, even for fixed alignment of the beams. Figure 4.18 below is a plot over a similar frequency range under identical conditions where, for each trace, the signal had been optimised at the frequency pair for the DOVE peak (3164 cm^{-1}) or for the Raman peak (ω_1 = 3197 cm^{-1}, so that $\omega_1 - \omega_2$ = 944 cm^{-1}).

In the case where the signal had been optimised for the Raman peak, the DOVE feature is discernible as a shoulder on the tail of the Raman peak. Here the Raman feature was to be significantly larger, due to a significantly higher nonlinear susceptibility (via the Raman cross-section) and the temporal overlap of the pulses. However, in the case where the signal had been optimised for the DOVE feature, the peak doesn't actually occur at the expected 3164 cm^{-1} but is spectrally broadened, with a clear shoulder at 3197 cm^{-1} on the tail of this central feature demarcating the Raman peak. These experiments provided the first indication of the complex interplay between the alignment of the input beams, their relative timing, and signal levels. The cause for this change in signal level is due in part to the sensitivity of the signal to the input angles (see section 2.3.2) but is most likely largely due to the

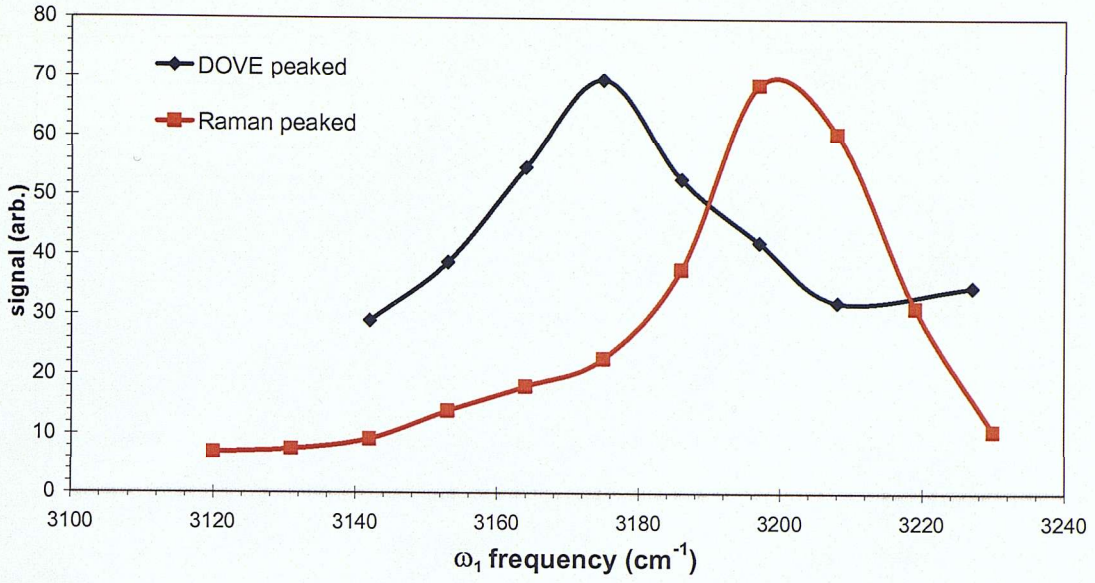


Figure 4.18. Two DOVE spectra of a 3:1 (molar ratio) solution of acetonitrile and deuterobenzene, with ω_2 fixed at 2253 cm^{-1}. These traces were acquired by optimising the signal with the final beam pointing and timing of the excitation beams when centred in ω_1 at the acetonitrile DOVE feature (blue) and at the deuterobenzene Raman feature (red), resulting in a shift of the centre peak frequency.

change in timing alone and will be further explored in section 4.8. It is assumed for plots henceforth that successive spectra presented in single graphs have been acquired with no change in the input pointing or relative timing of the excitation beams.

4.5.2. Carbon Disulphide/Bromochloromethane

The first two-dimensional data acquired during the course of this work was from a dilute solution of carbon disulphide (CS_2) in bromochloromethane (CH_2BrCl). CS_2 was chosen as a model sample for a number of reasons, namely because it is a very simple molecule and because its large integrated absorption cross section suggested high signal levels. Because of the simplicity of the molecule, it was predicted that the DOVE 2-D spectrum would be equally simple, and the repeat of these CS_2 experiments is shown in figure 4.19 as a 2-D contour plot. The sample is a 0.6 M solution of CS_2 in CH_2BrCl between two CaF_2 windows.

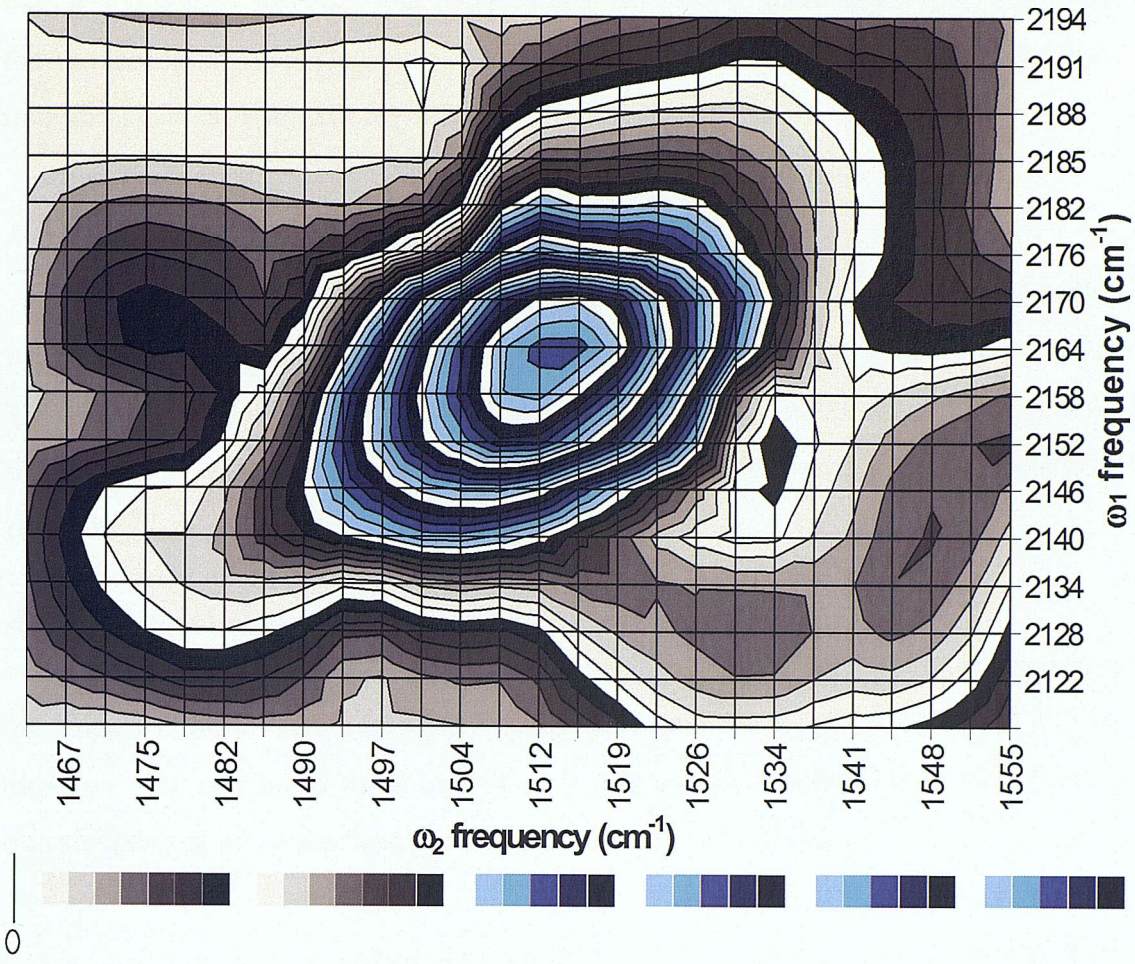


Figure 4.19. 2-D DOVE spectrum of a 0.6 M carbon disulphide in bromochloromethane solution. The pulses are all temporally coincident at T_0.

Here, as elsewhere in this thesis, the contours are on a repeated greyscale (8 divisions) followed by a repeated blue scale (6 divisions). A colour bar below the plot outlines the progression of intensity, which is presented in a linear scale throughout the progression.

A clear, central peak is visible at the frequency combination ~1514 cm^{-1} and 2164 cm^{-1}, corresponding to the peak measured by Wright's group within a few wavenumbers. The peak is ~26 cm^{-1} wide (FWHM) in the ω_1 dimension and ~30 cm^{-1} wide in the ω_2 dimension. The value for the linewidth in the ω_1 dimension is significantly higher than that measured from Wright's data on the same experiment (~16 cm^{-1}).[49] The peak is clearly broadened along the diagonal axis (parallel to a $\omega_1 = \omega_2$ axis), characteristically for a DOVE-IR process when pure dephasing is important.[23,27] Meyer notes[28] that both population (T_1) and pure dephasing (T_2^*) effects are observable in the broadening and stretching along a frequency diagonal of

the DOVE feature of CS_2. This result shows the need to incorporate both effects in the modelling of lineshapes in 2-D spectra, and was a successful first foray into multidimensional scanning for our work.

4.6. Signal sizes

The signal size that is measured depends on a number of factors aside from the macroscopic polarisability of the medium, as will be shown in the following sections. There are a number of controllable properties of the experiments which contribute to the overall measured signal size, and more than one FWM signal which can be at the detector.

4.6.1. Signal sizes of possible FWM signals

A first consideration of the signal measured at the detector is the possible presence of more than one signal component, comprising more than one FWM process. The mixing of three fields $\omega_{1\text{-}3}$ in any sample results in the production of fourth waves at all of the linear combinations of the input fields,

$$\omega_4 = n_1\omega_1 + n_2\omega_2 + n_3\omega_3 \qquad \textbf{(equation 4.3)}$$

where the n_i are integers. Each of the different combinations has an associated frequency (from the energy conservation condition) and direction (from the momentum conservation condition). If the experimental geometry has been optimised for the efficiency of a given combination, most of the other combinations will be poorly phase matched. In addition, the finite solid angle subtended by the detection optics or detector itself limits the number of these combinations that will reach the detector at all. Nevertheless, it is worth considering those processes that will result in signals that are similar to the optimised one in terms of frequency, direction, or phase matched signal level. For this case, the only possible process that fits this description is the IR-IR-Vis sum frequency, where all the n_i in equation 4.3 are considered to be +1. Table 4.2 shows the results obtained from the phase matching model (with refractive index dispersion not taken into account) and compares the characteristics of the DOVE process to the sum frequency process as

ω_1 is scanned around the $\nu_2 + \nu_4$ absorption in acetonitrile (ACN) and around the $\nu_1 + \nu_3$ absorption in carbon disulphide (CS_2) .

Process		DOVE	IR-IR-Vis sum
Signal wavelength λ (nm)	ACN *CS_2*	738-760 *740-749*	548-554 *607-613*
Output direction (degrees, measured from normal)	ACN *CS_2*	~3.2 *~2.8*	~0.4 *~0.8*
Phase match (relative to Δk=0, %)	ACN *CS_2*	~95 *~85*	~75 *~87*
OD of optical filters at signal wavelengths above	ACN *CS_2*	~0.3 *~0.4*	>8 *>1*

Table 4.2. Summary of the phase matched parameters for the acetonitrile and carbon disulphide experiments.

The output angles for these scans of ~150 cm^{-1} in ω_1 and the resultant signals vary somewhat and are given as approximate averages over the scan. Curiously, the sum frequency process is very well phase matched. However, the angular separation of the two output signals ensures that these signal beams are separated by >10 mm at the detector, placed 30 cm away. It is certain that the sum frequency signal in both cases would clip on the final turning mirror into the detector, the optical filter mounts, or on the entrance to the detector itself. In addition, the optical density at the sum frequency wavelength ensured that the sum frequency signal was not measured in the acetonitrile case, and the contrast ratio in the carbon disulphide case was >4 in favour of the DOVE signal.

A somewhat different situation was encountered for later work in the near-infrared (propanol and the ensuing amino acid work presented in Chapter 5), when the DOVE signal wavelength was further blue-shifted and the combination of optical filters was changed. In this case, the contrast ratio for the attenuation of the sum frequency signal relative to the DOVE signal was only ~2.5. However, the signals were separated by ~8.3 mm at the detector and again will certainly have been clipped by the detection optics/filters/detector housing, though some scatter into the PMT cannot be absolutely ruled out.

4.6.2. DOVE signal as a function of spacer thickness

Another parameter affecting the DOVE signal size is the thickness of the spacer in the sample cell, which ultimately determines the pathlength of the sample

exposed to the beam (given that the Rayleigh ranges for all the beams were on the order of millimeters and the physical overlap region exceeded the thickest samples by a factor of >5). The signal should vary quadratically with the total number of molecules in the beam overlap region, and thereby with the pathlength, assuming fixed spot sizes. This presumes that the beams will not be appreciably attenuated in the sample itself. However, the high absorption for some of the transitions in the samples meant that one or more of the input beams was attenuated greatly in the sample, and therefore there was some portion of the pathlength which did not contribute to the measured signal (the signal being the product of the input intensities, integrated over the effective pathlength). For this reason, later work to quantify signal sizes focused on progressively thinner and/or more dilute samples. Some early measurements of the signal as a function of spacer thickness are shown in figure 4.20.

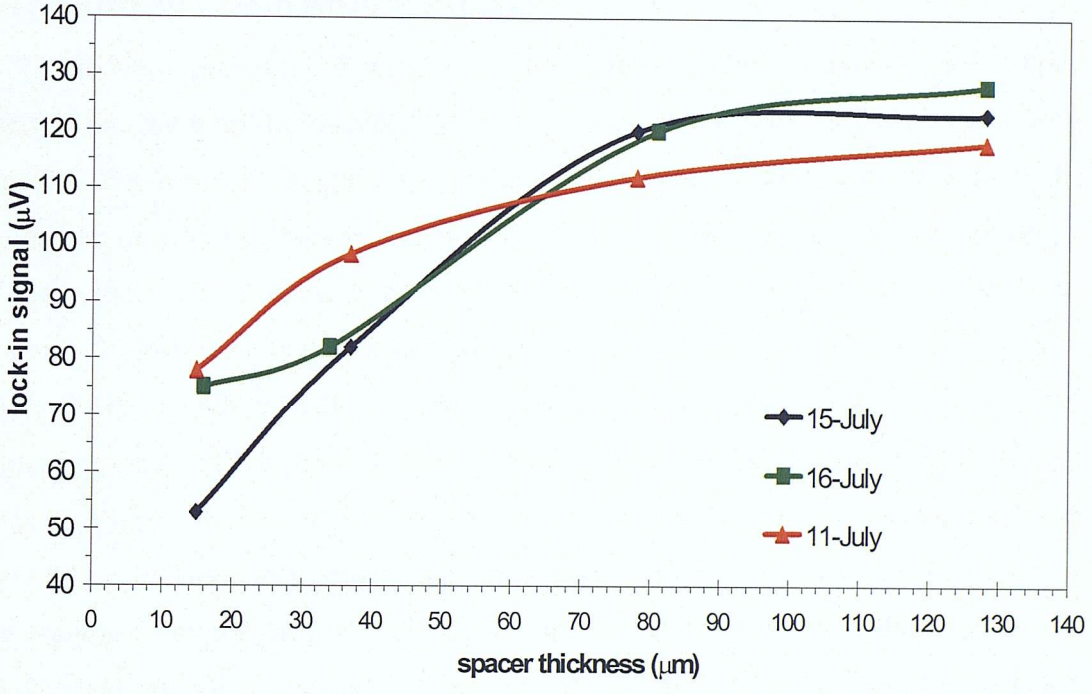


Figure 4.20. DOVE signal at the acetonitrile peak (3164/2253 cm^{-1}) as a function of spacer thickness. The signal is never quadratic in spacer thickness and asymptotically approaches a maximum near 120 μV for all cases.

The infrared frequencies are set for the acetonitrile DOVE peak (3164/2253 cm^{-1}) and the pulses overlapped at T_0. It is easy to see that the signal in all three cases is asymptotically approaching a limit of 120-130 μV, and even for thin spacers did not vary quadratically with the thickness. This suggests that even for very thin samples,

the optical density at ω_2 was high enough to prevent the whole sample from contributing to the measured signal.

Another feature of the plots is the variation of the signal for the very thin spacers. Note the pairings of the signals for the 15-July and 16-July plots at all but the lowest spacer thickness. However, for the ~10 μm spacer, the initial signal size is radically different. This is most likely an interference effect, discussed in detail in section 4.7, where the nonresonant signal provided by the windows interferes with the resonant signal from the acetonitrile. This effect is much more pronounced in the case where the samples are thin, and when the nonresonant signal is large—the samples were all placed between two, 1 mm thick sapphire windows, so that for the 10 μm case, the window pathlength was 100 times the sample pathlength (it is assumed that the back window contributes no signal because ω_2 has been completely absorbed in the sample).

4.7. Sample cell window effects

The very presence of windows in the sample cells complicates the output spectra, but the amplitude-level interferences are not the only variable to take into account: the absolute magnitude of the window contribution can vary as well, depending on window thickness, material, and orientation. Further, the surface finish of the windows also made a great difference to absolute signal levels. Both the calcium fluoride and sapphire windows were sufficiently thick (2 mm and 1 mm, respectively) to allow standard optical polishing and were generally of excellent optical quality. However, 100 μm thick borosilicate glass coverslips and 100 μm thick sapphire windows were also used. For minimal nonresonant background, the use of thinner windows seemed the obvious choice, especially for experiments where the signals from the sample were quite small. However, at such thicknesses, the mechanical stability precludes standard optical polishing techniques, and the resulting quality of polishing diminished greatly. Moreover, the thinner the windows, the more likely that they could flex under compression. It was found that these thin windows adopted a convex shape around a sample and thereby increased the pathlength, rather than forcing liquid out as the thicker, more rigid windows did. As a consequence, thin windows resulted in highly variable signal levels, and were very difficult to clean effectively between each experiment. Some of the data presented below is from experiments where these thin windows were used, but for

reproducibility experiments and in the case where the lineshapes were important, generally the thicker windows were employed. However, even experiments employing the thicker sapphire windows showed a lack of reproducibility, necessitating a further study of the effects of just the windows individually. The sample cell was loaded with a single sapphire window and a number of the ND filters were removed so that the signal from just the window could be measured. The entire sample cell was placed in a rotation mount, rotated about its centre, and the signal was recorded as a function of the angle of rotation. A polar plot of the result is shown in figure 4.21; θ is the rotation angle acquired in 20° steps and r is the signal level (arbitrary units).

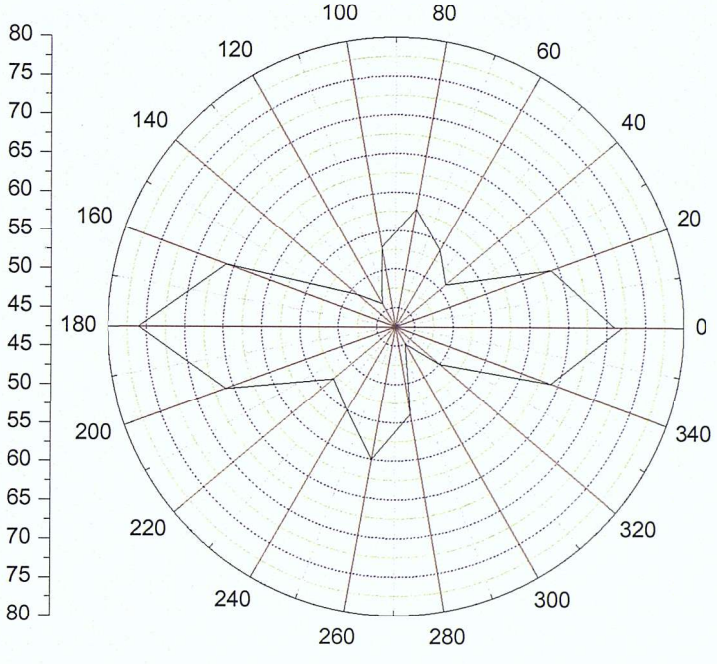


Figure 4.21. Polar plot of the signal (r) vs. the rotation angle (θ) of a 1 mm thick sapphire window. A large variation in signal is shown (nearly a factor of 2) and the functional dependence of the variation with sample cell rotation shows a familiar pattern.

The first feature to notice about this polar plot is the existence of two major and two minor peaks arranged almost perfectly symmetrically. This distinctive pattern is very reminiscent of a polar plot of second-harmonic generation as a function of input polarisation angle, a case in which the second-order nonlinear susceptibility is probed. This behaviour in the case of these windows suggests that the window contribution is in this case a real nonlinear effect in the bulk material.

Interestingly, this pattern was only seen in the experiment with this particular window; a similar experiment performed with a calcium fluoride window showed very little variation in signal level with rotation. This has been attributed to a difference in the crystal structure of the windows; while the calcium fluoride windows were specified by the manufacturer to be of amorphous structure, the sapphire windows were cut from single crystal (rhombohedral). It is reasonable then to expect a variation of signal with relative crystal orientation due to a change in polarisability for different orientations. However, the sapphire windows were specified by the manufacturer as being cut with random orientation relative to the C-axis of the crystal, so that there is little reason to expect the same functional relationship between signal and rotation for each different sapphire window. In fact, a repeat of the experiment with a different sapphire window (100 μm thick, but otherwise of the same specifications) resulted in the plot shown in figure 4.22:

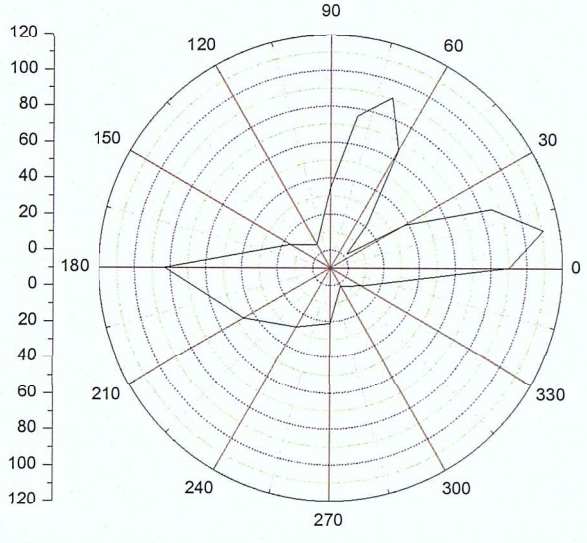


Figure 4.22. Polar plot as figure 4.21 of a 100μm thick sapphire window. Here the 2-fold symmetry is absent but the variation in signal is still very large.

In both cases it was found that vertical translation of the rotation mount containing the sample cell had relatively little effect on the signal level measured, supporting the case for variation due to differing crystal orientation. It is easy to see that this sensitivity to rotation of the sapphire windows made it imperative that the orientation of the windows was kept constant from sample to sample, both for absolute signal level reproducibility, and to ensure that the amplitude-level

interference of the window contribution with the sample/solvent contribution was kept constant.

4.8. Temporal behaviour of DOVE signals

4.8.1. Build-up of signals and discussion of interferences

There are a number of coherence pathways which can contribute to the measured nonlinear signal, outlined in detail in section 2.3.1. However, each of these coherences has an associated dephasing time, providing the possibility that different fields emitted by any material in the beam overlap region (sample cell windows, solvent, solute) can interfere constructively or destructively at the amplitude level, resulting in cross-terms in an expression for the overall signal intensity. Moreover, there is always a non-resonant background present from all the materials in the overlap region due to the electronic polarisability. This interference between a resonance and a background manifests itself in the spectra as a dispersive lineshape, as will be shown.

The different dephasing rates of different signal components and their interferences is best shown below. Here, the pulse delay t_{12} is defined as the time between the arrival of ω_1 and ω_2. Similarly the delay t_{23} is defined as the time between the arrival of ω_2 and ω_3. Figure 4.23 plots the decay of the measured nonlinear signal for a number of samples as a function of the t_{23} delay, with t_{12} fixed at 0—i.e. the infrared pulses are overlapped in time, so that at 0 on the graph, all three are overlapped, with the visible pulse arriving progressively later to the right. The values for ω_1 are listed in the legend to the graph and ω_2 was fixed at 2253 cm^{-1} for all of the traces. It appears that the shortest-lived signals are those from just a window (dotted red) and the neat deuterobenzene, which is expected because both should be nonresonant contributions and therefore decay instantaneously outside the pulse envelope. However, note the difference between the neat deuterobenzene traces at ω_1 = 3164 cm^{-1} and ω_1 = 3226 cm^{-1}. At 3226 cm^{-1}, the signal decays to $1/e$ of its peak value in 3 ps, whereas the 3164 cm^{-1} trace decays to the same fraction in ~0.7 ps.

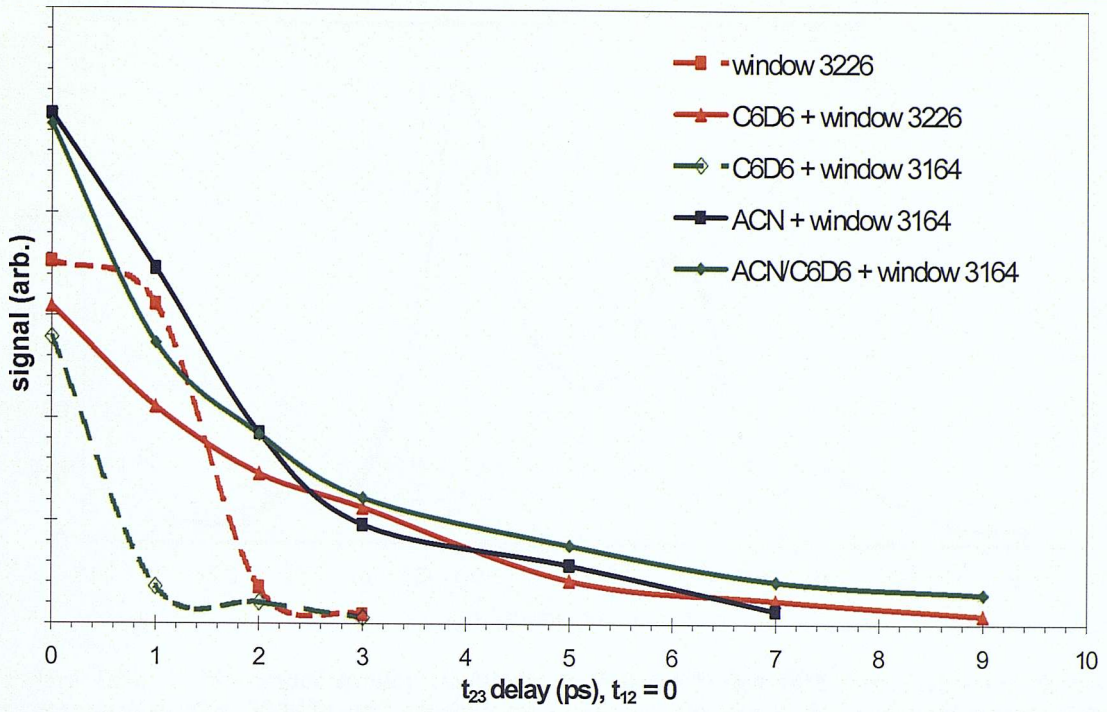


Figure 4.23. Decay of various signals as a function of the t_{23} delay, with t_{12} fixed at 0. The ω_1 values for each trace are listed in the legend, and ω_2 was fixed at 2253 cm^{-1}. Note the varying shapes of the decays and that the resonant conditions do not necessarily lead to longer-lived signals than the nonresonant ones.

While both these frequency settings are roughly equally spaced from what would be the CARS line (29 cm^{-1} lower and 33 cm^{-1} higher, respectively), it is noted that the ω_2 setting of 2253 cm^{-1} is still quite near the C-D stretch of the deuterobenzene (ν_{20} = 2280 cm^{-1}), and a strong band is visible in the neat deuterobenzene FTIR spectrum at 3234 cm^{-1}. While this band has been identified as the combination of the familiar ring-breathing mode at ν_1 = 944 cm^{-1} and the C-D stretch ν_{20},[14] no mention is made of it in the analysis of the resultant spectra. It is tempting to speculate that the result at 3226 cm^{-1} is a weak DOVE-IR signal, and thus likely to have a lower dephasing rate.

The data in figure 4.27 were collected at intervals of 1 ps, with later data collected at 2 ps intervals. Further, no data was taken after the signals decayed to the noise floor. Later work showed that the signal can actually oscillate as a function of the ω_3 delay; this is a consequence of the beating of the out-of-phase coherences with different dephasing rates.[28] More careful studies of the signal decay as a function of ω_3 delay were made on propanol, shown in figure 4.24.

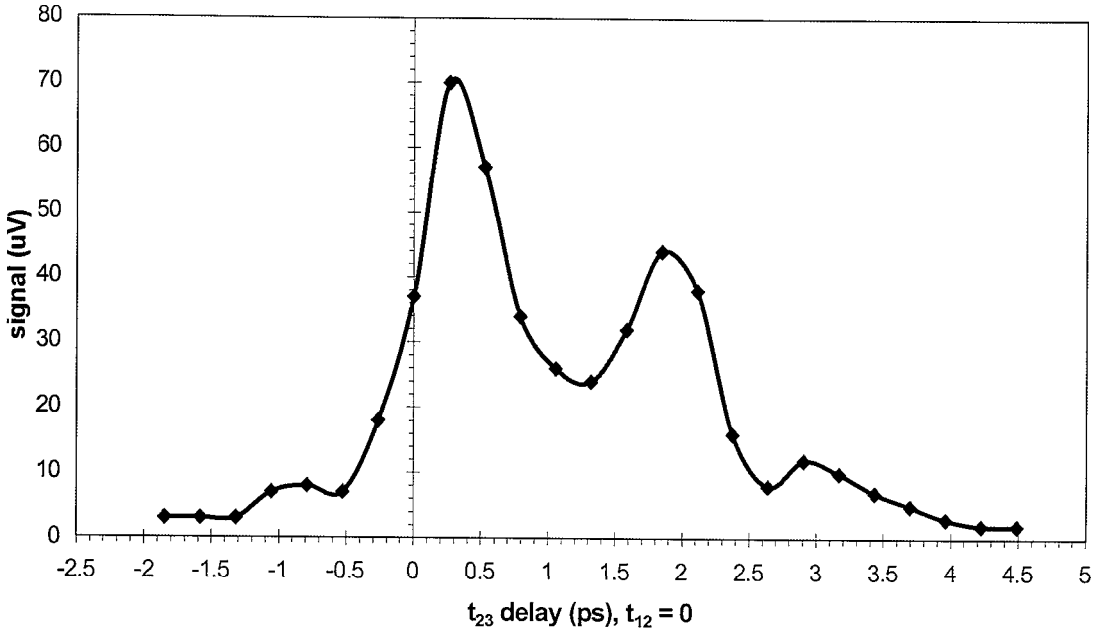


Figure 4.24. A plot under similar conditions to figure 4.23 but with frequencies set for the propanol peak at 4350/1458 cm^{-1} showing oscillations in the decay of a propanol signal. The signal is clearly not maximised at t_{23}=0.

Several effects in this figure are worthy of discussion. Firstly, there is a small peak visible at negative delay, signifying the ω_3 pulse arriving nearly a picosecond before the infrared pulses that create the coherences, an effect which is visible in more than one data set from the timing experiments. This suggests the possibility of satellite pulses on one or more of the excitation beams, but the effect is not present in all of the timing plots. It is definitely not noticeable in the cross-correlation traces obtained with the silicon photodiode, but the high nonlinearity of the multiphoton process in the cross-correlation suggests that satellite pulses may not be manifest in the resulting traces. Next, it can be seen that the signal is not actually at its peak at $t_{23} = 0$, again presumably a consequence of the beating coherences partially destructively interfering but quite possibly due to the group velocity mismatch addressed in section 3.4.3.

The frequency difference between the coherences is induced by the anharmonicity between the directly excited modes,[28] so that the period of the oscillations can be used to deduce this anharmonicity. In this case, the oscillations have a period of roughly 1.3 ps, which would correspond to an anharmonicity of ~26 cm^{-1}, far higher than the value obtained by comparing the frequency sum of the fundamentals with the frequency of the combination band (the anharmonic shift

$\Delta = 5$ cm^{-1}). Nevertheless, the decay is not strongly periodic and it is unclear how the window contributions/interferences can obscure the pure signal oscillations.

Considering the non-monotonic nature of the signal decay, it is instructive to look back at figure 4.27 and observe the shapes of the decay traces. The decay rates for some of the samples now clearly do not appear to be convolutions of the ω_3 pulse. Particularly interesting is the difference between the acetonitrile and acetonitrile+deuterobenzene traces. Though they start at approximately the same value and decay at nearly the same rate, the differing shapes show the influence of another signal component. Further, the question is raised as to whether the ripple in the final part of the deuterobenzene+window trace is an experimental artefact or a real oscillation which may have recovered at later times.

The interference at the field level of coherences created in the sample, the solute, and the sample windows leads to an extraordinary sensitivity of the spectral lineshapes obtained to the timing and direction of the input pulses, and to the physical properties of the sample itself.

Published simulations of the nonresonant background accounting for the refractive index dispersion through sample windows show a variation across the spectral space, changing particularly radically in the ω_2 dimension.[22] This effect will be explored further in Chapter 5 for the case of amino acid spectra. The nonresonant background, as well as being the ultimate limitation to detectivity, can change the lineshapes observed in both 1- and 2-D spectra. These lineshapes can change from absorptive to dispersive; figure 4.25 presents a set of spectra taken in propanol on three different days. It can be easily seen that the lineshape has dispersive character. The absorption peak in the FTIR spectra is present at 4336 cm^{-1}, in the middle of the feature shown above. The left peak shifts somewhat between the solid traces and the triangles, and the variation in the background at both the high- and low- frequency sides suggests not just a simple shift of background, but a tangible change in lineshape towards the dispersive.

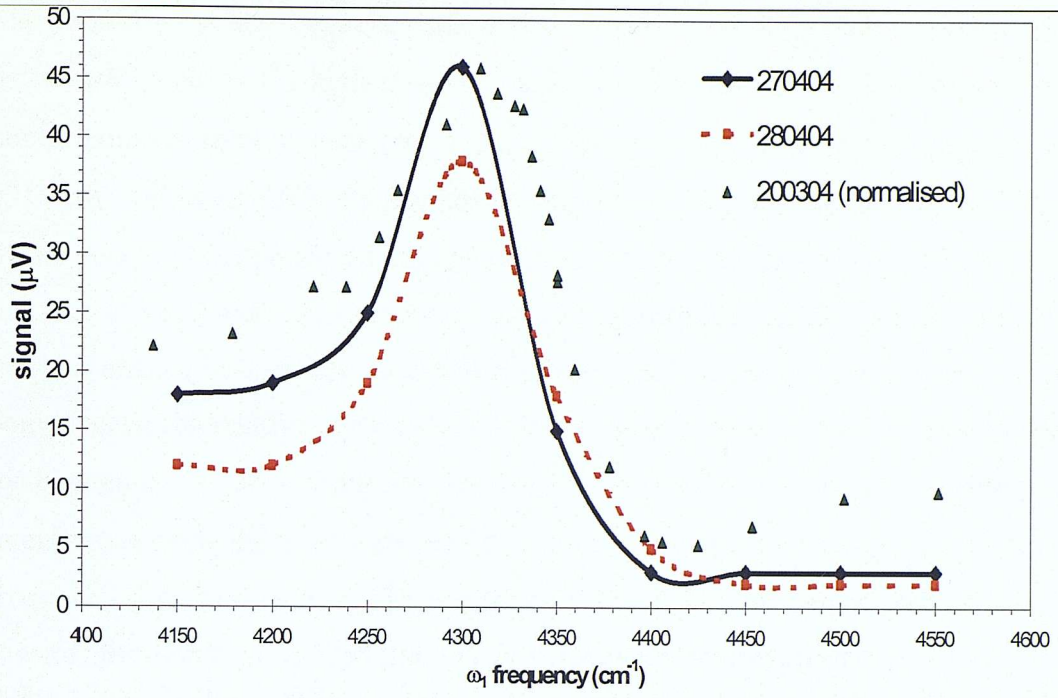


Figure 4.25. DOVE spectra at T_0 of neat propanol on three different days. Here ω_2 is fixed at 1458 cm^{-1}. The spectra show some variation in the centre frequency of the peak but also seem to show variation in the absorptive/dispersive character from day to day.

As a standard sample, daily repeats of just three points on this curve (at 4140, 4310, and 4450 cm^{-1}) served as a check of the spectrometer and an indication of reproducibility. A plot is shown in figure 4.26 with error bars representing 10 of these repeats, with the full 200304 plot from figure 4.25 shown for comparison.

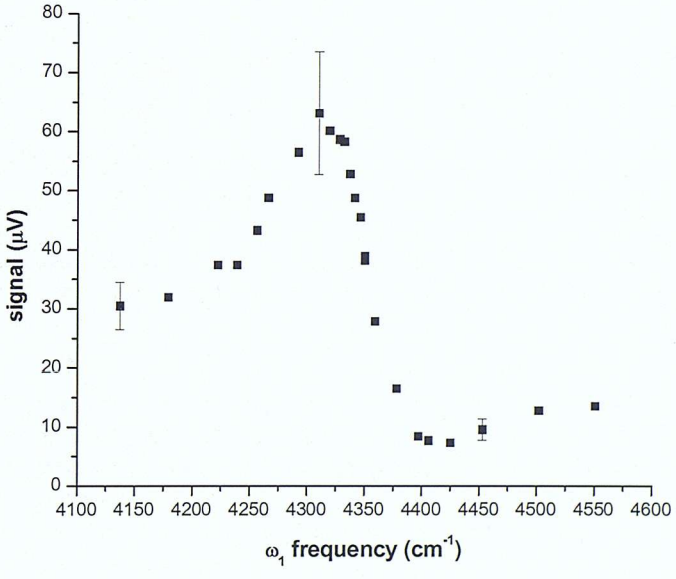


Figure 4.26. Standard deviation from 10 data sets for the three daily points taken in the propanol spectrum. The full scan is from figure 4.25. The peak point at 4310 cm^{-1} varies widely as the lineshape changes.

The points on the low-frequency side are clustered quite tightly around a mean value (σ = 4 μV), and on the high-frequency side are very near the noise floor so should not be expected to vary much (σ = 1.8 μV). Interestingly, however, the peak point at 4310 cm^{-1} varies significantly from day to day (σ = 10.4 μV), and the relative heights of the peak and the points on either side show daily changes not just in background but also in lineshape, again changing between absorptive and dispersive. It is clear that this change in lineshape is an effect of the interferences between different signal components; the relative contribution from the propanol signal can be varied instead by changing ω_2 away from the resonance value of 1458 cm^{-1}, eliminating the interference with the resonance which causes the dispersive lineshape As the ω_2 frequency gets further from the resonance value, the peak height increases, shifts towards the steady-state absorption peak value, and the background at both the low- and high-frequency side gets progressively lower, suggesting a tendency toward an absorptive lineshape.

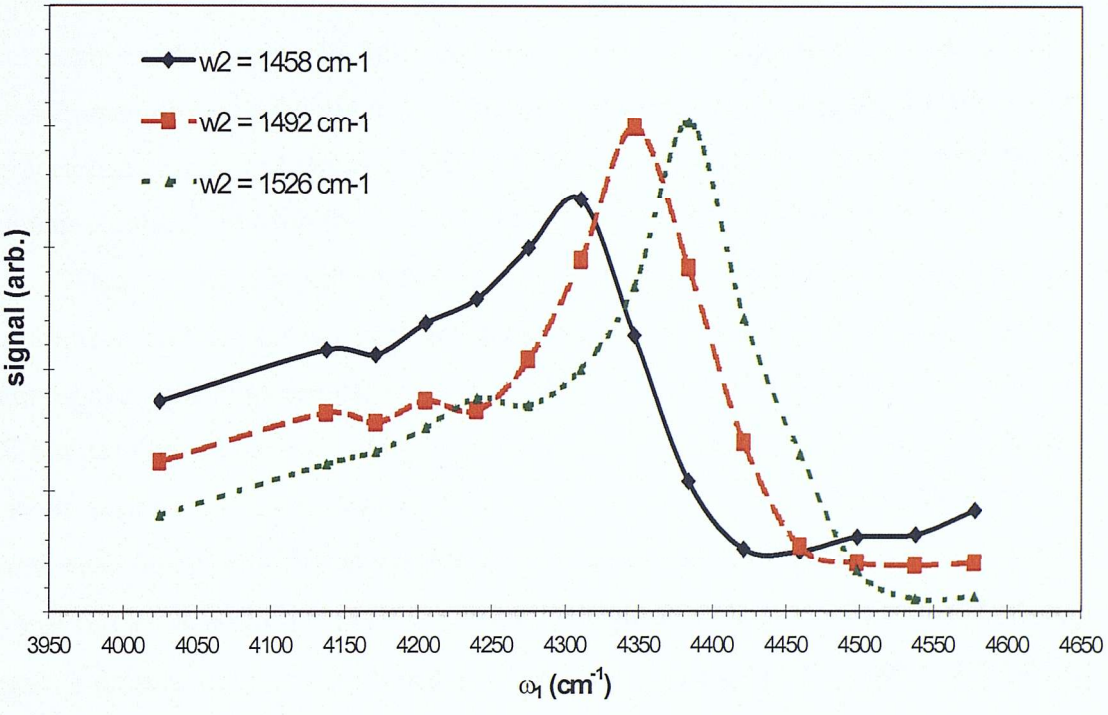


Figure 4.27. DOVE spectra at T_0 of propanol with varying ω_2 settings: on resonance at 1458 cm^{-1} (blue) and progressively further from resonance at 1492 cm^{-1} (red) and 1526 cm^{-1} (green). The shift of the centre frequency is consistent with a peak in the 2-D spectrum that is broadened along the diagonal, characteristic of pure dephasing effects.

4.8.2. Suppression of signal components

The signal detected in the experiment is actually a complicated combination of signal components, including DOVE, CARS, and nonresonant processes. However, because of the differing mechanisms by which these coherences and the ensuing detected signals are created, they have different properties in the time domain. Coherences involving real states dephase with a time constant on the order of picoseconds, but there are a number of nonresonant processes occurring in the solvent, in the solute, in the sample cell windows, etc. These nonresonant processes dephase almost instantaneously outside the pulse window. For example, in the acetonitrile/deuterobenzene case, the Raman-active deuterobenzene mode that is excited comprises no real states at either of the input infrared frequencies (as opposed to a DOVE-Raman process, which creates a coherence via a real vibrational state). As such, the mode is only excited when the pulses that create it are temporally overlapped. However, the DOVE feature in acetonitrile occurs only when both the input infrared frequencies are resonant with real vibrational states, so that each excitation results in a coherence that has a significant lifetime. As a consequence, by introducing a delay between the infrared pulses, the DOVE feature in acetonitrile will not decay appreciably within a coherence lifetime, whereas the Raman contribution from the deuterobenzene should be markedly suppressed.

Figure 4.28 is a plot of two ω_1 scans in the region of the DOVE peaks in acetonitrile and the CARS peak in deuterobenzene. The sample is a 3:1 mol:mol ratio of acetonitrile to deuterobenzene. The plot in blue is at T_0, where the pulses are all temporally overlapped. The large CARS peak dominates, and the DOVE peak can be seen as a shoulder on this peak near 3164 cm^{-1}. The plot in red shows the same scan taken with the delays set to t_{12} = 0.5 ps (ω_1 leads ω_2 by 0.5 ps) and t_{23} = 1.5 ps (ω_2 leads ω_3 by 1.5 ps). Now the DOVE peak is clearly visible and the Raman peak is present only as a high background on the high-frequency side of the DOVE peak.

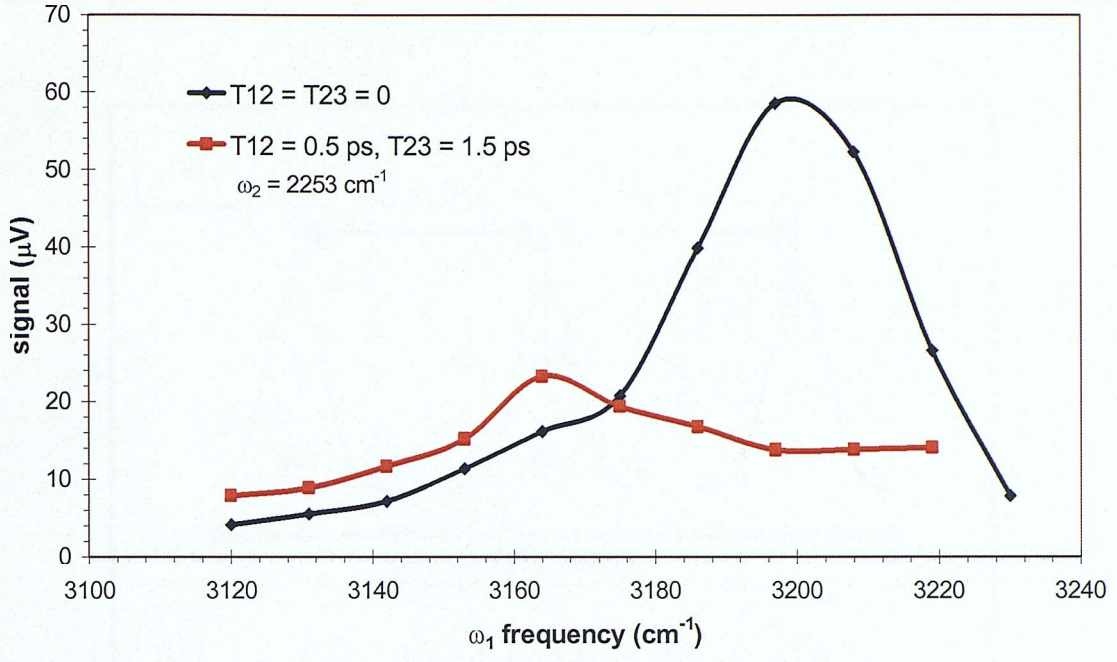


Figure 4.28. DOVE spectra on a 3:1 (molar ratio) acetonitrile/deuterobenzene solution for two different delay pairs t_{12}, t_{23}: (0,0, blue) and (+0.5, +1.5 ps, red). It is clear that the Raman peak at 3197 cm^{-1} is markedly suppressed when the pulses are not overlapped; it appears the DOVE peak at 3164 cm^{-1} is roughly the same size in both cases due to the coherence lifetimes induced by resonance with real states.

4.8.3. Two-dimensional temporal scans

The study of the suppression of the CARS feature in deuterobenzene led to further investigations of the functional dependence of the signal on both the delays. To this point, the only considered studies of varying the delays had been the variation of t_{23}, the time between the concurrent arrival of the infrared pulses and the final, visible pulse. By incrementing the t_{23} setting manually and taking scans in the t_{12} (the delay between the infrared pulses), it was possible to acquire temporal two-dimensional scans of the signal. Before exploring some of the data acquired in this way, it is worthwhile to discuss the notation and refer to the figure on the following page. Given that the ω_2 pulse is fixed in time (i.e. it is the only one of the excitation beams which is not temporally adjustable with a translation stage), t_{23} is always measured relative to the ω_2 pulse, even when ω_1 arrives after ω_2. For positive t_{12} delays, the ω_1 pulse leads ω_2 into the sample followed by the ω_3 pulse at a later time t_{23} (case (**a**)). For negative t_{12} delays, the ω_2 pulse (fundamental) leads the ω_1 pulse (combination band) into the sample (case (**b**)). A curious condition is reached for negative t_{12} values with magnitude greater than t_{23}: the relative delay of the ω_1 pulse is such that it arrives later than the ω_3 (case (**c**)).

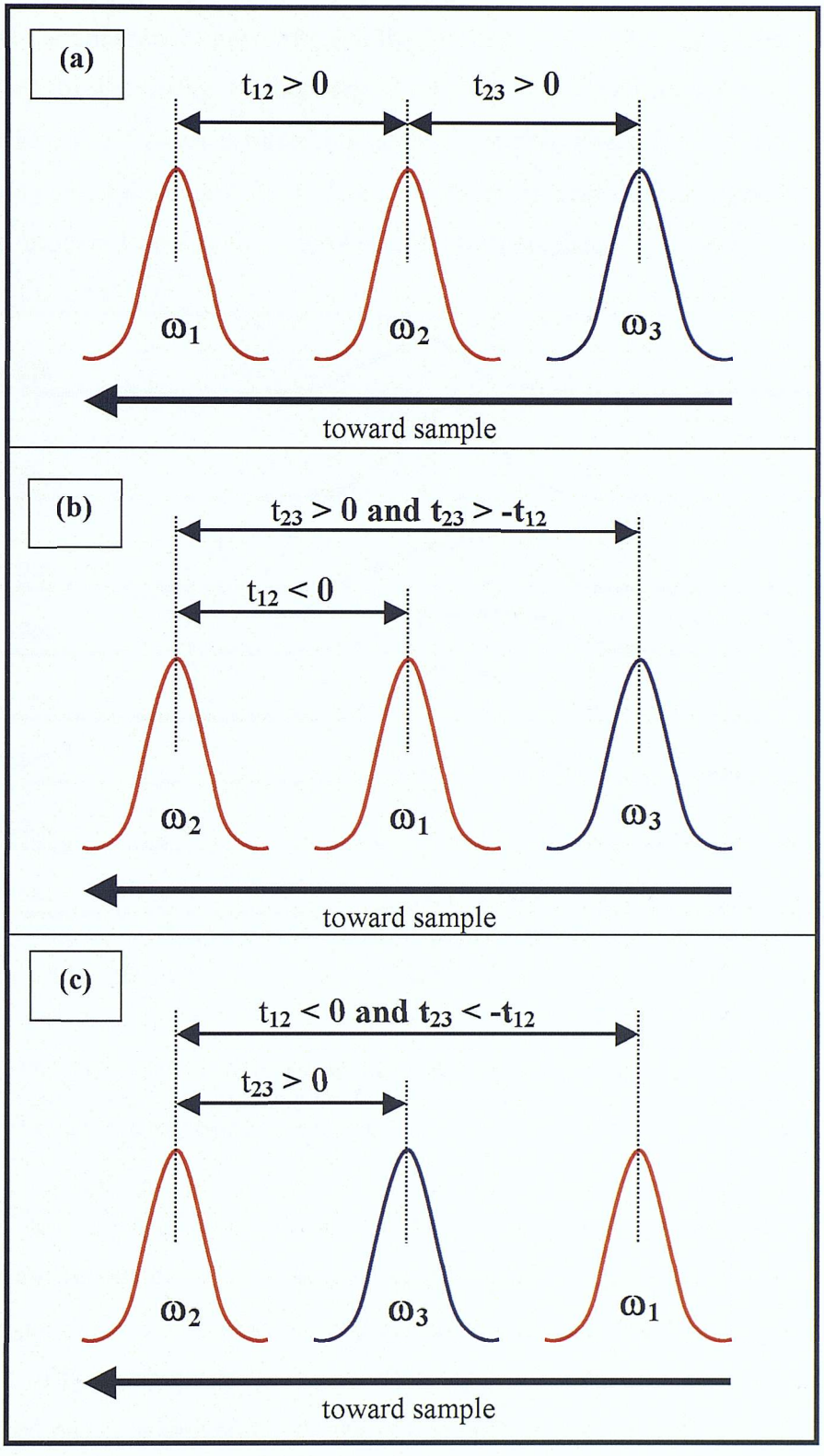


Figure 4.29. Schematic representation of various pulse orderings. The visible pulse is shown in blue, the infrared pulses in red.

It is useful to visualise the ω_3 pulse as a "readout beam" (not unlike the third pulse in a three pulse photon echo experiment), that is, taking a snapshot of the point to which the coherences have evolved by the time t_{23} after they have been created, as a function of the delay t_{12} between their creation. At this fixed readout time, constructive interference is occurring at the t_{12} setting where the peaks can be found. By way of example, figure 4.30 shows a number of traces of the signal vs. t_{12} delay in a neat propanol sample for a number of t_{23} settings listed to the left.

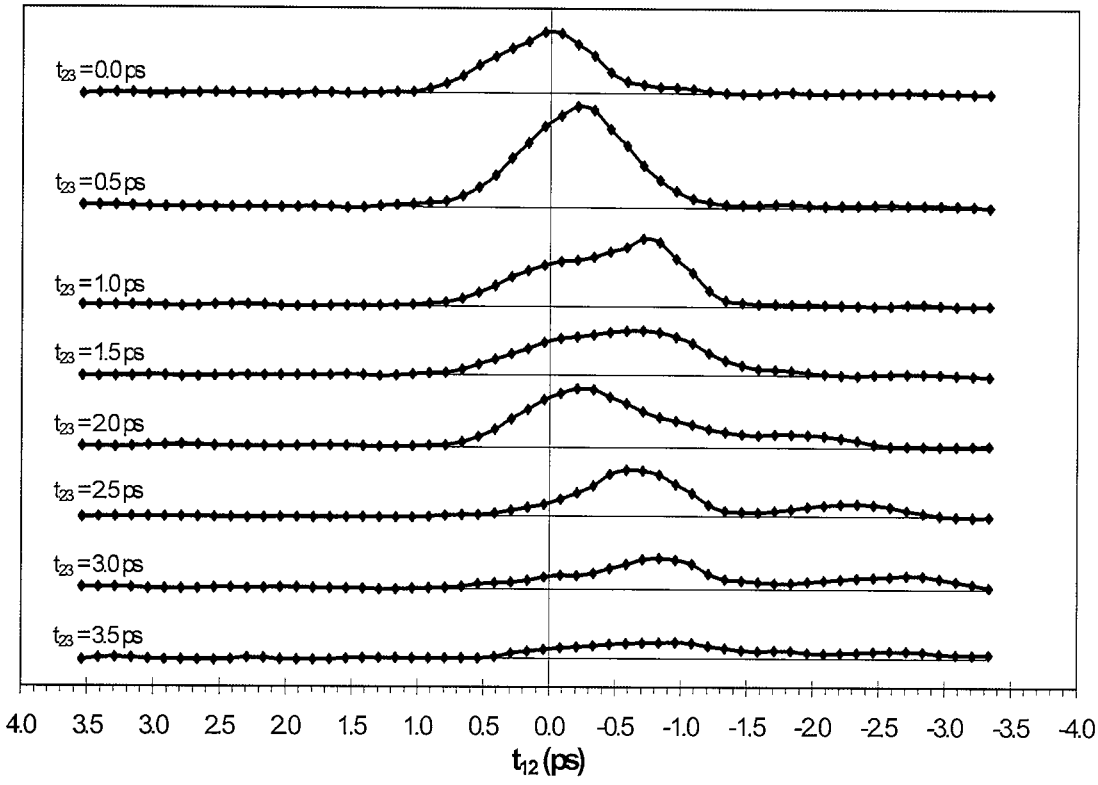


Figure 4.30. Temporal scans in t_{12} of the propanol signal, acquired at the frequency pair 4370/1458 cm^{-1}. The fixed t_{23} settings are listed at left. The single, symmetric peak at (0,0) shifts and splits in time as a consequence of the beating coherences which make up the signal.

As t_{23} is incremented (taking the snapshot at a later time), it can be easily seen that there is an overall change of the integrated signal strength (the area under all the peaks is not conserved, due to dephasing and rephasing of the coherences), and there is a shift of the main peak at $t_{12} = 0$, which appears to grow and then split into two unresolved peaks, which shift relative to one another for the remainder of the traces. Most interestingly, no features are visible for the case $t_{12} > 0$ where the ω_1 pulse is incident first. By way of comparison, the signal component suppression experiments showed that the delay pair used to suppress the deuterobenzene CARS contribution

was t_{12} = +0.5 ps and t_{23} = +1.5 ps, a temporal location where in these spectra the signal is quite low.

Studying the data presented in this way was a helpful step in determining the delays that were appropriate for an intial search for amino acid signals; clearly a pair of delays which resulted in no signal was undesirable, and the initial rationale was that by comparing the "solvent" and the "solvent + solute" temporal scans, it would be possible to locate changing peak heights and temporal peak locations in order to home in on delay pairs that accentuated the solute signal, or possibly to find delay pairs which changed the interferences between different signal components.

It is now instructive to look at the propanol data from figure 4.30 as a contour plot, with the two delay times as the coordinate axes. It is possible to identify the regions of these 2-D plots which correspond to the different pulse orderings labelled in figure 4.29. Case **(a)** referred to the pulse ordering ω_1, ω_2, ω_3 separated by t_{12} and t_{23}. Case **(b)** referred to the ω_2, ω_1, ω_3 pulse ordering separated by t_{12} and $t_{23} + t_{12}$ (where $t_{12} < 0$). Case **(c)** was for the order ω_2, ω_3, ω_1, separated by t_{23} and $t_{23} + t_{12}$.

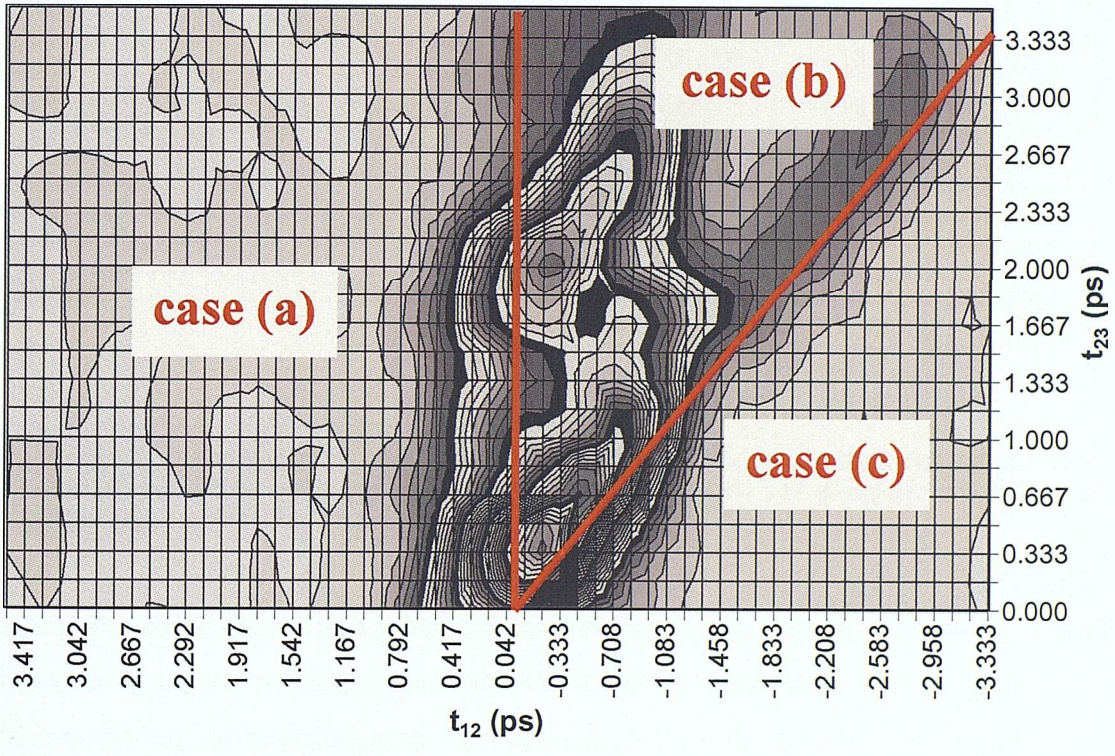


Figure 4.31. Schematic representation of the different pulse ordering cases from figure 4.29.

The data presented in figure 4.30 can now be envisioned as horizontal slices through these contour plots for the given values of t_{23}, and with the construction lines

drawn on figure 4.31 it is clear to see that no appreciable signal results from cases **(a)** and **(c)**. This was the case for all of the 2-D time plots presented in this chapter. Case **(c)** is easy to explain; the visible pulse is arriving before the second infrared and therefore is not probing the coherence induced in the second vibrational transition. The signal decays quickly to background outside the pulse envelope, as expected. Case **(a)** however is more difficult, and will be approached in the conclusion of this section.

Figures 4.32 and 4.33 compare two temporal 2-D plots of the signal from neat propanol and from neat D_2O in the same spectral region: ω_1 near 4370 cm^{-1} and ω_2 near 1465 cm^{-1}, the chosen pair of frequencies for the initial studies on alanine.

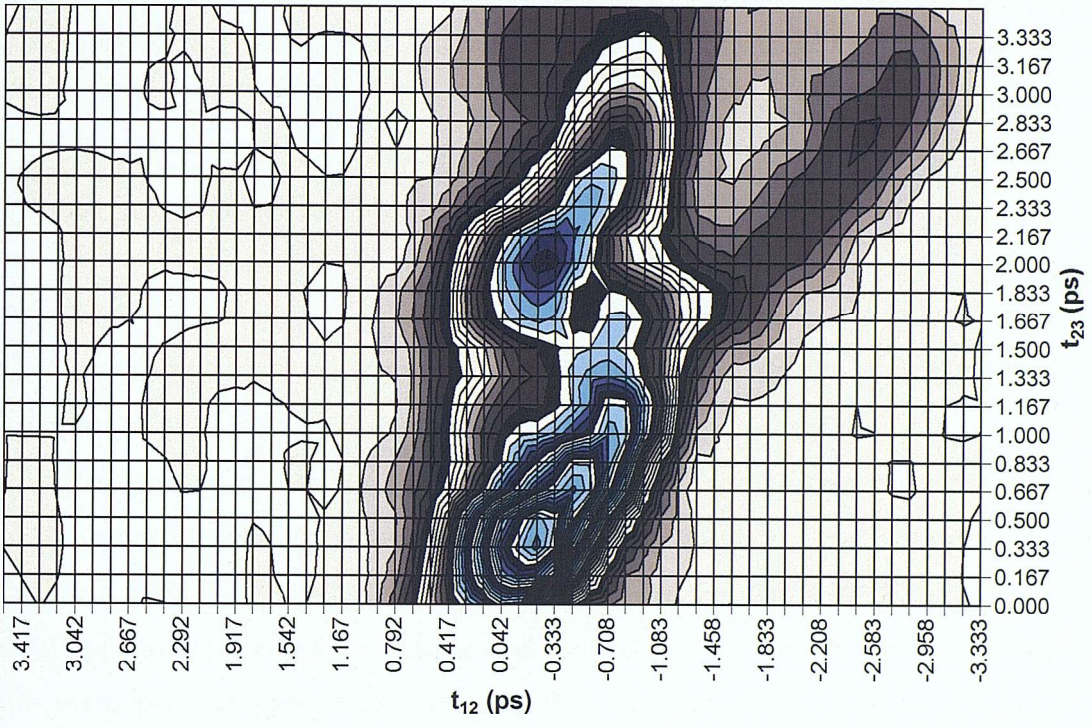


Figure 4.32. Temporal two-dimensional contour plots of the signal from neat propanol at 4370/1458 cm^{-1}. Here again a greyscale (8 divisions) is repeated and peaks are labelled with a repeated blue scale (6 divisions).

A comparison of these two plots is instructive as to the behaviour of signals, both comprising largely resonant (propanol) and largely nonresonant (D_2O) contributions. The number of contours suggests equivalent signal levels, but it should be noted that the post-sample ND filter combination included an OD~0.7 filter in the case of the propanol scan which was absent for the D_2O scan, so that the overall scale of the D_2O scan is ~5 times smaller. Also, the timescales of the two plots are slightly diff-

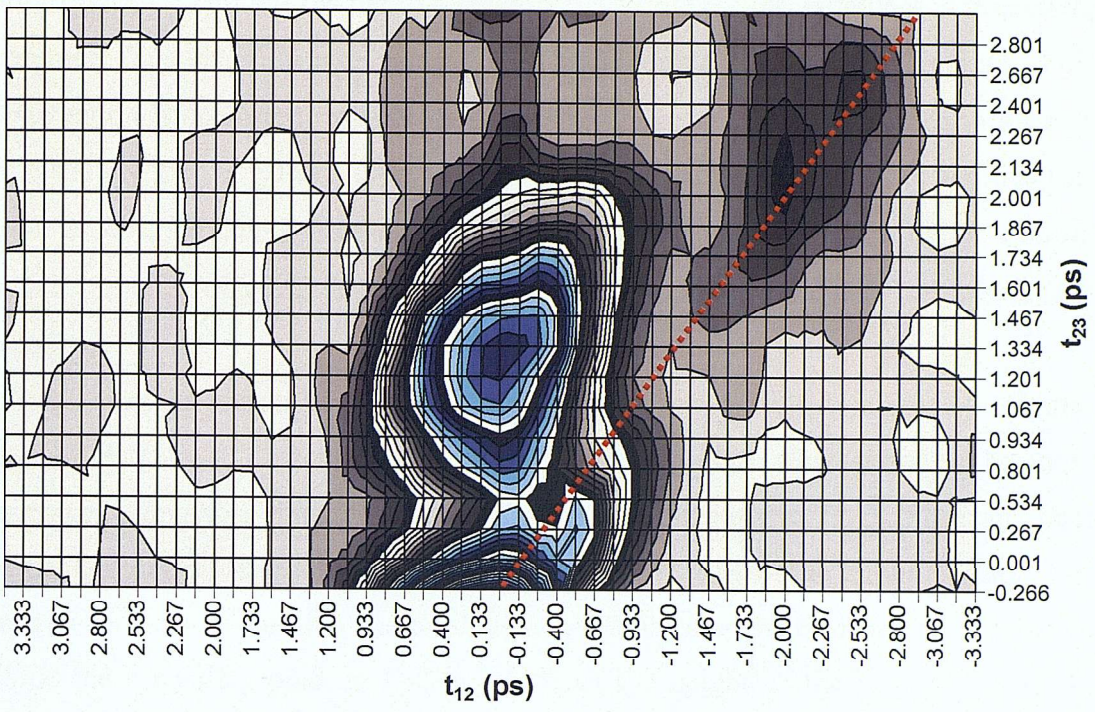


Figure 4.33. Temporal two-dimensional contour plot of the signal from neat D_2O at the frequency pair 4370/1465 cm^{-1}, showing qualitative similarity in shape to figure 4.32.

erent in the t_{23} dimension; it can be seen that the highest peak is at a lower value of t_{23} for the D_2O scan, whereas the propanol peak was nearly at the level of the background at $t_{23} = 0$.

What is clear from both plots is a very large central peak near the (t_{12}, t_{23}) pair (0,0)—complete overlap of the three input pulses. While the data for negative t_{23} are not shown for D_2O, by inspection it would appear that the peak (0,0) appears at a small negative t_{23} value and is larger than the secondary peak. In propanol, however, the main peak is present at (-0.2, +0.33). While neither of these timing pairs probably absolutely represent complete temporal overlap of the pulses, the identical sample cell conditions and excitation frequencies provide a relative measure of the timing conditions for peak signal.

In both plots, two major peaks are present. The secondary peaks seem shifted along just the $t_{12} = 0$ axis, with D_2O peaking again at (0, +1.33), and propanol at (-0.2, +2.0). This is consistent with the idea that the strongest contributor to the signals in this temporal space is the interferences of the coherences whose relative phase is set by the timing between the two infrared pulses. Both of the propanol peaks are clearly stretched along a time diagonal (parallel to the boundary between cases (**b**) and (**c**) in figure 4.31) where ω_2 is leading ω_1 into the sample by

progressively more but the relative delay between the ω_1 and ω_3 pulses is remaining constant. The signal in both cases decays monotonically along this diagonal. This observation is consistent with the idea that the t_{23} delay that corresponds to the two peaks along the $t_{12} = 0$ axis is sampling a constructive interference peak and that this peak is decaying due to the dephasing of the coherence set up by the first (ω_2) pulse, which along the diagonal is occurring progressively earlier relative to the second (ω_1) pulse.

The peaks present in the D_2O spectrum also show a lengthening along a similar pair of diagonals. Although the peaks in the propanol plot appear to be more narrowed along both time axes than the corresponding peaks in D_2O, this is an effect of the contour plotting and each has a FWHM of ~1.2 ps in the t_{12} dimension. The relative heights of the two peaks along $t_{12} = 0$ are somewhat different in the two plots; the secondary peak in D_2O is ~80% of the height of the primary peak. In propanol, this figure is ~50%.

Again, a broadening along the time diagonal can be seen in figure 4.34, acquired from a sample of 0.3 M CS_2 in CH_2BrCl with the frequencies set for the DOVE peak in CS_2 at ω_1 = 2168 cm^{-1} and ω_2 = 1500 cm^{-1}. The situation is analogous to the propanol plot in figure 4.32, but here the signal is exactly on resonance in a very different wavelength regime. The most significant difference between these experiments is the scale of the CS_2 signal, which was acquired with an

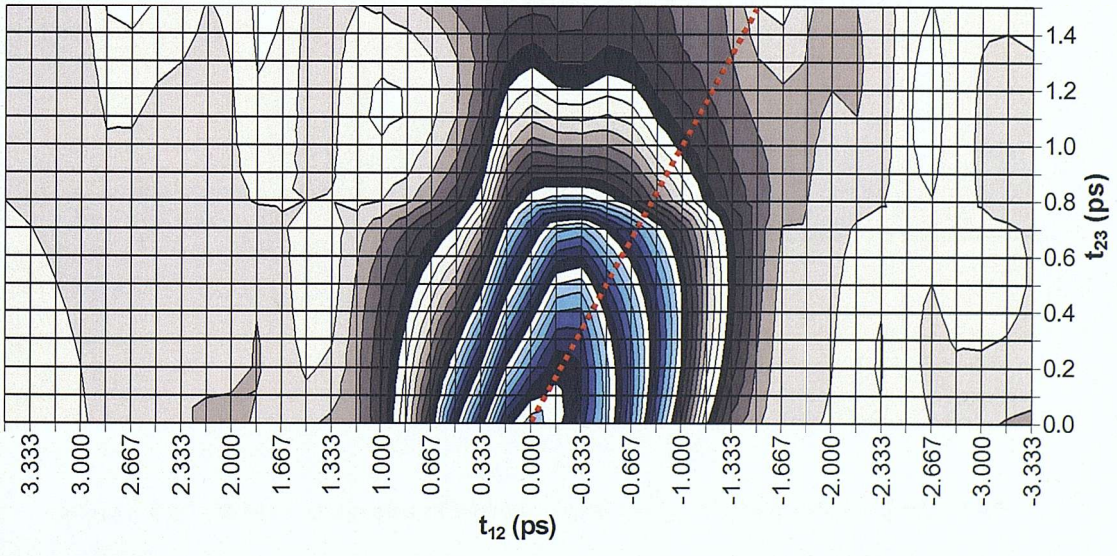


Figure 4.34. Temporal two-dimensional plot of the DOVE signal from a 0.3 M solution of carbon disulphide in bromochloromethane, acquired at the frequency pair 2168/1500 cm^{-1}.

additional ND filter of optical density 1.0, so that the CS_2 signal is ~10 times larger than the propanol and ~50 times larger than the D_2O. Here the scale of the t_{23} dimension is significantly smaller, spanning the range between $t_{23} = 0$ and 1.5 ps. The peak has a width in the t_{12} dimension of ~1.3 ps (FWHM). Because the plot does not show data for $t_{23} > 1.5$ ps it is difficult to speculate about the existence of a secondary peak along the $t_{12} = 0$ axis, but it is clear that for this fully resonant case, the peak is centred at (0,0). Further, the addition of the construction line shows that the peak is broadened nearly along the same time diagonal as the preceding figures. The fact that the peak is not broadened purely along this diagonal, but somewhat towards a vertical axis, seems to suggest that the signal may be recovering toward another peak along the $t_{12} = 0$ axis.

The most puzzling aspect of these 2-D plots is the absence of signal in the region of temporal space corresponding to case **(a)**. In this case, the higher frequency excitation (ω_1) arrives first. In figure 4.35 (a repeat of figure 2.4), it is clear that the first three coherence pathways (nonresonant, SIVE, and DOVE-IR) will make no distinction between the time ordering of the first two excitations; the only condition for this pathway to contribute is that each part of the wavefunction is

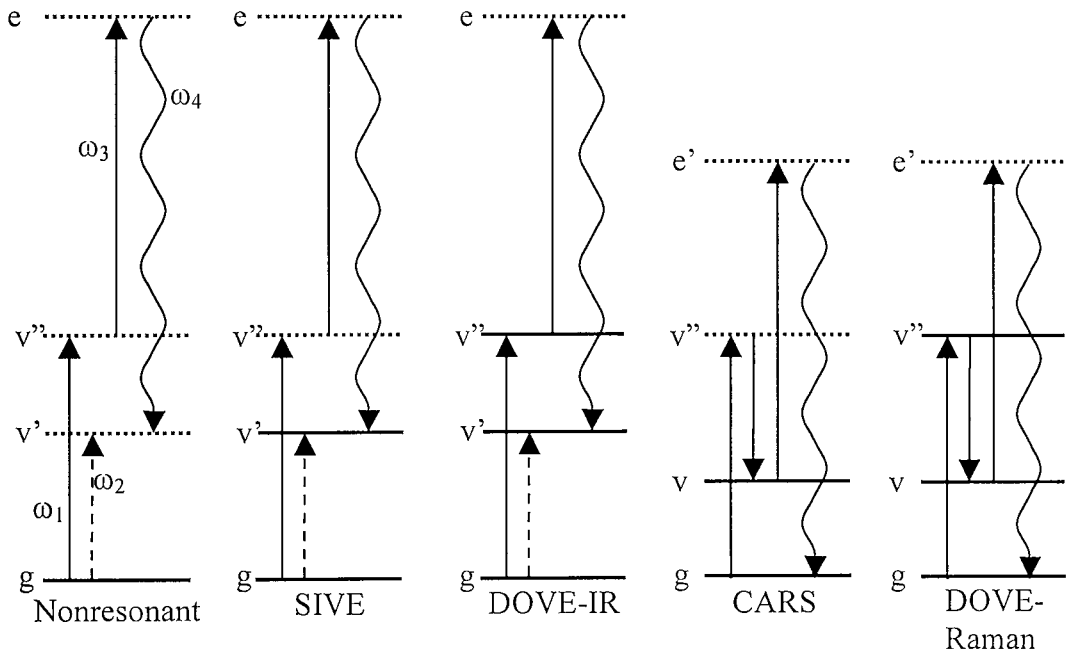


Figure 4.35. WMEL diagrams of various signal components, a repeat of figure 2.4.

involved in a coherence with two levels, resonant or nonresonant. In this regard, the signal levels from these processes should, in the absence of the quantum number dependence of dephasing discussed in Chapter 2, be symmetric around the $t_{12} = 0$ axis. No data as to the dephasing rates exist in the literature for the case of propanol, but it has been noted in the case of acetonitrile that the experimental and simulated linewidths for the $\nu_2 + \nu_4$ combination band is ~50% larger than that of the ν_2 fundamental, so that the combination band is significantly shorter-lived. It is also worth considering the time ordering of the pulses for the CARS and DOVE-Raman pathways: the initial excitation must be at the higher frequency to create the coherence from which the ket side of the wavefunction must originate for the second interaction.

If, as in the neat D_2O plot, the interactions are purely nonresonant, then only the diagram showing the nonresonant scheme is relevant, assuming no other coherence pathways which contribute. If however there is any one resonant level, as in the case of the propanol plot, the situation is somewhat different. In propanol, the frequencies have been set for the propanol fundamental and combination bands, so that the nonresonant, SIVE, and DOVE-IR pathways are viable for producing signal. However, because of the anharmonicity, CARS and DOVE-Raman contributions will not be significant—a point that will be further explored in Chapter 5. More about the asymmetry of the temporal 2-D plots could be ascertained with the ω_1 and ω_2 values set for the values necessary to induce the CARS and DOVE-Raman pathways. In such an experiment, the signal should be significantly higher in the region which, in the plots presented here, is virtually free of signal outside the pulsewidth.

The similarities between these temporal data for three different samples might suggest that the phenomena observed are a consequence of interactions occurring in the sample cell windows, which for all the samples were 2 mm thick CaF_2. However, the vast difference in the ω_1 frequency between figures 4.36/7 and 4.38—from ~4400 cm^{-1} to ~2100 cm^{-1}—rules out any unwanted nonlinear effects in the windows which are frequency dependent or even dependent on the difference frequency between the excitation beams ω_1 and ω_2, such as CARS, etc. It is postulated that the qualitative features of these 2-D plots can be explained by stimulated Raman processes, which are less dependent on the absolute frequencies or the higher-lying states in the vibrational energy level structure of the sample. The

features have a periodicity on the order of ~1.5 ps, corresponding to very low vibrational frequencies (~22 cm^{-1}). A final consideration which may shed some light on the functional form of these 2-D temporal data is the possibility of temporally chirped pulses. Pulses stretched in time would surely lead to broadening of features in temporal space, but it is also worth considering in the case where a pulse sequence could excite both DOVE-IR and DOVE-Raman pathways, that differing arrival times of spectral components of the pulses would complicate the temporal spectra greatly.

While these data are an interesting study of the temporal response of DOVE signals, the initial plan to compare these 2-D spectra as an aid to determining the timing pair best for the amino acid studies was effective only in choosing the time ordering of the pulses. However, for detailed studies of the effects of the presence of amino acids in D_2O, it was clear that broad scans in time would not be sufficiently informative.

4.9. Dilutions in D_2O

Having assessed the DOVE methodology and vastly improved signal reproducibility, the next step towards the study of more complex molecules was to acquire DOVE spectra of amino acids. However, to this point, only experiments in neat propanol as outlined in section 4.2 had been accomplished in the near-infrared wavelength regime. The lessons learned from repeating the propanol experiments, and especially the earlier dilutions of acetonitrile in toluene, had suggested that the reproducibility of the magnitude and the shape of the background could be a limiting factor in the acquisition of DOVE spectra of relatively dilute amino acids. The solutions of the first amino acid, alanine, were at a concentration of 1.9 M, as opposed to the neat propanol, with a molarity of 13.4 M. A central question as to the signal sizes was the degree to which the signal would vary linearly with concentration. Prior experiments had shown that the signal was in the regime of linearity in concentration for an solvent:acetonitrileby ratio of 5:1. This molar fraction of acetonitrile corresponds to a molarity of ~1.8 M, very close to the projected concentration of alanine. But the concentration of the solute alone is not a sufficient criterion for estimating the signal sizes. Instead, the approximate concentration calculated to be analogous to the amino acid case was determined by integrating the area under the propanol FTIR absorption spectrum for the two directly pumped modes and determining the dilution necessary to make the sum of

these integrated oscillator strengths equivalent for both cases. This calculation yielded a value of 6:1 mol:mol concentration of D_2O to propanol. It was decided to then make a series of dilutions of propanol in D_2O to observe the difference in peak heights and positions as the solutions progressed from neat toward this value. Figure 4.40 shows a set of spectra for these dilutions where ω_2 is fixed at 1526 cm^{-1}, a value away from the propanol resonance value of 1458 cm^{-1}. This was to avoid the strongly dispersive lineshape closer to the resonance. It was known that the signal was still strong at this ω_2 value, though the peak was shifted as shown in figure 4.27.

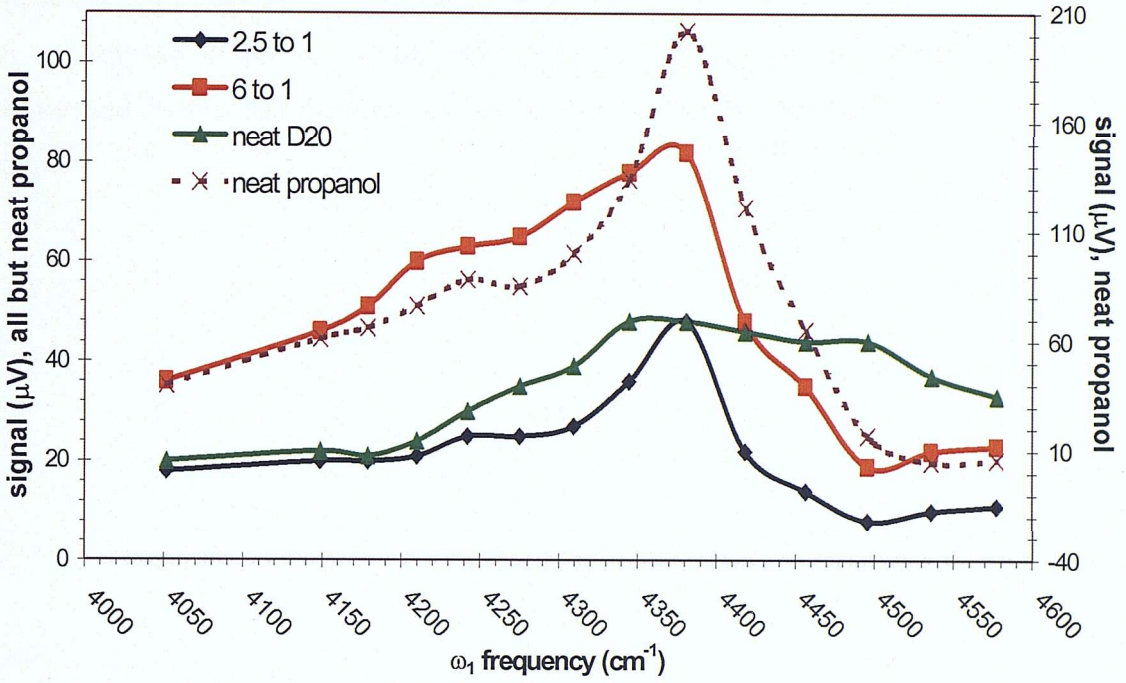


Figure 4.36. DOVE spectra with ω_2 fixed at 1458 cm^{-1} of successive dilutions of propanol in D_2O, starting with neat (dashed purple), 2.5:1 mol:mol (blue), 6:1 (red), and neat D_2O (green). The signal near 4380 cm^{-1} is discernible in all the solutions containing propanol.

The traces for both neat propanol (the same as the 1526 cm^{-1} spectrum from figure 4.27 and scaled down for comparison to the other spectra) and neat D_2O are shown for comparison. It is clear that the D_2O signal will contribute a great deal to the overall measured signal, and that the background, particularly for the short pathlength of 10 μm, could be expected to vary from sample to sample more than predicted by just a change in D_2O concentration. The interference from the background can be seen in the dilutions and makes the absolute determination of signal size difficult but it can be seen qualitatively that the peak is still clearly visible

at the 6:1 dilution. This result was very promising for the upcoming experiments on amino acids.

4.10. Concluding remarks

The experiments to this point had provided confidence in the methodology and highlighted a number of sensitivities of the technique to various experimental parameters, particularly for the cases of dilute solutions and thin samples. These sensitivities and the irreproducibility that they manifest were overcome with the knowledge gained during the experiments detailed in this chapter. Careful sample preparation and signal optimisation protocols were instituted, resulting in greatly improved reproducibility. With the benefit of the various experiments on propanol, an appropriate frequency range, pulse ordering, and signal size estimate for the amino acid studies had been found. These studies will be presented in the following chapter.

5. Further DOVE Results: Amino acids and polypeptide

5.1. Introduction

The experiments outlined in Chapter 4 provided confidence in finding DOVE spectral features from solvated amino acids as well as a spectral region in which to search and an understanding of the effects of various experimental variables and sensitivities of the results to them.

This chapter opens with a discussion of the amino acids chosen for these studies and the specific modes that were investigated. Each sample in turn is presented with FTIR spectra of the spectral space around those modes.

The following section outlines the attempts to locate a verifiable DOVE signal. While many of the experimental parameters such as excitation wavelengths and pulse ordering had been set using the knowledge gained from the experiments outlined in the previous chapter, it was known that several of the available experimental parameters were yet to be explored in the amino acid case, and the variation of the obtained spectra as a function of these parameters will be presented.

The next sections detail the 2-D DOVE spectra that were acquired once the final set of parameters had been determined. While some band assignments can be easily made, others are more tentative, as these data represent the first-ever 2-D IR spectra of amino acids in the "off-diagonal" region (with ω_1 far from ω_2 in frequency). However, the purpose had been to this point only to acquire the spectra in a number of different samples and compare their qualitative aspects. While the assignments made here represent hypotheses based on the linear IR assignments in the literature as well as the new 2-D spectra themselves, the band assignments were of secondary interest while determining the density and rough placement of spectral features in this portion of 2-D spectral space.

5.2. Survey of amino acids and solvents

Samples of all 20 of the naturally occurring amino acids were purchased from Sigma-Aldrich and investigated as possible samples for the DOVE experiments. The

spectral region corresponding to aliphatic modes in the amino acid side chains had already been identified as experimentally convenient, and the preliminary work carried out on propanol was focused on this region. However, this was the first foray into DOVE spectroscopy on molecules any more complex than the simple liquids presented thus far, and every effort was made to ensure that the resulting signals would be as high as possible. For this case, that implied solutions as concentrated as possible, which in turn suggested very high amino acid solubility in the given solvent. The end result was to use alanine, arginine, glycine due in part to their high solubility, but also due to the fact that some of their aliphatic vibrations were identified from a number of reports in the literature or easily determined from FTIR spectra. By extension, a study of the 2-D DOVE spectrum of polyalanine in solution is presented and compared to that of alanine for a first look at the effect of secondary structure and local environment on these side chain vibrational modes.

5.2.1. Choice of solvent

Although results had already been published demonstrating the power of DOVE spectroscopy to extract coupled features even when the excited modes existed under a strong absorption band of the solvent,[41,49] the intention was to make the discovery of the first amino acid signals and prediction of future ones as uncomplicated as possible. This necessitated careful analysis of the linear infrared spectra, so solvents whose absorption bands obscured the modes of interest were therefore avoided. Avoiding the strong absorption bands of the possible solvents also reduced the pre-resonant background on which the signals would appear. The 20 amino acids that were tested for solubility were dissolved in distilled water, deuterated water, ethanol, chloroform, ethylene glycol, and carbon tetrachloride. FTIR spectra were acquired of the resulting solutions, searching for the highest absorbance to background ratio for the planned absorptions. Water was eventually chosen, both for solubility concerns and because of its ubiquity as a solvent in biological applications, so that the results obtained could be carried forward to progressively more complex molecules without the need to consider further solvent/solvation/background issues. The remaining question was whether to employ H_2O or D_2O, but H_2O's strong H-O-H bending mode at 1640 cm^{-1} decays on the low-frequency side to a high background, as shown in figure 5.1, obscuring the

aliphatic fundamental deformation modes in the 1500 cm^{-1} region. It was for this reason that D_2O was chosen as the solvent for all of the spectra presented in this chapter.

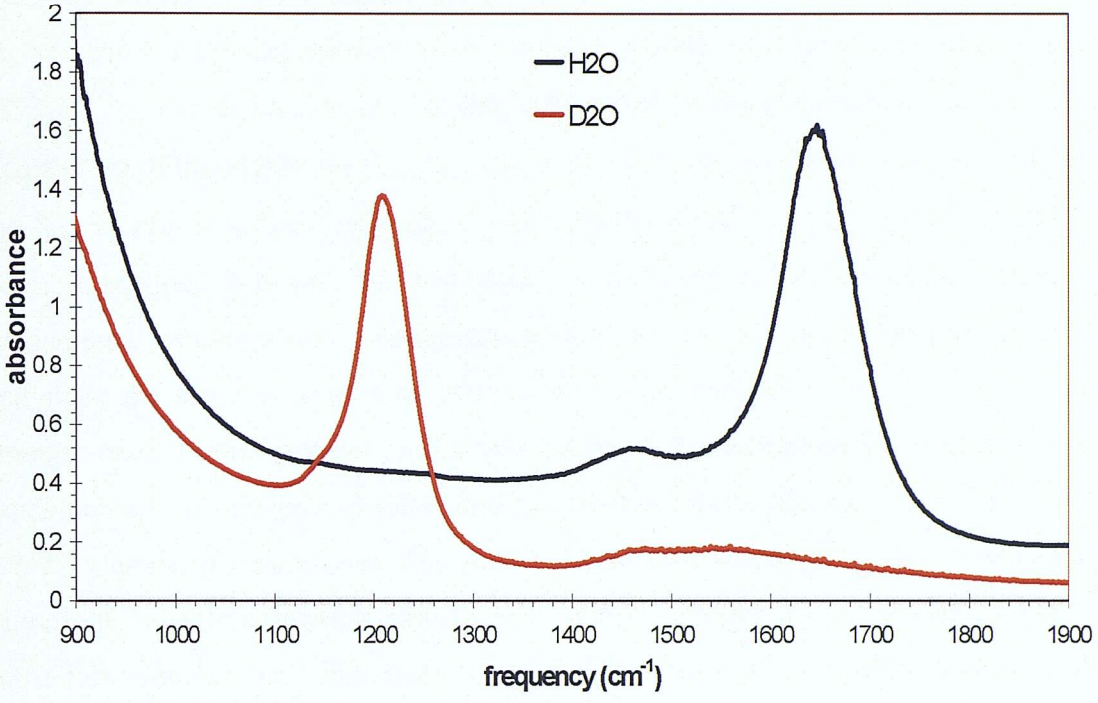


Figure 5.1. FTIR spectra of H_2O and D_2O. It is clear that the absorption in the region of CH fundamentals is significantly higher in H_2O, leading to higher pre-resonant background.

5.2.2. Sample preparation

Amino acids were obtained in crystalline form and used without further purification. These amino acids, all of >99% purity and in the levorotatory form, were ground with a mortar and pestle and added to deuterated water (D_2O, >99.5%, Sigma-Aldrich) until saturation had been reached. This was accomplished at room temperature, adding more amino acid crystals until no more dissolved upon manual shaking. No buffers were used in the course of the amino acid studies, and it is worth noting that the local pD of these amino acid solutions is unknown.

5.3. Overview of the relevant amino acid absorptions

5.3.1. Absorptions of L-alanine and poly-L-alanine – methyl groups

In alanine, the side chain is a methyl (CH_3) group, and the initial focus when trying to acquire DOVE signals from alanine was on the coupling between the asymmetric bend or deformation mode $\delta_a(CH_3)$ at 1465 cm^{-1} and its overtone $2\delta_a$ at 2893 cm^{-1}. The anharmonicity of this vibrational progression can be seen in the frequencies of the vibrations ($2 \times \delta_a - 2\delta_a = 37$ cm^{-1}), but moreover, the proximity of the $2\delta_a$ vibration to the fundamental symmetric stretch ν_a at 2949 cm^{-1} creates a Fermi resonance between the two modes. A Fermi resonance occurs when a fundamental vibration and a combination band or overtone are close in frequency and share the same symmetry of vibration.[52] The result is a sharing of oscillator strength (usually the overtone or combination band is enhanced at the expense of the fundamental), and the pair of vibrations is known as a Fermi doublet. For the case of DOVE signals, it was known that one of the excited transitions required a double vibrational quantum number change, and both overtones and combination bands fulfil this requirement. The attempt was made to scan in the region around these modes, in fact, prior to all of the propanol work presented in Chapter 4. It was only later that the decision was made to extend the work to the near-infrared region where combination bands involving the aliphatic modes had been identified. Figures 5.2 and 5.3 show the FTIR spectra of alanine in the regions around δ_a and $2\delta_a$.

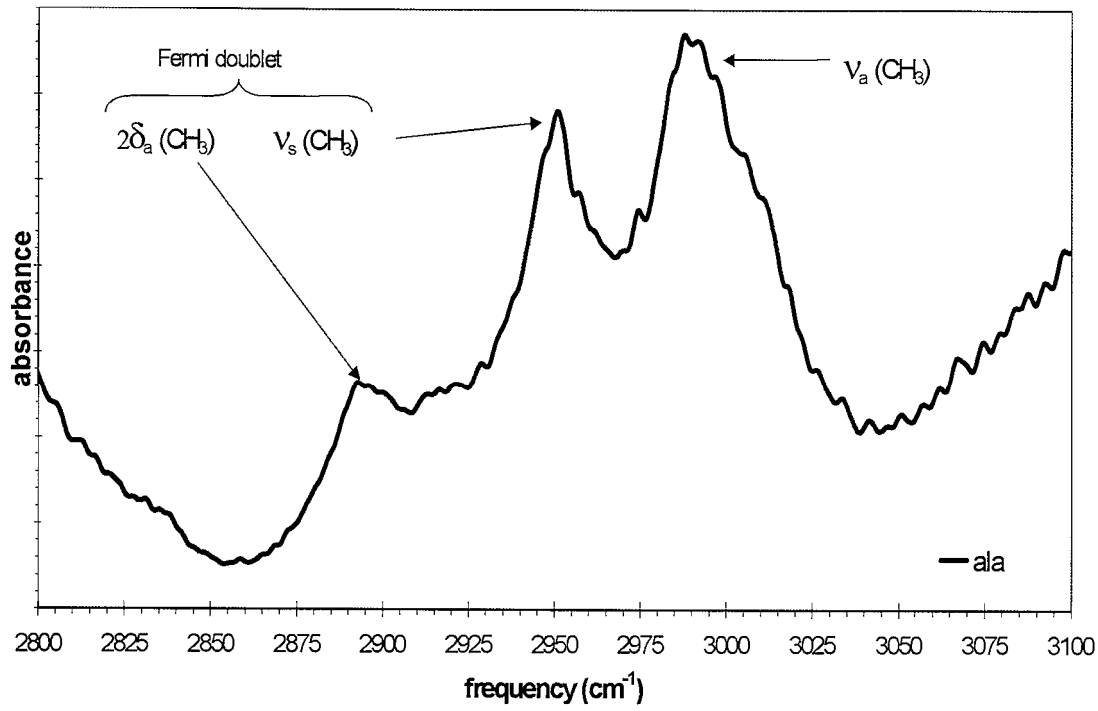


Figure 5.2. FTIR spectrum of alanine in the region of the Fermi-enhanced overtone of the methyl bend.

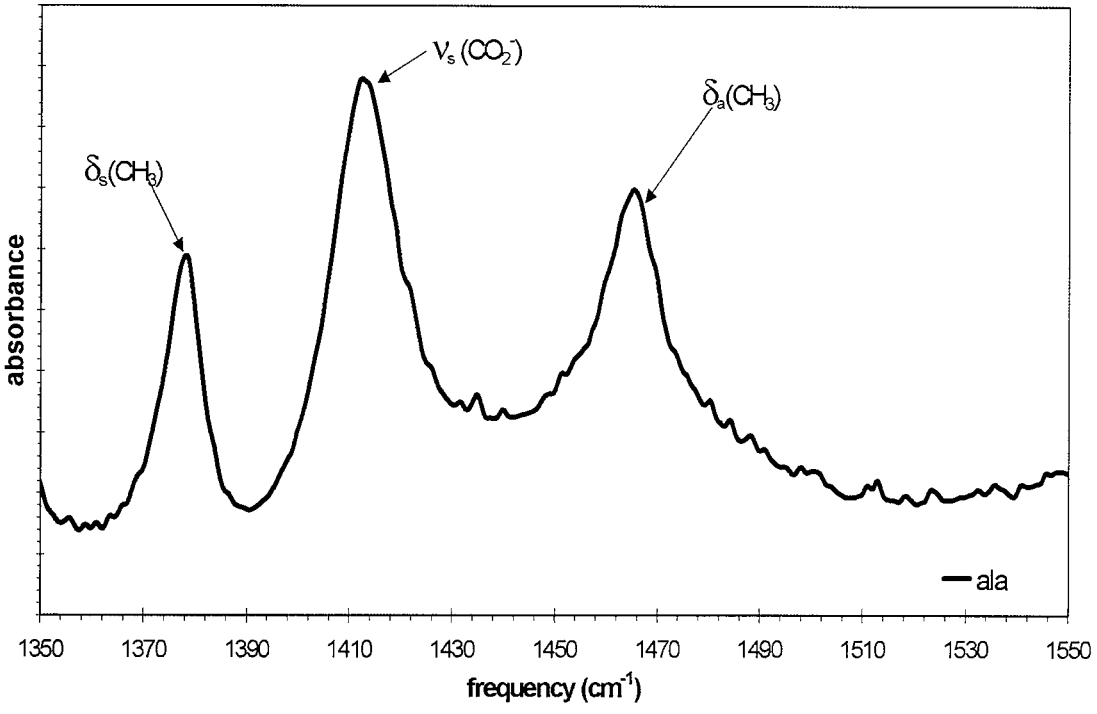


Figure 5.3. FTIR spectrum of alanine in the region of the fundamental of the symmetric and asymmetric methyl bend.

The next approach to discover a DOVE feature for these moieties was to focus on the coupling between the one of the asymmetric stretch modes, $\nu_a(CH_3)$, and the same asymmetric bend δ_a at 1465 cm^{-1} via a combination band near the sum of their fundamental frequencies. The ν_a appear at two frequencies, $\nu_a^{(1)}$ at 3008 cm^{-1} and $\nu_a^{(2)}$ at 2989 cm^{-1}, because the CH_3 stretch vibration's degeneracy is broken somewhat in solution. A combination band had been identified in the literature,[53] but its oscillator strength was ~6 times lower compared to the modes comprising the Fermi doublet. The FTIR spectra of alanine and polyalanine in the combination band region of the ω_1 scan are compared in figure 5.4.

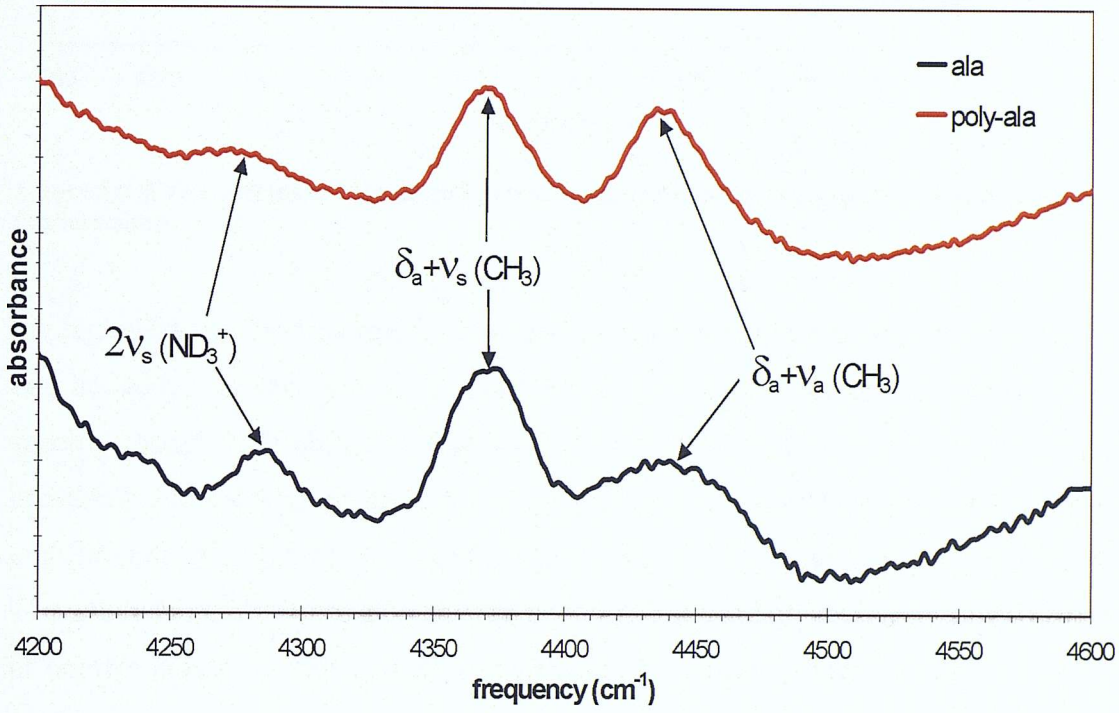


Figure 5.4 FTIR spectra of alanine and polyalanine in the combination band region of the ω_1 scan.

The most significant difference between these spectra is the narrowing of the broad combination band centred at 4438 cm^{-1}, which in alanine is probably made up of both $\nu_a^{(1)} + \delta_a$ and $\nu_a^{(2)} + \delta_a$. FTIR spectra in the region of the ν_a fundamentals (not shown) exhibit a marked reduction of the $\nu_a^{(1)}$ absorption in the case of polyalanine, presumably due to environmental changes around the methyl group inducing a reduction in the degeneracy splitting. With that in mind, the combination band in the polyalanine spectrum above is then largely $\nu_a^{(2)} + \delta_a$. The FTIR spectra in

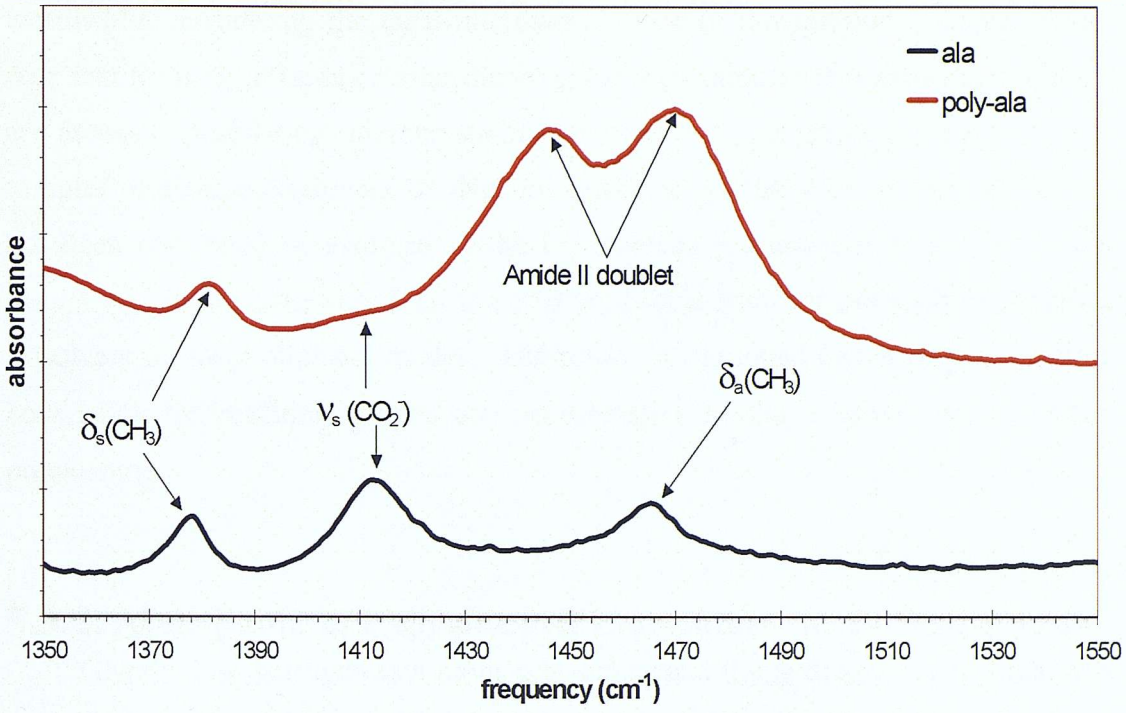


Figure 5.5 FTIR spectra of alanine and polyalanine, again in the region of the methyl bend fundamentals.

the region of the deformation fundamental ω_2 scan are shown in figure 5.5. Here it can be seen that the symmetric bend remains much the same size between the spectra, though it is shifted a few wavenumbers higher in frequency and appears broader in the polyalanine spectra. The asymmetric bend at 1465 cm^{-1} in alanine is undifferentiated in the polyalanine spectrum because of the rise of the amide II band. The amide II band is normally a single combination band arising from the formation of peptide bonds and comprises mostly the in-plane bend δ(NH) and stretch ν(CN). In this case, the band appears as a doublet because of coupling between ν(CN) and $\delta_a(CH_3)$ and is known to occur in polyalanine in D_2O at 1444 and 1476 cm^{-1}.[54] Finally, the asymmetric stretch of the COO^- group disappears almost completely for the polyalanine case, because this moiety has been incorporated into peptide bonds between the alanine residues and exists only at the end of each polymer.

One of the more exciting prospects for DOVE spectroscopy is the determination of the effects of secondary structure in solution. Polyalanine is known to form α-helices at room temperature,[55] and it was hoped that the comparison of the DOVE spectra of alanine and polyalanine would be a first step to implementing DOVE spectroscopy as a secondary structure analysis tool. However, because the sample of polyalanine as obtained was made up of chains of n~36 residues, it is

worthwhile considering the local microscopic state of the solution. Koçak *et. al.*. note that for n>5, infrared circular dichroism studies indicate that association effects are at work, postulating microcrystalline or even liquid crystalline phases in their samples of alanine oligomers.[56] Nevertheless, though the state of aggregation has not been controlled or assessed in the experiments presented in this chapter, the results will show at the very least the effects of local environment such as exposure to solvent on these aliphatic modes. The reader is cautioned that it remains unclear how much the resulting spectra are representative of the α-helical nature of the polyalanine.

5.3.2. Absorptions of L-glycine and L-arginine – methylene groups

Glycine's single hydrogen atom side group and the hydrogen from the amino acid backbone constitute a methylene (CH_2) group. Together with arginine's triplet of methylene groups in its alkyl side chain, glycine and arginine lent themselves to a comparative study of the aliphatic modes explored in alanine and polyalanine. Figure 5.6 plots the absorptions of glycine and arginine in the combination band region of the ω_1 scan.

The glycine spectrum shows a splitting of the combination band due to a pair of

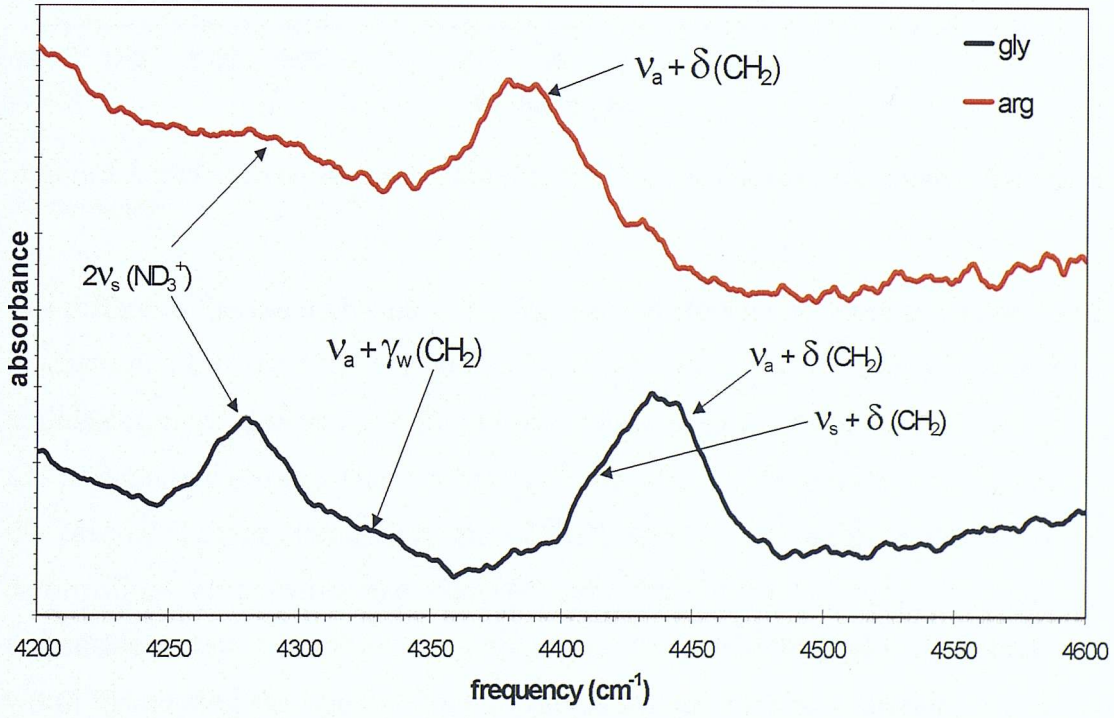


Figure 5.6. FTIR spectrum of glycine and arginine in the combination band region of the ω_1 scan.

methylene bending vibrations or "scissors" modes $\delta(CH_2)$, shown in figure 5.7. This mode displays two peaks in the solid phase spectrum, and the 2-D DOVE spectrum of glycine will bear out the nature of this splitting. Aside from the deuterated amine vibration near 4280 cm^{-1}, the only labeled vibration in arginine in this region is the combination band comprising the asymmetric stretch ν_a and the bend δ. It is quite broad, ~40 cm^{-1}, due to the varying environments of the three methylene groups in arginine's side chain. The spectral region for the ω_2 scan around the deformation fundamentals is shown in figure 5.7.

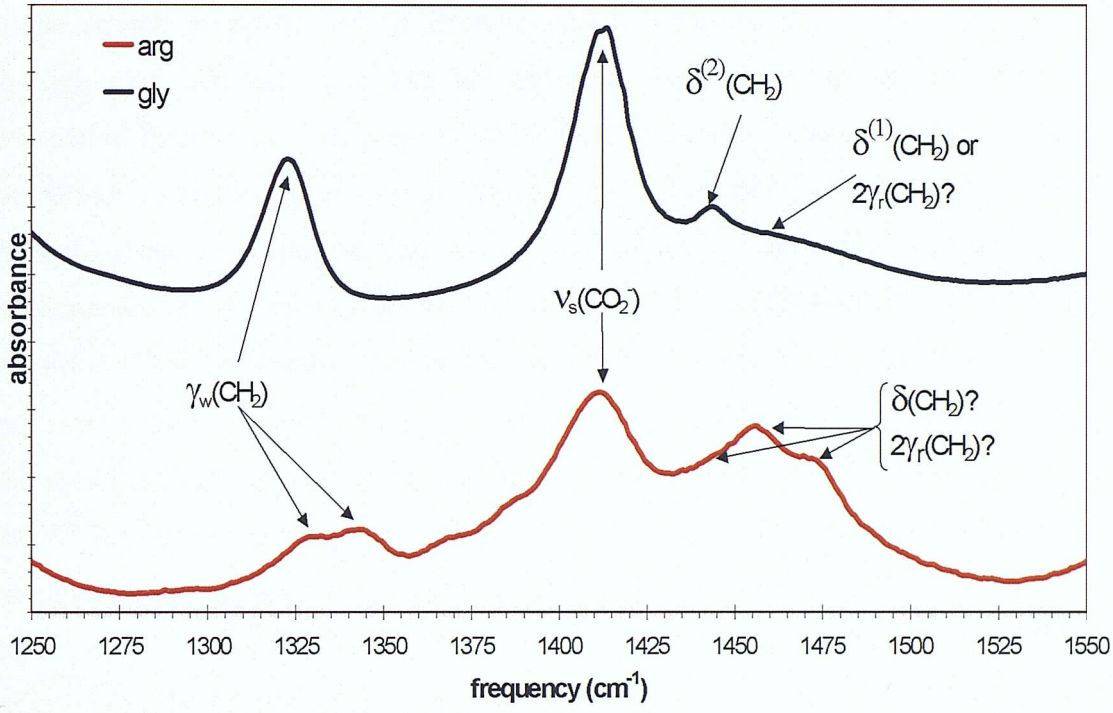


Figure 5.7. FTIR spectra of arginine and glycine in the fundamental deformation mode region of the ω_2 scan.

The difference between glycine's and arginine's methylene scissors and γ_w or "wag" modes near 1450 and 1325 cm^{-1} respectively are clear. The splitting of the peaks in arginine is again due to the differing environments of the three methylene groups, and a secondary scissors mode is seen as a shoulder on the glycine peak. Again, in the case of arginine, the assignment of the modes in the region of the methylene deformations is tentative and deduced from the DOVE spectra. It would be reasonable to expect a splitting resulting in as many as three peaks. However, it is worth mentioning that the overtone of the methylene rocking vibration $2\gamma_r$ may be present in the same spectral region. Limitations on the low-frequency side of the

sample cell windows preclude direct observation of the fundamental of this mode in the arginine samples. It normally occurs at 724-1174 cm^{-1} and is known to couple to adjacent methylene groups,[57] so it is quite likely that this mode could become more apparent in the DOVE spectrum than it is in the linear spectrum. Moreover, the feature near 1460 cm^{-1} in the glycine spectrum could equally be this overtone, and will be addressed with reference to glycine's DOVE spectrum.

5.4. Studies toward a $\delta_a/2\delta_a$ DOVE feature

The first attempts to locate a DOVE peak from alanine focused on the coupling of the stretch mode δ_a and its Fermi-enhanced overtone $2\delta_a$. This presented a possible new difficulty that had not yet been encountered in the experiments: destructive interference between the DOVE-IR and DOVE-Raman processes. For the perfectly harmonic case of a fundamental and its overtone, these processes are of identical frequency and overlap, creating a coherence between the ground and fundamental mode's energy levels both directly (DOVE-IR) and via a Raman-like transition (DOVE-Raman). The theoretical development of the nature of the signals produced shows that the terms in the expansion of the third-order susceptibility $\chi^{(3)}$, and thus the fields created in the sample, are out-of-phase for the DOVE-IR and the DOVE-Raman processes.[23] Therefore in the harmonic case, the signals are of equal magnitudes but opposite sign, complete destructive interference occurs, and there is no net signal. However, when any anharmonicity is introduced, the overlap of these processes at the fundamental's energy level is not perfect. Thus, the signals become out of phase, and the interference is very sensitive to the degree of anharmonicity. This situation is depicted in figure 5.8. In the left half of the figure, a purely harmonic system is depicted, where both DOVE-IR and DOVE-Raman processes can occur at the same frequency pair, culminating in a coherence between the ground state and the fundamental's energy level by two different coherence pathways. These signals will be of equal magnitude in the absence of pure dephasing, but will be of opposite sign and thus interfere destructively. In the right half of the figure, a small amount of anharmonicity Δ is introduced, and the first excitation is at $(2 \times \delta - \Delta)$. For the first case, DOVE-IR signal is created, but the corresponding DOVE-Raman process will not occur until the second excitation is lower in energy by Δ. The smaller the anharmonicity, the closer these signals will be in ω_2 frequency

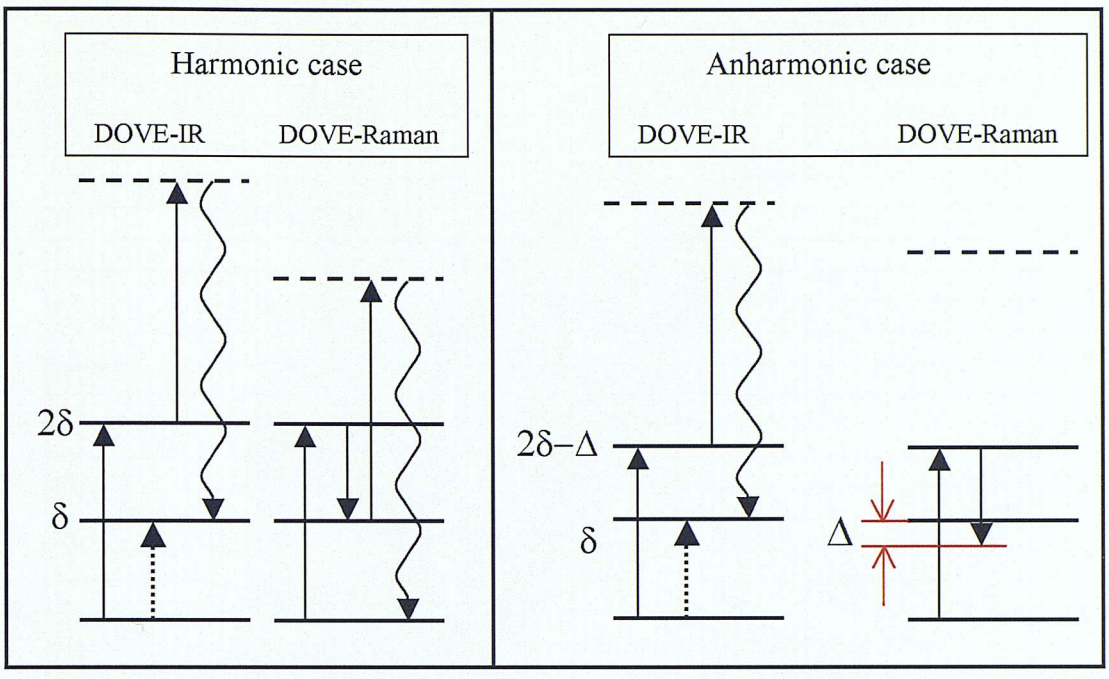


Figure 5.8. WMEL diagrams depicting harmonic and anharmonic energy level progressions. In the harmonic case, the pathways for DOVE-IR and DOVE-Raman overlap at the fundamental band's energy level; in the anharmonic case the two pathways are not simultaneously viable for the case of narrow-band excitation.

space and the more likely that they will interfere, changing lineshapes or perhaps obscuring the signal from both processes entirely. In the narrow-band excitation case, however, a large anharmonicity and thus a large spectral separation of the DOVE-IR and DOVE-Raman peaks suggests that the two processes will not be simultaneously excited and thus will not interfere.

It has been shown that if pure dephasing is not negligible, the relative contribution from each of these processes changes and the interference is not complete.[58] Different coherence pathways contributing to the interfering signal components involve different dephasing rates, so that it is quite possible that different pairs of delays would change the level of destructive interference, resulting in a measurable signal. To this end, another set of temporal 2-D data was acquired at the frequency pair 2890/1465 cm^{-1}, which is presented in figure 5.9. The most interesting aspect of this contour plot is the existence of a peak at the timing pair t_{12}= -2.17 ps, t_{23} = 1.63 ps. Here, the fundamental arrives first, followed by the visible beam 1.63 ps later, and the overtone arrives last after 0.54 ps. It is not surprising that there is a signal component here, as the overtone arrives before the visible pulse has decayed appreciably (given a FWHM pulsewidth of ~1.4 ps). It is however surprising that this should result in a peak fully outside the time diagonal (this dia-

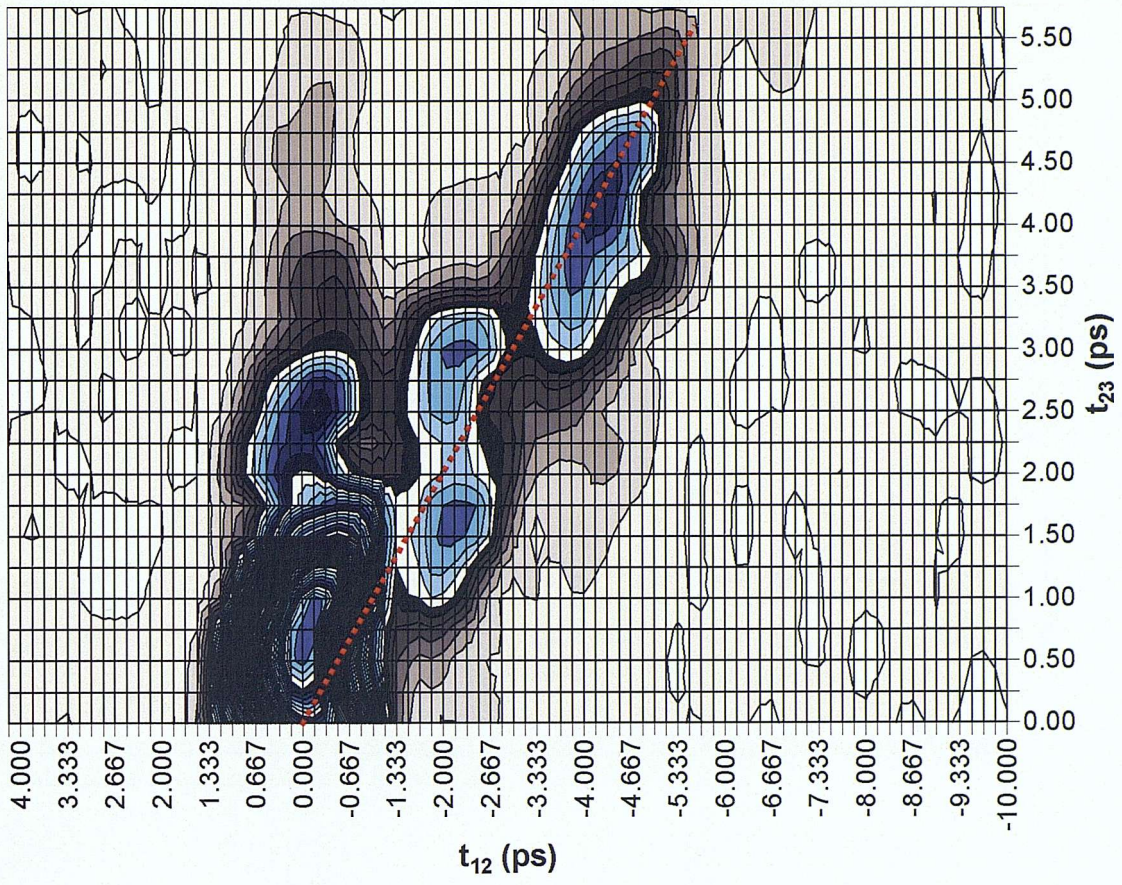


Figure 5.9. Temporal 2-D plot of the signal from an alanine/D_2O solution with ω_1 fixed at the methyl bend fundamental and ω_2 fixed at the Fermi enhanced overtone. Note that features exist below the diagonal line, corresponding to case (c) in figure 4.33.

gonal separates case (**b**) and (**c**) in figure 4.35), seeming to suggest a rephasing of the signal after the arrival of the visible pulse. In no other set of temporal data has this phenomenon been seen. In both the propanol and the D_2O data, the signal exists for all t_{23} fully inside this boundary, whereas for this case, even the signal at late t_{23} (>4 ps) is symmetric about the diagonal. The monotonic decay along the diagonal seen in the propanol and D_2O spectra is very different here; the peaks along t_{12} = -2.17 and the broad peak along the diagonal centred at $t_{12} = t_{23} \sim$ 4ps are of the same height, about 20% of the value of the main peak, showing an oscillatory behaviour along this diagonal. It is instructive to study a few slices of this contour plot for fixed t_{12} at the different pairs of peaks, t_{12} = 0, 2.167, and 4.333 ps, shown in figure 5.10.

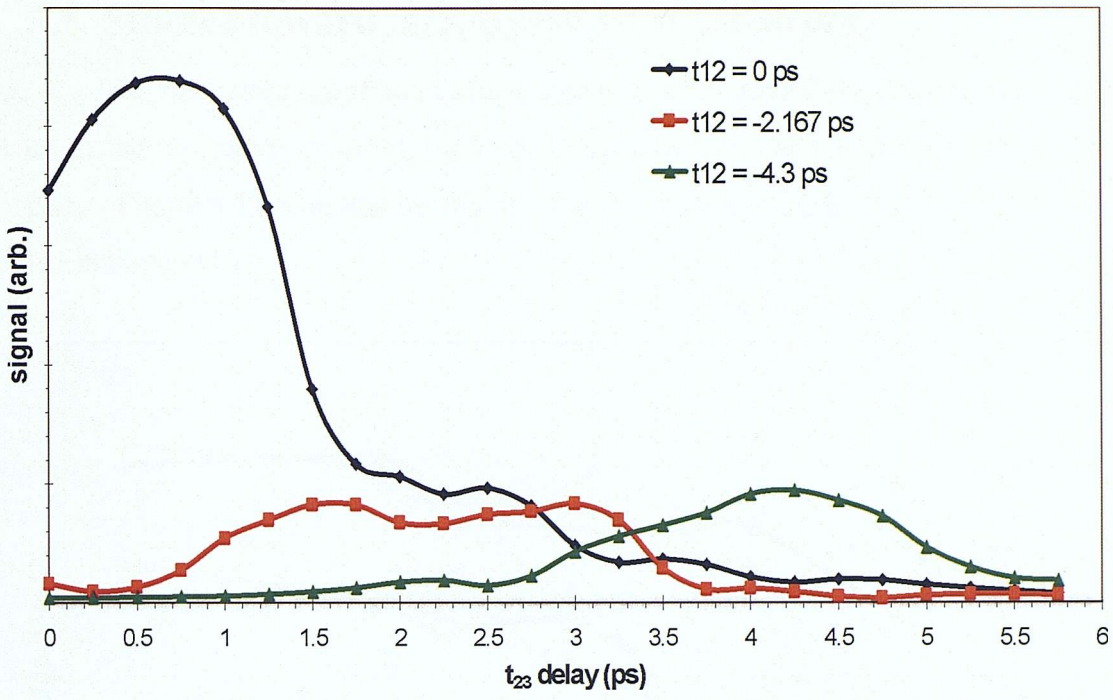


Figure 5.10. Temporal slices through figure 5.9 for fixed values of t_{12}, showing the presence and evolution of two components of the signal.

At t_{12}=0, there is a major and a minor peak, separated by ~1.75 ps. In the following traces, these peaks shift their relative heights but remain separated by the same t_{23} delay. It seems quite plausible that these peaks represent the DOVE-IR and DOVE-Raman pathways, that the t_{12} delay sets their relative phase, and that the t_{23} scans are sampling the same points of constructive interference. In this case, the later peak represents a coherence pathway which has a significantly longer overall dephasing time relative to the earlier peak; its intensity remains roughly the same for all t_{23}, suggesting the level-dependent dephasing discussed in section 2.2.7.

Based on the 2-D temporal scans, several delay pairs were chosen and ω_1 scans were acquired with fixed ω_2 in an attempt to find a DOVE peak. Despite the best efforts to locate a distinct (and crucially, repeatable) DOVE signal under these conditions, none was found. This pair of modes was for the time being abandoned to avoid the very sensitive interference phenomenon that was most likely minimising or obscuring the DOVE peaks. Instead, a new spectral region was considered, exploring the coupling between the bend fundamental and a combination band involving the bend δ and stretch ν of the methyl group.

5.5. Studies toward a $\delta_a/\delta_a + \nu$ DOVE feature

The next attempts at acquiring a signal in an alanine/D_2O solution were to fix ω_2 at the resonance value of 1465 cm^{-1} and scan in ω_1 at a number of fixed delay pairs. Figure 5.11 plots the results of these trials for a number of different t_{23} values (t_{12} is fixed at 0).

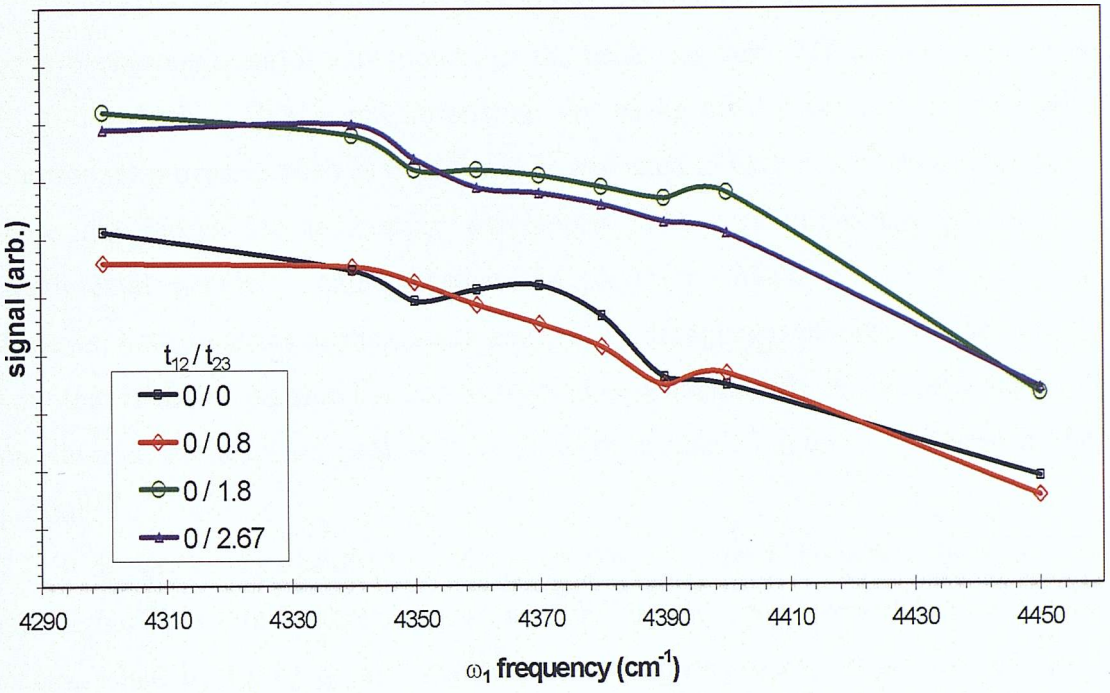


Figure 5.11. Scans in ω_1 to identify a DOVE peak in an alanine/D_2O solution for the fixed resonant ω_2 value of 1465 cm^{-1}. Different delay pairs are shown in the legend, and the clearest peak is at the delay pair (0,0).

It can be seen that the most distinct peak occurs at the delay pair (0,0), at the expected value of ~4370 cm^{-1}. Interestingly, all three of the other traces show a distinct spectral lineshape (both positively and negatively dispersive) on either side of the expected peak reminiscent of the dispersive lineshapes seen in propanol. Moreover, a comparison of these data with simulations of the lineshapes under varying background conditions[14] shows how this lineshape could be obtained. It is shown that for a real nonresonant background of magnitude +0.2 times that of the resonant contribution, a negative dispersive lineshape results (that is, the signal is below background level on the low-frequency side of the resonance and above it on the high-frequency side). For the case of a real nonresonant background which is - 0.2 times that of the resonant contribution, a positive dispersive lineshape results (the opposite case, and that seen in propanol). However, these simulations were

made for a constant background level throughout the scan range. In our case, the background is sloped toward the high frequency side, and therefore represents a different fraction of the resonant contribution as ω_1 is scanned. Under these conditions, the background could indeed cause the lineshape shown in the (0,0) trace, with dispersive character on both sides of the peak, though it is noted this would be an unlikely coincidence.

While the data show a distinct peak at the delay pair (0,0), it is not significantly above background, and it was found that the peak was very difficult to obtain on a day-to-day basis. This is not surprising; the background level for electronically nonresonant processes such as CARS can be expected to vary much more in the case where the pulses are temporally overlapped, and very slight changes to the experimental geometry could change the phase mismatch in the sample cell windows, both in terms of magnitude and real vs. imaginary character. Chen *et. al.* show that if the background is imaginary and constitutes 50% of the peak resonant contribution, the resonant peak will be perfectly cancelled and thus not seen in the spectra.[14]

It therefore was decided to find a delay pair far from (0,0) where the peak was both higher above the background and, most importantly, more repeatable. This was accomplished by fixing t_{23} and scanning t_{12}, comparing traces in alanine solutions with those obtained with neat D_2O. The most striking difference between the two was found for the case t_{23} = 3 ps, shown in figure 5.12. It can be seen that the two traces are nearly overlapped, but the first peak near t_{12} = -1 ps is significantly different, with the alanine contribution making the peak ~30% higher. With this in mind, spectra were taken with the delay pair (-1.0, +3.0 ps) in alanine solutions and compared with the (0,0) data and are shown in figure 5.13.

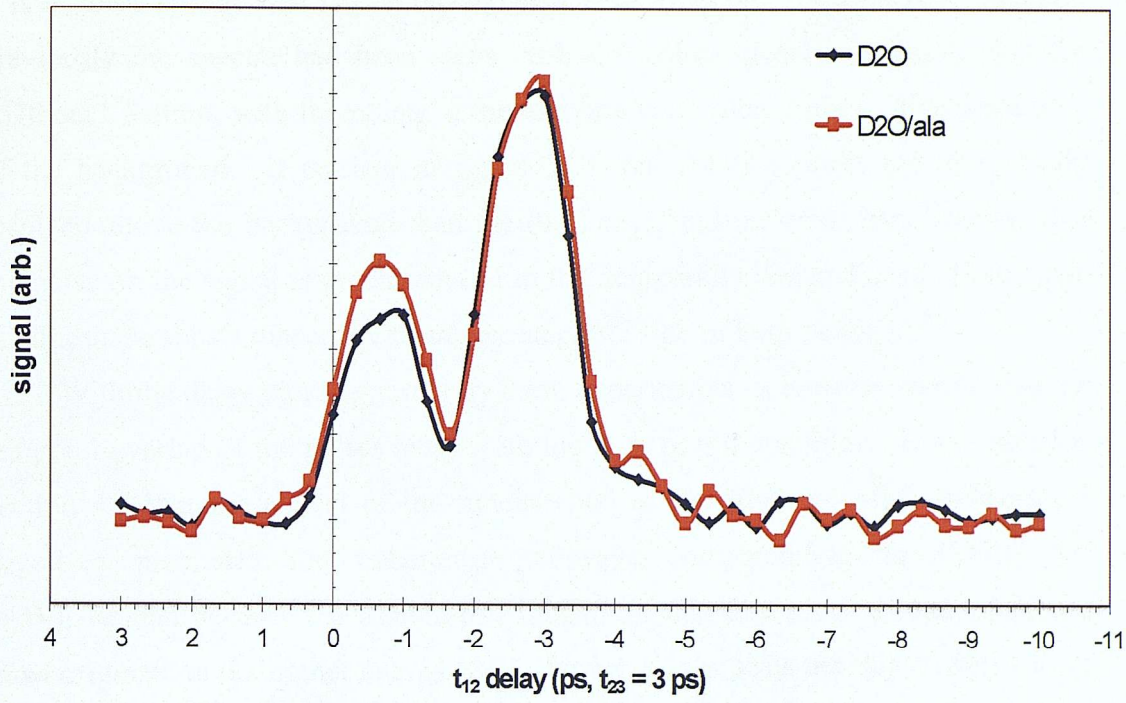


Figure 5.12. Traces showing the difference in the t_{12} temporal response of neat D_2O and an alanine/D_2O solution (at the frequency pair 4370/1465 cm^{-1} and with t_{23} fixed at 3 ps). The clearest difference is near t_{12} = -1 ps.

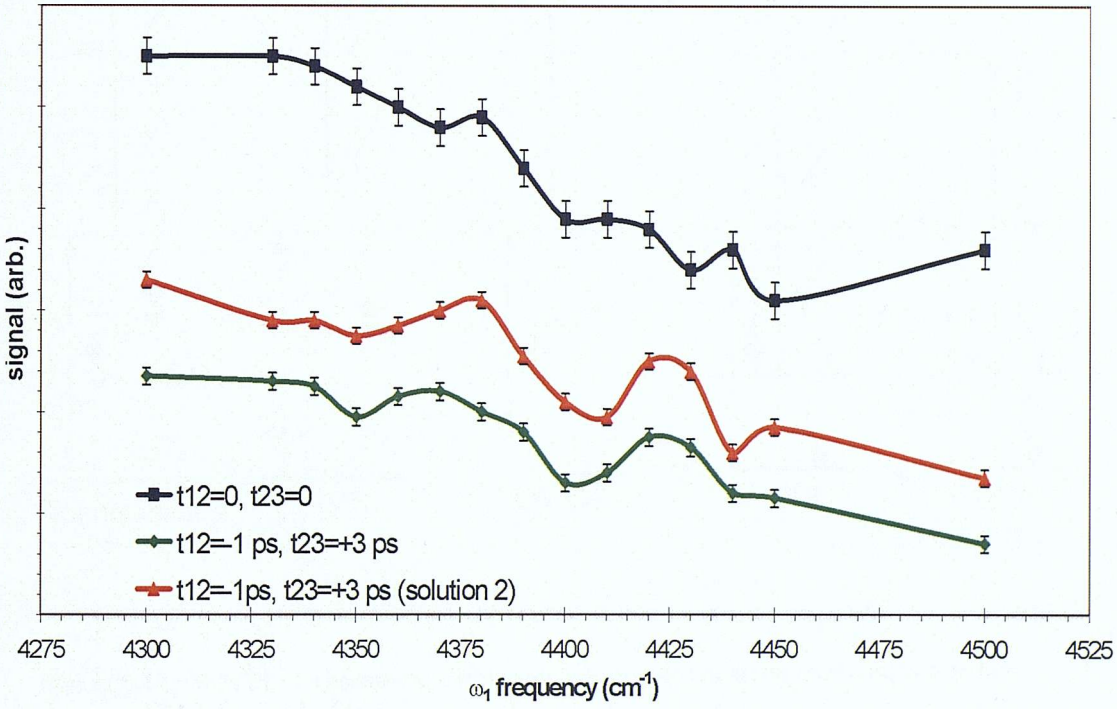


Figure 5.13. Comparison of 1-D DOVE spectra in alanine/D_2O (ω_2 is again fixed at 1465 cm^{-1}) for the pulse timings (0,0) and (-1, 3 ps). The pair of peaks in the detuned case are more above background and suffer from less noise.

It is in these spectra that the secondary peak near 4420 cm^{-1} first became apparent; previously the spectra had been taken with the points closely spaced around the 4370 cm^{-1} feature, with the points at the extreme ends taken only to give a measure of the background. It is clear in figure 5.13 that the two peaks are more easily resolved above the background than the (0,0) case, and the error bars bear out that the noise on the signal is much reduced in this temporally detuned case. Here again the lineshape shows dispersive character on either side of both peaks.

With the delay pair suggested by these experiments, it is worth considering the temporal overlap of the pulses away from the $t_{12} = t_{23} = 0$ condition. It was noted in section 4.8 that the arrival of the fundamental as the first excitation (when t_{12} is negative) precludes the coherence pathways corresponding to CARS and DOVE-Raman because the Raman-like transitions that create the second coherence must originate in the higher energy level. Figure 5.14 repeats the depictions of these pathways.

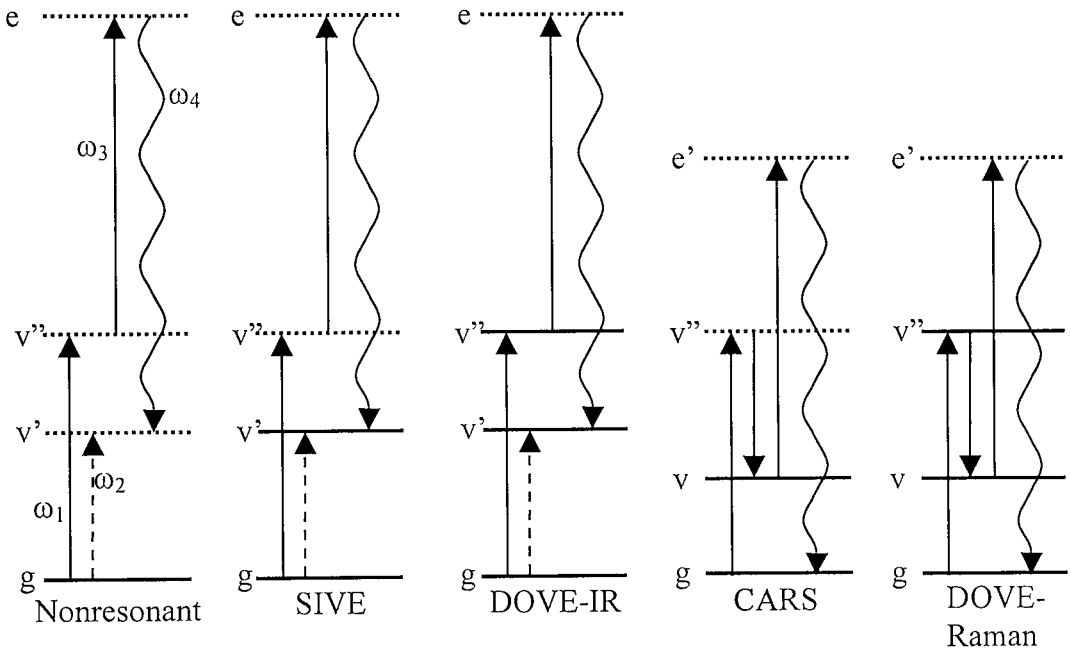


Figure 5.14. WMEL diagrams repeating the coherence pathways contributing to the measured signal.

It is instructive in this case to depict the pulses' overlap in order to see that these pathways remain viable, if somewhat suppressed by the delay conditions. This is shown in figure 5.15.

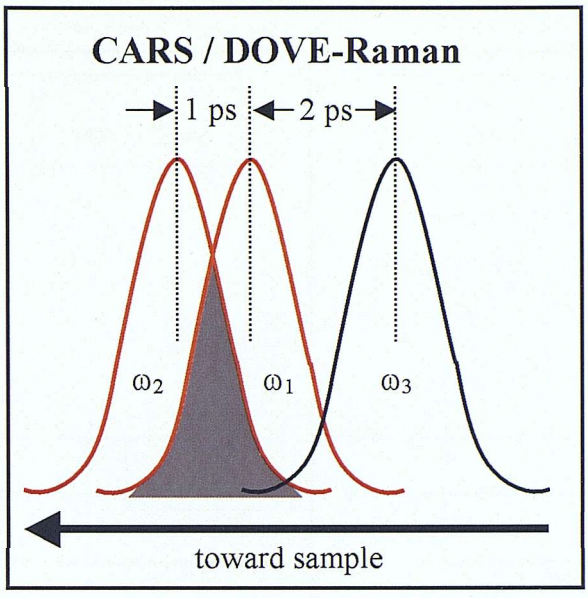


Figure 5.15. Diagram depicting the overlap of the excitation pulses for the delay pair (t_{12} = 1, t_{23} = 3 ps). The overlap is still significant, but the CARS and DOVE-Raman pathways only contribute during this overlap because of the Raman-like transition.

The pulses are depicted as Gaussian in time, and their separation is scaled to their width, assumed to be 1.4 ps (FWHM). It can be seen that there is still a significant pulse overlap at these times, and during pulse overlap both coherence pathways (ω_1 followed by ω_2 and vice versa) can occur. It is assumed in the cases where ω_2 is incident first, no signal from the CARS and DOVE-Raman pathways can contribute outside the decay of the ω_2 pulse.

A final consideration before the presentation of the 2-D spectra is the interference of DOVE-IR and DOVE-Raman processes. The frequency difference between these processes is related to the anharmonic shift between the fundamentals and any multiquantum transitions. This phenomenon has been encountered before, as in the anharmonic case of figure 5.8 but becomes most evident in the 2-D spectra. For clarity, the situation is schematically depicted in the WMEL diagrams of figure 5.16.

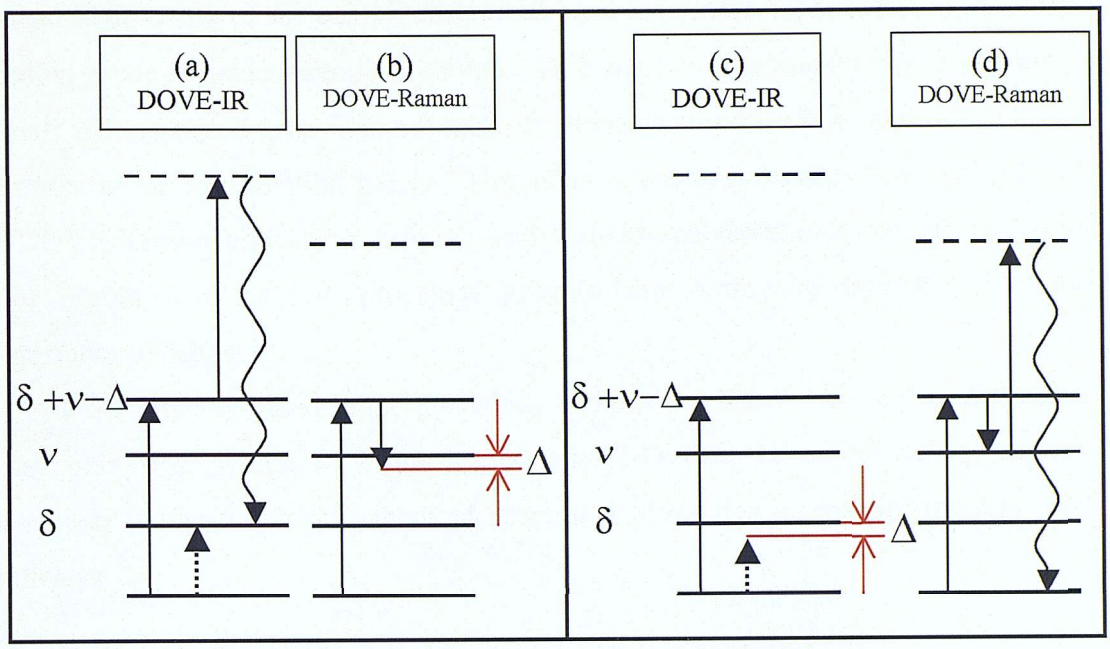


Figure 5.16. WMEL diagrams representing the different resonance conditions that give rise to the DOVE-IR and DOVE-Raman contributions to the signal. Here the anharmonic case of figure 5.8 is assumed.

The figure shows four cases in which the initial excitation is at the same frequency ω_1, the combination band $\delta + \nu - \Delta$, that is, a combination band of δ and ν that is lower in energy than the sum of the fundamental frequencies by Δ due to anharmonicity. In cases (**a**) and (**b**), the frequency of the second transition is resonant with the bending vibration, whereas in cases (**c**) and (**d**) it is less than this value by the anharmonic shift Δ. In the left half of the figure, DOVE-IR processes as case (**a**) dominate, because the frequency of ω_1 is resonant with the bending vibration δ, but in the corresponding DOVE-Raman process (**b**), ω_1 does not create a coherence between the combination band and the stretching vibration ν because it is too high in energy by the anharmonic shift. Conversely, the energy of ω_1 is too low in case (**c**) to create a coherence between the ground state and the bending vibration, but can create a coherence between the combination band and the stretching fundamental in the Raman-like case (**d**) because its energy is exactly $(\delta - \Delta)$.

An interesting consequence of the different coherence pathways by which these peaks are generated is the different energy levels that are being probed. In the DOVE-IR case (**a**), the peak location corresponds to couplings between the bending vibration and the combination band; the stretching fundamental is never directly

involved. By contrast, in the DOVE-Raman case (**d**), peak locations correspond instead to coupling of the combination band with the stretching mode ν, because the bending mode is never directly involved. Thus the two mechanisms by which these signals are generated give different but complementary information about the modes comprising the combination bands. This is an interesting parallel between DOVE-IR/DOVE-Raman and linear infrared and Raman spectroscopies, whose selection rules ensure that the two processes provide complementary information about vibrational structure.

The studies outlined in the preceding sections provided a spectral region and a delay pair with which to acquire spectrally 2-D data in amino acids, and an awareness of the rough placement of spectral features due to competing coherence pathways.

5.6. 2-D DOVE spectra of alanine, polyalanine, arginine and glycine

In the following subsections, 2-D DOVE spectra of the amino acids and polypeptide outlined in the opening sections of this chapter will be presented. An effort has been made to identify the coupled modes which are known from assigned combination bands. Other assignments are made from a combination of interpretation of linear spectra and the 2-D spectrum.

It is in these sections that the real power of DOVE spectroscopy becomes apparent, eliminating uncoupled modes and spreading out spectral information into two spectral dimensions, so that the various contributions which overlap or are obscured altogether in the linear spectra become separated and clear. In the simplest case, the linear spectra at some fixed ω_1 can be viewed as the sum of all of the contributions as ω_2 is scanned through the entire vibrational region of the electromagnetic spectrum. Under the conditions of high signal and low background the features in the 2-D spectra are clear and easy to assign. However, there will necessarily be features which do not directly correlate with linear spectra. Most significantly, DOVE spectroscopy isolates only coupled modes, so that the overall intensity in DOVE spectra for a given finite spectral space will not necessarily add up to the linear spectrum, and strong coupling as demonstrated by intense DOVE peaks will not necessarily lead to bands in the linear spectrum which dominate

modes from uncoupled transitions. Another significant contributor is interferences of various kinds; the interferences of resonant features with the nonresonant background as well as between DOVE-IR and DOVE-Raman signals have already been shown to shift centre frequencies of peaks as well as distort lineshapes.

Various CH moieties have been chosen for study in the amino acids, and it is noted that the greatest anharmonic shifts occur for the lightest atoms, suggesting that the anharmonic shifts of the modes explored here will result in a greater spectral separation between DOVE-IR and DOVE-Raman processes and thereby reduce interferences which may make the spectra more difficult to interpret. However, the other field-level interferences from e.g. the sample cell windows evolve in time, so these spectra represent a "snapshot" in time at the given pair of delays, and the variation of signal levels and peak locations with the various pulse delays has already been shown. In this sense, the spectra presented here are not steady-state, and it is with caution that the assignments are made where they do not exist in or coincide with reports in the literature. Nevertheless, great care has been taken to acquire these spectra under identical conditions of sample cell preparation, beam alignment, relative pulse timings, etc. and therefore are most valuable as a relative comparison to one another rather than a definitive statement about specific mode coupling or structure.

Each 2-D spectrum is presented on a separate page, again as a contour plot, with repeated greyscale and bluescale contour lines to accentuate the peaks and a relative intensity scale is given at the bottom of each. Opposite each labelled axis is a linear absorption (FTIR) spectrum of the same spectral range for comparison, and the assignments made in section 5.3 are repeated here for convenience. The inset figure given at the left is a perspective view of the contour plot to more easily visualise what is shown in the plan view. In the body of the text, just the contour plot is repeated with peaks numbered, and an associated table lists the peaks and their tentative assignments.

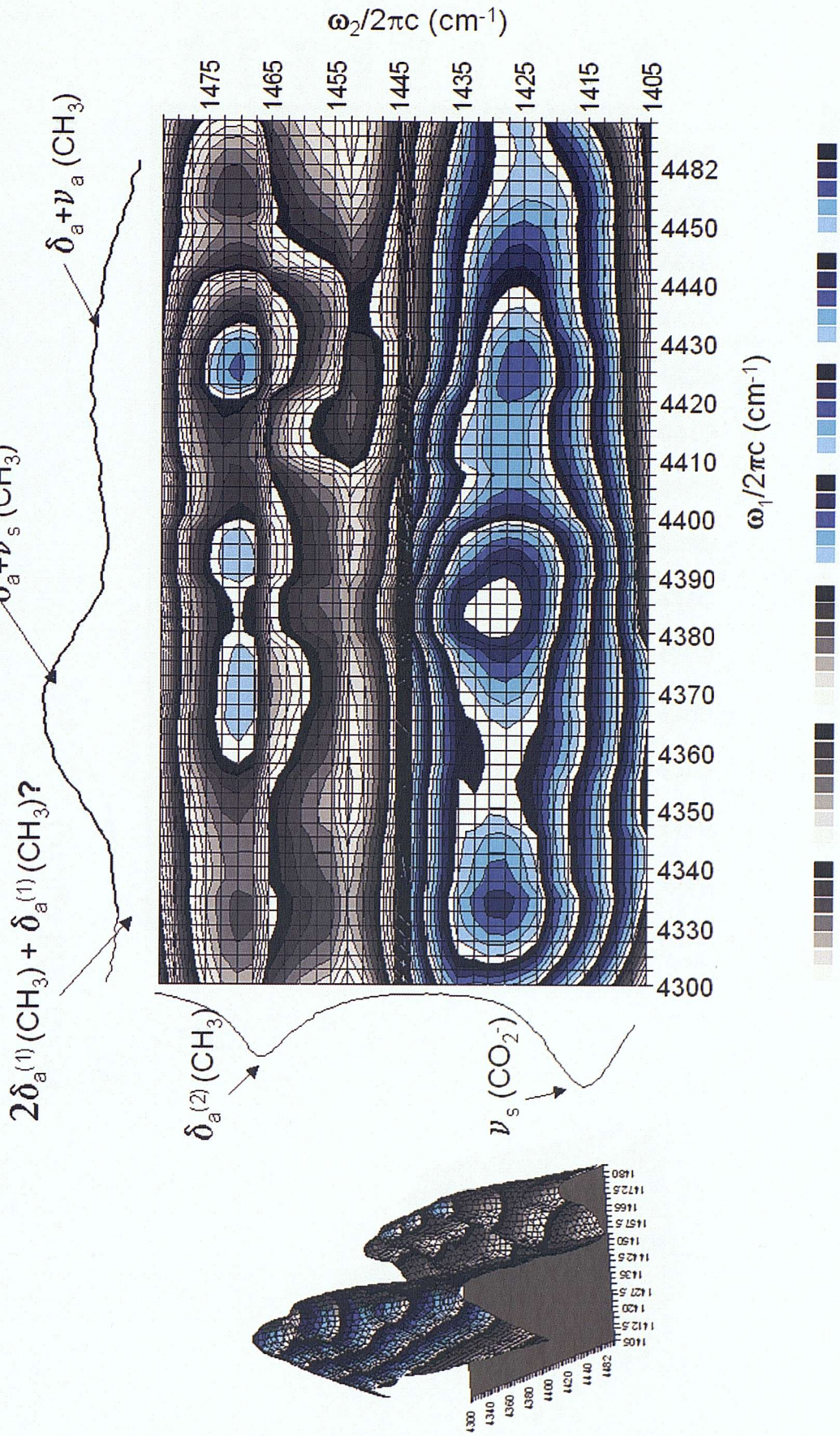


Figure 5.17. 2-D DOVE spectrum of 1.9 M alanine in D_2O. In all of the 2-D spectra in this chapter, the timings are set at t_{12} = -1 ps and t_{23} at +3 ps, as outlined in section 5.5.

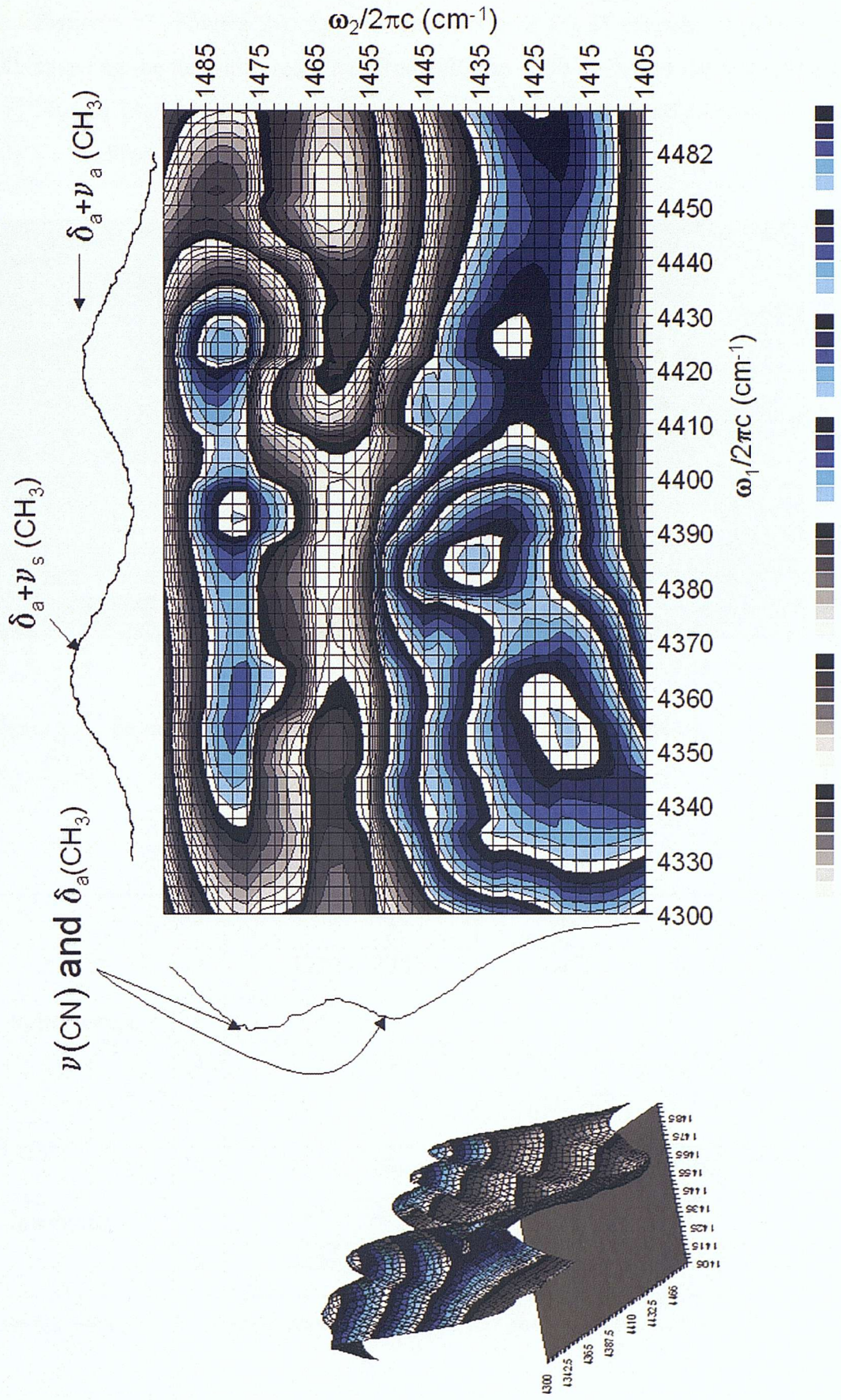


Figure 5.18. 2-D DOVE spectrum of 47 mM polyalanine (1.7 res M) in D_2O.

5.6.1. Alanine

Figure 5.17 shows a 2-D DOVE spectrum of a 1.9 M solution of alanine in D_2O, spanning the near-infrared range from 4300 to 4500 cm^{-1}, and the mid-infrared from 1405 to 1480 cm^{-1}. Figure 5.19 repeats this plot with the peaks numbered and table 5.1 numbers the peaks that are evident.

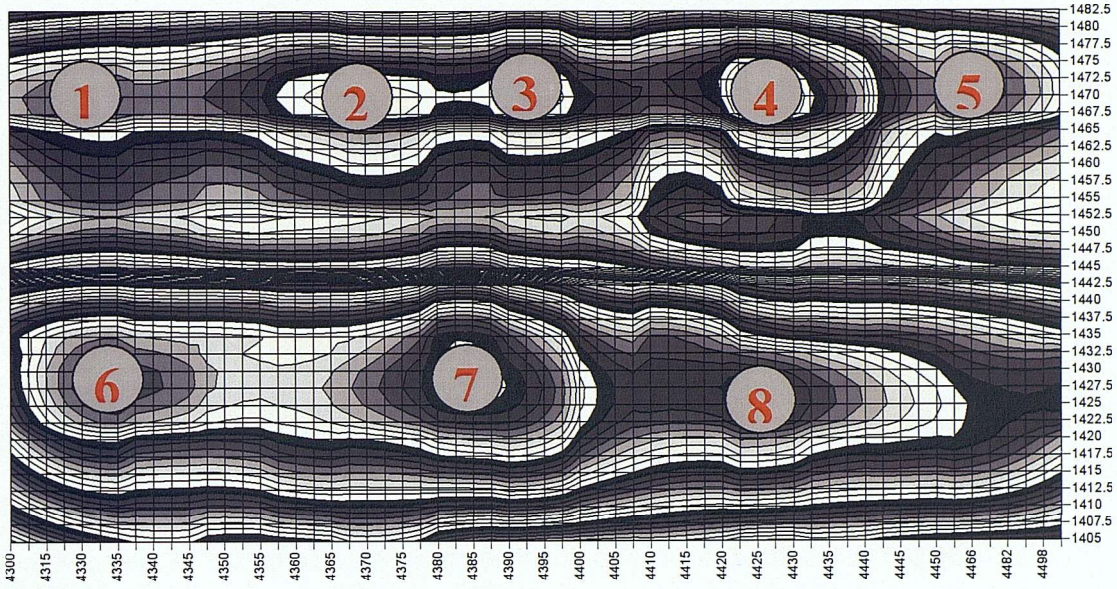


Figure 5.19. Repeat of the 2-D plot in figure 5.17 with the peaks numbered 1-8.

		frequency (ω_1 / ω_2, cm^{-1})	assignment
upper ridge	1	4333 / 1470	$2\delta_a(CH_3) + \delta_a(CH_3)$ *(IR)*
	2	4370 / 1470	$\nu_s(CH_3) + \delta_a(CH_3)$ *(IR)*
	3	4393 / 1470	??
	4	4425 / 1470	$\nu_a^{(2)}(CH_3) + \delta_a(CH_3)$ *(IR)*
	5	4460 / 1470	$\nu_a^{(1)}(CH_3) + \delta_a(CH_3)$ *(IR)*
lower ridge	6	4334 / 1430	$2\delta_a^{(1)}(CH_3) + \delta_a(CH_3)$ *(Raman)*
	7	4385 / 1430	??
	8	4425 / 1426	$\nu_a^{(2)}(CH_3) + \delta_a(CH_3)$ *(Raman)*

Table 5.1. Summary of the peaks numbered in figure 5.19 and their tentative assignments.

The first feature to note is that the peaks appear to occur along two lines defined by fixed frequencies in ω_2: ~1470 and ~ 1430 cm^{-1}. It is possible that SIVE interactions could be the cause of these ridges, given that there are resonant features near these frequencies. SIVE signals are known to appear as lines in 2-D spectra at fixed ω_1 or ω_2 when just one of the frequencies is resonant with a vibrational transition. However, SIVE contributions are comparatively weak, so it is more likely that this landscape on which the peaks appear is an interference phenomenon with the nonresonant background. A large and variable background was evident in many ω_2 scans for the various amino acid trials prior to acquisition of the first alanine signal. Nevertheless, these ridges appear at or very near resonant frequencies in ω_2 to a greater or lesser degree in all of the amino acid 2-D spectra presented in this chapter, so that the SIVE process cannot be absolutely ruled out.

The DOVE peaks that were initially predicted in alanine focused on the coupling between the methyl group asymmetric stretch δ_a at 1465 cm^{-1} and the combination bands $\delta_a+\nu_s$ at 4368 cm^{-1} and $\delta_a+\nu_a$ at 4435 cm^{-1}. It is clear that the peaks in the 2-D spectrum do not appear directly on this line, seeming instead to be centred at 1470 cm^{-1}. This may be due in part to an inaccuracy in the wavelength measurement, which is taken to be accurate within 3 cm^{-1}, but it can also be seen that these peaks have a greater extent on the low frequency side, seeming to slope down more slowly than on the higher frequency side. It is likely that the peaks are centred closer to 1465 cm^{-1} but that the dominant background on which they appear is not. The expected peak at 4368/1465 cm^{-1} is clearly present as peak (**2**), though broadened along the ω_1 axis towards the blue. The expected peak at 4435/1465 cm^{-1} appears closer to 4425 cm^{-1} (peak **4**). Peak (**1**) is presumed to be a coupling of the fundamental and overtone of the δ_a bend. Peak (**3**) does not have an obvious explanation; it seems unlikely that it is the DOVE-Raman version of a DOVE-IR process occurring at higher ω_2 because there are no peaks in the mid-IR spectrum within 50 cm^{-1}. Peak (**5**) appears to be a similar coupling to that of peak (**4**) but to another of the nearly degenerate ν_a modes.

Considering the cases presented in figure 5.16, it can be seen that the upper ridge in the 2-D alanine spectrum is dominated by DOVE-IR features arising from case (**a**), and that the lower ridge in the spectrum is dominated by features due to the DOVE-Raman processes as in case (**d**), under the assumption that the anharmonic

shift is the difference in ω_1 frequency between the two, $\Delta \sim 40$ cm^{-1}. However, this is somewhat higher than the value obtained by considering the position of the combination band relative to the sum of the fundamental frequencies (~35 cm^{-1}). With this in mind, peaks (**6**) and (**8**) correspond to peaks (**1**) and (**4**) respectively. Peak (**7**) is most likely an overlapped combination of the DOVE-Raman processes corresponding to peaks (**2**) and (**3**) because it is significantly broader than neighbouring peaks.

5.6.2. Polyalanine

Figure 5.18 shows a 2-D DOVE spectrum of a 47 mM solution of polyalanine in D_2O. As it is a ~36-mer polypeptide, the methyl group molarity is ~1.7 M, comparable to the alanine sample employed for the previous spectrum. The spectrum spans the near-infrared range from 4300 to 4500 cm^{-1}, and the mid-infrared from 1405 to 1490 cm^{-1}.

The figure is repeated below with the peaks numbered for comparison to the alanine case. Table 5.2 compares the positions of the peaks in polyalanine versus those in alanine.

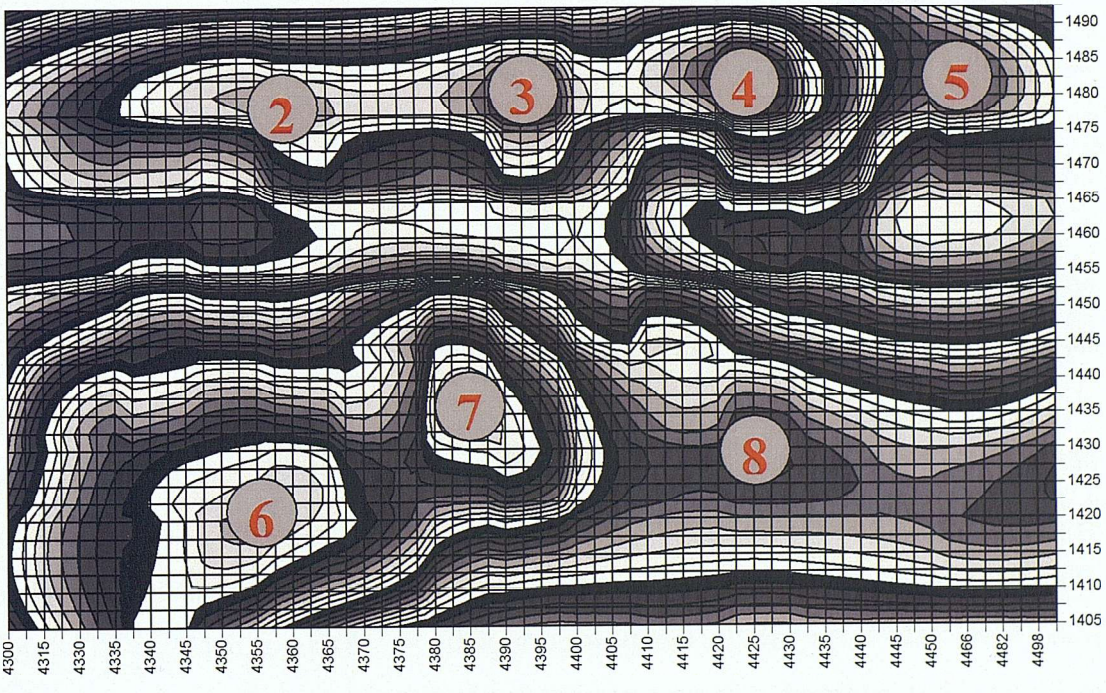


Figure 5.20. Repeat of the 2-D plot in figure 5.18 with the peaks numbered 2-8.

		alanine frequency (ω_1 / ω_2, cm^{-1})	polyalanine frequency (ω_1 / ω_2, cm^{-1})	assignment
upper ridge	1	4333 / 1470	-	-
	2	4370 / 1470	4358 / 1478	$\nu_s(CH_3) + \delta_a^{(2)}(CH_3)$ *(IR)*
	3	4393 /1470	4393 / 1478	?? *(IR)*
	4	4425 / 1470	4424 / 1481	$\nu_a^{(2)}(CH_3) + \delta_a^{(2)}(CH_3)$ *(IR)*
	5	4460 / 1470	4460 / 1481	$\nu_a^{(1)}(CH_3) + \delta_a^{(2)}(CH_3)$ *(IR)*
lower ridge	6	4334 / 1430	4353 / 1420	$\nu_s(CH_3) + \delta_a^{(2)}(CH_3)$ *(Raman)*
	7	4385 / 1430	4385 / 1436	?? *(Raman)* *and* $\nu_s(CH_3) + \delta_a^{(1)}(CH_3)$ *(IR)*
	8	4425 /1426	4425 / 1429	$\nu_a^{(2)}(CH_3) + \delta_a^{(2)}(CH_3)$ *(Raman)*

Table 5.2 Summary of the peaks numbered in figure 5.20 and their tentative assignments.

From the 3-D projection, it is clear that there is a marked difference in the relative heights of the two ridges on which the peaks appear; in the alanine case, the peaks on the lesser ridge at 1465 cm^{-1} are at 65% of the peak height of the ridge at 1430 cm^{-1}, whereas for the polyalanine case this figure is 80%. The most significant difference for the polyalanine case, however, is the shift of some but not all of the peaks on each of the ridges, which clearly correspond to one another in the two spectra.

On the upper ridge, peak (**1**) does not clearly appear in the polyalanine spectrum. Peak (**2**) is shifted up both in ω_1 and ω_2 by ~8 cm^{-1}. Peaks (**3**)-(**5**) are all shifted up in ω_2 by ~10 cm^{-1} but appear at nearly identical positions in ω_1. This is consistent with the coupling of identically the same modes, but in polyalanine the linear spectrum shows a splitting of the δ_a mode with the presence of the amide II band, so that the $\delta_a(CH_3)$ mode is blueshifted by approximately the same amount. On the lower ridge, peak (**8**) is within error at identically the same place, and again shifted directly down in ω_1 from the corresponding peak (**4**, ascribed to $\delta_a^{(2)}+\nu_a^{(2)}$) so that peaks (**4**) and (**8**) clearly comprise modes which do not change their coupling when present as part of the polypeptide.

The most interesting difference between the two spectra is the shifts along ω_2 of the peaks that appear on the bottom ridge. Here again peaks (**3**) and (**7**) do not have a clear explanation, but peak (**7**) has shifted higher in ω_2. Most likely this is because the degeneracy splitting of the δ_a modes has caused DOVE-IR processes to occur separately for the δ_a modes. These new peaks will be nearby in frequency to the DOVE-Raman peaks caused by the same couplings of the upper ridge and will interfere, causing lineshape changes and broadening of these peaks in both spectral dimensions. This broadening is very apparent in the polyalanine peaks of the lower ridge.

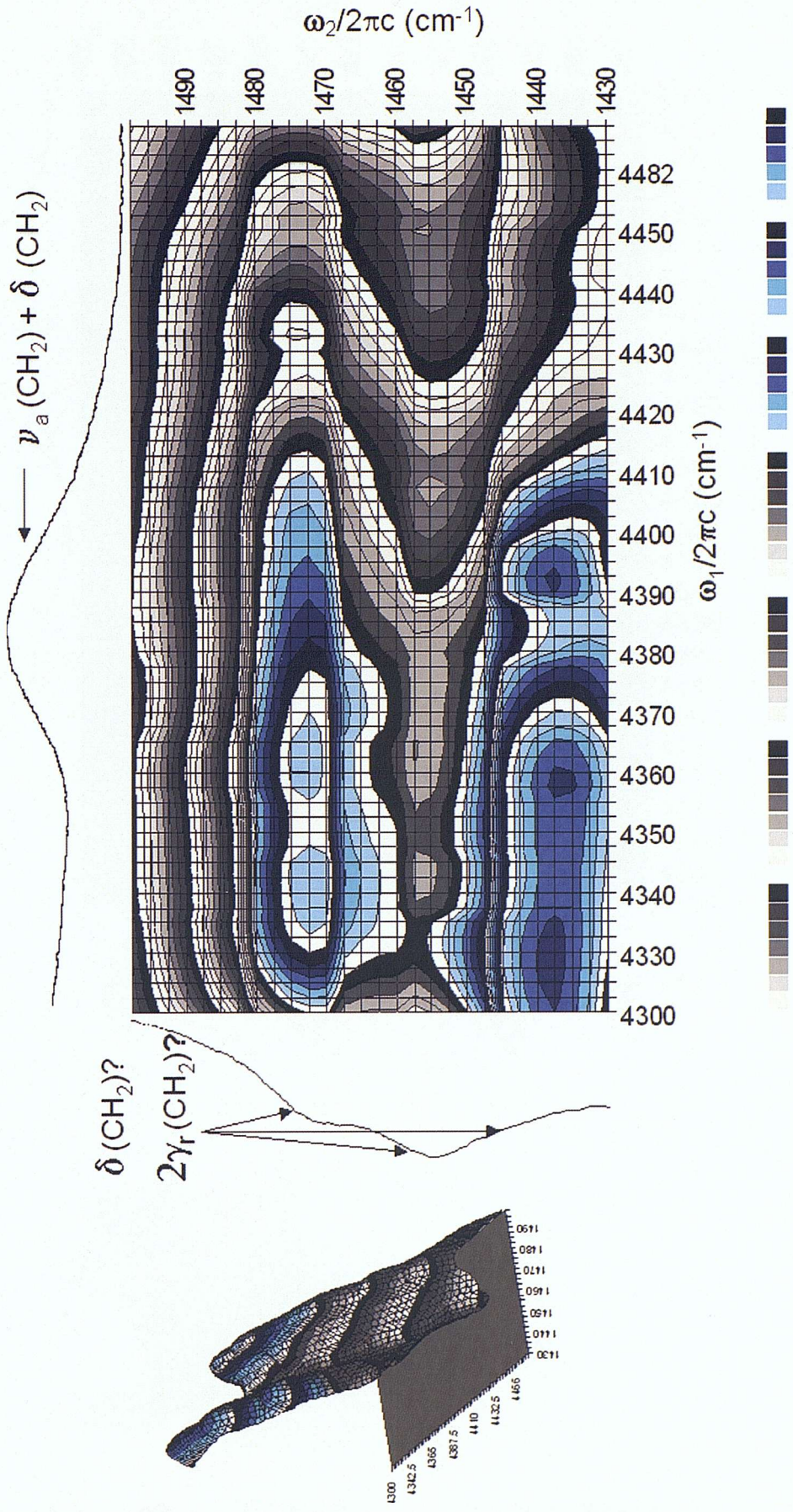


Figure 5.21. 2-D DOVE spectrum of 1.0 M arginine in D_2O.

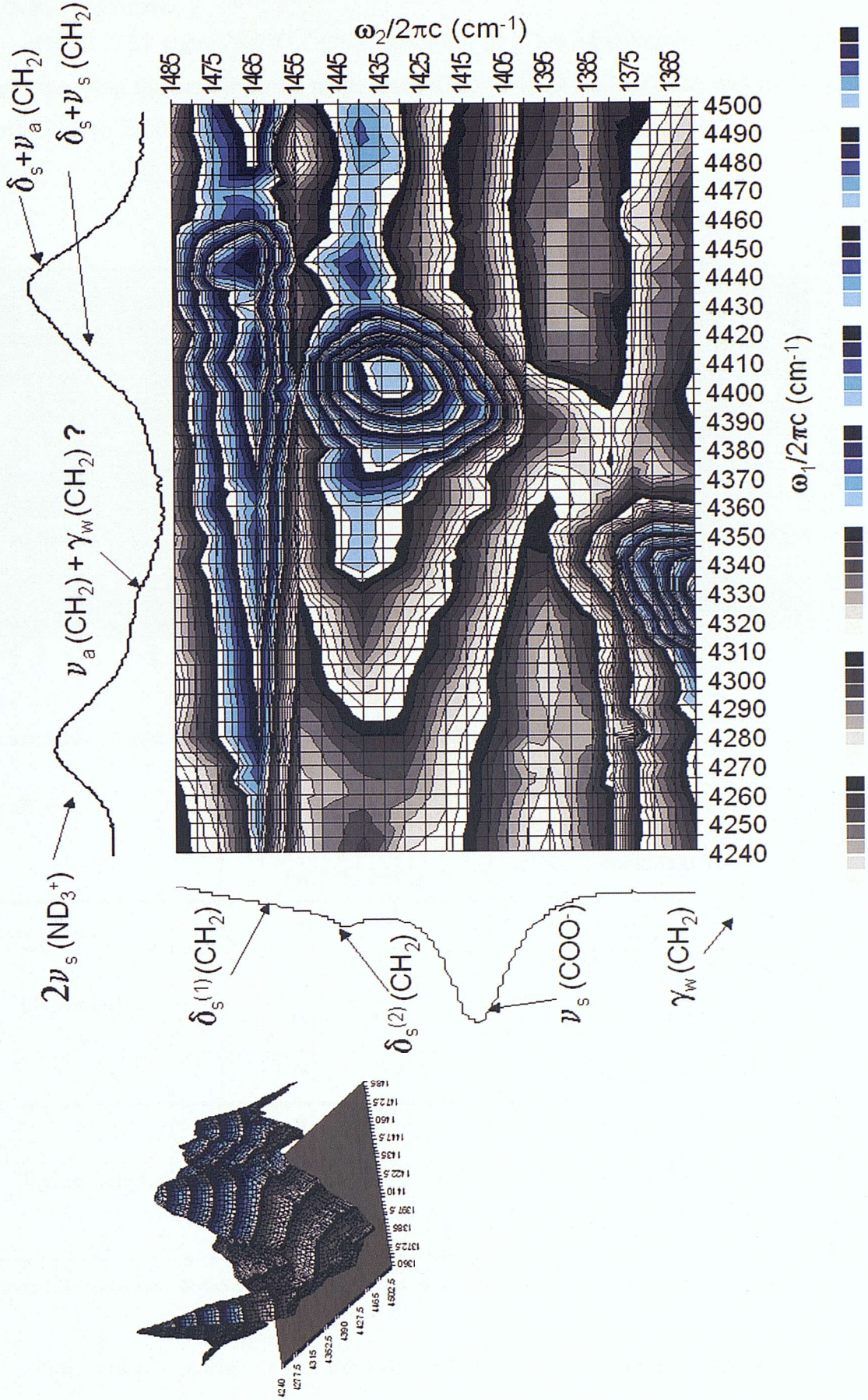


Figure 5.22. 2-D DOVE spectra of 3 M glycine in D_2O. Acquisition of the data by P. Donaldson is gratefully acknowledged.

5.6.3. Arginine

Figure 5.21 shows a 2-D DOVE spectrum of a 1.0 M solution of arginine in D_2O, spanning the near-infrared range from 4300 to 4500 cm^{-1}, and the mid-infrared from 1430 to 1500 cm^{-1}. Figure 5.23 numbers the peaks, which are detailed in table 5.3.

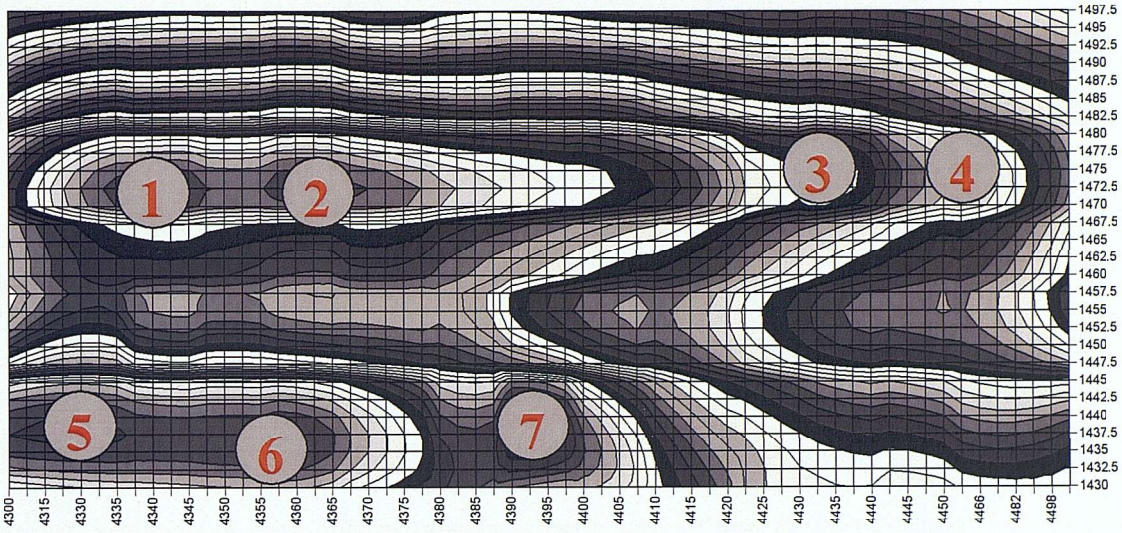


Figure 5.23. Repeat of the 2-D plot in figure 5.21 with the peaks numbered 1-7.

		frequency (ω_1 / ω_2, cm^{-1})	assignment
upper ridge	1	4341 / 1473	$\nu_a^{(1)}(CH_2) + \delta(CH_2)$ *(IR)*
	2	4363 / 1473	$\nu_a^{(2)}(CH_2) + \delta(CH_2)$ *(IR)*
	3	4433 /1474 ?	$\nu_a^{(1)}(CH_2) + 2\gamma_r(CH_2)$
	4	4451 / 1474 ?	$\nu_a^{(2)}(CH_2) + 2\gamma_r(CH_2)$
lower ridge	5	4325 / 1438	$\nu_a^{(1)}(CH_2) + \delta(CH_2)$ *(Raman)*
	6	4359 /1437	$\nu_a^{(2)}(CH_2) + \delta(CH_2)$ *(Raman)*
	7	4392 / 1438	$\nu_a^{(3)}(CH_2) + \delta(CH_2)$ *(Raman)*

Table 5.3. Summary of the peaks numbered in figure 5.23 and their tentative assignments.

The lower molarity of the solution suggests that the resonant signals will be reduced by a factor of between 2 and 4 from the previous spectra (depending on the

degree to which the linearity-in-concentration condition is met at these number densities), and the peaks are less distinct above the background in this case. It is easy to see from the 3-D projection that the shape of the background in ω_2 has changed markedly, and again the small peaks occur atop the ridges at fixed ω_2. Here again the ridges could be ascribed to SIVE interactions with one of the fundamental modes, but for this low signal:background regime it seems more likely that they are due largely to the nonresonant background. Further, the background slopes down in the ω_1 dimension, reducing by 4500 cm^{-1} to less than half the value of the peaks. The upward slope of the linear spectrum in ω_2 is at the low frequency side toward the assigned overtone of the ND_3^+ vibration, but it seems clear that the features in the spectrum suggest a number of combination bands which lie under the tail of this strong absorption.

As previously mentioned, the overtone of the methylene rocking vibration will likely be in this same region in ω_2. The in-phase mode at 724 cm^{-1} is the strongest of the fundamentals of this vibration,[13] so that the overtone would be $\leqslant$1448 cm^{-1}. As before, however, a high anharmonicity is expected, so that if the overtone were of a fundamental at 724 cm^{-1} it would be likely to occur at a value less than the 1438 cm^{-1} on which the features appear in the 2-D spectrum. A careful study of the FTIR spectrum in the region of the fundamental shows a number of very weak bands, appearing at 718, 742, and 773 cm^{-1}. These bands are not assigned in the literature, but the γ_r fundamental is known occur between ~724 and 1174 cm^{-1} and it is therefore plausible that these three bands correspond to three γ_r fundamentals for the different methylene groups. Let us first consider the most distinct peak in the spectrum, peak (**7**). It is far more likely from a transition dipole moment consideration that the largest peaks would be attributable to coupling between the fundamental stretching vibration and a fundamental deformation, (as indicated in the ν_a (CH_2) + δ (CH_2) combination band assigned in the linear spectrum) rather than coupling between a fundamental and an overtone. It is therefore postulated that the peaks along ω_2 = 1438 cm^{-1} (**5**, **6**, and **7**) are due to (one of) the δ mode(s). With this in mind, it is easy to assign peaks (**5**) and (**6**) to lesser coupling between this δ mode and the other two of the three non-degenerate asymmetric stretch modes ν_a in the arginine alkyl chain.

The other ridge along the ω_1 axis at 1473 cm^{-1} could equally be a similar coupling of these ν_a with another of the δ modes, but it seems clear given the assignments in the alanine and polyalanine spectra that peaks (**1**) and (**2**) are a mirror of those at (**5**) and (**6**), but due to a DOVE-IR process rather than a DOVE-Raman process. Further, a weaker peak can be discerned at 4433 cm^{-1} (peak (**3**)), and the curvature of the contours suggests another at 4455 cm^{-1} (peak (**4**)). It is possible that the overtone of one of the rocking vibrations, $2\gamma_r$, is very nearly degenerate with one of the bending vibrations δ_s, and that the stronger pair of peaks (**1**) and (**2**) are due to the coupling of the asymmetric stretch ν_a with the bending mode δ, whereas the lesser peaks (**3**) and (**4**) are due to coupling of ν_a with the rocking overtone $2\gamma_r$, though it is understood that these assignments are very speculative in the absence of definitive assignment of the γ_r fundamental(s).

The situation is clearly complicated in this small spectral range when all of the modes probed are due to three identical moieties in three non-identical environments, thus splitting normally degenerate modes enough to broaden the linear spectrum, but not enough to resolve the bands.

5.6.4. Glycine

Figure 5.22 shows a 2-D DOVE spectrum of a ~3 M solution of glycine in D_2O, spanning the near-infrared range from 4240 to 4500 cm^{-1}, and the mid-infrared from 1360 to 1485 cm^{-1}. Figure 5.24 and Table 5.4 outline the peaks.

Glycine's structural simplicity and its high solubility in D_2O make this situation much clearer. The level of the background, and hence the interferences with it, are much reduced, though here again two ridges are evident on which peaks (**1-4**) appear. The extreme elongation of the upper ridge toward the low-frequency side of ω_1 and the broadening of peak (**3**) along a parallel axis seem to suggest SIVE processes here, not necessarily the nonresonant background interference. A reduction in the molecule's complexity leads to fewer splittings of the degeneracies of various modes, and despite the fact that a significantly larger spectral space is shown, there are fewer peaks. It is quite straightforward to assign the first four peaks based on the linear spectrum to coupling between the symmetric and asymmetric stretch modes ν_s/ν_a with the two bending modes δ. The significant intensity difference and broadening of peak (**3**) suggests that the DOVE-IR process of ν_s with

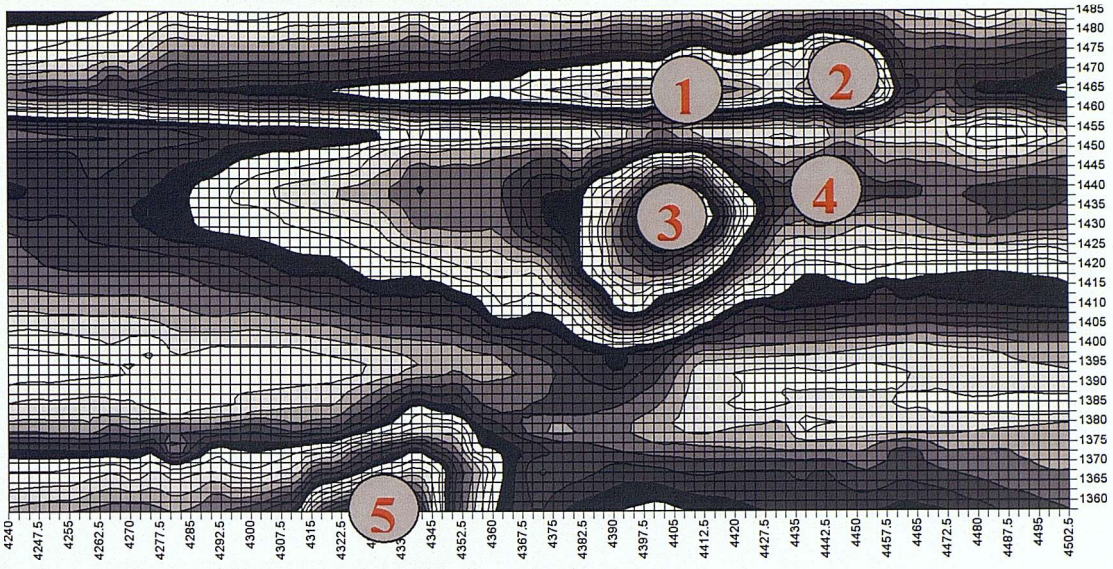


Figure 5.24. Repeat of the 2-D plot in figure 5.22 with the peaks numbered 1-5.

	frequency (ω_1 / ω_2, cm^{-1})	assignment
1	4415 / 1465	$\nu_s(CH_2) + \delta^{(1)}(CH_2)$ *(IR)*
2	4445 / 1465	$\nu_a(CH_2) + \delta^{(1)}(CH_2)$ *(IR)*
3	4400 / 1440	$\nu_s(CH_2) + \delta^{(1)}(CH_2)$ *(Raman)* *and* $\nu_s(CH_2) + \delta^{(2)}(CH_2)$ *(IR)*
4	4437 / 1440	$\nu_a(CH_2) + \delta^{(1)}(CH_2)$ *(Raman)* *and* $\nu_a(CH_2) + \delta^{(2)}(CH_2)$ *(IR)*
5	4330 / ~1350	$\nu_s(CH_2) + \gamma_w(CH_2)$

Table 5.4. Summary of the peaks numbered in figure 5.24 and their tentative assignments.

$\delta^{(2)}$ is coincident with and interfering constructively with the DOVE-Raman process of ν_s with $\delta^{(1)}$. Another possibility of the presence again of the overtone of the rocking vibration γ_r (CH_2) in the same spectral region as the bend, so that it could be contributing either to the broadening in the numbered peaks, or could in fact be the source of the features at the extreme right of the 2-D spectrum near $\omega_1 = 4500\ cm^{-1}$. Here again without the benefit of an assigned rocking fundamental the assignment is difficult, though it is assumed the oscillator strength of the overtone would be

smaller than that of the bend, suggesting that at least the numbered peaks are more likely to be due to the bending vibrations.

Peak (**5**) is not fully explored in this spectral region, but it is clear that it is the largest feature observed. It has been assigned to a coupling between the ν_s (CH_2) mode and the wagging mode γ_w (CH_2), which is a very strong band at 1324 cm^{-1} (see figure 5.7) and is quite likely to couple to the stretch vibration. It would be interesting to explore this region in ω_2 for arginine in order to observe the same coupling, and to observe the spectral differences when this coupling arises from three methylene groups rather than glycine's singular one.

5.7. Concluding remarks

The 2-D DOVE spectra presented in this chapter are a striking demonstration of the strengths of the DOVE spectroscopic method to vastly simplify the interpretation of overlapped bands in linear spectra. These first-ever off-diagonal explorations of comparatively complex biomolecules have allowed the assignment of vibrational bands which have been heretofore impossible to resolve, and have provided a spectral fingerprint for the amino acids studied here, as well as provided strong evidence that such fingerprinting will be possible for polypeptides and proteins. A number of improvements to the methodology, both in terms of sensitivity and throughput, have been proposed and will be discussed in the closing chapter.

6. Conclusions, Perspectives, Current and Future Work

The design, implementation, and use of the DOVE spectrometer as laid out in this thesis has lain the groundwork for its use with progressively more complex molecules.

DOVE spectroscopy has in the preceding chapters proven itself a method of extreme utility in the analysis of relatively complex molecules. This chapter aims to outline the improvements that are necessary to make DOVE spectroscopy an extraordinarily sensitive method with high throughput. Further, an appraisal of the method and future research directions will be presented.

Some of the improvements to the methodology and to the spectrometer itself outlined in this chapter have already been implemented since the conclusion of the work presented here. Several of these improvements have long been planned, but the changes to throughput or ease of use were until now not outweighed by the need to further explore the method or acquire results. There are two fundamentally different kinds of improvements to be made to the spectrometer and the method: those of throughput, and those of sensitivity.

6.1. Throughput improvements—ratioing

The single greatest contributor to the signal-to-noise ratio in these experiments is the variation in pulse energies as produced by the OPAs. The nonlinear signal scales as the product of these input energies and therefore any variation of any of the energies is present as noise on the output signal. As a consequence, during the course of the research outlined in Chapters 4 and 5, the laser system had to be at peak performance, with extremely low pulse-to-pulse energy variation and with very good long-term stability, requiring frequent minuscule adjustments to the system during the course of experimenting in order to keep the system operating below an established noise threshold.

A method of accounting for the pulse-to-pulse variations is to ratio the output signal with the pulse energies, normalised to some average value. This is another advantage of the use of spatial filters in the paths of all three of the excitation beams:

any changes in output pulse energies as well as any drifts of the output direction from the OPAs manifest themselves only as intensity variations on the output side of the spatial filters. By monitoring these variations, the net change on the signal can be divided out, effectively eliminating any noise on the measured signal which is due purely to laser intensity or pointing changes. This is accomplished by measuring a fraction of the pulse energy that passes through the spatial filters with the use of a surface reflection off a calcium fluoride plate. These beams, on the order of a few percent of the total pulse energy, are focused onto a pyroelectric Joulemeter (in the case of the IR) or a silicon photodiode (in the case of the visible beam). Data acquisition cards and Labview software divide the total input signal from the detector by the normalised pulse energies. Thus, when any or all of the pulses change intensity as measured after the spatial filter, the net signal change due to the laser changes is divided out. This approach has been employed for nonlinear experiments in this laboratory before, resulting in a signal-to-noise improvement as high as a factor of 20. To date, the implementation of the ratioing procedure has reduced the effect of long-term laser system drifts by a factor of ~10, so that the experimental noise floor is defined by the shot noise of the PMT detector.

6.1.1. Automation

A fundamental limitation to the throughput of the spectrometer is the painstaking nature of tuning the output wavelengths of the infrared beams. For the case of near-IR output, this requires the optimisation of two different micrometers for the grating and BBO crystal. In the mid-IR, it is also necessary to optimise the angle of the $AgGaS_2$ crystal. While the implementation of tuning curves for each of these adjustments made the change of wavelength much quicker and more repeatable, it still remained for the experimenter to manually change these parameters for each data point taken, a process which often accounted for more of the time per data point than the signal averaging itself. The high reproducibility of wavelength with micrometer settings and the lack of hysteresis in the tuning process made it possible to fully automate the tuning process with the use of stepper motor-driven micrometers and Labview code. Further, the data acquisition has been integrated with this tuning program, so that the user can input the frequency range, step size, and signal averaging parameters and the program simply acquires a full data set unattended.

The spectra presented in Chapter 5 represent the averages of two full data sets, each of which took approximately 12 hours to collect. With the improvements in signal to noise afforded by the ratioing step and the increase in throughput by the automation of the frequency tuning and data acquisition steps, data of the same spectral scope and signal-to-noise figure can now be acquired in ~1/2 hour.

6.1.2. Multiplexing model

A further step to increase the throughput of the spectrometer is multiplexing, which has been theoretically explored but has not yet been experimentally implemented. The collection of spectrally resolved data in the case of a single-channel detector such as a photodiode or PMT is very time consuming, even in the case of automated tuning. In the interest of speeding up the process, the possibility of multiplexing the experiment has been investigated. Initially explored by CARS spectroscopists,[59,60] the general idea of multiplexing is to use a broadband excitation pulse, resulting in a broadband output pulse, and spectrally disperse the output onto a multichannel detector. Alternatively, we can take advantage of the unique signal output direction or wavelength that is defined by the input angles and wavelengths of the $\omega_{1\text{-}3}$ beams (see section 2.2.4). In the picosecond configuration of the stretcher/compressor, the output bandwidth is ~25 cm^{-1}, resulting in a very small spread of output angles. If the inputs are spectrally broad pulses, however, the output angle spread is increased. This can be achieved by switching the stretcher/compressor grating pair to the femtosecond configuration. The output of the regenerative amplifier and thus the OPAs is then pulses of temporal width ~100 fs and bandwidth >200 cm^{-1}. In this case, a wide frequency band can be explored in a single shot, reducing or eliminating the need to tune the OPAs at all. In another implementation, it is possible to use a single broadband input and a single narrowband input pulse to create a spectrally broad output representative of one of the spectral regions defined by the ω_i. Here, the CARS approach would apply: spectrally dispersing the output with a grating or monochromator onto a multichannel detector. In order to explore these possibilities, a number of simulations were run with a modified version of the phase matching model that allowed for the input of spectrally broad pulses.

A consideration for the implementation of the multiplexing setup is the available energy per bandwidth. Current picosecond experiments utilise mid-IR

pulses with energy ~3 μJ (at the sample) and the near-IR pulses with energy ~6 μJ. In the femtosecond configuration, these pulse energies are somewhat larger, but the bandwidth is 10 times higher. Taking the pulse energy increase into account, the energy per bandwidth reduction is a factor of ~6. As much as 300 μJ is available in the ω_3 beam, and since the signal scales as the product of the input intensities, it would be possible to make up the difference in total intensity by increasing the ω_3 pulse energy. To date, damage threshold considerations have to this point limited the amount of pulse energy that is usable, but it is well known that the damage threshold in the condensed phase obeys a $\tau^{-1/2}$ scaling law. That is, the damage threshold increases as the pulsewidth decreases at a rate proportional to the square root of the pulsewidth.[61] Given that the pulsewidth would be reduced by a factor of ~15, the damage threshold (and therefore the amount of usable ω_3 pulse energy) would increase by a factor of ~3.9. Overall this results in a total integrated signal intensity reduction of a factor of ~1.5. This signal would then be spread across an array detector, so the total photon number incident on each detector element must be considered.

The phase matching condition suggests that there is an output direction and frequency (wavelength) associated with a signal created with a given input set of excitation wavelengths. Though it is possible to spectrally separate signals arising from different coherence pathways with different energy conservation conditions, it is not possible to associate an output wavelength with any particular pair of input wavelengths because the energy conservation condition for DOVE and the equivalent pathways of figure 5.13,

$$\omega_4 = (\omega_1 - \omega_2) + \omega_3 \qquad \textbf{(equation 6.1)}$$

is such that the output frequency (and thus the wavelength) is dependent on the difference frequency between the infrared excitations ω_1 and ω_2, so that the wavelength of the output signal will be the same along diagonals in the 2-D frequency space. On the other hand, the phase matching condition does specify a unique output *direction* for each input frequency pair.

For the DOVE experiments presented in this thesis, a planar geometry for the input beams was used; i.e., all the $\mathbf{k}_i$ lay in a plane parallel to the laser tabletop. In

this configuration, a full two-dimensional spread of the output signal is not possible; given that all of the input photons' momentum lies in this plane, the signal photons must necessarily lie in that plane for momentum conservation. The output would then be a fan of rays in one plane and the spectrally resolved signal contributions from both the mid-IR beams would spatially interfere on the detector. If instead two of the input beams were out of this plane, the spectral spread in the input beams would result in an angular spread of the output—that is, the spectral information would be coded into the spatial dimensions of the output beam. Hence, an array detector such as a one- or two-dimensional charge-coupled device (CCD) array could be implemented to detect the output signal. It is known from multiplex CARS experiments that the "forward box" geometry is appropriate for this purpose. In short, the forward box geometry is implemented by arranging the three input beams such that they originate from three corners of an imaginary rectangle normal to the propagation direction. The signal beam is then roughly in the direction of the fourth corner of the rectangle on the opposite side of the sample. A depiction of the forward box geometry is shown in figure 6.1.

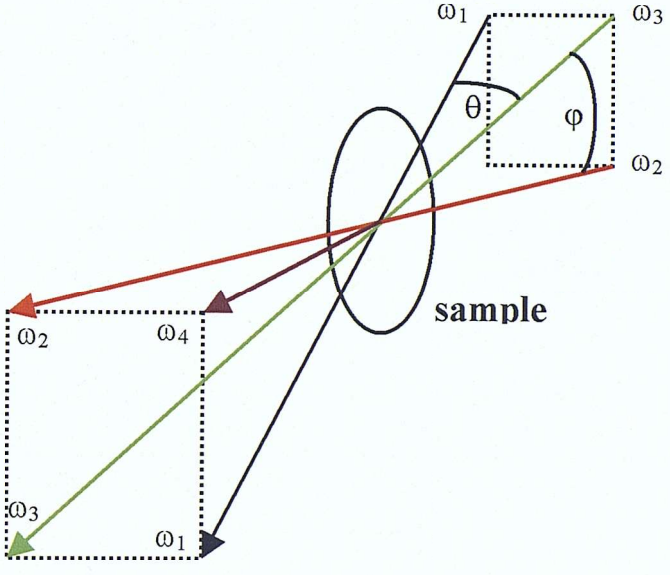


Figure 6.1. A schematic depiction of the forward-box phase matching geometry.

When this input beam geometry is assumed, it is possible to determine how the output angle spread depends on the input wavelengths and angles. The multiplexing model has been implemented for the case of the acetonitrile experiments described in Chapter 4. The results show that the spectral spread in ω_1 results in an angular spread of the output beam in one direction, whereas the spectral spread in ω_2 results in an angular spread in different direction, with the angle between these directions set by the relative input angles. Figure 6.2 plots the output array of angles parametrically. Here, each series is a fixed value of ω_1, and each point in the series corresponds to a value of ω_2, which has been scanned in 6 cm^{-1} increments from 2200 to 2300 cm^{-1} through the ν_2 absorption. The points are plotted as a function of θ and φ, the horizontal and vertical angles relative to a normal passing through the sample. The input angles relative to the normal are shown in Table 6.1.

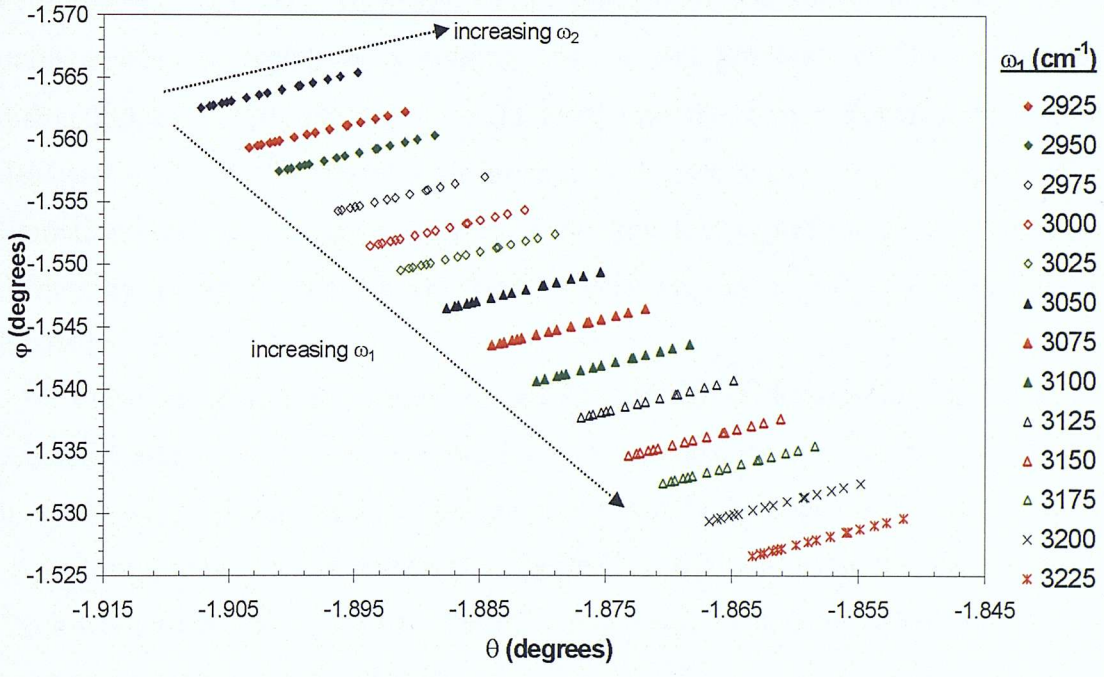


Figure 6.2. Angle map for the output signal as a function of the input frequencies. ω_2 is scanned in each series for fixed values of ω_1 listed in the legend. Note the irregular spacing of points and series.

	θ (degrees)	φ (degrees)	scan range (cm^{-1})
ω_1	0	0	2925-3225
ω_2	0	+2	2200-2300
ω_3	+2	+2	fixed

Table 6.1. Angles and frequencies of the input excitation beams for figures 6.2 and 6.3.

The first point of interest about these plots is that the points are not evenly spaced either within or across the traces, an effect of the refractive index dispersion. There is a greater spacing between traces for varying ω_1; this is due to the greater energy of ω_1 photons. The closest spacing of the points within each trace (varying ω_2) corresponds to an angular spread of ~15 μrad, and across the traces (varying ω_1) is ~50 μrad. In principle, by allowing the output signal to propagate, the minimum spread between any point would be easily within the specifications of available 2-D detectors such as CCDs. However, the multiplexing model considers the signal as a point source—in reality it is coming from a 100 μm spot at the sample and diffraction of a 100 μm beam would overcome the spread between the points depicted in the figure, thereby smearing out the spectrally resolved data. This limitation could be overcome by raising the spot size at the sample to reduce the diffraction, assuming input pulse energies high enough to overcome this loss in intensity.

Once the signal is acquired on a 2-D detector, it remains to divide out the predicted signal level based on phase matching considerations alone. Figure 6.3 plots the signal level predicted by the phase matching model across this spectral space for the same input parameters as figure 6.2. A 3-D projection is also shown in the lower part of the figure with the refractive index dispersion spectra for the two spectral regions shown at lower left.

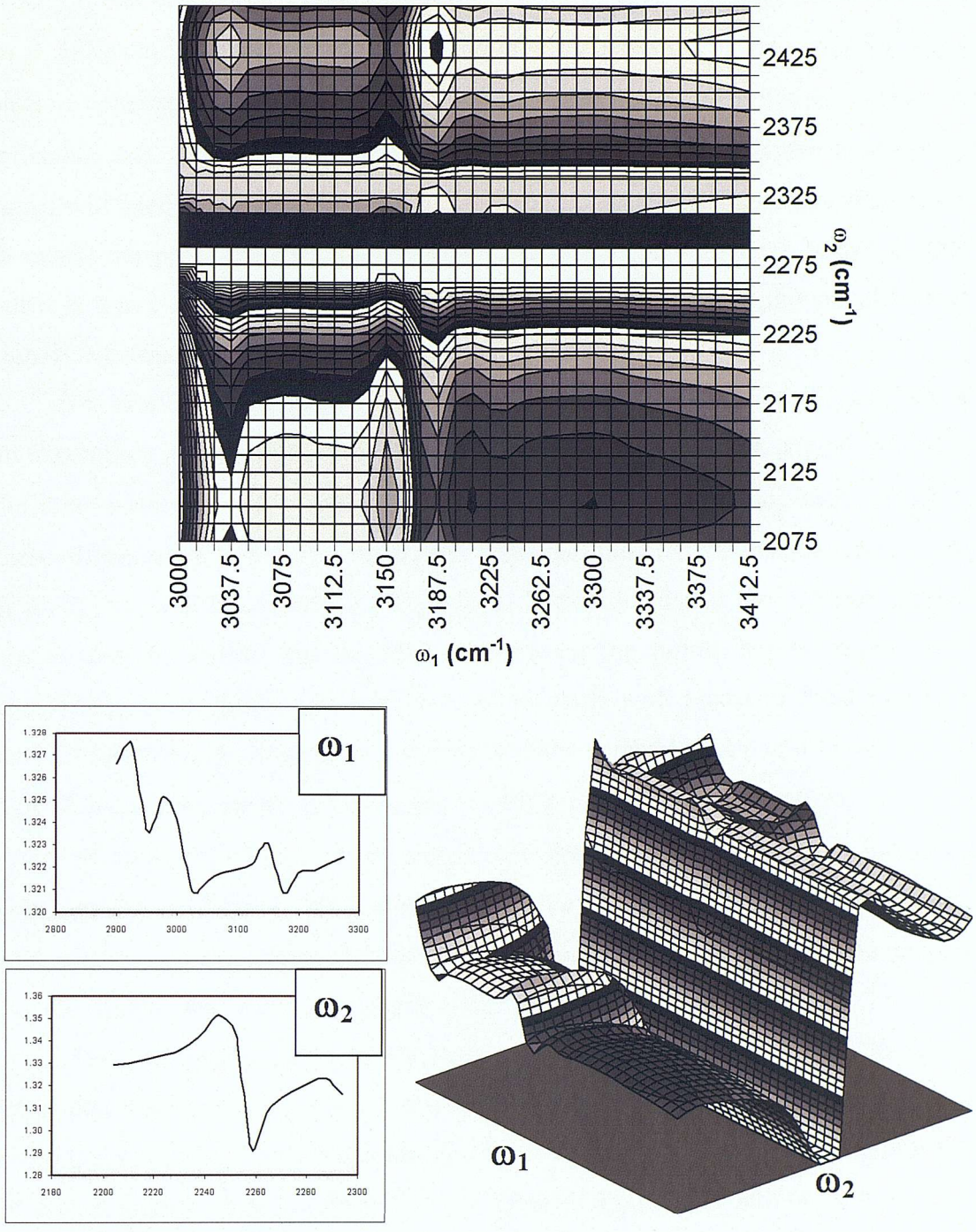


Figure 6.3. 2-D contour plot and 3-D projection of the output signal level as a function of excitation frequencies ω_1 and ω_2. The inset figures at bottom left are dispersion spectra. The effects of the strong ν_2 absorption and weaker $\nu_2 + \nu_4$ absorption are evident in the phase matched signal level near their frequencies $\omega_2 = 2253$ cm^{-1} and $\omega_1 = 3164$ cm^{-1}, respectively.

The variation in the phase matched signal level is clear in this plot. The very strong ν_2 absorption at $\omega_2 = 2253$ cm^{-1} drives the signal down to nearly zero for all values of ω_1. Alternative input geometries which are optimised for signal at this ω_2 frequency have a similar drop in signal on either side. Also, the comparatively

weaker effect of the $\nu_2 + \nu_4$ combination band can be seen vertically in the plot near $\omega_1 = 3160$ cm^{-1}. The functional variation of the dispersion in the lower left hand plots is apparent in the shape of the 3-D plot, with the shape in the ω_1 dimension reflecting that of the ω_1 dispersion and similarly for ω_2. Clearly the multiplexed signal will need to be normalised with these values. Rigorous theoretical approaches to model the phase-matched signals from CMDVS techniques have been reported, but it is noted that for the specific case of DOVE spectroscopy, the calculation of signals is particularly complicated.[62]

It is worthwhile to consider the limitations of this kind of modelling. There is an uncertainty in the output angle that is introduced due to both the angular spread in the input beam (from focusing) and the frequency spread in the ω_3 beam. Both of these effects serve to broaden the output angle and thus reduce the resolution in the spatially resolved measurement. The model has assumed that the input excitations are at discrete angles, but the blurring between the points has been calculated considering the experimental conditions of focusing with a lens of focal length 20 cm. Unsurprisingly, the greatest contributor to the spread in the output angle given a pair of input frequencies is due to the focusing of the ω_3 beam (roughly twice the effect of either ω_1 or ω_2), amounting to ~20 times the spread between the points acquired in 6 cm^{-1} steps. This problem could be easily ameliorated by the removal of the focusing optics, but significantly higher input pulse energies would be required in order to maintain similar intensities in the sample.

Also, any spatial chirp in the beam (a distribution of the frequencies in the pulse that is spread out spatially across the beam, the spatial analogue to the temporal chirp that is effected in the regenerative amplifier) will complicate the determination of output angles. It is unfortunate that such spatial chirp is common in difference- and sum-frequency applications such as the scheme employed here; however, the problem could be mitigated by homogenising the beams with, e.g. rotating Dove prisms made from an infrared-transparent material such as germanium or calcium fluoride. It is assumed in the model that the beams are spatially homogeneous.

From the preceding plots it can be seen that the DOVE spectra are significantly distorted and the data interpretation made more difficult when acquired via the technique of multiplexing with the phase matching conditions alone. If a different approach is used, however, the output can be simplified—one broadband and one

narrowband input could be employed, so that the output signal corresponds to just one of the series in figure 6.2. The output could be dispersed off of a grating onto a linear array detector. In this case, the signal due to different pairs of input frequencies will be linearly dispersed and for the small pathlength needed when employing a grating, no spatial variation of the signal needs to be accounted for. While this reduces the throughput compared to the technique of multiplexing by the phase matching conditions alone, it vastly simplifies the output spectra.

6.2. Sensitivity improvements

The improvements outlined in section 6.1 serve to increase the speed with which spectral data can be acquired. However, the results presented in Chapters 4 and 5 have shown that the true limitation of the methodology at this point is its sensitivity, ultimately limited by the nonresonant background on which the DOVE signals appear, and importantly, with which they interfere on a microscopic level. This limitation was identified early on in the development of the technique by Wright *et. al.*. but was treated as an effect to be modelled rather than removed. One approach to eliminate contributions from the sample cell windows was to employ a windowless laminar flow cell, in which the sample was supported through surface tension between two parallel wires oriented vertically, with a peristaltic pump replenishing the sample present in the beam overlap region.[25] In the case of aqueous solutions, however, we believe that the limiting nonresonant contribution will come from the solvent, regardless of window contributions, so this method was not adapted for these purposes. Instead, a novel method of sample preparation was introduced.

6.2.1. Titanium dioxide (TiO_2) films

A group with which our own is in close collaboration has spent a number of years developing titanium dioxide (TiO_2, or titania) films. Their primary interest is implementing the films for use in dye-sensitised solar cells, but a number of publications have been dedicated to the use of these films for adsorption of proteins.[63-66] These nanocrystalline films are well known for their adsorption of large molecules at high density because the films are porous, not unlike a sponge. Further, the physical and optical properties of these films are ideal for optical experiments of biomolecules: they are optically transparent in both the visible and

infrared, high-quality non-scattering films can be easily and inexpensively made, the thickness of the films can be readily controlled, and the films can be dehydrated and rehydrated easily. Further, the films are electrically conducting, so that a bias applied to the films can change the redox state of proteins adsorbed into the films.

By employing the films as a substrate for proteins in the DOVE experiments, both the solvent and at least one of the sample cell windows can be eliminated; the films are deposited onto a substrate (to date, a 100 μm thick borosilicate glass coverslip) and placed in a concentrated protein solution to promote adsorption. Preliminary experiments have shown a concentration of ~10^{19} molecules/cm^3, which in turn corresponds to ~10^{12} molecules in the beam overlap region for DOVE experiments (by comparison, the corresponding number in the overlap region for the acetonitrile experiments was ~10^{14}).

A further reduction in the background can be achieved by etching away the glass on the back of the coverslip with a concentrated hydrofluoric acid solution. In this way, substrate thicknesses in the focal spot region of just 20 μm have been achieved, but the mechanical stability of the sample is maintained by the thicker surrounding glass. Figure 6.4 shows a scanning electron micrograph of a sample of the titania film and a picture of one of the samples prepared in this way. The substrate is a 22 mm diameter, 100 μm thick coverslip onto which a 12 μm thick titania film has been deposited. The reverse of the slide was etched out in the middle to a thickness of ~20 μm and then placed in a solution of cytochrome c.

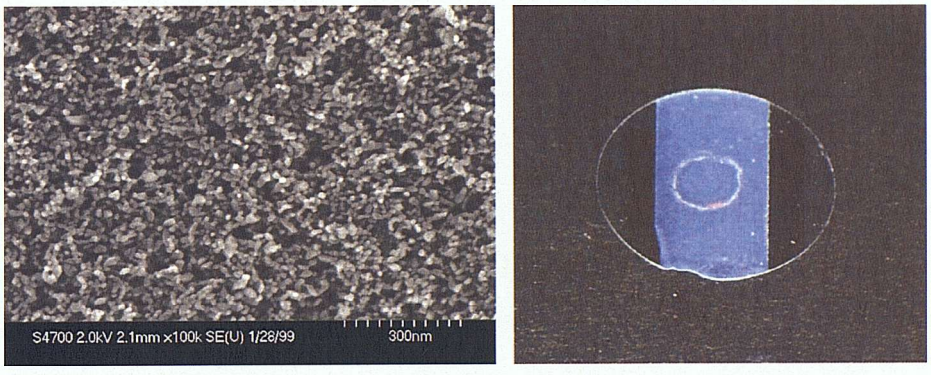


Figure 6.4. Left, scanning electron micrograph of a TiO_2 film, and right, a picture of a film onto which cytochrome c has been adsorbed. The film has been deposited on a 100 μm thick borosilicate coverslip which has been acid etched to a thickness of ~20 μm in the central region.

6.2.2. Reflection geometries

All of the data presented in this thesis were collected in transmission—that is, the excitation and signal beams passed through the sample and the sample cell windows. Another method to reduce the contribution of the sample cell windows is to accomplish the experiments in a reflection geometry. With the advent of surface-deposited samples such as those on the titania films (and more recently, samples simply evaporated onto substrates), it is possible to present the sample to the beams at near-grazing incidence. The phase matching conditions are maintained, but the resulting output angle of the signal must be calculated and the angle of detection adjusted. By illuminating the sample in this way, the beam overlap region is spread in a transverse direction along the sample, and the excitation beams largely reflect from the sample and only penetrate the substrate on which the sample is deposited to a depth of about a wavelength. Consequently, a substrate of any material can be used and need not have favourable optical properties. Given that surface-deposited samples need no solvent, the overall contribution of nonresonant background by solvent and windows is reduced to negligible levels. Data acquired in this way show a spectrally flat nonresonant background and clearly resolved peaks that are >20 times higher than the background.[67]

6.2.3. Active heterodyning

Heterodyne detection can increase the sensitivity of any nonlinear spectroscopy by removing the quadratic dependence of the signal on concentration. The detected intensity in the DOVE experiments can be defined as follows:

$$I = (E_{LO})^2 + (E_{HO})^2 + (E_{LO} \times E_{HO})\cos\phi \qquad \textbf{(equation 6.2)}$$

E_{HO} is the homodyne signal from the sample; it is simply the sum electric field as previously described. E_{LO} is the "local oscillator" field, that is, a field of identical frequency present on the detector with a fixed phase relationship to the homodyne signal. The phase difference between the two is denoted ϕ. In standard homodyne detection, there is no local oscillator field, and the intensity is simply the homodyne term $(E_{HO})^2$, which varies quadratically in concentration. In the case of dilute solutions, the local oscillator field is taken to be the nonresonant background, but equally this field can be externally provided by, e.g. focusing some of the pump

beam ω_3 into a crystal and creating a white-light continuum, which is then focused onto the detector and phase-locked to the signal from the sample. By so doing, and removing the $(E_{LO})^2$ term by lock-in detection, the cross term $(E_{LO} \times E_{HO})\cos\phi$ can be made to dominate the equation. With knowledge of the local oscillator strength, the output field is linear in concentration, clearly a sensitivity improvement when the sample concentrations are low. Further, this places no constraints on the size or spectral response of the nonresonant background.

6.2.4. Background suppression techniques

While the above methods to reduce the nonresonant background represent a great leap ahead in terms of both sensitivity and of sample preparation, it is worthwhile considering techniques to overcome the problem of nonresonant background in solution in order to keep the DOVE methodology flexible and widely applicable. One of the experimental parameters which has not been varied in any of the reported experiments is the manipulation of various polarisations. These experiments have been carried out with excitation beams all polarised in the same plane, and no effort has been made to isolate or measure the polarisation of the signal beam. These experiments thus are probing $\chi^{(3)}_{1111}$.

A number of efforts have been made to suppress the nonresonant background in CARS experiments, where this background also proves to be an ultimate limiting factor to the detectivity of the experiments. In the late 1970's, a novel method of background suppression was introduced known as the polarisation-sensitive CARS technique, where by analysing the output polarisation of the signal beam, the background can be selectively suppressed. The nonlinear interactions in the sample tend to depolarise the input beams, but there is a marked difference between the depolarisation induced by nonresonant interactions and that due to vibrational resonances. Thus the output signal contains information about both encoded in the polarisation. By taking difference spectra with varying orientations of a polariser between the sample and the detector, this depolarisation difference can selectively enhance the spectral features due to resonant interactions. Moreover, the interferences between the resonant and nonresonant contributions to the signal can be removed by separately measuring the real and imaginary parts of the resonant nonlinear susceptibility to allow a complete lineshape analysis.[68] Brakel *et.al.*[69] extend the methodology to highly absorbing solutions but note that purely symmetric

vibrations tend toward the same depolarisation ratio as the nonresonant background, so that for these vibrations, the background subtraction method may obscure resonances altogether.

A more successful method of background suppression was presented by Scholten *et. al.*.[24,70] suggesting that the phase matching angles can be arranged such that the nonresonant contribution from the sample cell windows exactly compensates the nonresonant contribution from the sample/solvent. This method avoids the shortcomings of the polarisation-sensitive technique, and an improvement of the signal-to-noise ratio of on the order of 50 has been achieved (albeit with a factor of 30 loss in the absolute signal size, a significant consideration in the small-signal regime).[24]

6.2.5. Resonance enhancement with visible excitation

The vibrational enhancements that give DOVE its name are the enabling feature that allows nonlinear vibrational spectroscopies in which the signals are not dominated by the nonresonant electronic polarisability. In the expressions for the density matrix elements and nonlinear susceptibilities in Chapter 2, the contributions from the electronic state are assumed to be sufficiently far from resonance that they do not change in the course of spectral scans over a few hundred wavenumbers, and are incorporated into the total expressions as multiplicative constants.[23] Resonance Raman studies have shown that a signal enhancement of as much as 10^6 over normal Raman spectroscopy can be gained from some vibrations if the excitation field falls within the electronic absorption envelope.[71] In analogy to the resonance Raman technique, it is possible to greatly increase DOVE signal sizes when the ω_3 excitation is resonant with an electronic absorption of the sample. Because the ω_3 excitation is always the final interaction in the coherence pathways, the electronic ground state is still being probed, and the high directionality and well-defined frequency of the output allows both spatial and spectral isolation of the output beam in the case of fluorescent samples, which typically produce a large amount of light but spread out into the full solid angle of 4π srad. Pilot studies were carried out on a sample of indocyanine green because of its electronic absorption at the ω_3 value of ~785 nm. The results show an increase of $\sim 10^4$ in signal intensity over the electronically nonresonant case. This triply resonant technique also opens the possibility of site-

selective spectroscopy for molecular samples such as haems in which a particular atom has a well-separated electronic absorption and the environment local to the haem group can be probed independently of the surrounding molecular structure.

6.3. Further dimensionality of the technique

All of the data presented in this thesis has concentrated on the DOVE coherence pathways. To date, only a very small spectral space has been covered and it is clear from the 2-D spectra of amino acids that this spectral space is fairly dense with features despite the relative simplicity of these molecules, suggesting that for more complex systems that the spectra may be too crowded with interfering peaks to serve as "fingerprints". However, we have at our disposal an incredible range of wavelengths to explore; the OPAs are capable of producing radiation from ~300 nm to >10 μm, so that a 2-D fingerprint could either span a larger range, or there may be spectral spaces of a similar size which will be less densely packed with features.

More importantly, we effectively have a number of other "dimensions" to explore with the technique. The shifts of peak positions or changes in lineshapes with adjustment of the temporal delays between pulses presented Chapters 4 and 5 have been until now treated as an experimental difficulty. However, these changes are indicative of dephasing processes, and will certainly be different for different molecules, or for similar molecules in different environments. Thus, these delays represent another dimension with which to explore the mode coupling—that is, the "fingerprinting" process could include fingerprints at more than one time.

Another dimension available but as yet unexplored is the existence of extra nonlinear signals; in Chapter 3 the possibility of simultaneous acquisition of DOVE and IR-IR-Vis sum frequency signals was explored. As mentioned in Chapter 2, all of the linear combinations of the input fields are being produced in the sample, with their relative intensities subject to phase matching conditions. It would be possible for instance to collect an IR-Vis sum-frequency signal (ω_1 or $\omega_2 + \omega_3$, spatially separated from the DOVE beam) as well as the DOVE signal. While such a second-order signal is precluded in centrosymmetric media, it has been shown to be possible for chiral molecules,[72] such as α-helices.

6.4. Future research directions

With the benefit of the sensitivity improvements outlined in section 6.2, a great many possibilities have been made available for current and future DOVE spectroscopy studies. In particular, recently developed sample preparation and presentation methods such as those presented in section 6.2.1 and 6.2.2 will permit the detailed study of samples that yield small signals. These studies have to date been limited due to the very complex interplay of resonant and nonresonant signals. Chapter 5 presented the possibility of cataloguing amino acid spectra, and with future studies of progressively more complex polypeptides and proteins in broader spectral spaces, DOVE may prove to be a complementary technique to MALDI-TOF and 2-D PAGE for the purpose of proteomics, metabolomics, etc. in which the composition of a complex mixture of biomolecules is of interest without a specific focus on structure or dynamics.

The preliminary study of polyalanine in Chapter 5 has paved the way for using DOVE as a probe of secondary structure in proteins, but much theoretical work is necessary to produce quantitative structural information from the DOVE spectra. The application of CMDVS techniques to biological systems is one arena where the experiments are leading the theory, despite the fact that many of the techniques now being implemented were postulated a number of years ago by nonlinear optical theorists. However, because the spectroscopy community has recognised the power of these techniques, a strong push towards a fuller understanding of multidimensional infrared spectra is being felt. A collaboration between ours and a theoretical group within the department has long been established and a more quantitative approach to unraveling the DOVE spectra is already underway.

Another key question about DOVE spectroscopy is its sensitivity to the phosphorylation of protein residues, which are well known as a ubiquitous cellular signaling mechanism but the sites and degrees of phosphorylation are difficult to nondestructively probe. DOVE spectroscopy can potentially outperform mass spectrometry and linear spectroscopies in terms of specificity and ease of sample preparation and data analysis.

6.5. Conclusions and perspectives

This thesis has presented DOVE spectroscopy as one of the optical analogues to multidimensional NMR and demonstrated the enormous power of CMDVS techniques to simplify the infrared spectra of biomolecules, giving a first insight into coupling origins and strengths that have heretofore been purely speculative. While the experiments are inherently very difficult and sensitive to the experimental conditions, a great many protocols have been developed in order to make the method repeatable and quantitative. The shortcomings of the method in terms of the complexity of resultant spectra have been addressed with novel sample preparation methods, and the limitations to throughput have already been largely solved by standard improvements presented in this chapter.

Given evidence such as that presented in this thesis and the attention that CMDVS techniques have recently received in the literature, there is little doubt that these techniques will develop in the near future to become a valued methodology for analytical chemistry, structural studies, and perhaps even to the microscopy community.[5] DOVE spectroscopy in particular provides incredible sensitivity compared to other leading CMDVS methods such as 2-D pump/probe. It can only be hoped, with the continued advancement of infrared sources and theoretical developments, that the analogous relationship between NMR and CMDVS techniques does not stop at a theoretical level and that these methods will eventually be equally commonplace, easily implemented, and reliable for the study of significantly more complex systems.

References

[1] Turner, J. J. in *Handbook of Vibrational Spectroscopy* (ed. Griffiths, P. R.) 101-127 (John Wiley and Sons, Chichester, UK, 2002).

[2] Scheurer, C., Mukamel, S. Infrared analogs of heteronuclear nuclear magnetic resonance coherence transfer experiments in peptides. *Journal of Chemical Physics* **116**, 6803-6816 (2002).

[3] Scheurer, C., Mukamel, S. Magnetic resonance analogies in multidimensional vibrational spectroscopy. *Bulletin of the Chemical Society of Japan* **75**, 989-999 (2002).

[4] Jonas, D. M. Optical Analogs of 2D NMR. *Science* **300**, 1515-1517 (2003).

[5] Wright, J. C. Coherent multidimensional vibrational spectroscopy. *International Reviews in Physical Chemistry* **21**, 185-255 (2002).

[6] Zanni, M. T., Ge, N., Kim, Y. S., Hochstrasser, R. M. Two-dimensional IR spectroscopy can be designed to eliminate the diagonal peaks and expose only the crosspeaks needed for structure determination. *Proceedings of the National Academy of Sciences of the United States of America* **98**, 11265-11270 (2001).

[7] Wright, J. C., Carlson, R. J., Hurst, G. B., Steehler, J. K., Riebe, M. T., Price, B. B., Nguyen, D. C., Lee, S. H. Molecular, Multiresonant Coherent 4-Wave-Mixing Spectroscopy. *International Reviews in Physical Chemistry* **10**, 349-390 (1991).

[8] Jonas, D. M. Two-Dimensional Femtosecond Spectroscopy. *Annual Review of Physical Chemistry* **54**, 425-463 (2003).

[9] Mukamel, S. Multidimensional femtosecond correlation spectroscopies of electronic and vibrational excitations. *Annual Review of Physical Chemistry* **51**, 691-729 (2000).

[10] Atkins, P. W., Friedman, R. S. *Molecular Quantum Mechanics* (Oxford University Press, Oxford, UK, 1997).

[11] Hamaguchi, H., Gustafson, T. L. Ultrafast Time-Resolved Spontaneous and Coherent Raman Spectroscopy: The Structure and Dynamics of Photogenerated Transient Species. *Annual Review of Physical Chemistry* **45**, 593-622 (1994).

[12] Deak, J. C., Iwaki, L. K., Dlott, D. D. When vibrations interact: ultrafast energy relaxation of vibrational pairs in polyatomic liquids. *Chemical Physics Letters* **293**, 405-411 (1998).

[13] Barth, A., Zscherp, C. What vibrations tell us about proteins. *Quarterly Reviews of Biophysics* **35**, 369-430 (2002).

[14] Chen, P. C., Hamilton, J. P., Zilian, A., Labuda, M. J., Wright, J. C. Experimental studies for a new family of infrared four-wave mixing spectroscopies. *Applied Spectroscopy* **52**, 380-392 (1998).

[15] Besemann, D. M., Condon, N. J., Meyer, K. A., Zhao, W., Wright, J. C. Experimental Determinations of Coherent Multidimensional Vibrational Spectroscopy. *Bulletin of the Korean Chemical Society* **24**, 1119-1125 (2003).

[16] Hamm, P. in *ESF Summer School in Ultrafast Spectroscopy* (Berlin, 2001).

[17] Wright, J. C., Chen, P. C., Hamilton, J. P., Zilian, A., LaBuda, M. J. Theoretical foundations for a new family of infrared four-wave mixing spectroscopies. *Applied Spectroscopy* **51**, 949-958 (1997).

[18] Carlson, R. J., Wright, J. C. Diagrammatic calculation of resonant optical susceptibilities in the presence of excited state populations and population feeding. *Physical Review A* **40**, 5092-5102 (1989).

[19] Steffen, T., Fourkas, J. T., Duppen, K. Time resolved four- and six-wave mixing in liquids. I. Theory. *Journal of Chemical Physics* **105**, 7364-7382 (1996).
[20] Khalil, M., Tokmakoff, A. Signatures of vibrational interactions in coherent two-dimensional infrared spectroscopy. *Chemical Physics* **266**, 213-230 (2001).
[21] Ivanecky, J. E., Wright, J. C. An investigation of the origins and efficiencies of higher-order nonlinear spectroscopic processes. *Chemical Physics Letters* **206**, 437-444 (1993).
[22] Besemann, D. M., Condon, N. J., Murdoch, K. M., Zhao, W., Meyer, K. A., Wright, J. C. Interference, dephasing, and vibrational coupling effects between coherence pathways in doubly vibrationally enhanced nonlinear spectroscopies. *Chemical Physics* **266**, 177-195 (2001).
[23] Wright, J. C., Condon, N. J., Murdoch, K. M., Besemann, D. M., Meyer, K. A. Quantitative Modeling of Nonlinear Processes in Coherent Two-Dimensional Vibrational Spectroscopy. *Journal of Physical Chemistry A* **107**, 8166-8176 (2003).
[24] Scholten, T., Lucassen, G. W., Koelewijn, E., Demul, F. F. M., Greve, J. Non-Resonant Background Suppression in Preresonance Cars Spectra of Flavin Adenine-Dinucleotide - Demonstration of a Background Suppression Technique Using Phase Mismatching and Comparison with the Polarization-Sensitive Cars Technique. *Journal of Raman Spectroscopy* **20**, 503-516 (1989).
[25] Murdoch, K. M., Thompson, D. E., Meyer, K. A., Wright, J. C. Modeling window contributions to four-wave mixing spectra and measurements of third-order optical susceptibilities. *Applied Spectroscopy* **54**, 1495-1505 (2000).
[26] Thompson, D. E., Wright, J. C. Model for spectral artifacts in two-dimensional four-wave mixing spectra from absorption and refractive index dispersion at infrared resonances. *Journal of Physical Chemistry A* **104**, 11282-11289 (2000).
[27] Tokmakoff, A. Two-dimensional line shapes derived from coherent third-order nonlinear spectroscopy. *Journal of Physical Chemistry A* **104**, 4247-4255 (2000).
[28] Meyer, K. A., Wright, J. C. Interference, Dephasing, and Coherent Control in Time-Resolved Frequency Domain Two-Dimensional Vibrational Spectra. *Journal of Physical Chemistry A* **107**, 8388-8395 (2003).
[29] Kwak, K., Cha, S., Cho, M. H., Wright, J. C. Vibrational interactions of acetonitrile: Doubly vibrationally resonant IR-IR-visible four-wave-mixing spectroscopy. *Journal of Chemical Physics* **117**, 5675-5687 (2002).
[30] Hamm, P., Wiemann, S., Zurek, M., Zinth, W. Highly sensitive multichannel spectrometer for subpicosecond spectroscopy in the midinfrared. *Optics Letters* **19**, 1642-1644 (1994).
[31] Bertie, J. E., Lan, Z. The Refractive-Index of Colorless Liquids in the Visible and Infrared - Contributions from the Absorption of Infrared and Ultraviolet-Radiation and the Electronic Molar Polarizability Below 20500 cm^{-1}. *Journal of Chemical Physics* **103**, 10152-10161 (1995).
[32] Bertie, J. E., Lan, Z. D. Liquid water-acetonitrile mixtures at 25 degrees C: The hydrogen-bonded structure studied through infrared absolute integrated absorption intensities. *Journal of Physical Chemistry B* **101**, 4111-4119 (1997).
[33] Siegman, A. E., Sasnett, M. W., Johnston, T. F. Choice of Clip Levels for Beam Width Measurements Using Knife- Edge Techniques. *IEEE Journal of Quantum Electronics* **27**, 1098-1104 (1991).
[34] Gutierrez, A., Dorn, P., Zeller, J., King, D., Lester, L. F., Rudolph, W., Sheik-Bahae, M. Autocorrelation measurement of femtosecond laser pulses by use of a ZnSe two-photon detector array. *Optics Letters* **24**, 1175-1177 (1999).

[35] Rudolph, W., Sheik-Bahae, M., Bernstein, A., Lester, L. F. Femtosecond autocorrelation measurements based on two-photon photoconductivity in ZnSe. *Optics Letters* **22**, 313-315 (1997).
[36] Barry, L. P., Bollond, P. G., Dudley, J. M., Harvey, J. D., Leonhardt, R. Autocorrelation of ultrashort pulses at 1.5 μm based on nonlinear response of silicon photodiodes. *Electronics Letters* **32**, 1922-1923 (1996).
[37] Takagi, Y., Kobayashi, T., Yoshihara, K., Imamura, S. Multiple- and single-shot autocorrelator based on two-photon conductivity in semiconductors. *Optics Letters* **17**, 658-660 (1992).
[38] Ranka, J. K., Gaeta, A. L., Baltuska, A., Pshenichnikov, M. S., Wiersma, D. A. Autocorrelation measurement of 6-fs pulses based on the two- photon-induced photocurrent in a GaAsP photodiode. *Optics Letters* **22**, 1344-1346 (1997).
[39] Briggman, K. A., Richter, L. J., Stephenson, J. C. Imaging and autocorrelation of ultrafast infrared laser pulses in the 3-11 μm range with silicon CCD cameras and photodiodes. *Optics Letters* **26**, 238-240 (2001).
[40] Zhao, W., Murdoch, K. M., Condon, N. J., Besemann, D. M., Meyer, K. A., Chen, P. C., Hamilton, J. P., Zilian, A., Labuda, M. J., Thompson, D. E., Carlson, R. J., Hurst, G. B., Riebe, M. T., Steehler, J. K., Wright, J. C. Comparisons between 2D doubly vibrationally enhanced four wave mixing and site selective spectroscopy. *Journal of Luminescence* **87-9**, 90-95 (2000).
[41] Zhao, W., Murdoch, K. M., Besemann, D. M., Condon, N. J., Meyer, K. A., Wright, J. C. Nonlinear two-dimensional vibrational spectroscopy. *Applied Spectroscopy* **54**, 1000-1004 (2000).
[42] Zhao, W., Wright, J. C. Measurement of $\chi^{(3)}$ for Doubly Vibrationally Enhanced Four Wave Mixing Spectroscopy. *Physical Review Letters* **83**, 1950-1953 (1999).
[43] Zhao, W., Wright, J. C. Doubly vibrationally enhanced four wave mixing: The optical analog to 2D NMR. *Physical Review Letters* **84**, 1411-1414 (2000).
[44] Zhao, W., Wright, J. C. Spectral simplification in vibrational spectroscopy using doubly vibrationally enhanced infrared four wave mixing. *Journal of the American Chemical Society* **121**, 10994-10998 (1999).
[45] Murdoch, K. M., Condon, N. J., Zhao, W., Besemann, D. M., Meyer, K. A., Wright, J. C. Isotope and mode selectivity in two-dimensional vibrational four wave mixing spectroscopy. *Chemical Physics Letters* **335**, 349-356 (2001).
[46] LaBuda, M. J., Wright, J. C. Measurement of vibrationally resonant $\chi^{(3)}$ and the feasibility of new vibrational spectroscopies. *Physical Review Letters* **79**, 2446-2449 (1997).
[47] Zhao, W., Wright, J. C. Analytical application of doubly vibrationally enhanced IR four-wave mixing: The optical analog to 2-D NMR. *Abstracts of Papers of the American Chemical Society* **218**, 168-ANYL (1999).
[48] Mollner, A. K., Brooksby, P. A., Loring, J. S., Bako, I., Palinkas, G., Fawcett, W. R. Ion-Solvent Interactions in Acetonitrile Solutions of Lithium Iodide and Tetrabutylammonium Iodide. *Journal of Physical Chemistry A* **108**, 3344-3349 (2004).
[49] Meyer, K. A., Wright, J. C. Detection limits for time-resolved coherent two-dimensional vibrational spectroscopy. *Analytical Chemistry* **73**, 5020-5025 (2001).
[50] Weyer, L. G., Lo, S.-C. in *Handbook of Vibrational Spectroscopy* (ed. Chalmers, J. M.) 1817-1837 (Wiley, 2002).
[51] Gore, R. C., Barnes, R. B., Petersen, E. Infrared Absorption of Aqueous Solutions of Organic Acids and Their Salts. *Analytical Chemistry* **21**, 382-386 (1949).

[52] Workman, J. Interpretive Spectroscopy for Near Infrared. *Applied Spectroscopy Reviews* **31**, 251-320 (1996).
[53] Holly, S., Egyed, O., Jalsovszky, G. q. Assignment problems of amino acids, di- and tripeptides and proteins in the near-infrared region. *Spectrochimica Acta* **48(A)**, 101-109 (1992).
[54] Mikhonin, A. V., Asher, S. A. Uncoupled peptide bond vibrations in α-helical and polyproline II conformations of polyalanine peptides. *Journal of Physical Chemistry B* **109**, 3047-3052 (2005).
[55] Quadrifoglio, F., Urry, D. W. Ultraviolet Rotatory Properties of Polypeptides in Solution. I. Helical Poly-L-alanine. *Journal of the American Chemical Society* **90**, 2755-2765 (1968).
[56] Koçak, A., Luque, R., Diem, M. The Solution Structure of Small Peptides: An IR CD Study of Aqueous Solutions of $(L\text{-}Ala)_n$ [n = 3, 4, 5, 6] at Different Temperatures and Ionic Strengths. *Biopolymers* **46**, 455-463 (1998).
[57] Barth, A. The infrared absorption of amino acid side chains. *Progress in Biophysics & Molecular Biology* **74**, 141-173 (2001).
[58] Hurst, G. B., Wright, J. C. Vibronic spectroscopy of amorphous materials using higher order, multiresonant coherent anti-Stokes Raman spectroscopy. *Journal of Chemical Physics* **97**, 3940-3949 (1992).
[59] Roh, W. B. Single-pulse coherent anti-Stokes Raman scattering. *Applied Physics Letters* **29**, 174-176 (1976).
[60] Tretzel, J., Schneider, F. W. Resonance multiplex cars of fluorescing acridines. *Chemical Physics Letters* **59**, 514-518 (1978).
[61] Stuart, B. C., Feit, M. D., Rubenchik, A. M., Shore, B. W., Perry, M. D. Laser-induced damage in dielectrics with nanosecond to subpicosecond pulses. *Physical Review Letters* **74**, 2248-2251 (1995).
[62] Kato, T., Tanimura, Y. Multi-dimensional vibrational spectroscopy measured from different phase-matching conditions. *Chemical Physics Letters* **341**, 329-337 (2001).
[63] Topoglidis, E., Cass, A. E. G., O'Regan, B., Durrant, J. R. Immobilisation and bioelectrochemistry of proteins on nanoporous TiO_2 and ZnO films. *Journal of Electroanalytical Chemistry* **517**, 20-27 (2001).
[64] Topoglidis, E., Campbell, C. J., Cass, A. E. G., Durrant, J. R. Factors that affect protein adsorption on nanostructured titania films. A novel spectroelectrochemical application to sensing. *Langmuir* **17**, 7899-7906 (2001).
[65] Topoglidis, E., Campbell, C. J., Palomares, E., Durrant, J. R. Photoelectrochemical study of Zn cytochrome-c immobilised on a nanoporous metal oxide electrode. *Chemical Communications* **8**, 1518-1519 (2002).
[66] Topoglidis, E., Cass, A. E. G., Gilardi, G., Sadeghi, S., Beaumont, N., Durrant, J. R. Protein adsorption on nanocrystalline TiO_2 films: An immobilization strategy for bioanalytical devices. *Analytical Chemistry* **70**, 5111-5113 (1998).
[67] Donaldson, P. M. (Imperial College London, forthcoming Ph.D. thesis).
[68] Oudar, J., Smith, R. W., Shen, Y. R. Polarization-sensitive coherent anti-Stokes Raman spectroscopy. *Applied Physics Letters* **34**, 758-760 (1979).
[69] Brakel, R., Mudogo, V., Schneider, F. W. Polarization sensitive resonance CARS spectroscopy. *Journal of Chemical Physics* **84**, 2451-2458 (1986).
[70] Scholten, T., Lucassen, G. W., Demul, F. F. M., Greve, J. Nonresonant Background Suppression in Cars Spectra of Dispersive Media Using Phase Mismatching. *Applied Optics* **28**, 1387-1400 (1989).

[71] McHale, J. L. in *Handbook of Vibrational Spectroscopy* (eds. Chalmers, J. M. & Griffiths, P. R.) 534-556 (John Wiley and Sons, Chichester, UK, 2002).
[72] Fischer, P., Albrecht, A. C., Wise, F. W. Chiral and achiral contributions to sum-frequency generation from optically active solutions of binaphthol. *Journal of Physical Chemistry A* **107**, 8232-8238 (2003).